EBM Experimental Biology and Medicine

Volume 249 | Issue 4

Experimental Biology and Medicine

Chief Editor

Steven Richard Goodman
University of Tennessee Health Science Center, Memphis, USA

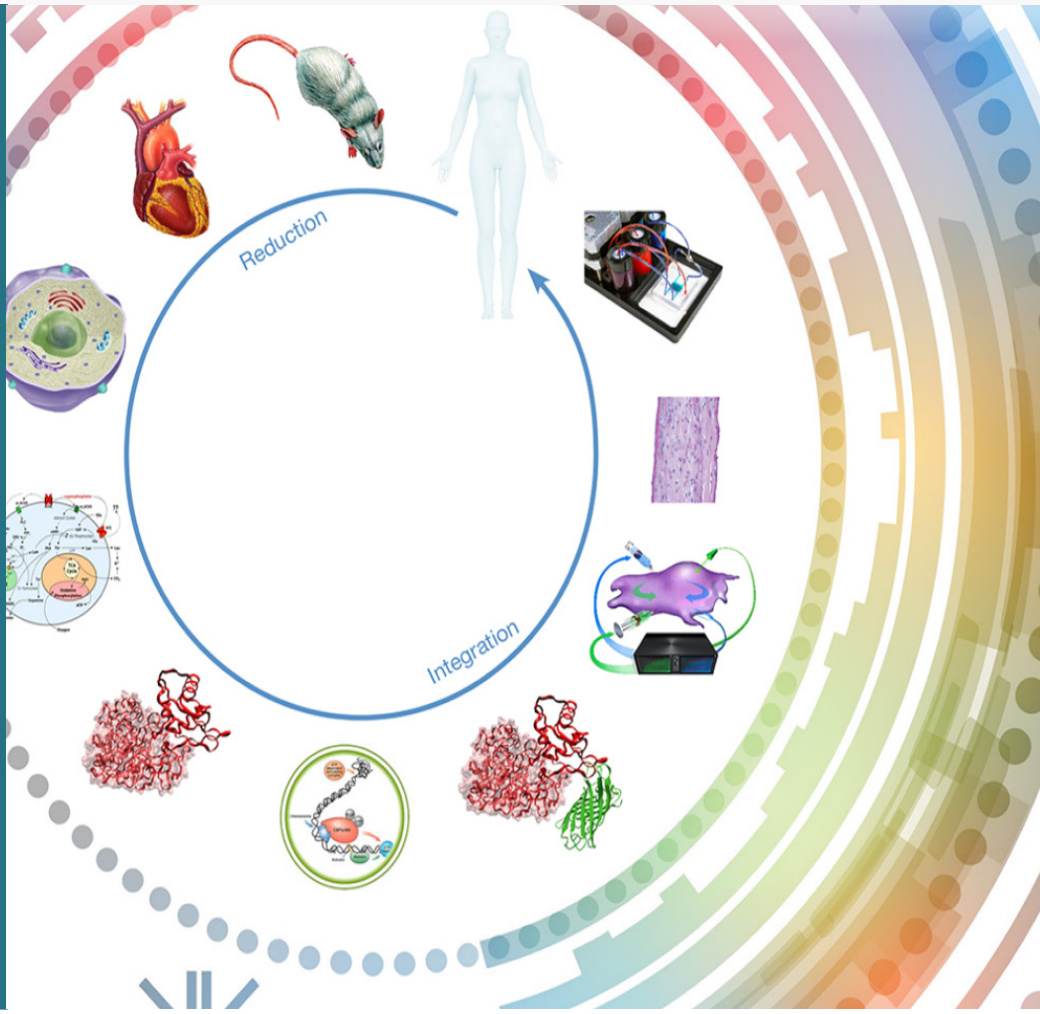

ISBN 978-2-8325-5184-4
DOI 10.3389/978-2-8325-5184-4

frontiers | Publishing Partnerships

SEBM Executive Council

Publication Committee

Society for Experimental Biology and Medicine
3220 N Street NW, #179
Washington DC 20007, USA
Executive Director – ed@sebm.org
Assistant to Editor-in-Chief – bzimmer@sebm.org

www.sebm.org

EBM Experimental Biology and Medicine

Editorial Board

ISSN 1535-3699
ISBN 978-2-8325-5184-4
DOI 10.3389/978-2-8325-5184-4

EBM Experimental Biology and Medicine

2024 | Volume 249 | Issue 4 | ISSN 1535-3699

Table of contents

Pharmacology and Toxicology

Original Research

Translational Research

Highlight

Review

Retraction

EBM Experimental Biology and Medicine

TYPE Original Research
PUBLISHED 31 May 2024
DOI 10.3389/ebm.2024.10122

OPEN ACCESS

*CORRESPONDENCE
Hikaru Kristi Ishibashi,
hikaru4@hirosaki-u.ac.jp

RECEIVED 19 July 2023
ACCEPTED 13 May 2024
PUBLISHED 31 May 2024

CITATION
Ishibashi HK, Nakamura Y, Saruga T, Imaizumi T, Kurose A, Kawaguchi S, Seya K, Sasaki E and Ishibashi Y (2024), TLR3 signaling-induced interferon-stimulated gene 56 plays a role in the pathogenesis of rheumatoid arthritis. *Exp. Biol. Med.* 249:10122. doi: 10.3389/ebm.2024.10122

TLR3 signaling-induced interferon-stimulated gene 56 plays a role in the pathogenesis of rheumatoid arthritis

Hikaru Kristi Ishibashi[1]*, Yuzuru Nakamura[1], Tatsuro Saruga[1], Tadaatsu Imaizumi[2], Akira Kurose[3], Shogo Kawaguchi[2], Kazuhiko Seya[2], Eiji Sasaki[1] and Yasuyuki Ishibashi[1]

[1]Department of Orthopaedic Surgery, Hirosaki University Graduate School of Medicine, Hirosaki, Aomori, Japan, [2]Department of Vascular Biology, Hirosaki University Graduate School of Medicine, Hirosaki, Aomori, Japan, [3]Department of Anatomic Pathology, Hirosaki University Graduate School of Medicine, Hirosaki, Aomori, Japan

Abstract

Rheumatoid fibroblast-like synoviocytes (RFLS) have an important role in the inflammatory pathogenesis of rheumatoid arthritis (RA). Toll-like receptor 3 (TLR3) is upregulated in RFLS; its activation leads to the production of interferon-β (IFN-β), a type I IFN. IFN-stimulated gene 56 (ISG56) is induced by IFN and is involved in innate immune responses; however, its role in RA remains unknown. Therefore, the purpose of this study was to investigate the role of TLR3-induced ISG56 in human RFLS. RFLS were treated with polyinosinic-polycytidylic acid (poly I:C), which served as a TLR3 ligand. ISG56, melanoma differentiation-associated gene 5 (MDA5), and C-X-C motif chemokine ligand 10 (CXCL10) expression were measured using quantitative reverse transcription-polymerase chain reaction, western blotting, and enzyme-linked immunosorbent assay. Using immunohistochemistry, we found that ISG56 was expressed in synovial tissues of patients with RA and osteoarthritis. Under poly I:C treatment, ISG56 was upregulated in RFLS. In addition, we found that the type I IFN-neutralizing antibody mixture suppressed ISG56 expression. ISG56 knockdown decreased CXCL10 expression and MDA5 knockdown decreased ISG56 expression. In addition, we found that ISG56 was strongly expressed in the synovial cells of patients with RA. TLR3 signaling induced ISG56 expression in RFLS and type I IFN was involved in ISG56 expression. ISG56 was also found to be associated with CXCL10 expression, suggesting that ISG56 may be involved in TLR3/type I IFN/CXCL10 axis, and play a role in RA synovial inflammation.

KEYWORDS

rheumatoid arthritis, ISG56, CXCL10, TLR3, synovitis

Impact statement

In human mesangial cells, the interferon (IFN)-stimulated gene 56 (ISG56) is induced by Toll-like receptor 3 (TLR3) signaling and is involved in innate inflammatory responses. The role of ISG56 in rheumatoid fibroblast-like synoviocytes (RFLS) remains unclear. Therefore, we evaluated ISG56 expression in cultured human RFLS using the TLR3 agonist. Under poly I:C treatment, ISG56 expression was upregulated in RFLS, and a type I IFN-neutralizing antibody mixture suppressed ISG56 expression. ISG56 knockdown decreased CXCL10 expression. ISG56 was strongly expressed in the synovial cells of patients with RA. TLR3 signaling induced ISG56 expression in RFLS and type I IFN was involved in ISG56 expression. These findings suggest that ISG56 is involved in the TLR3/type I IFN/CXCL10 axis, which plays an important role in the inflammatory responses in RFLS. Thus, ISG56 may be a potential target for the development of novel RA treatments.

Introduction

Rheumatoid arthritis (RA) is a systemic autoimmune disease that causes chronic inflammation of synovial joints as well as the cartilage and bones within the joint primarily. Fibroblast-like synoviocytes (FLS) are important in the pathogenesis of RA because FLS produce inflammatory cytokines and proteases that contribute to cartilage destruction [1]. Therefore, in recent years, RA therapies have focused on FLS targeting [2, 3]. Toll-like receptors (TLRs) are pattern recognition receptors (PRRs), present in various cells and tissues [4], capable of recognizing pathogen-associated molecular patterns (PAMPs; expressed by microbes) and danger-associated molecular patterns (DAMPs; expressed by dead or injured cells). TLR3 detects double-stranded RNA (dsRNA) to activate innate immune responses. In the joint fluid of RA patients, dsRNA levels are elevated [5], suggesting that dsRNA functions as DAMPs in RFLS. Activation of TLRs, including TLR3, in synoviocytes aggravates arthritis [6]. Therefore, understanding the contribution of TLR3 signaling in RFLS could provide a basis for the development of new therapeutic interventions. However, the molecular mechanisms underlying TLR3-mediated inflammation in RFLS have not been fully elucidated. The binding of dsRNA to TLR3 leads to the production of a type I interferon (IFN), IFN-β. IFN-β is a key cytokine in antiviral immunity. IFNs exert their biological effects by inducing the expression of hundreds of IFN-stimulated genes (ISGs). ISGs encode several chemokines which are small molecular proteins that induce the chemotactic activity of leukocytes, leading to pro-inflammatory reactions. An ISG example is the C-X-C motif chemokine ligand 10 (CXCL10). CXCL10 expression is upregulated in serum and tissue of patients with RA [7]. Owing to its role in leukocyte homing to inflamed tissues and the persistence of inflammation, CXCL10 upregulation may contribute significantly to tissue damage. In addition to CXCL10, other ISGs may contribute to rheumatoid synovial inflammation. Melanoma differentiation-associated gene 5 (MDA5) is a type I IFN-induced ISG in melanoma cells [8]. MDA5 is a DExH group RNA helicase; it functions as an ATPase and a signaling molecule that regulates inflammatory responses [9]. Saruga et al. [10] showed that the TLR3/type I IFN/CXCL10 axis plays an important role in the RFLS inflammatory response. In addition, MDA5 may be associated with this axis. Another ISG, ISG56 (official gene symbol: interferon-induced protein with tetratricopeptide repeat (IFIT) 1) is induced by dsRNA, type I IFN, and viruses [11]. It is associated with the innate immune response [12]. In addition, ISG56 is involved in immune and inflammatory responses induced by TLR3 signaling in human mesangial [9] and astrocytoma cells [13]. However, the expression and role of ISG56 in RFLS remains unknown. We hypothesized that ISG56 plays a role in rheumatoid synovitis downstream of TLR3. Therefore, in the current study, we aimed to investigate the expression and role of ISG56 in RFLS, using the TLR3 agonist polyinosinic-polycytidylic acid (poly I:C). In addition, we investigated the relationship between ISG56 and the TLR3/type I IFN/CXCL10 axis. In addition, we evaluated the expression of the ISG56 protein in the tissues of patients with RA.

Materials and methods

Cell culture

Patient-derived human RFLS were purchased from the Health Science Research Resource Bank (Sennan, Japan). The cells were cultured in Dulbecco's modified Eagle's medium supplemented with 10% fetal bovine serum and treated with 0.4–50 μg/mL poly I:C (Sigma-Aldrich, St. Louis, MO, United States). The cells were incubated for up to 24 h at 37°C. For experiments performed with the anti-human type I IFN-neutralizing antibody mixture (PBL Assay Science, Piscataway, NJ, United States), the cells were preincubated with the antibody mixture (1:25 dilution) for 1 h and stimulated with 10 μg/mL poly I:C for 16 h. For RNA interference, RFLS were transfected with non-silencing control small interfering RNA (siRNA) and siRNA against ISG56 or MDA5 (Qiagen, Hilden, Germany) using the Lipofectamine RNAiMAX reagent (ThermoFisher, Waltham, MA, United States), according to the manufacturer's instructions. The transfected cells were incubated for 48 h at 37°C. Subsequently, the cells were treated with poly I:C. This

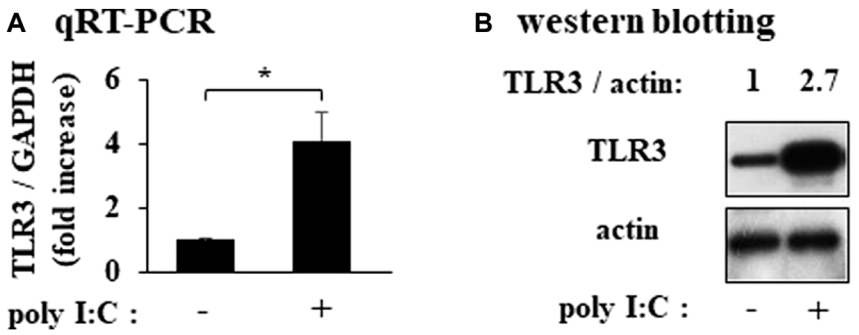

FIGURE 1
Expression of TLR3 in cultured human rheumatoid fibroblast-like synoviocytes (RFLS) incubated with polyinosinic-polycytidylic acid (poly I:C) **(A)** Cultured RFLS were treated with 10 μg/mL poly I:C for 8 h. After RNA extraction, cDNA was synthesized, and quantitative real-time PCR was performed to amplify TLR3 and GAPDH cDNA.TLR3 mRNA expression was normalized to that of GAPDH. Data for TLR3 are shown as fold increase relative to that of unstimulated cells. **(B)** Cells were treated with poly I:C and lysed after 16 h incubation. The lysates were subjected to western blotting to determine TLR3 and actin protein expression. *$p < 0.01$, by Student's t-test.

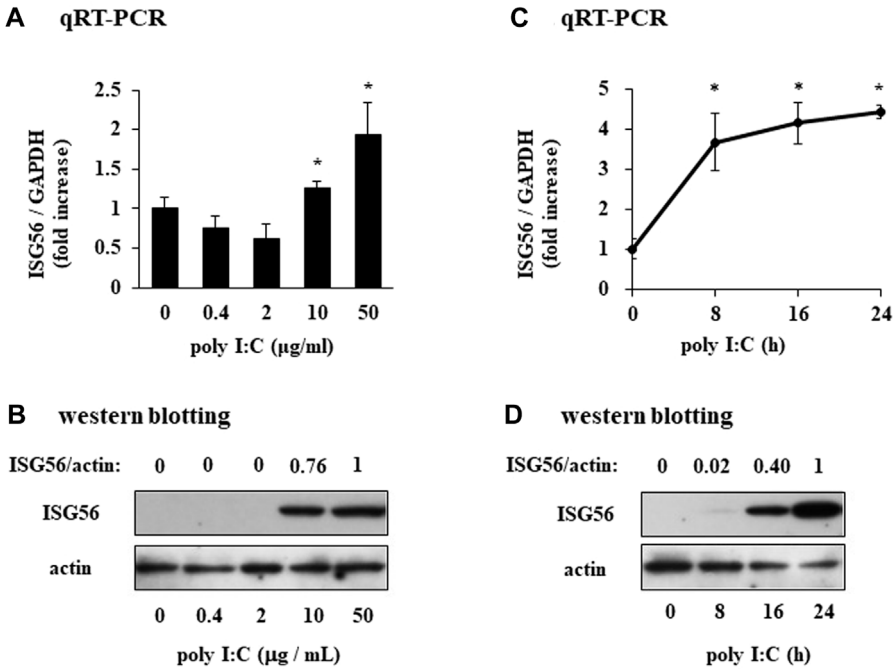

FIGURE 2
Expression of ISG56 in cultured human RFLS incubated with poly I:C **(A)** RFLS were cultured and treated with 0.4–50 μg/mL poly I:C. After 8 h of incubation, RNA was extracted, cDNA was synthesized, and quantitative real-time PCR was performed to amplify ISG56 and GAPDH cDNA. ISG56 mRNA expression was normalized to that of GAPDH. Data for ISG56 are shown as fold increase relative to that of unstimulated cells. **(B)** Cells were treated with poly I:C and lysed 16 h post-incubation. The lysates were subjected to western blotting to determine ISG56 and actin protein expression. **(C,D)** Time course of ISG56 mRNA and protein expression in RFLS incubated with poly I:C. The cells were treated with 30 μg/mL poly I:C for up to 24 h, and RNA and protein were obtained. ISG56 mRNA and protein expression was measured using qRT-PCR **(C)** and western blotting **(D)**, respectively. Data in **(A,C)** represent the mean ± standard deviation ($n = 3$). *$p < 0.01$, by Student's t-test.

study was approved by the Hirosaki University Graduate School of Medicine Ethics Committee (2018-1117) [10]. The sequences of siRNAs are as follows.

ISG56 sense strand; 5′-GGCUGUCCGCUUAAAUCCATT-3′,

ISG56 antisense strand; 5′-UGGAUUUAAGCGGACAGC CTG-3′,

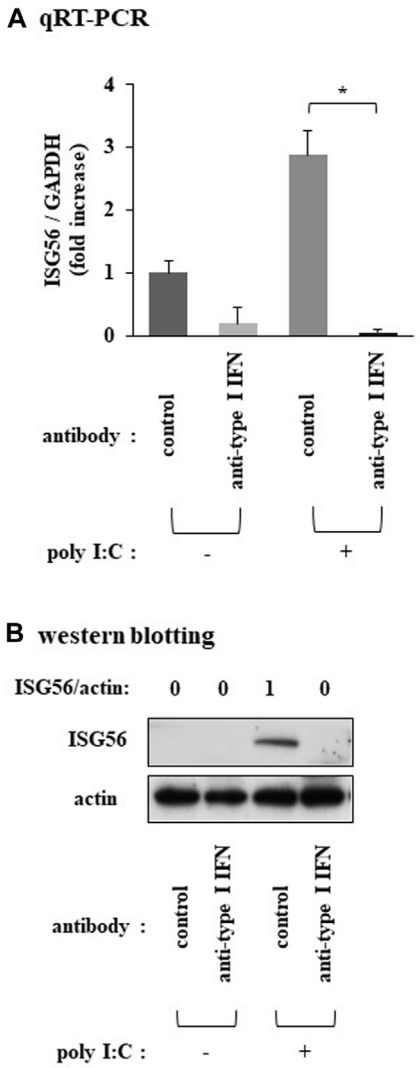

FIGURE 3
Expression of ISG56 under treatment with a neutralizing type I IFN antibody mixture in RFLS incubated with poly I:C Cells were preincubated with human type I IFN-neutralizing antibody mixture (1:25 dilution) for 1 h and further treated with 30 μg/mL poly I:C for 16 h. **(A)** RNA was extracted and qRT-PCR was performed. **(B)** Cells were lysed and ISG56 and actin protein expression were determined using western blotting. Data in **(A)** represent the mean ± standard deviation (n = 3). *p < 0.01, by Student's t-test.

MDA5 sense strand; 5′-GGUGUAAGAGAGCUACUA ATT-3′, and MDA5 antisense strand; 5′-UUAGUAGCUCUC UUACACCTG-3′.

Quantitative reverse transcription-polymerase chain reaction (qRT-PCR)

Total RNA was extracted from incubated cells and purified using the illustraRNA spin kit (GE healthcare, Buckinghamshire, England). Using the purified RNA product as the template and the oligo(dT)$_{18}$ primer and Moloney Murine Leukemia Virus reverse transcriptase (ThermoFisher), single-stranded cDNA was synthesized. The following primers were used for cDNA amplification:

TLR3-F: 5′- CTCAGAAGATTACCAGCCGCC -3′,
TLR3-R: 5′- CCATTATGAGACAGATCTAATG -3′,
ISG56-F: 5′-TAGCCAACATGTCCTCACAGAC-3′,
ISG56-R: 5′-TCTTCTACCACTGGTTTC-A-T-GC-3′,
CXCL10-F: 5′-TTCAAGGAGTACCTCTCTCTAG-3′,
CXCL10-R: 5′-CTGGATTCAGAC-A-T-CTCTTCTC-3′,
MDA5-F: 5′-GTTGAAAAGGCTGGCTGAAAAC-3′
MDA5-R: 5′-TCGATAACTCCTGAACCACTG-3′
GAPDH-F: 5′-GCACCGTCAAGGCTGAGAAC-3′,
GAPDH-R: 5′-ATGGTGGTGAAGACGCCAGT-3′.

To quantify ISG56, CXCL10, and MDA5 mRNA expression, a real-time PCR system was utilized with the SsoAdvanced Universal SYBR Green Supermix (Bio-Rad, Hercules, CA, United States). GAPDH was used as an internal control. ISG56 and MDA5 expression were each represented as a fold change relative to that in untreated cells. CXCL10 expression was below the CXCL10 expression detection limit in untreated cells; therefore, the data was expressed in arbitrary units.

Western blotting

Cultured cells were washed and lysed in Laemmli sample buffer. Cell lysates were subjected to electrophoretic separation using polyacrylamide gel electrophoresis. Then, the proteins were transferred to polyvinylidene fluoride membranes. The membranes were blocked and incubated, with rabbit antibodies against TLR3 (Cell Signaling Technology, Danvers, MA, United States; 1:1000 dilution), IFIT1/ISG56 (Genetex, Irvine, CA, United States; 1:2500 dilution), MDA5 (Immuno-Biological Laboratories, Gunma, Japan; 1:2000 dilution), or actin (Sigma-Aldrich; 1:5,000 dilution), overnight at 4°C. ISG56 and actin protein signals were obtained using a horseradish peroxidase (HRP)-conjugated anti-rabbit IgG gout antibody (Medical and Biological Laboratories, Tokyo, Japan; 1: 10,000 dilution) and an HRP chemiluminescent substrate. The bands of western blotting were quantified with ImageJ (National Institute of Health, United States).

Enzyme-linked immunosorbent assay (ELISA)

The cell culture medium was collected and centrifuged. The CXCL10 protein concentration, in the supernatant, was determined using a sandwich ELISA kit (R&D systems, Minneapolis, MN, United States).

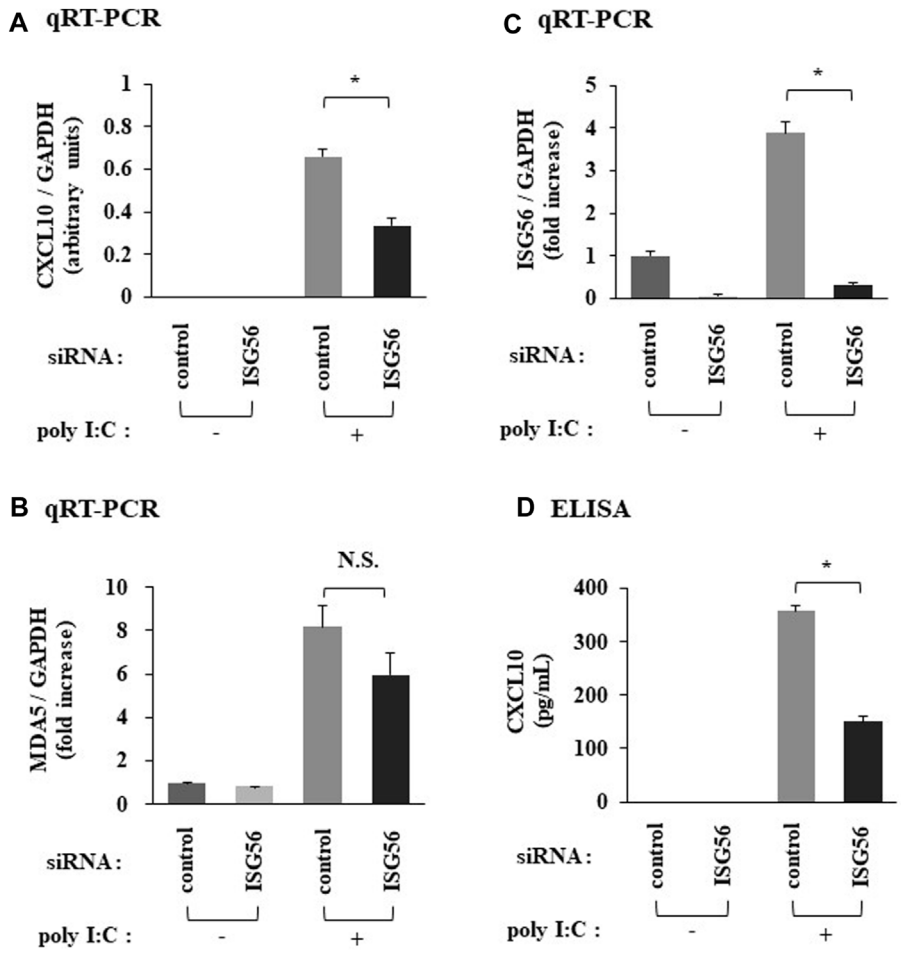

FIGURE 4
Expression of CXCL10 and MDA5 in poly IC-treated RFLS under the introduction of small interfering RNA (siRNA) against ISG56 Cells were transfected with siRNA against ISG56 and incubated for 48 h. Next, cells were treated with 30 μg/mL poly I:C for another 16 h. RNA was extracted and qRT-PCR was performed to determine CXCL10 **(A)**, MDA5 **(B)**, and ISG56 **(C)** mRNA expression. **(D)** The medium was collected and subjected to CXCL10 ELISA. Data from **(A–D)** represent the mean ± standard deviation (n = 3). *p < 0.01 by Student's t-test. NS, not significant by Student's t-test.

Statistics

Differences between groups were analyzed using the Student's t-tests. Data inputs and analyses were performed using SPSS version 29.0 (SPSS Inc., Chicago, IL, United States). Statistical significance was set at p-value < 0.05.

Immunohistochemical analysis

To determine ISG56 expression in human rheumatoid synovial tissue, we obtained knee synovial tissues from four RA and four osteoarthritis (OA) patients who had undergone total knee arthroplasty. Synovial tissues from patients with knee OA were used as controls. The obtained tissue samples were fixed in formalin, paraffin-embedded, and sliced into 3 μm thick sections. Sections were probed with rabbit anti-ISG56/IFIT1 polyclonal antibody (1:50, GTX31570, GeneTex) and incubated with biotinylated anti-rabbit IgG antibody and HRP-conjugated streptavidin. The ISG56 protein was detected using 3,3′-Diaminobenzidine, and the protein intensity was measured by a pathologist with more than 20 years of experience.

The study was performed in accordance with the 1964 Declaration of Helsinki and its later amendments or comparable ethical standards. Approval was obtained from the ethics committee of Hirosaki University Graduate School of Medicine (2018-1117). Written informed consent was obtained from all the participants.

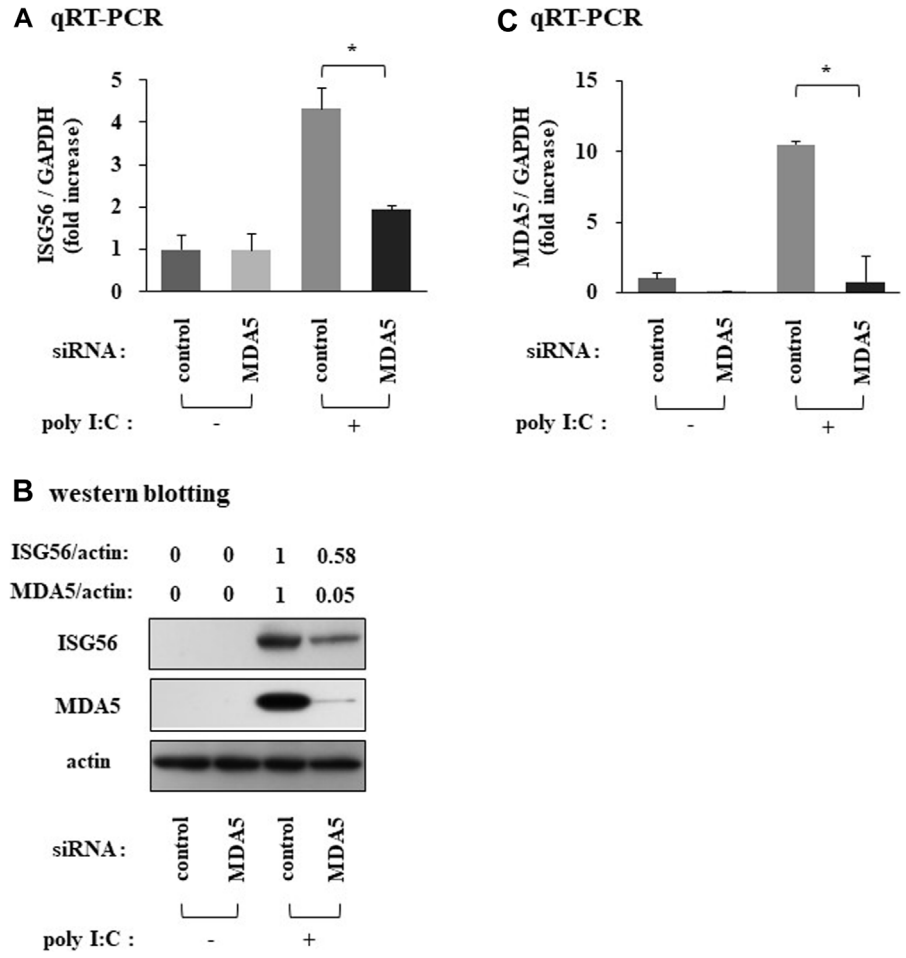

FIGURE 5
Expression of ISG56 under treatment with siRNA against MDA5 in RFLS Cells were transfected with siRNA against MDA5 and incubated for 48 h. Next, cells were treated with 30 μg/mL poly I:C for 16 h. RNA was extracted and qRT-PCR was performed to determine ISG56 **(A)** and MDA5 **(C)** mRNA expression. **(B)** Cells were lysed; ISG56, MDA5 and actin protein expression were measured using western blotting. Data from **(A,C)** represent the mean ± standard deviation (n = 3). *p < 0.01, by Student's t-test.

Results

TLR3 was expressed in RFLS

In cultured RFLS, TLR3 mRNA and protein were expressed and the expression were increased by treatment with poly I:C (Figures 1A, B).

Poly I:C induces the expression of ISG56 in cultured RFLS

In unstimulated RFLS, ISG56 expression was weak and the protein was undetectable (Figures 2A, B). In RFLS stimulated with low poly I:C concentrations (0.4 and 2 μg/mL), ISG56 mRNA was not upregulated. However, higher poly I:C concentrations (10 and 50 μg/mL) induced ISG56 mRNA (Figure 2A) and protein (Figure 2B) expression in RFLS. ISG56 mRNA and protein expression increased–8–24 h and, 16–24 h after poly IC treatment, respectively (Figures 2C, D).

Type I IFN is implicated in the expression of ISG56 under poly I:C treatment

Pretreatment of cells with a neutralizing anti-type I IFN antibody mixture almost completely reduced the poly I:C-mediated induction of ISG56 mRNA (Figure 3A) and protein (Figure 3B).

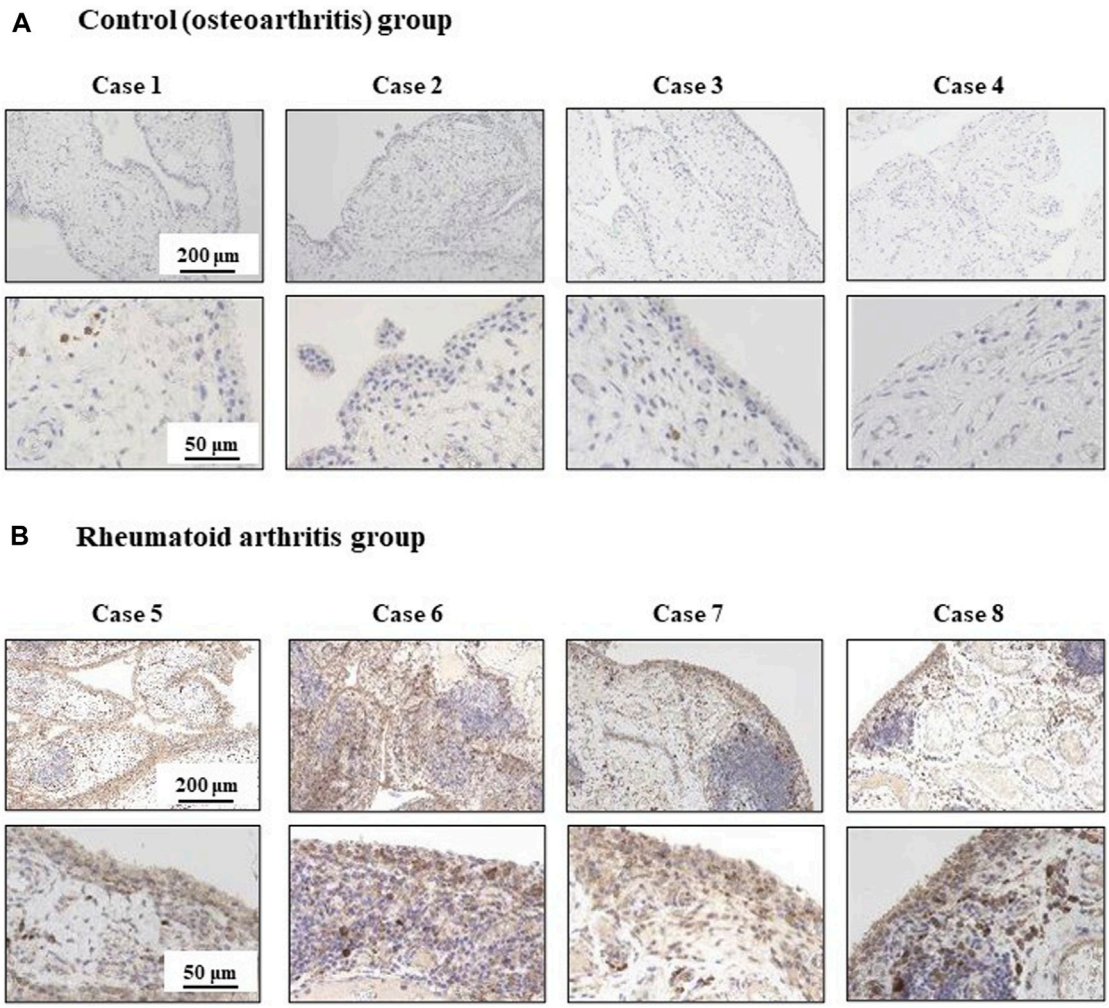

FIGURE 6
Immunohistochemical analysis for ISG56 in knee synovial tissue from osteoarthritis and rheumatoid arthritis patients Synovial tissue was collected from patients that underwent total knee arthroplasty. This included patients with osteoarthritis (OA) [cases 1-4, *n* = 4, **(A)**] and rheumatoid arthritis (RA) [cases 5-8, *n* = 4, **(B)**]. ISG56 expression was examined by immunohistochemistry. The immunoreactivity of ISG56 was stronger in RA synovial cells than in OA synovial cells.

ISG56 positively regulates the expression of CXCL10 under poly I:C treatment

Transfection of cells, under poly I:C treatment, with siRNA against ISG56 significantly reduced CXCL10 mRNA (Figure 4A) and protein (Figure 4D) expression. In ISG56 knockdown cells poly I:C did not significantly induce MDA5 mRNA expression (Figure 4B). ISG56 knockdown was confirmed using qRT-PCR (Figure 4C).

MDA5 positively mediates the expression of ISG56 under poly I:C treatment

SiRNA against MDA5 reduced the poly I:C-induced ISG56 mRNA (Figure 5A) and protein (Figure 5B) expression. MDA5 knockdown was confirmed using qRT-PCR and western blotting (Figures 5B, C).

ISG56 expression is upregulated in RA synovial cells

The immunohistochemistry results are shown in Figure 6. In the tissues of patients with OA, ISG56 immunoreactivity was positive in plasma cells, but negligible in synovial cells (case 1-4). In contrast, intense ISG56 immunoreactivity was observed in both the plasma and synovial cells of patients with RA (case 5–8).

Discussion

Multiple genetic and environmental factors are associated with the development of RA. Upon RA onset, innate and adaptive immunity are activated; as a result, a variety of immunoregulatory and proinflammatory molecules are

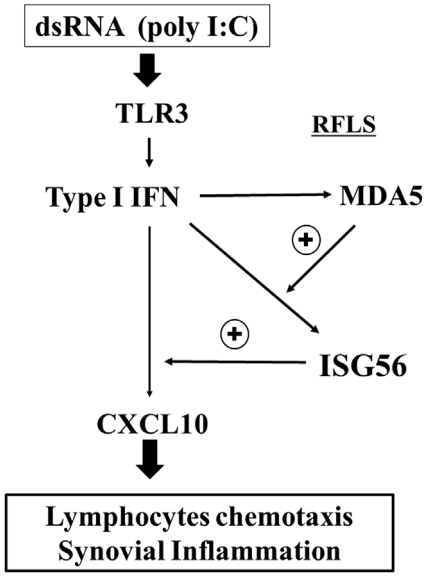

FIGURE 7
Predicted role of ISG56 expression via TLR3 in RFLS
TLR3 activation by poly I:C induces the expression of CXCL10 in RFLS. CXCL10 induction is positively regulated by ISG56, and ISG56 expression is upregulated by type I IFN and positively regulated by MDA5. CXCL10 induces lymphocyte chemotaxis followed by synovial inflammation. Thus, ISG56 may be involved in rheumatoid synovial inflammation, at least in part, by enhancing TLR3-mediated CXCL10 expression.

expressed [14]. FLS are an important cell type in RA pathogenesis [15]; therefore, elucidating the role of FLS in the pathogenesis of RA may provide important insights for developing new RA therapies. In this study, we evaluated the expression of ISG56, an IFN-inducible molecule involved in innate immunity, in cultured human RFLS. Here, we report that the treatment of RFLS with poly I:C, a TLR3 agonist, induced ISG56 expression. In addition, we showed that the neutralizing type I IFN antibody mixture inhibited poly IC-induced ISG56 expression, indicating that ISG56 may be induced in type I IFN-dependent manner. The involvement of TLR3 signaling in the pathogenesis of RA has been previously reported [16]; however, this is the first study that highlights the role of ISG56 in RFLS.

ISG56 is a member of the IFIT RNA-binding protein family. IFIT proteins function as anti-viral molecules via multiple mechanisms, such as inhibiting the translation of non-self RNA, during viral infection [17]. In addition to their antiviral functions, IFIT proteins are also associated with inflammation. ISG56 is associated with autoimmune diseases, such as systemic lupus erythematosus [18] and lupus nephritis [19, 20]. Therefore, the results of the present study strongly suggests that ISG56 is associated with RA pathogenesis.

Cytokines produced by FLS bind to their receptors, activate signaling cascades, and mediate inflammatory responses, leading to synovitis, cartilage, and bone destruction [1, 21]. Chemokines induce leukocyte chemotaxis; and chemokines as well as chemokine receptors play a pathogenic role in RA [22]. CXCL10, a chemokine, contributes to the pathogenesis of autoimmune diseases [23]. CXCL10 expression is higher in the synovial fluid and serum of patients with RA [7, 24]. In patients with RA, CXCL10 upregulates the receptor activator of nuclear factor-B ligand (RANKL), which is involved in bone destruction [25]. In addition, a human phase II clinical trial showed that an anti-CXCL10 monoclonal antibody significantly improved the American College of Rheumatology 20% improvement criteria [26]. These findings suggest that CXCL10 plays an important role in the pathogenesis of RA and that it is important to clarify the mechanisms underlying the role of CXCL10 in RFLS. In RFLS treated with poly I:C, CXCL10 is produced via the TLR3/type I IFN/CXCL10 axis; a reaction that also involves MDA5 (another ISG) [10]. In this study, we found that ISG56 knockdown decreases the expression of CXCL10, but not MDA5. In addition, we found that MDA5 knockdown decreases ISG56 expression. These results suggest that ISG56 may be involved in MDA5-mediated CXCL10 expression in RFLS and CXCL10-mediated synovial inflammation in rheumatic joints. Although the precise molecular mechanisms are not yet clear, the study results indicate that a complex network of ISGs may be involved in the RFLS signaling pathways. Further investigations are required to elucidate the molecular mechanisms.

We also found that ISG56 was upregulated in synoviocytes of patients with RA using immunohistochemical analysis. In contrast, ISG56 expression in synoviocytes of patients with OA was negligible. This suggests that ISG56 plays a role in synovial inflammation in the joints of patients with RA.

The current study has several limitations. In the present study, we did not elucidate the precise molecular mechanism underlying ISG56-mediated CXCL10 expression in poly I:C-treated RFLS. However, the immunohistochemistry results demonstrated a clear difference in ISG56 expression between patients with RA and OA. A small sample size was used. In addition, experiments using animal models have not yet been conducted. Therefore, further research is necessary to verify the results of the study.

Conclusion

This study showed that ISG56 expression is induced in cultured RFLS via the TLR3/type I IFN axis. In addition, it was shown that ISG56 may positively regulate CXCL10 expression, induced by TLR3 activation (Figure 7). Furthermore, ISG56 was upregulated in the synovial joint cells of patients with RA. These results indicate that ISG56 plays a role in RA pathogenesis. Thus, ISG56 may be a potential target for the development of novel RA therapies.

Author contributions

HI and TI took part in all the experiments and in the preparation of the manuscript. YN, TS, and AK participated in data collection, assisted with the statistical analysis. SK and KS contributed to cell culture. ES, YI, and TI conceived and designed the study. YI and TI supervised the team, facilitated the acquisition of data, and provided directions for the critical review of the manuscript. All authors contributed to the article and approved the submitted version.

Data availability

The original contributions presented in the study are included in the article/supplementary material, further inquiries can be directed to the corresponding author.

Ethics statement

The studies involving humans were approved by the ethics committee of the Hirosaki University Graduate School of Medicine (2018-1117). The studies were conducted in accordance with the local legislation and institutional requirements. The participants provided their written informed consent to participate in this study.

Funding

The authors declare that no financial support was received for the research, authorship, and/or publication of this article.

Acknowledgments

The authors thank Ms. Mao Takagi for her excellent technical assistance.

Conflict of interest

The authors declare that the research was conducted in the absence of any commercial or financial relationships that could be construed as a potential conflict of interest.

References

1. Müller-Ladner U, Kriegsmann J, Franklin BN, Matsumoto S, Geiler T, Gay RE, et al. Synovial fibroblasts of patients with rheumatoid arthritis attach to and invade normal human cartilage when engrafted into SCID mice. *Am J Pathol* (1996) **149**:1607–15.

2. Bartok B, Firestein GS. Fibroblast-like synoviocytes: key effector cells in rheumatoid arthritis. *Immunological Rev* (2010) **233**:233–55. doi:10.1111/j.0105-2896.2009.00859.x

3. Filer A. The fibroblast as a therapeutic target in rheumatoid arthritis. *Curr Opin Pharmacol* (2013) **13**:413–9. doi:10.1016/j.coph.2013.02.006

4. Akira S, Uematsu S, Takeuchi O. Pathogen recognition and innate immunity. *Cell* (2006) **124**:783–801. doi:10.1016/j.cell.2006.02.015

5. Bokarewa M, Tarkowski A, Lind M, Dahlberg L, Magnusson M. Arthritogenic dsRNA is present in synovial fluid from rheumatoid arthritis patients with an erosive disease course. *Eur J Immunol* (2008) **38**:3237–44. doi:10.1002/eji.200838362

6. Lin J, Luo F, Han S, Xia M, Chen Z, Liu P. Study on the mechanism of hydrolyzed seawater pearl tablet in treating chronic sleep deprivation mice model. *Endocr Metab Immune Disord - Drug Targets* (2023) **23**:927–36. doi:10.2174/1871530323666230206160722

7. Hanaoka R, Kasama T, Muramatsu M, Yajima N, Shiozawa F, Miwa Y, et al. A novel mechanism for the regulation of IFN-gamma inducible protein-10 expression in rheumatoid arthritis. *Arthritis Res Ther* (2003) **5**:74–81. doi:10.1186/ar616

8. Kang DC, Gopalkrishnan RV, Wu Q, Jankowsky E, Pyle AM, Fisher PB. mda-5: an interferon-inducible putative RNA helicase with double-stranded RNA-dependent ATPase activity and melanoma growth-suppressive properties. *Proc Natl Acad Sci U S A* (2002) **99**:637–42. doi:10.1073/pnas.022637199

9. Imaizumi T, Aizawa-Yashiro T, Matsumiya T, Yoshida H, Watanabe S, Tsuruga K, et al. Interaction between interferon-stimulated gene 56 and melanoma differentiation-associated gene 5 in Toll-like receptor 3 signaling in normal human mesangial cells. *Am J Nephrol* (2013) **37**:118–25. doi:10.1159/000346415

10. Saruga T, Imaizumi T, Kawaguchi S, Seya K, Matsumiya T, Sasaki E, et al. Role of MDA5 in regulating CXCL10 expression induced by TLR3 signaling in human rheumatoid fibroblast-like synoviocytes. *Mol Biol Rep* (2021) **48**(1):425–33. doi:10.1007/s11033-020-06069-z

11. Levy D, Larner A, Chaudhuri A, Babiss LE, Darnell JE, Jr. Interferon-stimulated transcription: isolation of an inducible gene and identification of its regulatory region. *Proc Natl Acad Sci U S A* (1986) **83**(23):8929–33. doi:10.1073/pnas.83.23.8929

12. Terenzi F, Hui DJ, Merrick WC, Sen GC. Distinct induction patterns and functions of two closely related interferon-inducible human genes, ISG54 and ISG56. *J Biol Chem* (2006) **281**(45):34064–71. doi:10.1074/jbc.m605771200

13. Imaizumi T, Numata A, Yano C, Yoshida H, Meng P, Hayakari R, et al. ISG54 and ISG56 are induced by TLR3 signaling in U373MG human astrocytoma cells: possible involvement in CXCL10 expression. *Neurosci Res* (2014) **84**:34–42. doi:10.1016/j.neures.2014.03.001

14. Giannini D, Antonucci M, Petrelli F, Bilia S, Alunno A, Puxeddu I. One year in review 2020: pathogenesis of rheumatoid arthritis. *Clin Exp Rheumatol* (2020) **38**(3):387–97. doi:10.55563/clinexprheumatol/3uj1ng

15. Mahmoud AB, Ajina R, Aref S, Darwish M, Alsayb M, Taher M, et al. Advances in immunotherapy for glioblastoma multiforme. *Front Immunol* (2022) **13**:944452. doi:10.3389/fimmu.2022.944452

16. Laska MJ, Hansen B, Troldborg A, Lorenzen T, Stengaard-Pedersen K, Junker P, et al. A non-synonymous single-nucleotide polymorphism in the gene encoding Toll-like Receptor 3 (TLR3) is associated with sero-negative rheumatoid arthritis (RA) in a Danish population. *BMC Res Notes* (2014) **7**:716. doi:10.1186/1756-0500-7-716

17. Fensterl V, Sen GC. Interferon-induced Ifit proteins: their role in viral pathogenesis. *J Virol* (2015) **89**(5):2462–8. doi:10.1128/jvi.02744-14

18. Feng X, Wu H, Grossman JM, Hanvivadhanakul P, FitzGerald JD, Park GS, et al. Association of increased interferon-inducible gene expression with disease activity and lupus nephritis in patients with systemic lupus erythematosus. *Arthritis Rheum* (2006) **54**(9):2951–62. doi:10.1002/art.22044

19. Tanaka H, Imaizumi T. Inflammatory chemokine expression via Toll-like receptor 3 signaling in normal human mesangial cells. *Clin Dev Immunol* (2013) **2013**:1–6. doi:10.1155/2013/984708

20. Joseph S, George NI, Green-Knox B, Treadwell EL, Word B, Yim S, et al. Epigenome-wide association study of peripheral blood mononuclear cells in systemic lupus erythematosus: identifying DNA methylation signatures associated with interferon-related genes based on ethnicity and SLEDAI. *J Autoimmun* (2019) **96**:147–57. doi:10.1016/j.jaut.2018.09.007

21. Scott DL, Wolfe F, Huizinga TW. Rheumatoid arthritis. *The Lancet* (2010) **376**(9746):1094–108. doi:10.1016/s0140-6736(10)60826-4

22. Maruyama T, Miyazaki H, Lim YJ, Gu J, Ishikawa M, Yoshida T, et al. Pyrolyzed deketene curcumin controls regulatory T cell generation and gastric cancer metabolism cooperate with 2-deoxy-d-glucose. *Front Immunol* (2023) **14**: 1049713. doi:10.3389/fimmu.2023.1049713

23. Antonelli A, Ferrari SM, Giuggioli D, Ferrannini E, Ferri C, Fallahi P. Chemokine (C-X-C motif) ligand (CXCL)10 in autoimmune diseases. *Autoimmun Rev* (2014) **13**(3):272–80. doi:10.1016/j.autrev.2013.10.010

24. Sucur A, Jajic Z, Artukovic M, Matijasevic MI, Anic B, Flegar D, et al. Chemokine signals are crucial for enhanced homing and differentiation of circulating osteoclast progenitor cells. *Arthritis Res Ther* (2017) **19**(1):142. doi:10.1186/s13075-017-1337-6

25. Kwak HB, Ha H, Kim HN, Lee JH, Kim HS, Lee S, et al. Reciprocal cross-talk between RANKL and interferon-gamma-inducible protein 10 is responsible for bone-erosive experimental arthritis. *Arthritis Rheum* (2008) **58**(5):1332–42. doi:10.1002/art.23372

26. Yellin M, Paliienko I, Balanescu A, Ter-Vartanian S, Tseluyko V, Xu LA, et al. A phase II, randomized, double-blind, placebo-controlled study evaluating the efficacy and safety of MDX-1100, a fully human anti-CXCL10 monoclonal antibody, in combination with methotrexate in patients with rheumatoid arthritis. *Arthritis Rheum* (2012) **64**(6):1730–9. doi:10.1002/art.34330

EBM Experimental Biology and Medicine

TYPE Original Research
PUBLISHED 27 June 2024
DOI 10.3389/ebm.2024.10106

OPEN ACCESS

*CORRESPONDENCE
Wei Wang,
wwwy@wnmc.edu.cn

†These authors have contributed equally to this work and share first authorship

RECEIVED 08 June 2023
ACCEPTED 02 October 2023
PUBLISHED 27 June 2024

CITATION
Wu Q, Lu M, Ouyang H, Zhou T, Lei J, Wang P and Wang W (2024), CDKL3 is a promising biomarker for diagnosis and prognosis prediction in patients with hepatocellular carcinoma.
Exp. Biol. Med. 249:10106.
doi: 10.3389/ebm.2024.10106

CDKL3 is a promising biomarker for diagnosis and prognosis prediction in patients with hepatocellular carcinoma

Qingsi Wu[1,2†], Mengran Lu[3†], Huijuan Ouyang[3†], Tingting Zhou[3], Jingyuan Lei[3], Panpan Wang[3] and Wei Wang[4*]

[1]Department of Blood Transfusion, Second Affiliated Hospital of Anhui Medical University, Hefei, Anhui, China, [2]Anhui Provincial Key Laboratory of Microbiology and Parasitology, Hefei, Anhui, China, [3]School of Public Health, Department of Hygiene Inspection and Quarantine, Anhui Medical University, Hefei, Anhui, China, [4]Department of Gastroenterology, Yijishan Hospital of Wannan Medical College, Wuhu, Anhui, China

Abstract

Cyclin-dependent kinase-like 3 (CDKL3) has been identified as an oncogene in certain types of tumors. Nonetheless, its function in hepatocellular carcinoma (HCC) is poorly understood. In this study, we conducted a comprehensive analysis of CDKL3 based on data from the HCC cohort of The Cancer Genome Atlas (TCGA). Our analysis included gene expression, diagnosis, prognosis, functional enrichment, tumor microenvironment and metabolic characteristics, tumor burden, mRNA expression-based stemness, alternative splicing, and prediction of therapy response. Additionally, we performed a cell counting kit-8 assay, TdT-mediated dUTP nick-end Labeling staining, migration assay, wound healing assay, colony formation assay, and nude mouse experiments to confirm the functional relevance of CDKL3 in HCC. Our findings showed that CDKL3 was significantly upregulated in HCC patients compared to controls. Various bioinformatic analyses suggested that CDKL3 could serve as a potential marker for HCC diagnosis and prognosis. Furthermore, CDKL3 was found to be involved in various mechanisms linked to the development of HCC, including copy number variation, tumor burden, genomic heterogeneity, cancer stemness, and alternative splicing of CDKL3. Notably, CDKL3 was also closely correlated with tumor immune cell infiltration and the expression of immune checkpoint markers. Additionally, CDKL3 was shown to independently function as a risk predictor for overall survival in HCC patients by multivariate Cox regression analysis. Furthermore, the knockdown of CDKL3 significantly inhibited cell proliferation *in vitro* and *in vivo*, indicating its role as an oncogene in HCC. Taken together, our findings suggest that CDKL3 shows promise as a biomarker for the detection and treatment outcome prediction of HCC patients.

KEYWORDS

CDKL3, biomarker, hepatocellular carcinoma, the cancer genome atlas, prognosis

Impact statement

Cyclin-dependent kinase-like 3 (CDKL3) has been reported as an oncogene in certain types of tumors. Nevertheless, its significance in hepatocellular carcinoma (HCC) has not been well investigated. This study demonstrated that CDKL3 was significantly upregulated in HCC patients compared to controls. Our analysis also showed that CDKL3 had independent prognostic value in HCC. Functional experiments further confirmed the oncogenic function of CDKL3 in HCC. Further research on the mechanisms underlying the function of CDKL3 in HCC is warranted.

Introduction

Hepatocellular carcinoma (HCC) represents the predominant subtype among primary liver cancers, constituting a majority, exceeding 90% of total cases [1]. This malignancy is frequently linked to well-recognized risk factors, namely, metabolic syndrome, hepatitis B and C viral infections, diabetes mellitus, and alcohol abuse [1]. The complex nature of HCC, with its diverse presentations and tumor heterogeneity, makes it challenging to treat. Additionally, HCC has a worse prognosis compared to many other types of cancer, and its mortality and incidence rates continue to rise globally [2]. Unfortunately, the diagnoses of a significant number of HCC patients are made when the malignancy has already progressed to an advanced stage, leading to dismal survival outcomes due to increased recurrence rates [3]. Therefore, it is crucial to investigate potential therapeutic targets and diagnostic/prognostic biomarkers for HCC to improve patient outcomes.

Cyclin-dependent kinase-like 3 (CDKL3), also referred to as NKIAMRE, is a constituent of the cyclin-dependent protein kinase-like family [4, 5]. It is located on human chromosome 5q31.1 and encodes a 52 kDa protein consisting of 455 amino acids [6]. CDKL3 was first identified in 2001 and plays a role in cell proliferation [7]. Although it is expressed at low levels in all tissues, it appears to have an essential function in regulating the cell cycle of tumor cells [8, 9]. Recent studies have found abnormal expression of CDKL3 in several cancers, particularly osteosarcoma, esophageal squamous cell carcinoma, colorectal cancer, glioma, and cholangiocarcinoma [6, 8, 10–12]. This abnormal expression is closely associated with tumor occurrence, development, and prognosis [13].

While some new diagnostic and prognostic markers for HCC have been reported in recent years [14, 15], research on CDKL3 in the context of tumors remains limited. Previous studies have primarily focused on diseases of the central nervous system [16–18]. However, a recent study by Sun et al. indicated that exosomal microRNA (miRNA)-205-5p from bone marrow mesenchymal stem cells can inhibit liver cancer, partially through the knockdown of CDKL3 [19]. Yet the role of CDKL3 in HCC has not been explored comprehensively. In this study, we utilized publicly available RNA sequencing (RNA-seq) data to examine the impact of CDKL3 in HCC patients. Furthermore, we conducted *in vitro* and *in vivo* functional assays to elucidate the potential biological function of CDKL3 in HCC.

Materials and methods

Data processing

The RNA-seq data consisting of copy number variation (CNV) data, messenger RNAs (mRNAs), long non-coding RNAs (lncRNAs), somatic mutation data (MuTect2), miRNAs, as well as clinicopathological information of HCC patients were obtained from The Cancer Genome Atlas (TCGA) database (LIHC dataset). The data were collected in December 2021 and preprocessed using the "TCGAbiolinks" package [20]. Additionally, DNA methylation data were acquired from UCSC Xena[1] and underwent preprocessing procedures consistent with previously documented methodologies [21]. The median beta value corresponding to the CDKL3 gene probes was mapped to its promoter, including 1stExon, 5′ untranslated region, transcription start site (TSS)200, and TSS1500 [22]. The mRNA and lncRNA data, originally presented in fragments per kilobase per million reads (FPKM), underwent a conversion to transcripts per kilobase million (TPM) values, followed by a subsequent $\log_2$ conversion. The mature miRNA (mirbase version 21) data, initially in row count values, were transmuted into reads per million mapped reads (RPM) and subjected to log2 conversion. Inclusion criteria for this study were patients diagnosed with primary solid HCC who were 18 years or older. Exclusion criteria included a history of preoperative adjuvant therapy, lack of survival time data, the recorded survival time <30 days, or multiple samples from a single patient [23]. A total of 330 HCC patients and 47 controls were ultimately enrolled. The clinicopathological information of the HCC patients can be found in Supplementary Table S1.

Expression and prognosis analyses

The investigation into pan-cancer expression profiles was facilitated through the TIMER 2.0 tool[2] [24]. The expression difference of CDKL3 between HCC patients and controls in the LIHC dataset was analyzed. Kaplan-Meier (KM) overall survival (OS) analysis with the log-rank test was conducted by dividing HCC patients into the high-CDKL3 (hCDKL3) group and the low-CDKL3 (lCDKL3) group. This division was based on the

1 https://xena.ucsc.edu

2 Accessible at http://timer.comp-genomics.org/

optimal cut-off expression values determined using the maximally selected rank statistics algorithm. The univariate Cox regression model was applied for survival analysis, and the expression difference of CDKL3 between the hCDKL3 and lCDKL3 groups was investigated. Multivariate Cox analysis was implemented to assess the independence of CDKL3 for OS prediction. Furthermore, a nomogram incorporating other independent parameters for OS prediction was established. Internal validation was executed by computing the adjusted Harrell's concordance index (C-index) utilizing the bootstrapping approach with 1,000 resamples [23]. The performance of the independent parameters of OS and the nomogram were evaluated using the areas under the curve (AUC) values, decision curve analysis (DCA), and calibration curves [25–27].

Bioinformatic analysis

To investigate the potential difference in biological function between the two groups, a gene set enrichment analysis (GSEA) was undertaken utilizing the Kyoto Encyclopedia of Genes and Genomes (KEGG) and HALLMARK gene sets derived from the Molecular Signatures Database (MSigDB[3]) [28]. To establish significance, we conducted a screening process that involved identifying p values < 0.05 and a false discovery rate >0.25. Furthermore, the functional annotation of genes in the KEGG pathway was performed using the online tool KOBAS-i[4] [29]. Single-sample GSEA (ssGSEA) was performed to explore the tumor microenvironment (TME) and metabolic characteristics using 29 functional gene expression signatures (Fges), which were recently proposed by Bagaev et al. [30]. Moreover, gene set variation analysis was employed to analyze metabolism-associated signatures, as detailed in established methods [31]. Immune checkpoint gene (ICG) expression discrepancies between the two groups were also analyzed. Somatic copy number alternation (SCNA) burden was assessed, representing the gain or depletion of total gene count at the focal and arm levels. This analysis was carried out using the GISTIC 2.0 module[5] [32, 33]. The calculation of tumor mutation burden (TMB) for every patient adhered to the methodology outlined in prior descriptions [34]. The mRNA expression-based stemness index (mRNAsi) for HCC patients was obtained from a published reference [35]. Additionally, the percent splice-in (PSI) value of CDKL3 was retrieved from the SpliceSeq database using default parameters[6] [36]. For the missing PSI values, the average value of each event was used to fill them up. Only events with a mean PSI value greater than 0.1 were retained for further analysis in this study. The details for analyzing competitive endogenous RNA regulatory networks and estimating the benefits of immunotherapy and chemotherapy can be found in the Supplementary Material.

Cell culture, transfection, quantitative real-time polymerase chain reaction (qPCR), and Western blot assays

The human HCC cell lines SMMC-7721 and HepG2 were acquired from GeneChem Corporation (Shanghai, China) and the Cell Bank of Type Culture Collection of the Chinese Academy of Sciences (Shanghai, China), respectively. Subsequently, RPMI-1640 (Gibco, Waltham, MA, United States) or Dulbecco's modified Eagle's medium (DMEM) added with 10% heat-inactivated fetal calf serum (FBS, Gibco, Thermo Fisher Scientific, Inc.) was used to culture these cell lines at 37°C. Concentrated and purified lentiviral particles expressing a short hairpin RNA (shRNA) were purchased from GeneChem Corporation (Shanghai, China). To perform transfection, the control lentivirus (shCtrl) or the target lentivirus (shCDKL3) was added to tumor cells (7×10^4 cells/well) in a six-well plate (Corning Incorporated, United States). After 72 h, the expression level of CDKL3 was assessed using qPCR and Western blot assays. More detailed information regarding the qPCR and Western blot assays can be found in the Supplementary Material.

Cell proliferation, colony formation, and apoptosis assays

The HCC cells, following infection, were placed in a 96-well plate (Corning Incorporated, United States) and subsequently cultured for a span of 4 days. To assess cellular proliferative capacity, we performed a daily cell counting kit-8 (CCK-8) assay (Beyotime's kit from Shanghai, China) as per package guidelines [37]. A colony formation experiment involved plating 2,000 infected cells per well over a 6-well plate. After 2 weeks of incubation, 4% paraformaldehyde solution (Beyotime, Shanghai, China) was employed to fix the tumor cells for 30 min. Subsequently, crystal violet solution (Beyotime, Shanghai, China) at 0.1% was utilized to stain the cells for 20 min. Under a light microscopy, the number of viable colonies (>50 cells/colony) was determined. To perform the apoptosis assay, we plated the infected cells on prepositioned slides in a 12-well plate (Corning Incorporated, United States). After an overnight incubation, the cells were immobilized with a 4% paraformaldehyde solution for 30 min. The nuclei were stained using DAPI (Beyotime, Shanghai, China). The

3 https://www.gsea-msigdb.org
4 http://kobas.cbi.pku.edu.cn/
5 https://www.genepattern.org/
6 http://bioinformatics.mdanderson.org/TCGASpliceSeq/index.jsp

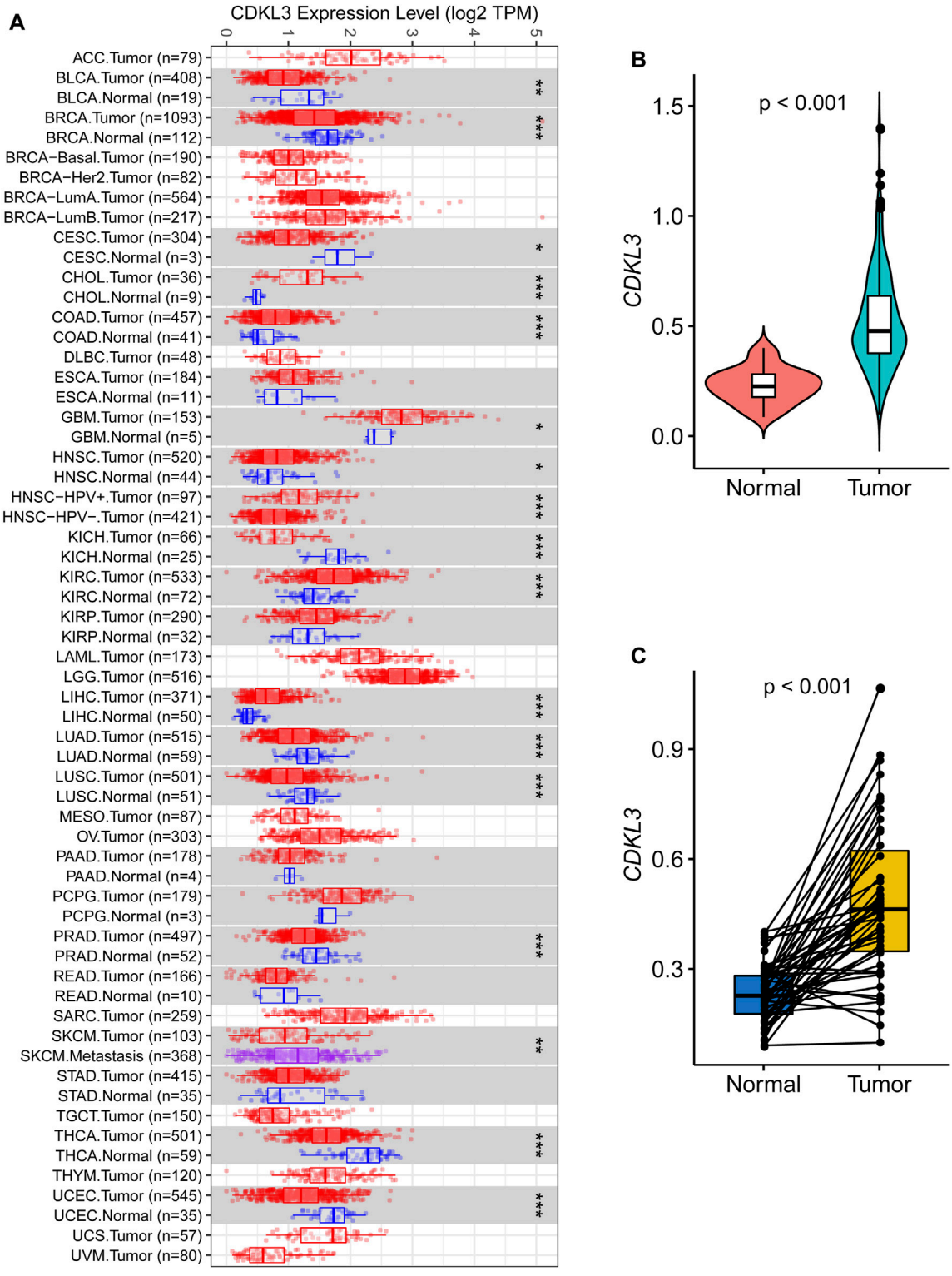

FIGURE 1
Expression of CDKL3 in HCC. **(A)** The expression of CDKL3 in Pan-cancer based on TCGA data via Tumor IMmune Estimation Resource 2.0 (TIMER 2.0, http://timer.comp-genomics.org/). Comparative CDKL3 expression levels in HCC and adjacent normal tissue: plots of unpaired **(B)** and paired **(C)** data. HCC, hepatocellular carcinoma.

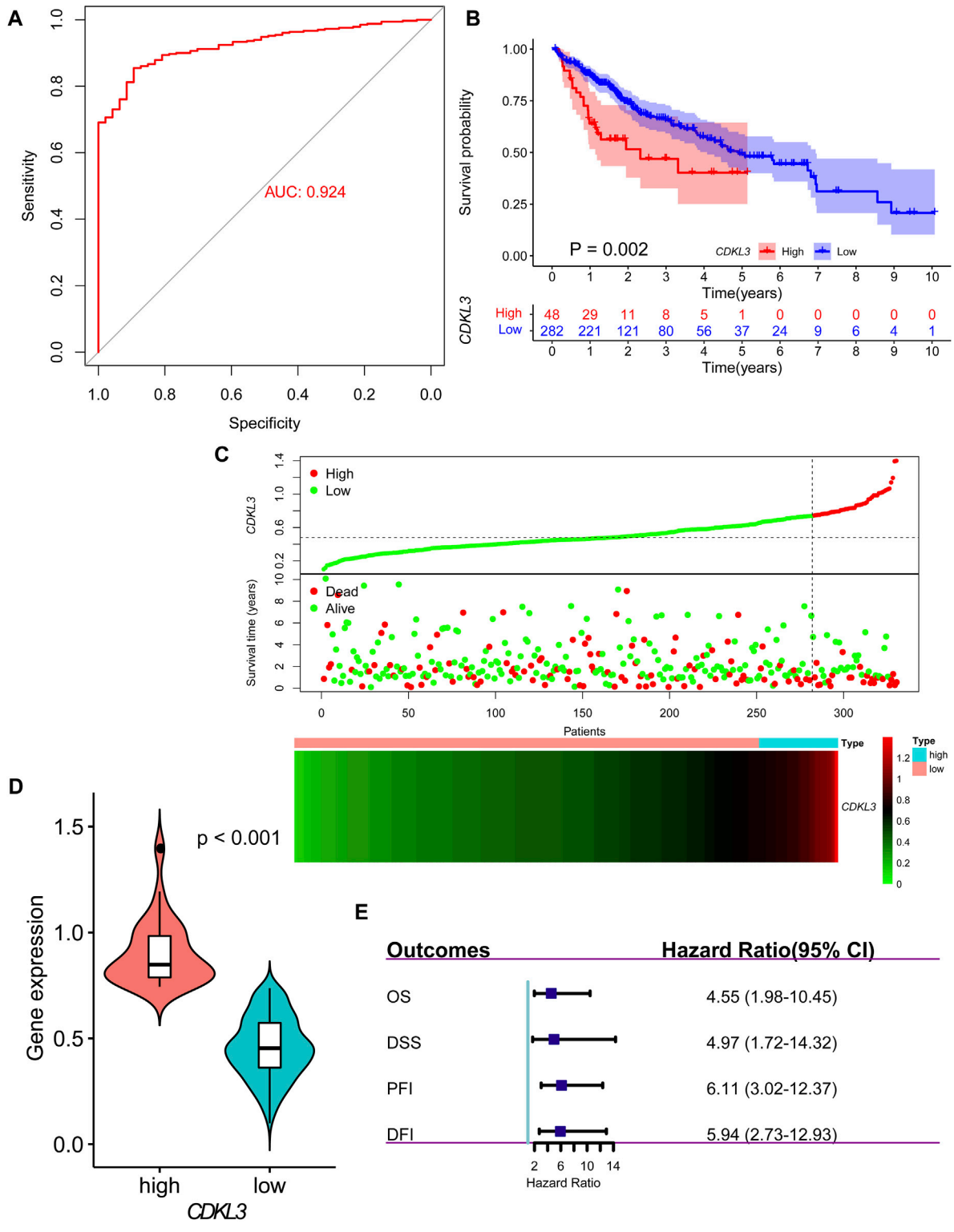

FIGURE 2
Diagnosis and prognosis of CDKL3 in HCC. **(A)** ROC curve for CDKL3 expression in HCC. **(B)** Kaplan-Meier overall survival curves of hCDKL3 and lCDKL3 and the survival difference was evaluated by log-rank test. **(C)** The dot plot and heatmap demonstrating the survival status and expression of CDKL3 in hCDKL3 and lCDKL3, respectively. **(D)** The expression of CDKL3 was compared between

(*Continued*)

FIGURE 2 (Continued)
hCDKL3 and lCDKL3. **(E)** Forest plot showing the results of univariate Cox analyses for overall survival, disease-specific survival, progression-free interval and disease-free interval. HCC, hepatocellular carcinoma; hCDKL3, high-CDKL3 group; lCDKL3, low-CDKL3 group.

detection of cell apoptotic rate was carried out utilizing a TdT-mediated dUTP nick-end labeling (TUNEL) kit (Beyotime, Shanghai, China), as described previously [38].

Tumour xenograft assay

For the tumor xenograft assay, six BALB/C nude mice (Henan Scrobes Company, China), aged 5 weeks, were used in each group (n = 6/group). At the Center for Laboratory Animal Research in Anhui Medical University, the mice were housed in a pathogen-free environment. All experiments with animals were done in compliance with institutional guidelines and with appropriate oversight. The Experimental Animal Ethics Committee of Anhui Medical University approved this study (No. 20200695). Subcutaneous transplantation of SMMC-7721 cells stably expressing shControl or shCDKL3 (3×10^6 cells) was performed on the upper right back of the mice. The size of the tumor (computed as: [(π/6) × (length) × (width) [2]]) and its weight were measured every 4 days over a duration of 4 weeks until the humane euthanasia of mice.

Statistical analysis

Categorical data were compared utilizing the chi-square or Fisher's exact test, whereas the Wilcoxon rank-sum test or Kruskal–Wallis test was employed for the comparison of continuous variables. The correlation was tested using a rank correlation method, either Pearson's or Spearman's. R 4.0.1 (The R Foundation for Statistical Computing, Vienna, Austria) and GraphPad Prism 8.0.2 (GraphPad Software, Inc.) were used to perform all statistical tests. Statistical significance was assumed when the p-value was <0.05 (two-tailed) unless otherwise specified.

Results

CDKL3 is a potential prognostic factor for HCC patients

Analysis of data from TIMER 2.0 revealed that CDKL3 was significantly dysregulated in various solid tumors (Figure 1A). In the TCGA dataset, both unpaired and paired analyses demonstrated markedly upregulated levels of CDKL3 in HCC patients compared to controls (Figures 1B, C). Notably, CDKL3 displayed excellent diagnostic performance for HCC, with an impressive AUC value of 0.924 (Figure 2A). KM analysis revealed that the OS of the hCDKL3 group was lower than the lCDKL3 group (Figures 2B, C). Consistent results were observed for progression-free interval (PFI), disease-free interval (DFI), and disease-specific survival (DSS) (Supplementary Figure S1). Figure 2D illustrates the gene expression differences between the hCDKL3 and lCDKL3 groups. Univariate Cox analysis highlighted the association of CDKL3 level with OS, DSS, DFI, and PFI (Figure 2E). Additionally, we explored how CDKL3 expression related to clinicopathological variables (like tumor grade and family history of cancer), and found a substantial link between the two (Supplementary Figure S2).

Construction of a survival nomogram

CDKL3 was shown to independently function as a predictor of OS in a multivariate Cox regression study (Figure 3A). To aid in clinical decision-making, a nomogram was devised incorporating CDKL3 level and other independent clinicopathological variables (Figure 3B). The predicted and observed survival rates were highly consistent, as shown by calibration curve graphs (Supplementary Figure S3A). Receiver operating characteristic (ROC) curve analysis illustrated that the nomogram outperformed individual factors alone in estimating 1-, 3-, and 5-year OS, as indicated by higher AUC values (0.78, 0.75, and 0.78, respectively) (Supplementary Figure S3B). Furthermore, DCA demonstrated that the nomogram yielded greater net benefits compared to individual factors (Supplementary Figure S3C). Internal validation yielded an adjusted C-index of 0.713, indicating the reliability of the nomogram in prognostic prediction.

Genetic features between the hCDKL3 and lCDKL3

The Supplementary Figures S4, S5 presented the mutation-related findings of CDKL3. In terms of the mRNAsi, the hCDKL3 group exhibited a score superior to that of the lCDKL3 cohort (Figure 4A). Furthermore, the CDKL3 expression was positively linked to the mRNAsi score

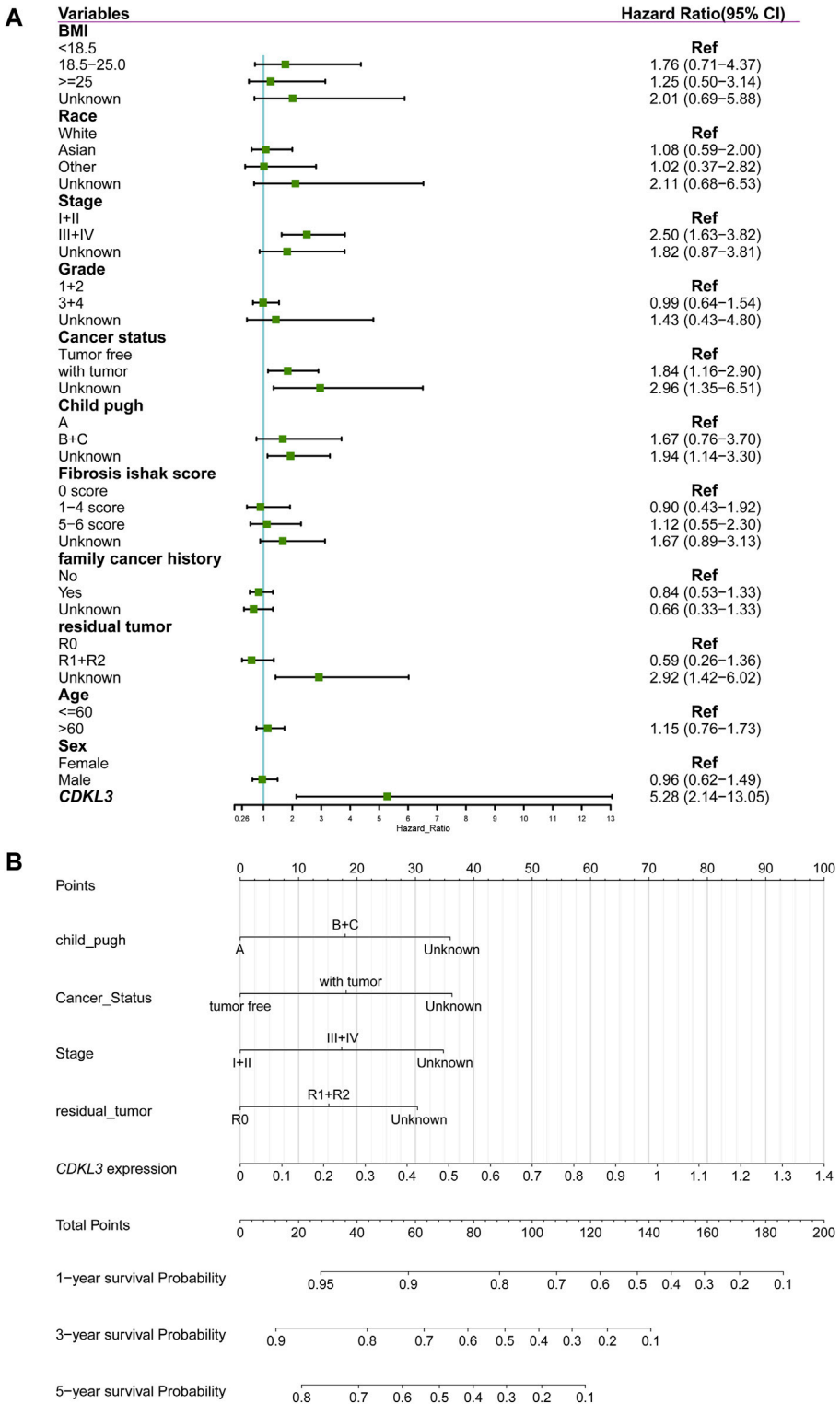

FIGURE 3
Construction of nomogram for predicting overall survival of hepatocellular carcinoma in TCGA cohort. **(A)** Forest plot showing the results of multivariate Cox analysis. **(B)** Nomogram.

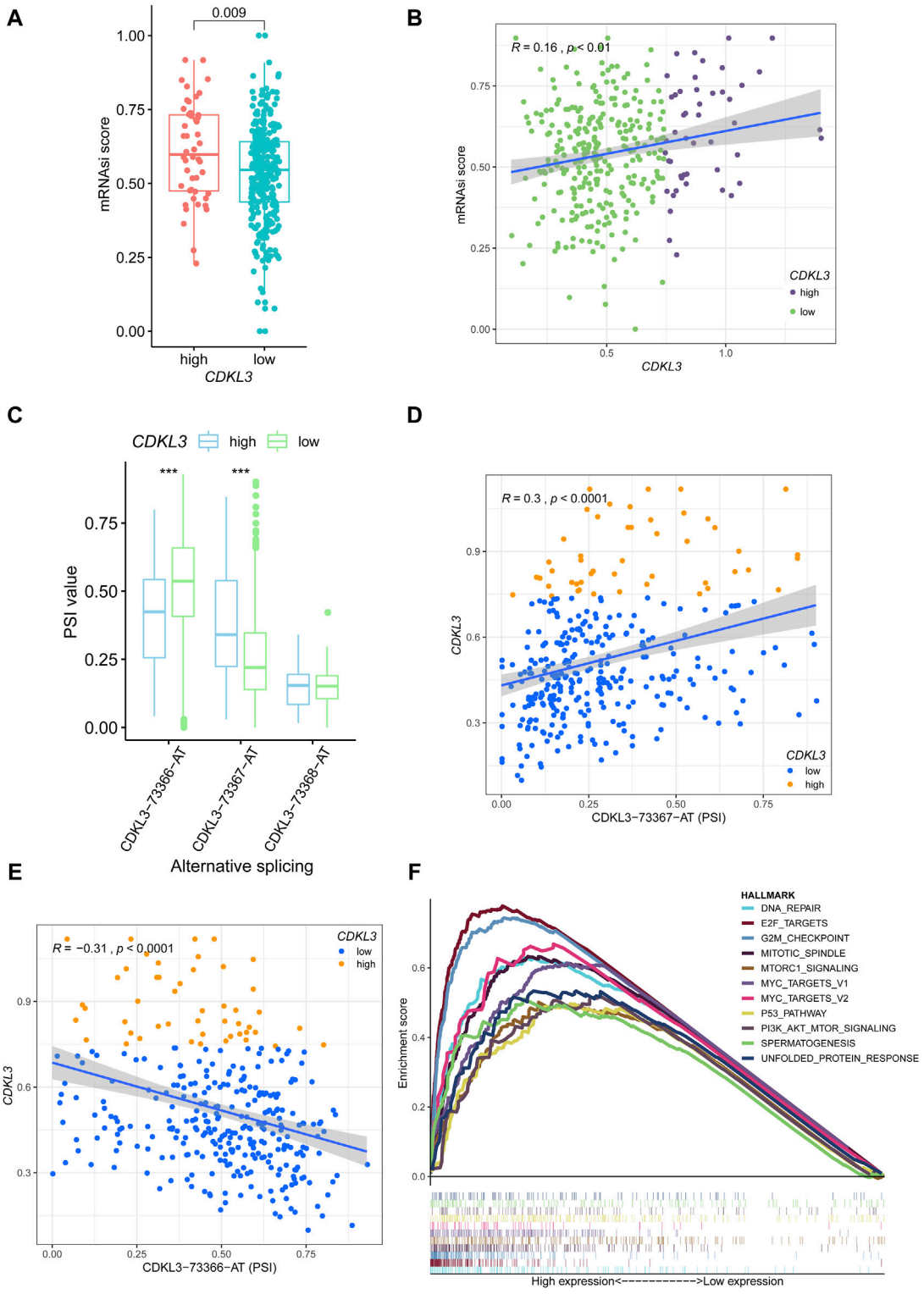

FIGURE 4
Genetic features of CDKL3 in HCC. **(A)** The mRNAsi score was compared between hCDKL3 and lCDKL3. **(B)** The relationship between the CDKL3 expression and mRNAsi score. **(C)** The PSI values of three alternative splicings were compared between hCDKL3 and lCDKL3. **(D)** The relationship between CDKL3 expression and PSI values of CDKL3-73367-AT. **(E)** The relationship

(*Continued*)

FIGURE 4 (Continued)
between CDKL3 expression and PSI values of CDKL3-73366-AT. **(F)** The hallmarks of tumor sets were enriched in hCDKL3 using GSEA. ***$p < 0.001$. HCC, hepatocellular carcinoma; hCDKL3, high-CDKL3 group; lCDKL3, low-CDKL3 group; PSI, percent splice-in.

(Figure 4B). Figure 4C demonstrated three alternative splicing events for CDKL3. The hCDKL3 group displayed a higher PSI value for CDKL3−73367−AT and a lower PSI value for CDKL3−73366−AT when compared to the lCDKL3 group. Additionally, the expression of CDKL3 had a positive correlation with the PSI value of CDKL3−73367−AT and a negative correlation with the PSI value of CDKL3−73366−AT (Figures 4D, E). Interestingly, Figure 4F revealed that the hCDKL3 group was significantly enriched in hallmark pathways associated with tumorigenesis, especially the G2/M checkpoint, E2F targets, DNA repair, MYC targets V1 and V2, the P53 pathway, and PI3K−AKT−MTOR signaling. These findings strongly suggest that the hCDKL3 and lCDKL3 groups exhibit distinct genetic features.

TME and metabolism characteristics of the hCDKL3 and lCDKL3 groups

Figure 5A demonstrates that the lCDKL3 group is characterized by a significantly decreased enrichment score of the proliferation rate signature and a notably elevated enrichment score of Fges, which is related to the cluster of antitumor immune infiltrates. This enrichment included antitumor cytokines, B cells, NK cells, effector cells, the Th1 signature, and T-cell traffic signatures. Correlation analysis confirmed a positive link between CDKL3 expression and the enrichment score of the proliferation rate signature, and a negative correlation with the enrichment score of antitumor cytokines, B cells, NK cells, effector cells, the Th1 signature, and T-cell traffic signatures (Supplementary Figure S6). Moreover, an investigation into the difference in T-cell exhaustion markers between the lCDKL3 and hCDKL3 groups highlighted that hCDKL3 was associated with increased expression of markers such as BTNL2, CD276, CD40, HAVCR2, LAIR1, LGALS9, NRP1, TNFRSF4, TNFSF9, and VTCN1 (Figure 5B). Additionally, the results of GSEA of KEGG pathways indicated that both the lCDKL3 and hCDKL3 groups were significantly enriched in multiple metabolic pathways (Figure 6). Further exploration of the enrichment scores of metabolism-associated pathways in the four categories (amino acids, carbohydrates, lipids, and others) between the lCDKL3 and hCDKL3 groups revealed significant differences. Notably, the hCDKL3 group exhibited significantly decreased pathway enrichment scores for lipid and other pathways. Similar patterns were observed in most amino acid and carbohydrate pathways, except for the GLUCOSE, PURINE, PYRIMIDINE, and SELENOAMINO ACID metabolism pathways (Supplementary Figures S7A–D). Additionally, the CDKL3 levels were inversely linked to the enrichment score of most differentially enriched pathways (Supplementary Figure S7E). Altogether, these findings suggest that the lCDKL3 and hCDKL3 groups possess distinct TME and metabolism characteristics.

Functional annotations and tumour immune single-cell analysis

We conducted a thorough screening of 50 protein-coding genes that showed a strong positive correlation with CDKL3, as well as 50 genes that displayed a negative correlation (Supplementary Table S2). Utilizing KOBAS-i, we executed functional annotation of these genes in the KEGG pathway, and observed significant enrichment in various clusters and functions (Supplementary Figure S8). Specifically, these genes were found to be closely associated with metabolism pathways, the TGF-beta signalling pathway, and the PPAR signalling pathway, all of which were considered to impart a substantial role in the growth of HCC (adjusted p-value <0.05). For further analysis, we turned to the TISCH database, where we conducted a single-cell analysis to assess the expression of CDKL3 in different cell types. However, our findings did not reveal any significant differences in CDKL3 expression among these cell types (Supplementary Figure S9). Additional details regarding these results can be found in the Supplementary Material. The results for analyzing competitive endogenous RNA regulatory networks and estimating the benefits of immunotherapy and chemotherapy can be found in the Supplementary Figures S10, S11.

Verification of the function of CDKL3 *in vitro* and *in vivo*

To verify the effectiveness of CDKL3 knockdown, we performed qPCR and western blot assays, which confirmed the stable knockdown of CDKL3 in SMMC-7221 and HepG2 cells (Figures 7A, B). Through the CCK-8 assay, we were able to confirm that the knockdown of CDKL3 significantly reduced the proliferation of SMMC-7221 and HepG2 cells (Figure 7C). Furthermore, colony forming ability was also greatly inhibited in these cells as a result of CDKL3 knockdown (Figure 7D). Notably, the apoptosis rate in SMMC-7221 and HepG2 cells was markedly increased

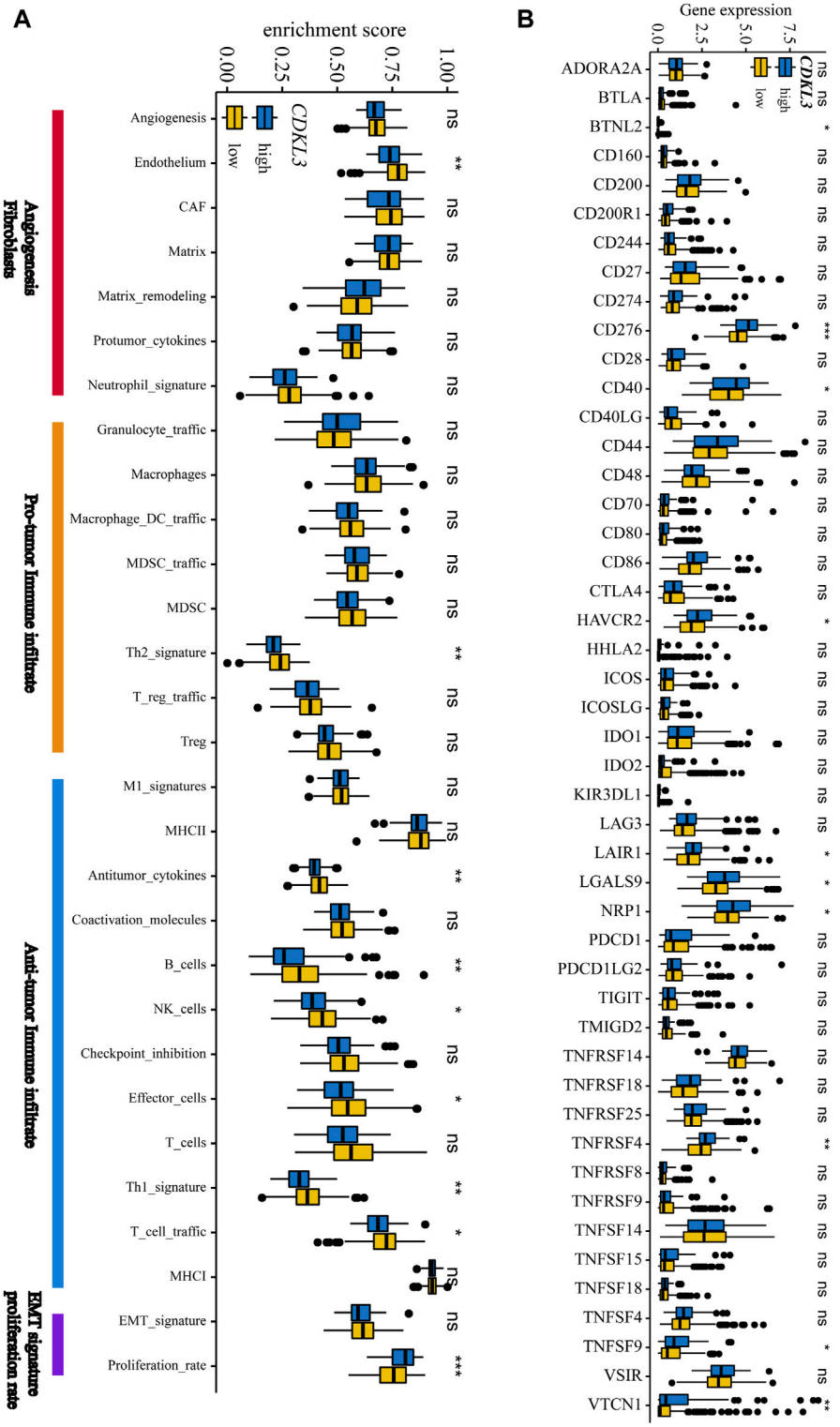

FIGURE 5
The tumour microenvironment characteristics of hCDKL3 and lCDKL3. **(A)** ssGSEA enrichment score of 29 Fges in hCDKL3 and lCDKL3. **(B)** Expression levels of immunosuppression-related molecules in hCDKL3 and lCDKL3. *$p < 0.05$, **$p < 0.01$, ***$p < 0.001$, ns, not significantly significant. hCDKL3, high-CDKL3 group; lCDKL3, low-CDKL3 group; ssGSEA, single-sample gene set enrichment analysis.

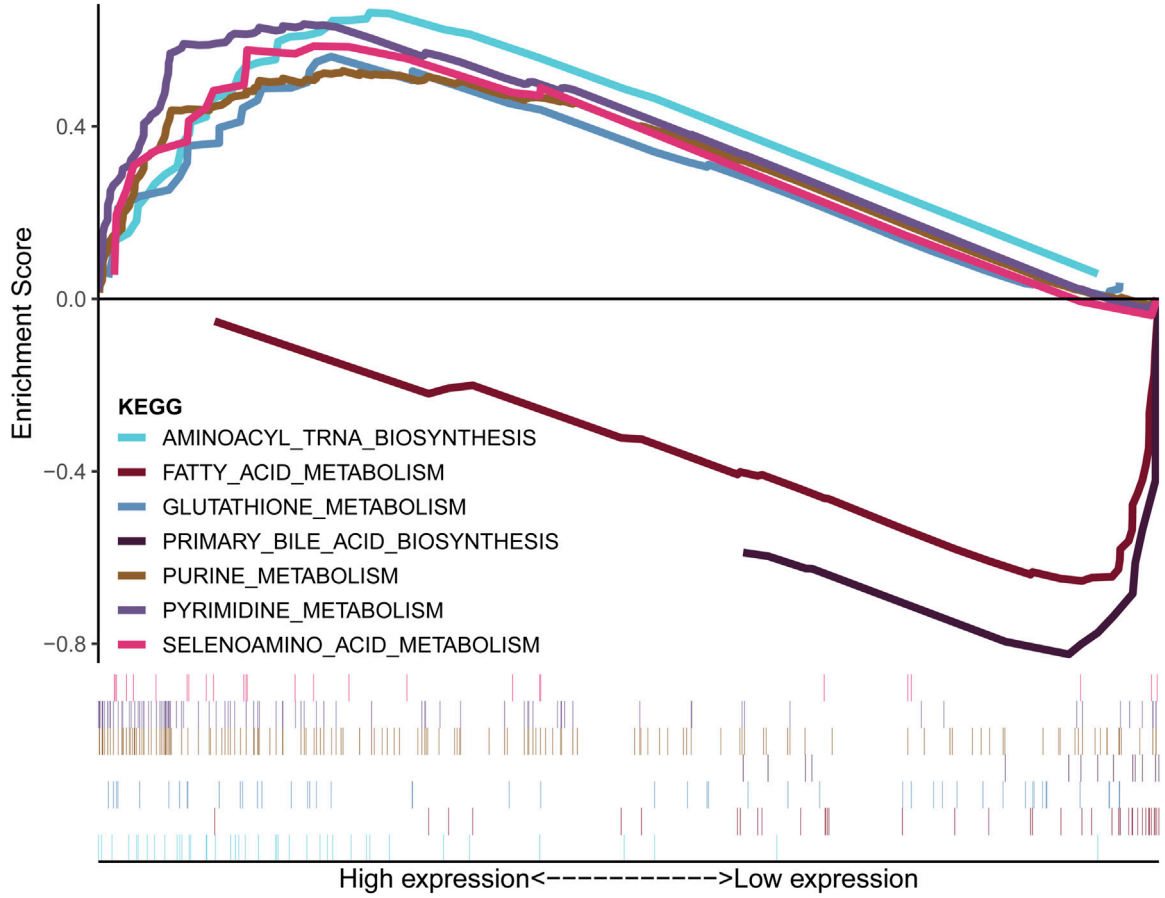

FIGURE 6
Metabolism-related KEGG pathways were enriched, as demonstrated using GSEA. KEGG: Kyoto Encyclopedia of Genes and Genomes; GSEA: gene set enrichment analysis.

following CDKL3 knockdown, as demonstrated in Figure 8. Additionally, the migration of cells was significantly reduced upon CDKL3 knockdown (Supplementary Figure S12). Moreover, in the shCDKL3 group, the tumors formed by SMMC-7721 cells exhibited smaller volumes compared to those in the shCtrl group (Figure 9). These findings suggest that CDKL3 contributes to the tumorigenesis and advancement of HCC.

Discussion

Recent studies have investigated the oncogenic role of CDKL3 in various tumors, including glioma [6], oesophageal squamous cell carcinoma [10], osteosarcoma [11], colorectal cancer [12], breast cancer [39], and cholangiocarcinoma [8]. However, the role of CDKL3 in HCC has not been thoroughly examined. In this study, we comprehensively analyzed the genetic characteristics and prognosis of CDKL3 using the LIHC dataset and confirmed its crucial function in the proliferation and progression of HCC.

According to pancancer analysis, the expression of CDKL3 is aberrant in different types of cancer, and it is higher in HCC tumor tissue compared to normal tissue. ROC analysis demonstrated that CDKL3 could serve as a potential diagnostic marker for distinguishing HCC from normal tissues. Furthermore, we found that high expression of CDKL3 is an independent predictor of poor prognosis. The nomogram that incorporates CDKL3 and independent clinicopathological factors demonstrated reliable performance in predicting prognosis. However, there have been limited studies that have focused on the genetic, TME, and metabolic features of CDKL3 in HCC biology using bioinformatic analysis. Our study fills this gap and highlights the significant genetic differences between the hCDKL3 group and the lCDKL3 group, including a higher occurrence of TP53 mutations, a greater burden of SCNA, a higher mRNAsi score, a higher PSI value of CDKL3–73367–AT, and a lower PSI value of

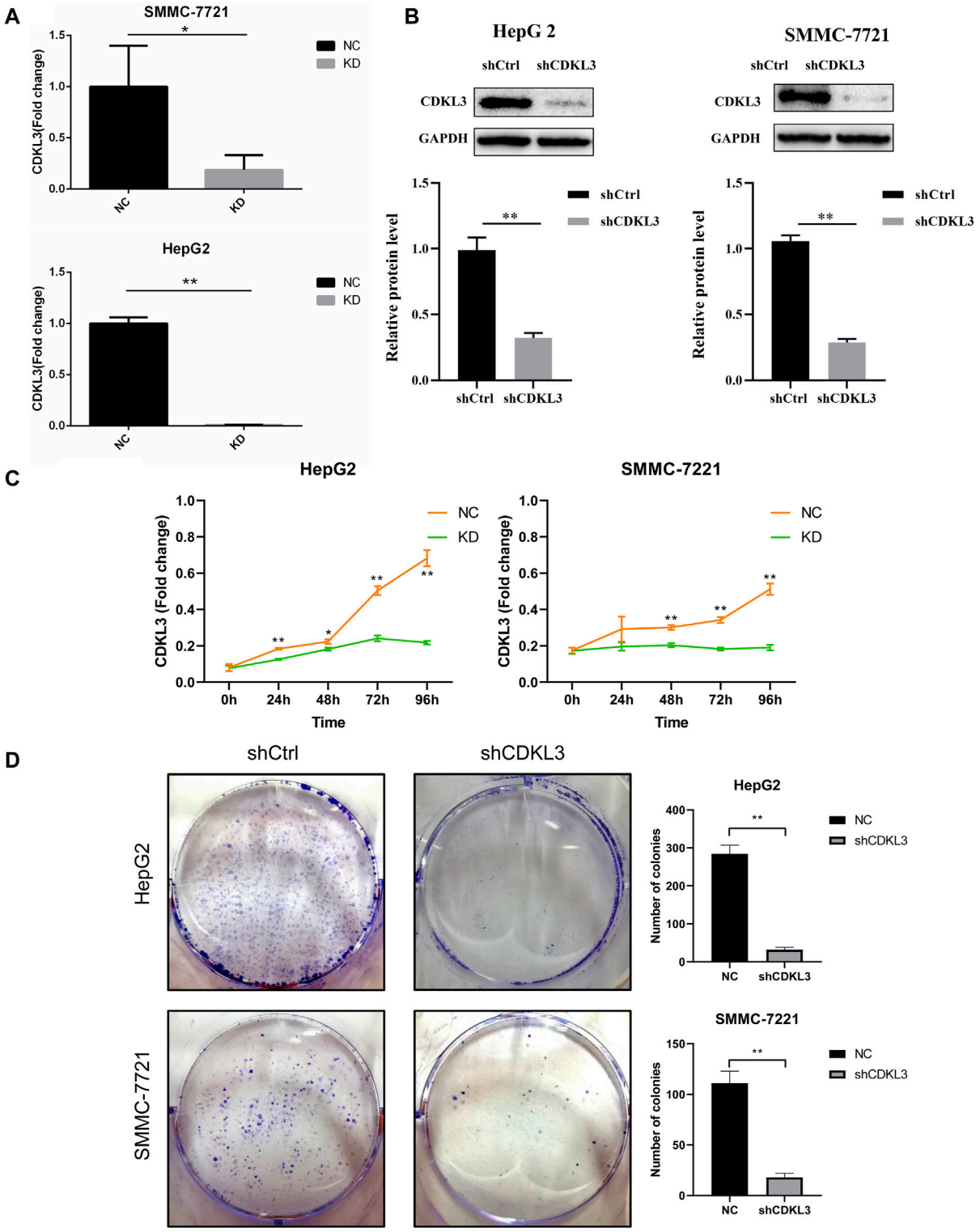

FIGURE 7
Verification of CDKL3 function *in vitro*. **(A)** qRT-PCR and **(B)** western blot assays were performed to evaluate the expression level of CDKL3 after transfection by shCDKL3 in hepatocellular carcinoma cell lines. **(C)** Cell viability was determined using CCK8 assays. **(D)** Colony formations assays were performed to evaluate cell proliferation ability. $*p < 0.05$, $**p < 0.01$. Error bars indicate mean ± SD. qRT-PCR, quantitative real-time polymerase chain reaction; CCK8, Cell Counting Kit-8.

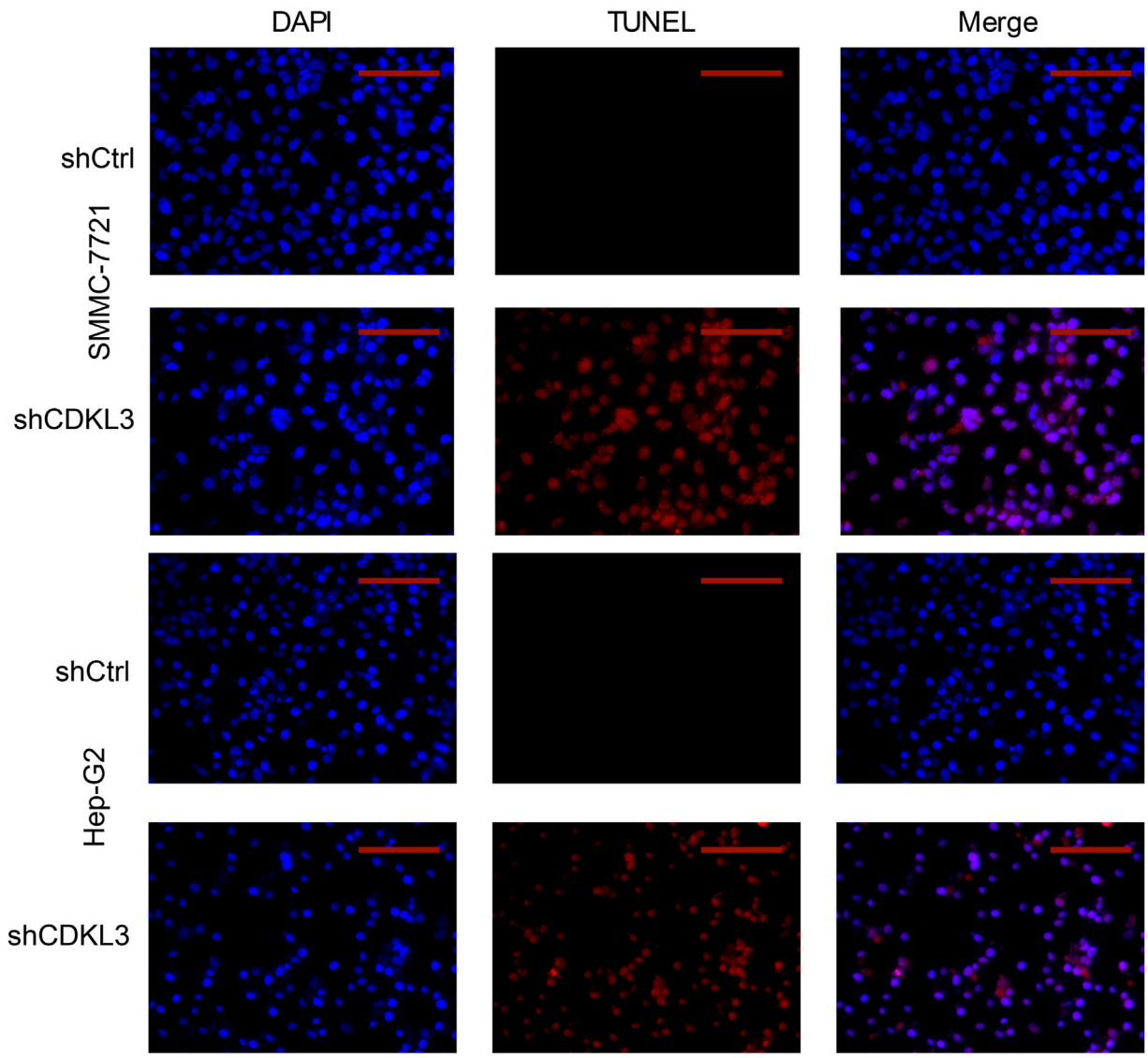

FIGURE 8
TUNEL (Scale bar, 400 μm) assay was performed to detect cell apoptosis. TUNEL, TdT-mediated dUTP Nick-End Labeling.

CDKL3−73366−AT. Moreover, we elucidated the distinct TME and metabolic characteristics between the hCDKL3 and lCDKL3 groups. Additionally, we discovered that chemotherapeutic agents such as cisplatin, docetaxel, cytarabine, gemcitabine, bleomycin, paclitaxel, rapamycin, and sunitinib had higher IC50 values in the lCDKL3 group, suggesting that CDKL3 could potentially serve as a marker for diagnosing and predicting prognosis in HCC patients.

Consistent with previous findings showing that SCNA upregulation in tumors is linked to dismal patient survival [40], we observed that the hCDKL3 group had a higher level of SCNA and worse prognosis compared to the lCDKL3 group. Higher mRNAsi scores indicate active biological processes in cancer stem cells, which have been reported to contribute to tumor progression, recurrence, and therapeutic resistance [41]. Recently, evidence suggests that higher mRNAsi scores are related to a worse outcome for HCC patients [42]. Similarly, when comparing the hCDKL3 to the lCDKL3 group, we discovered that the former exhibited greater mRNAsi scores and a grim prognosis. Aberrant alternative splicing is closely linked to tumor proliferation, progression, prognosis, and therapeutic resistance [43, 44]. Changes in the expression of splicing factors can result in alterations in the alternative splicing of the target gene [43]. In our study, hCDKL3 with a higher PSI value of CDKL3−73367−AT and a lower PSI value of CDKL3−73366−AT may contribute to the posttranscriptional regulation of CDKL3, thereby leading to an unfavorable

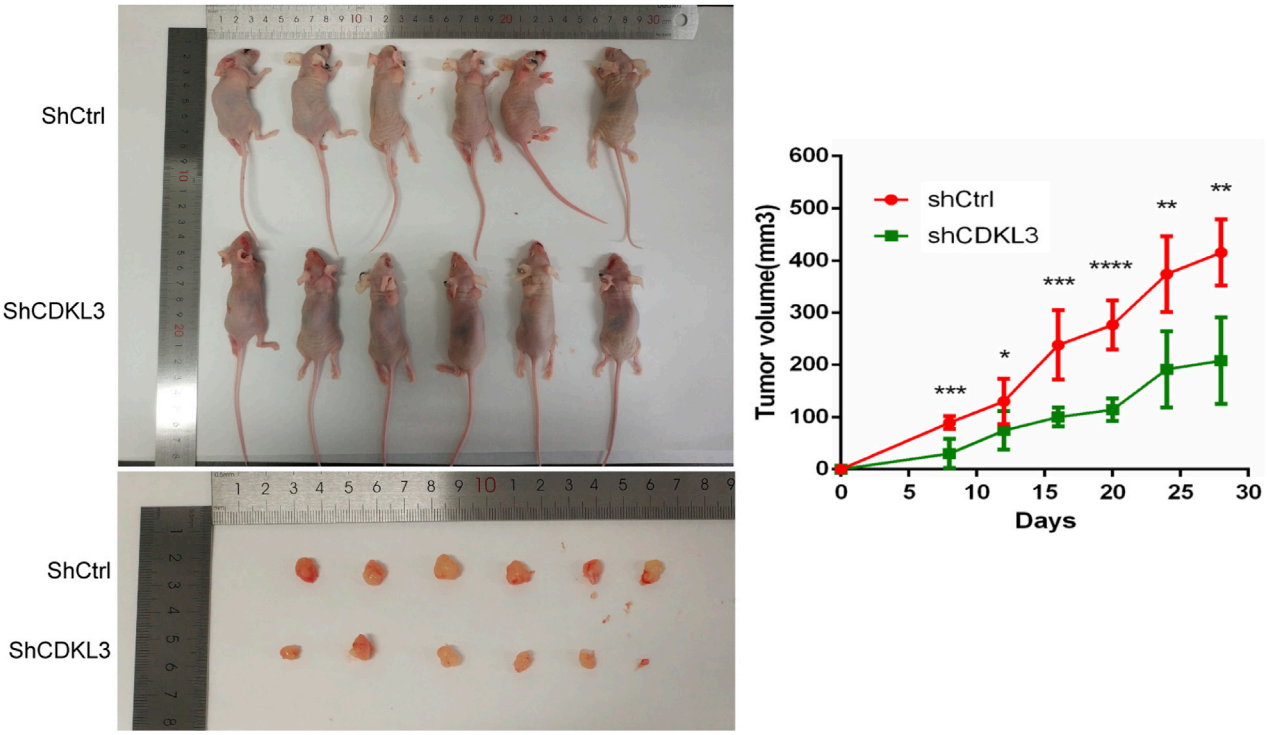

FIGURE 9
Knowdown of CDKL3 reduced tumor proliferation in xenografted nude mice. *$p < 0.05$, **$p < 0.01$, ***$p < 0.005$, ****$p < 0.001$. Error bars indicate mean ± SD.

prognosis. Additionally, the hCDKL3 group exhibited increased expression of T-cell exhaustion markers and a worse prognosis. T-cell exhaustion has been shown to limit the anti-tumor response of the immune system and play a significant role in immune escape [45, 46]. Thus, the activation of T-cell exhaustion in hCDKL3 cells might contribute to a poorer prognosis. Overall, the distinct prognosis between the hCDKL3 and lCDKL3 groups is likely driven by the different genomic features of these two cohorts.

We undertook additional investigations to verify the functional relevance of CDKL3 in both *in vitro* and *in vivo* settings. Our results illustrated that suppressing CDKL3 expression contributed to a decline in cell proliferation, colony formation, and migration ability while inducing apoptosis in HCC cell lines. Additionally, *in vivo* experiments demonstrated a reduction in tumor volume upon the knockdown of CDKL3. These findings align with previous studies by Zhang et al., which highlighted curcumol-mediated inhibition of cholangiocarcinoma cell progression through CDKL3 knockdown [8], and Sun et al., whose research indicated that exosomal miRNA-205-5p from bone marrow mesenchymal stem cells could inhibit liver cancer, partially due to CDKL3 knockdown [19]. Our study strengthens and supports the antitumorigenic role of CDKL3.

Nevertheless, it is important to acknowledge several limitations in our present research. Firstly, despite using a public database to determine the prognostic implications of CDKL3, further investigations involving clinical samples are necessary to validate our results. Secondly, assessing the impact of CDKL3 on the immune microenvironment requires validation through molecular assays in future studies. Thirdly, additional biological experiments investigating the precise molecular mechanisms by which CDKL3 influences HCC progression, such as exploring the mechanistic pathways involved, are warranted.

Conclusion

In conclusion, our findings suggest that CDKL3 may function as a significant molecular biomarker for diagnosing and estimating HCC prognosis. The observed tumor-inhibiting effect resulting from reduced CDKL3 expression indicates that CDKL3 may also be a promising molecular target for HCC therapy.

Author contributions

QW, ML, and HO: conducted the experiments, analyzed the data and wrote this manuscript. TZ, JL, and PW: conducted prepared figures. WW: conceived and supervised this study. All authors contributed to the article and approved the submitted version.

Data availability

The original contributions presented in the study are included in the article/Supplementary Material, further inquiries can be directed to the corresponding author.

Ethics statement

Ethical approval was not required for the studies on humans in accordance with the local legislation and institutional requirements because only commercially available established cell lines were used. The animal study was approved by the Experimental Animal Ethics Committee of Anhui Medical University approved this study (No. 20200695). The study was conducted in accordance with the local legislation and institutional requirements.

Funding

The authors declare financial support was received for the research, authorship, and/or publication of this article. This work was supported by Natural Science Research Projects for Anhui Universities, China (No. KJ2017A827).

Conflict of interest

The authors declare that the research was conducted in the absence of any commercial or financial relationships that could be construed as a potential conflict of interest.

Publisher's note

Please note that the review of this paper was conducted at the previous publisher, SAGE.

Supplementary material

The Supplementary Material for this article can be found online at: https://www.ebm-journal.org/articles/10.3389/ebm.2024.10106/full#supplementary-material

References

1. Llovet JM, Kelley RK, Villanueva A, Singal AG, Pikarsky E, Roayaie S, et al. Hepatocellular carcinoma. *Nat Rev Dis Primers* (2021) **7**:6. doi:10.1038/s41572-020-00240-3

2. Shi Y, Zhang DD, Liu JB, Yang XL, Xin R, Jia CY, et al. Comprehensive analysis to identify DLEU2L/TAOK1 axis as a prognostic biomarker in hepatocellular carcinoma. *Mol Ther - Nucleic Acids* (2021) **23**:702–18. doi:10.1016/j.omtn.2020.12.016

3. Forner A, Gilabert M, Bruix J, Raoul JL. Treatment of intermediate-stage hepatocellular carcinoma. *Nat Rev Clin Oncol* (2014) **11**:525–35. doi:10.1038/nrclinonc.2014.122

4. Malumbres M, Harlow E, Hunt T, Hunter T, Lahti JM, Manning G, et al. Cyclin-dependent kinases: a family portrait. *Nat Cel Biol* (2009) **11**:1275–6. doi:10.1038/ncb1109-1275

5. Midmer M, Haq R, Squire JA, Zanke BW. Identification of NKIAMRE, the human homologue to the mitogen-activated protein kinase-/cyclin-dependent kinase-related protein kinase NKIATRE, and its loss in leukemic blasts with chromosome arm 5q deletion. *Cancer Res* (1999) **59**:4069–74.

6. Cui Y, Yang Z, Wang H, Yan Y, Huang Q, Gong Z, et al. Identification of CDKL3 as a critical regulator in development of glioma through regulating RRM2 and the JNK signaling pathway. *Cancer Sci* (2021) **112**:3150–62. doi:10.1111/cas.15010

7. Haq R, Randall S, Midmer M, Yee K, Zanke B. NKIATRE is a novel conserved cdc2-related kinase. *Genomics* (2001) **71**:131–41. doi:10.1006/geno.2000.6424

8. Zhang J, Su G, Tang Z, Wang L, Fu W, Zhao S, et al. Curcumol exerts anticancer effect in cholangiocarcinoma cells via down-regulating CDKL3. *Front Physiol* (2018) **9**:234. doi:10.3389/fphys.2018.00234

9. Evan GI, Vousden KH. Proliferation, cell cycle and apoptosis in cancer. *Nature* (2001) **411**:342–8. doi:10.1038/35077213

10. Ye W, Zhu J, He D, Yu D, Yang H, Wang W, et al. Increased CDKL3 expression predicts poor prognosis and enhances malignant phenotypes in esophageal squamous cell carcinoma. *J Cell Biochem* (2019) **120**:7174–84. doi:10.1002/jcb.27991

11. He A, Ma L, Huang Y, Zhang H, Duan W, Li Z, et al. CDKL3 promotes osteosarcoma progression by activating Akt/PKB. *Life Sci Alliance* (2020) **3**:e202000648. doi:10.26508/lsa.202000648

12. Yan S, Wei H, Li Q, Si M, Feng W, Chen Z. CircTP53 promotes colorectal cancer by acting as a miR-876-3p sponge to increase cyclin-dependent kinase-like 3 expression. *Cell Signal* (2021) **78**:109845. doi:10.1016/j.cellsig.2020.109845

13. Canning P, Park K, Gonçalves J, Li C, Howard CJ, Sharpe TD, et al. CDKL family kinases have evolved distinct structural features and ciliary function. *Cel Rep* (2018) **22**:885–94. doi:10.1016/j.celrep.2017.12.083

14. Wu Z, Cheng H, Liu J, Zhang S, Zhang M, Liu F, et al. The oncogenic and diagnostic potential of stanniocalcin 2 in hepatocellular carcinoma. *J Hepatocellular Carcinoma* (2022) **9**:141–55. doi:10.2147/jhc.s351882

15. Cao L, Cheng H, Jiang Q, Li H, Wu Z. APEX1 is a novel diagnostic and prognostic biomarker for hepatocellular carcinoma. *Aging (Albany NY)* (2020) **12**:4573–91. doi:10.18632/aging.102913

16. Dubos A, Pannetier S, Hanauer A. Inactivation of the CDKL3 gene at 5q31.1 by a balanced t(X;5) translocation associated with nonspecific mild mental retardation. *Am J Med Genet A* (2008) **146A**:1267–79. doi:10.1002/ajmg.a.32274

17. Liu Z, Xu D, Zhao Y, Zheng J. Non-syndromic mild mental retardation candidate gene CDKL3 regulates neuronal morphogenesis. *Neurobiol Dis* (2010) **39**:242–51. doi:10.1016/j.nbd.2010.03.015

18. Liu Z, Tao D. Inactivition of CDKL3 mildly inhibits proliferation of cells at VZ/SVZ in brain. *Neurol Sci* (2015) **36**:297–302. doi:10.1007/s10072-014-1952-9

19. Sun Q, Zhang X, Tan Z, Gu H, Ding S, Ji Y. Bone marrow mesenchymal stem cells-secreted exosomal microRNA-205-5p exerts inhibitory effect on the progression of liver cancer through regulating CDKL3. *Pathol - Res Pract* (2021) **225**:153549. doi:10.1016/j.prp.2021.153549

20. Colaprico A, Silva TC, Olsen C, Garofano L, Cava C, Garolini D, et al. TCGAbiolinks: an R/Bioconductor package for integrative analysis of TCGA data. *Nucleic Acids Res* (2016) **44**:e71. doi:10.1093/nar/gkv1507

21. Ding W, Chen G, Shi T. Integrative analysis identifies potential DNA methylation biomarkers for pan-cancer diagnosis and prognosis. *Epigenetics* (2019) **14**:67–80. doi:10.1080/15592294.2019.1568178

22. Sharma P, Bhunia S, Poojary SS, Tekcham DS, Barbhuiya MA, Gupta S, et al. Global methylation profiling to identify epigenetic signature of gallbladder cancer and gallstone disease. *Tumor Biol* (2016) **37**:14687–99. doi:10.1007/s13277-016-5355-9

23. Tong C, Wang W, He C. m1A methylation modification patterns and metabolic characteristics in hepatocellular carcinoma. *BMC Gastroenterol* (2022) **22**:93. doi:10.1186/s12876-022-02160-w

24. Li T, Fu J, Zeng Z, Cohen D, Li J, Chen Q, et al. TIMER2.0 for analysis of tumor-infiltrating immune cells. *Nucleic Acids Res* (2020) **48**:W509–14. doi:10.1093/nar/gkaa407

25. Vickers AJ, Holland F. Decision curve analysis to evaluate the clinical benefit of prediction models. *Spine J* (2021) **21**:1643–8. doi:10.1016/j.spinee.2021.02.024

26. Austin PC, Steyerberg EW. Bootstrap confidence intervals for loess-based calibration curves. *Stat Med* (2014) **33**:2699–700. doi:10.1002/sim.6167

27. Tong C, Wang W, Xia Y, He C. A potential novel biomarker in predicting lymph node metastasis of gastric signet ring cell carcinoma: a derived monocyte to lymphocyte ratio. *Am J Surg* (2022) **223**:1144–50. doi:10.1016/j.amjsurg.2021.10.026

28. Subramanian A, Tamayo P, Mootha VK, Mukherjee S, Ebert BL, Gillette MA, et al. Gene set enrichment analysis: a knowledge-based approach for interpreting genome-wide expression profiles. *Proc Natl Acad Sci* (2005) **102**:15545–50. doi:10.1073/pnas.0506580102

29. Bu D, Luo H, Huo P, Wang Z, Zhang S, He Z, et al. KOBAS-i: intelligent prioritization and exploratory visualization of biological functions for gene enrichment analysis. *Nucleic Acids Res* (2021) **49**:W317–25. doi:10.1093/nar/gkab447

30. Bagaev A, Kotlov N, Nomie K, Svekolkin V, Gafurov A, Isaeva O, et al. Conserved pan-cancer microenvironment subtypes predict response to immunotherapy. *Cancer Cell* (2021) **39**:845–65.e7. doi:10.1016/j.ccell.2021.04.014

31. Shen X, Hu B, Xu J, Qin W, Fu Y, Wang S, et al. The m6A methylation landscape stratifies hepatocellular carcinoma into 3 subtypes with distinct metabolic characteristics. *Cancer Biol Med* (2020) **17**:937–52. doi:10.20892/j.issn.2095-3941.2020.0402

32. Shen R, Li P, Li B, Zhang B, Feng L, Cheng S, et al. Identification of distinct immune subtypes in colorectal cancer based on the stromal compartment. *Front Oncol* (2019) **9**:1497. doi:10.3389/fonc.2019.01497

33. Mermel CH, Schumacher SE, Hill B, Meyerson ML, Beroukhim R, Getz G. GISTIC2.0 facilitates sensitive and confident localization of the targets of focal somatic copy-number alteration in human cancers. *Genome Biol* (2011) **12**:R41. doi:10.1186/gb-2011-12-4-r41

34. Chalmers ZR, Connelly CF, Fabrizio D, Gay L, Ali SM, Ennis R, et al. Analysis of 100,000 human cancer genomes reveals the landscape of tumor mutational burden. *Genome Med* (2017) **9**:34. doi:10.1186/s13073-017-0424-2

35. Malta TM, Sokolov A, Gentles AJ, Burzykowski T, Poisson L, Weinstein JN, et al. Machine learning identifies stemness features associated with oncogenic dedifferentiation. *Cell* (2018) **173**:338–54.e15. doi:10.1016/j.cell.2018.03.034

36. Ryan MC, Cleland J, Kim R, Wong WC, Weinstein JN. SpliceSeq: a resource for analysis and visualization of RNA-Seq data on alternative splicing and its functional impacts. *Bioinformatics* (2012) **28**:2385–7. doi:10.1093/bioinformatics/bts452

37. Zhou Y, Xiao D, Jiang X. LncRNA RP3-525N10.2-NFKB1-PROS1 triplet-mediated low PROS1 expression is an onco-immunological biomarker in low-grade gliomas: a pan-cancer analysis with experimental verification. *J Transl Med* (2022) **20**:335. doi:10.1186/s12967-022-03536-y

38. Wang Y, Liu S, Liu H, Li W, Lin F, Jiang L, et al. SARS-CoV-2 infection of the liver directly contributes to hepatic impairment in patients with COVID-19. *J Hepatol* (2020) **73**:807–16. doi:10.1016/j.jhep.2020.05.002

39. Zeng DX, Sheng GF, Liu YP, Zhang YP, Qian Z, Li Z, et al. Cyclin-dependent kinase like 3 promotes triple-negative breast cancer progression via inhibiting the p53 signaling pathway. *Neoplasma* (2021) **68**:1033–42. doi:10.4149/neo_2021_210331n427

40. Davoli T, Uno H, Wooten EC, Elledge SJ. Tumor aneuploidy correlates with markers of immune evasion and with reduced response to immunotherapy. *Science* (2017) **355**:eaaf8399. doi:10.1126/science.aaf8399

41. Pan S, Zhan Y, Chen X, Wu B, Liu B. Identification of biomarkers for controlling cancer stem cell characteristics in bladder cancer by network analysis of transcriptome data stemness indices. *Front Oncol* (2019) **9**:613. doi:10.3389/fonc.2019.00613

42. Chen D, Liu J, Zang L, Xiao T, Zhang X, Li Z, et al. Integrated machine learning and bioinformatic analyses constructed a novel stemness-related classifier to predict prognosis and immunotherapy responses for hepatocellular carcinoma patients. *Int J Biol Sci* (2022) **18**:360–73. doi:10.7150/ijbs.66913

43. Yao J, Tang YC, Yi B, Yang J, Chai Y, Yin N, et al. Signature of gene aberrant alternative splicing events in pancreatic adenocarcinoma prognosis. *J Cancer* (2021) **12**:3164–79. doi:10.7150/jca.48661

44. Mao S, Li Y, Lu Z, Che Y, Huang J, Lei Y, et al. PHD finger protein 5A promoted lung adenocarcinoma progression via alternative splicing. *Cancer Med* (2019) **8**:2429–41. doi:10.1002/cam4.2115

45. Jiang W, He Y, He W, Wu G, Zhou X, Sheng Q, et al. Exhausted CD8+T cells in the tumor immune microenvironment: new pathways to therapy. *Front Immunol* (2020) **11**:622509. doi:10.3389/fimmu.2020.622509

46. Kumar S, Singh SK, Rana B, Rana A. Tumor-infiltrating CD8+ T cell antitumor efficacy and exhaustion: molecular insights. *Drug Discov Today* (2021) **26**:951–67. doi:10.1016/j.drudis.2021.01.002

EBM Experimental Biology and Medicine

TYPE Original Research
PUBLISHED 20 June 2024
DOI 10.3389/ebm.2024.10161

OPEN ACCESS

*CORRESPONDENCE
Sulev Koks,
sulev.koks@murdoch.edu.au

RECEIVED 08 March 2024
ACCEPTED 29 May 2024
PUBLISHED 20 June 2024

CITATION
Poudel BH and Koks S (2024), The whole transcriptome analysis using FFPE and fresh tissue samples identifies the molecular fingerprint of osteosarcoma. *Exp. Biol. Med.* 249:10161.
doi: 10.3389/ebm.2024.10161

The whole transcriptome analysis using FFPE and fresh tissue samples identifies the molecular fingerprint of osteosarcoma

Bal Hari Poudel[1,2,3] and Sulev Koks[1,2]*

[1]Center for Molecular Medicine and Innovative Therapy, Murdoch University, Perth, WA, Australia, [2]Perron Institute of Neurological Diseases, Perth, WA, Australia, [3]Central Department of Biotechnology, Tribhuvan University, Kathmandu, Nepal

Abstract

Osteosarcoma is a form of bone cancer that predominantly impacts osteoblasts, the cells responsible for creating fresh bone tissue. Typical indications include bone pain, inflammation, sensitivity, mobility constraints, and fractures. Utilising imaging techniques such as X-rays, MRI scans, and CT scans can provide insights into the size and location of the tumour. Additionally, a biopsy is employed to confirm the diagnosis. Analysing genes with distinct expression patterns unique to osteosarcoma can be valuable for early detection and the development of effective treatment approaches. In this research, we comprehensively examined the entire transcriptome and pinpointed genes with altered expression profiles specific to osteosarcoma. The study mainly aimed to identify the molecular fingerprint of osteosarcoma. In this study, we processed 90 FFPE samples from PathWest with an almost equal number of osteosarcoma and healthy tissues. RNA was extracted from Paraffin-embedded tissue; RNA was sequenced, the sequencing data was analysed, and gene expression was compared to the healthy samples of the same patients. Differentially expressed genes in osteosarcoma-derived samples were identified, and the functions of those genes were explored. This result was combined with our previous studies based on FFPE and fresh samples to perform a meta-analysis. We identified 1,500 identical differentially expressed genes in PathWest osteosarcoma samples compared to normal tissue samples of the same patients. Meta-analysis with combined fresh tissue samples identified 530 differentially expressed genes. *IFITM5, MMP13, PANX3*, and *MAGEA6* were some of the most overexpressed genes in osteosarcoma samples, while *SLC4A1, HBA1, HBB, AQP7* genes were some of the top downregulated genes. Through the meta-analysis, 530 differentially expressed genes were identified to be identical among FFPE (105 FFPE samples) and 36 fresh bone samples. Deconvolution analysis with single-cell RNAseq data confirmed the presence of specific cell clusters in FFPE samples. We propose these 530 DEGs as a molecular fingerprint of osteosarcoma.

KEYWORDS

osteosarcoma, osteogenic sarcoma, transcriptome, RNA sequencing, differential gene expression

Impact statement

Although rare, osteosarcoma attracts global attention because of the unsatisfactory outcomes associated with current treatment approaches. In our investigation, we examined total RNA extracted from 90 FFPE paired samples, consisting of 50 tumoral bone specimens and their matched non-tumoral counterparts, sourced from osteosarcoma patients. By comparing our findings with previous studies, we uncovered differences in gene expression patterns between normal and affected bone tissues, particularly emphasizing changes in the regulation of collagen and extracellular matrix degradation and cell cycle regulation. These findings deepen our understanding of osteosarcoma and provide potential directions for future research endeavors.

Introduction

Bone cancer (osteosarcoma, OS) is the most common primary tumour of the bone in children and young adults [1, 2]. Osteosarcoma arises from the cells forming bone tissue and can be found in the bone's metaphysis, the region where the growth plate is located. The exact cause of osteosarcoma is not fully understood, but several risk factors have been identified [3]. Some individuals may have a genetic predisposition to developing osteosarcoma, although it is not typically inherited in a Mendelian pattern. Certain preexisting conditions, such as hereditary retinoblastoma (a rare eye cancer) and Paget's disease of bone, have been linked to an increased risk of osteosarcoma [4].

Symptoms of osteosarcoma may include pain and swelling in the affected bone or joint, limited range of motion in the nearby joint, a mass or lump in the affected area, fractures or bone weakening in the affected bone [5, 6]. Diagnosis typically involves a combination of imaging studies like X-rays, MRI, and CT scans, as well as a biopsy to confirm the presence of cancerous cells [5, 6]. Treatment for osteosarcoma usually involves a multimodal approach, which may include surgery, chemotherapy and radiation therapy [6], however, none of them are accurate and also have strong adverse effect with chemotherapy and radiation therapy. In addition, there is higher chances of getting a second cancer [7, 8].

The prognosis for osteosarcoma varies depending on factors such as the extent of the disease, response to treatment, and the presence of metastasis [9]. Early diagnosis and aggressive treatment can significantly improve the chances of successful outcomes. Long-term follow-up care is essential to monitor for any potential recurrence or late effects of treatment. Treatment plans are usually developed in collaboration with a team of oncologists, surgeons, and other healthcare professionals.

Whole transcriptome analysis is a powerful tool used in modern-day molecular biology to study the entries set of RNA molecules produced by a cell or a population of cells [10, 11]. Transcriptome analysis provides snapshots of the genes expressed and can be compared with normal [11]. However, the differentially expressed genes (DEGs) may vary from sample to sample according to the quality of the samples. For rare diseases like osteosarcoma, there are not many options for getting fresh samples due to the death of patients and getting fresh bone samples is not easy; hence, formalin-fixed paraffin-embedded tissues (FFPEs) are the best way to analyse the sample. However, RNA gets degraded [12] due to formalin fixation in FFPE.

In this paper, we report a complex transcriptomic analysis that is based on four independent studies. We performed two original experiments and combined these results with previously published studies. This study provides the molecular signature of osteosarcoma to generate fundamental knowledge to develop new drugs against this disease. Through this study, we compared the DEGs in FFPE with fresh bone samples to identify whether or not the FFPE DEGs aligned with the fresh bone samples. We performed RNAseq analysis on a new set of 90 samples. We later compared it to the two other independent studies (FFPE and fresh) to conduct a meta-analysis of OS transcriptome. Identified molecular mechanisms and genes could be used as a potential target for osteosarcoma drug development and will be evaluated in future studies.

Materials and methods

The sample processing and whole transcriptome analysis

Our original sample analysis is based on two independent analyses of the formalin-fixed paraffin-embedded (FFPE) samples. The paraffin blocks were cut, and RNA was extracted. This way, any archived biological samples can be analysed for rare diseases like osteosarcoma; using FFPE samples is the only option to get meaningful and large samples for the complex transcriptomic analysis. The FFPE samples (N = 90: 50 OS + 40 healthy control) were obtained through PathWest Nedlands (QEII Medical Centre, Australia) and were processed in two batches, and total RNA was extracted using the Norgen FFPE RNA purification kit (#25300) using the manufacturer's standard protocol. The purified RNA samples were sent to the Australian Genome Research Facility (AGRF) Melbourne for sequencing also in two separate batches.

FFPE sample analysis

We combined two PathWest FFPE studies (90 samples altogether) into a single analysis to increase the formal statistical power of the analysis. Details of the samples are shown in Supplementary Table S1. Briefly, this table highlights the gender, sample group (tumour or normal), age at onset, deceased or alive and chemotherapy or non-chemotherapy. The raw FASTQ files obtained after sequencing were used for the data analysis. DEGs were detected by comparing the OS with normal samples using

TABLE 1 List of top highly upregulated genes compared to normal tissue.

Gene name	Symbol	Base mean	log2FoldChange	Padj
Matrix metallopeptidase 9	MMP9	707.4	7.5	4.12E-25
Cellular communication network factor 4	CCN4	238.0	6.8	5.30E-24
Hyaluronan and proteoglycan link protein 1	HAPLN1	70.6	6.4	1.12E-24
Alkaline phosphatase, biomineralization associated	ALPL	158.1	6.4	8.19E-23
Matrix metallopeptidase 13	MMP13	276.9	6.3	8.61E-21
Pannexin 3	PANX3	117.7	6.1	9.43E-21
Rhomboid like 2	RHBDL2	51.6	6.0	8.19E-23
Collagen triple helix repeat containing 1	CTHRC1	123.4	6.0	8.92E-20
Glucosamine-phosphate N-acetyltransferase 1	GNPNAT1	137.6	5.9	1.41E-19
Transmembrane O-mannosyltransferase targeting cadherins 2	TMTC2	134.7	5.9	1.41E-19
Anillin, actin binding protein	ANLN	91.7	5.9	3.21E-21
Collagen type XXIV alpha 1 chain	COL24A1	61.4	5.8	3.90E-21
Collagen type XI alpha 1 chain	COL11A1	824.5	5.8	3.52E-14
Interferon induced transmembrane protein 5	IFITM5	32.5	5.7	1.04E-21
DLG associated protein 5	DLGAP5	41.9	5.7	9.00E-23
Integrin binding sialoprotein	IBSP	263.7	5.7	1.63E-16
Parathyroid hormone 1 receptor	PTH1R	100.8	5.7	2.45E-18
Lymphoid enhancer binding factor 1	LEF1	75.1	5.6	3.83E-20
Proline rich 11	PRR11	115.6	5.6	3.84E-18
SRY-box transcription factor 11	SOX11	53.2	5.5	8.81E-21
Cyclin B2	CCNB2	31.6	5.5	2.03E-22
DNA polymerase eta	POLH	99.4	5.5	1.12E-19
Fibrillin 2	FBN2	159.2	5.4	1.04E-15
Sp7 transcription factor	SP7	169.0	5.4	9.98E-16
Spindle apparatus coiled-coil protein 1	SPDL1	62.2	5.4	1.28E-19
Sterile alpha motif domain containing 5	SAMD5	182.1	5.3	1.16E-14
Collagen type X alpha 1 chain	COL10A1	103.3	5.3	6.69E-16
MyoD family inhibitor	MDFI	72.7	5.3	2.02E-17
Kinetochore scaffold 1	KNL1	149.9	5.3	4.68E-16
Neuron derived neurotrophic factor	NDNF	208.4	5.2	5.31E-14

Salmon [13]. Statistical analysis of data and differential gene expression was also performed by using the DESeq2 package of R [14, 15]. The magnitude of the differential gene expression between tumour and healthy samples was calculated by analysing the log-2-fold change of the genes (logFC, the cut-off value of 0.5). Benjamini-Hochberg method available in the DESeq2 package was used to adjust the nominal *p*-value (padj) in order to correct against false positive findings caused by multiple tests. The significance level was set at padj<0.05 [15].

The results from this study were used in the further meta-analysis and combined with two previously published data.

Meta-analysis

The results from four different whole transcriptome studies of osteosarcoma were combined to identify the differentially expressed genes. Two studies are from the present analysis,

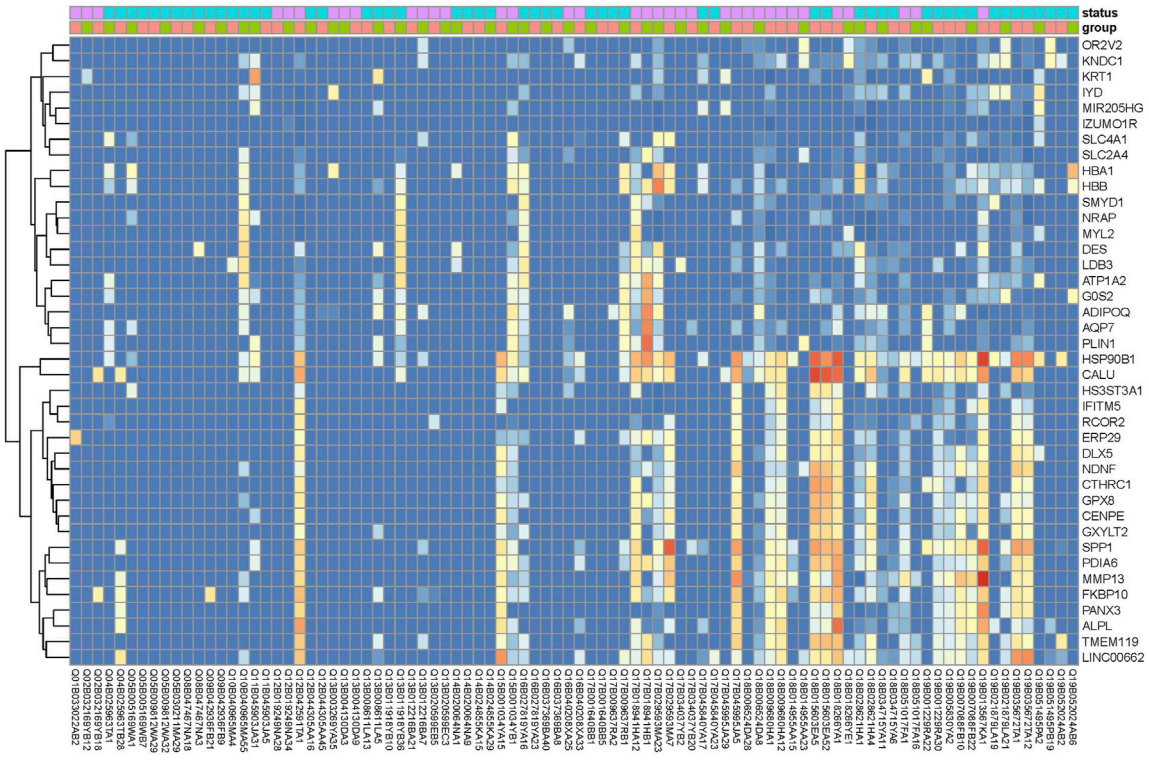

FIGURE 1
Heat map of top differentially expressed genes with largest fold change differences between tumor and normal samples.

two others are from our previously published papers. Three studies were based on FFPE samples and one previous study from Estonia and Vietnam was based on fresh OS samples [16]. (Study 1: Estonia + Vietnam FFPE samples N = 15, Study 2: PathWest FFPE 1: N = 24 OS + 16 healthy controls, Study 3: PathWest FFPE 2N = 26 OS + 24 healthy controls and Study 4: Estonia and Vietnam fresh bones N = 18 OS + 18 healthy controls). The DEGs found in individual studies were compared to each other to find common DEGs.

Deconvolution with single-cell transcriptomics

Deconvolution was based on a previously published single-cell transcriptomic study in OS [17]. Cell profiles in scRNAseq study were from six OS patient samples (GSE162454). 'Seurat' package was used to find conserved markers that define cell clusters. To identify canonical cell type marker genes that are conserved across all conditions (tumour and treatment), we used the "FindConservedMarkers ()" function. This function tests differential gene expression for each dataset/group and combines the *p*-values using meta-analysis methods from the "MetaDE" R package [18]. "Granulator" package was used to identify the cluster-specific profiles in bulk FFPE RNAseq data.

Functional analysis of the differentially expressed genes

To understand the variation of different groups of gene functions in osteosarcoma, gene ontology (GO) analysis and Kyoto Encyclopedia of Genes and Genomes (KEGG) were used to interpret the change in gene expression along with their cellular locations, biological processes, and involvement in the molecular pathway [19, 20].

Results

FFPE RNA-seq and meta-analysis

Transcriptome analysis of the PathWest FFPE samples showed a large number of differentially expressed genes in tumours compared to healthy bone, as shown in Table 1 and in Figure 1 (heatmap of the top genes form the FFPE 90 sample). Some of the overexpressed genes were *MMP9, CCN4, HAPLN1,*

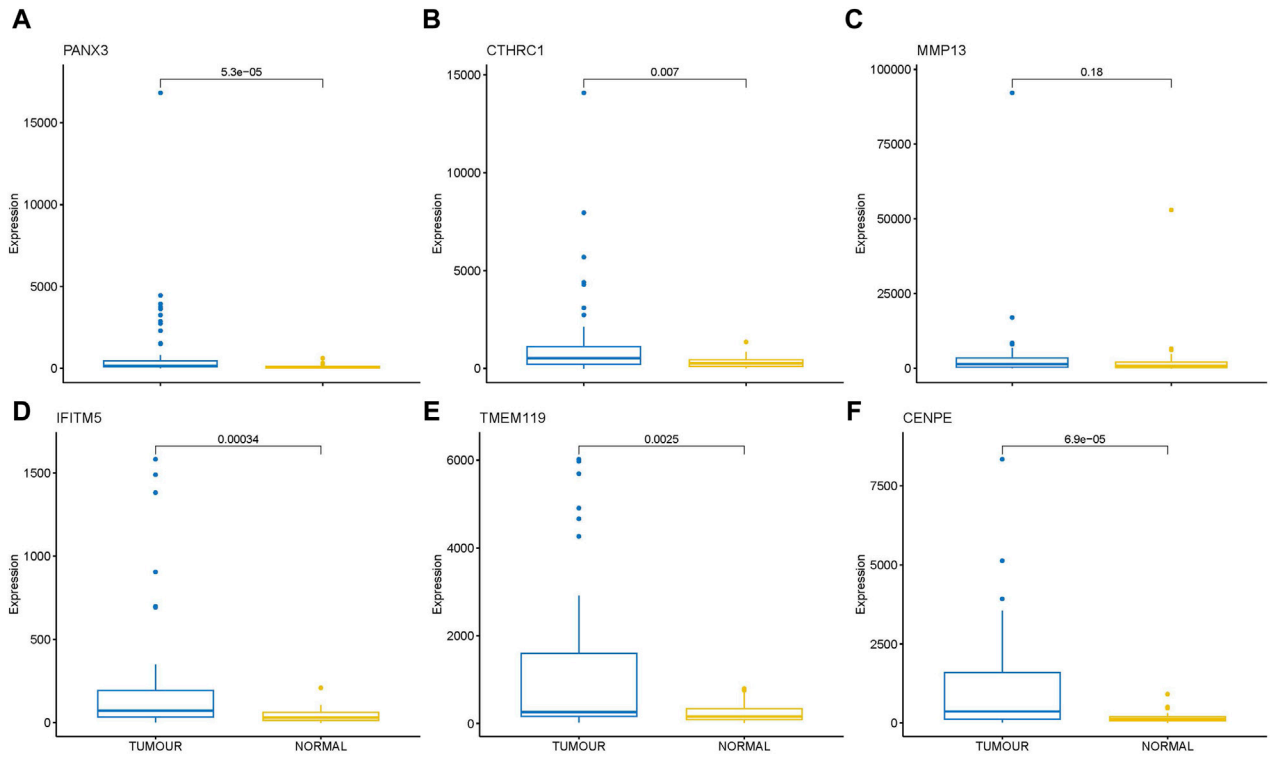

FIGURE 2
Box plot showing direct comparison of gene expression in tumor and normal samples for some upregulated genes, gene expressions are presented in normalized count. **(A)** PANX3 **(B)** CTHRC1 **(C)** MMP13 **(D)** IFITM5 **(E)** TMEM119 **(F)** CENPE.

ALPL, MMP13, PANX3, IFITM5, , CTHRC1, , TMEM119,. In addition, *COLLA11A1, FBN2, IBSP, COLA10A1, MDFI, GPX8* were also found to be overexpressed. A comparison of gene expressions in normal and tumours for some of the top differentially (upregulated and downregulated) expressed genes is presented in Figures 2, 3.

For the meta-analysis, two PathWest studies were treated as independent studies because the samples were collected, extracted and sequenced independently from each other. During the meta-analysis we observed 6,536 DEGs similar among our PathWest FFPE 2 study and EE-VN study. However, the number of overlapping DEGs was smaller (1,505) in PathWest FFPE 2 and PathWest FFPE 1 (Figures 4A, B). In addition, 1,211 DEGs were similar among PathWest FFPE1 and EE-VN FFPE study. Among those 105 FFPE samples from three studies, we observed 1,072 identical DEGs. The DEGs observed with fresh bone OS samples were then compared with combined FFPE samples, and we observed 530 similar genes to be differentially expressed as indicated in Figure 4, and the number of similar and unique genes across different samples are presented in the Venn diagram (Figure 4B). Some of the top differentially expressed genes observed in OS compared to normal samples are presented in Figure 2. The clustering shows that OS has a remarkable transcriptome heterogeneity and indicates the molecular heterogeneity in the pathogenetic mechanisms causing the osteosarcoma. Our previous study found similar heterogeneity with only fresh tissue OS samples. Malignancies are known to have multiple mutations and complex molecular mechanisms that drive pathogenesis.

Deconvolution analysis was performed to identify the cellular populations from the FFPE-derived bulk RNAseq. Using the Seurat package and publicly available scRNA seq data from the OS sample, we could identify 11 clusters characteristic of the OS (Figures 5, 6). The clusters had specific patterns that could be designated to different cell populations, and cluster 2 was confirmed to be osteoblast-specific as it had typical osteoblast markers expressed. Our 90 samples from the Pathwest FFPE collection all had a stable proportion (20%) of osteoblastic cells Figure 5. Cluster 9 varied quite a lot between samples. The exact identity of these cellular clusters needs further analysis, but remarkably, deconvolution is possible from the FFPE-based bulk RNAseq data.

In addition, we compared the differential gene expression among the PathWest FFPE samples for chemo and non-chemo and observed 615 common DEGs (Figure 7). These genes are not affected by chemotherapy and are specific for the pathogenesis of the OS. Chemotherapy itself affected a large number of genes and could be a significant confounding factor. This is why

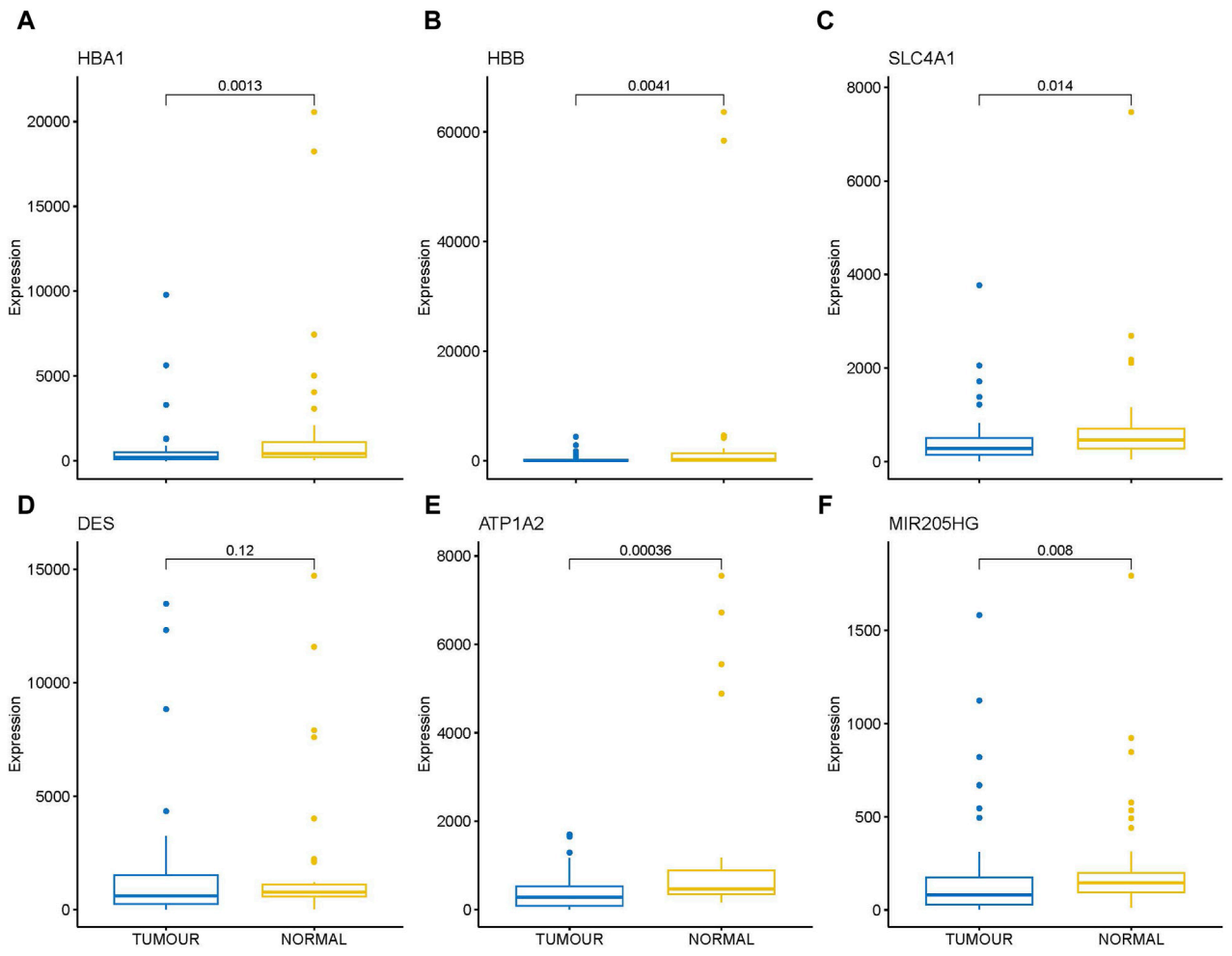

FIGURE 3
Box plot showing direct comparison of gene expression in tumor and normal for some down regulated genes, gene expressions are presented in normalized count. **(A)** HBA1 **(B)** HBB **(C)** SLC4A1 **(D)** DES **(E)** ATP1A2 **(F)** MIR205HG.

meta-analysis is needed to combine the statistical outcomes from independent studies. It is almost impossible to get clinical samples without treatment effects, and this is a common challenge for all real-life data-based studies, including genomics. We also observed many genes to be downregulated in OS compared to normal, as shown in Table 2. Some of the downregulated genes were SLC4A1, HBA1, HBA2, HBB, DES, ATP1A2, KRT1, LDB3, AQP7, FosB, G0S2, NRAP, and PLIN4, as shown in Table 2 with a log2FC value.

The volcano plot (Figure 8) shows the top highly expressed and top downregulated genes in osteosarcoma compared to normal samples, with some of the genes labelled and indicated on the plot. This gives a good overview of the extent and statistical significance of the differentially regulated genes in all studies combined and illustrates the transcriptomic fingerprint of osteosarcoma.

Functional analysis

GO and KEGG analyses were carried out to investigate the activation of the cellular pathways and common functional themes activated by the differentially expressed genes. This analysis is based on the differences among gene groups with various expressions and provides a preliminary interpretation of the biological activities of the differentially expressed genes. Similarly, disease ontology was performed to identify the disease patterns in the differentially expressed genes. We identified that the gene expression pattern we found matches with the osteosarcoma verifying our results again. A disease ontology study showed (Figure 9) that the DEGs are highly associated with osteosarcoma, bone cancer, connective tissue cancer, bone development disease and many other cancers (Figure 9) and also observed to be correlated with movement disease.

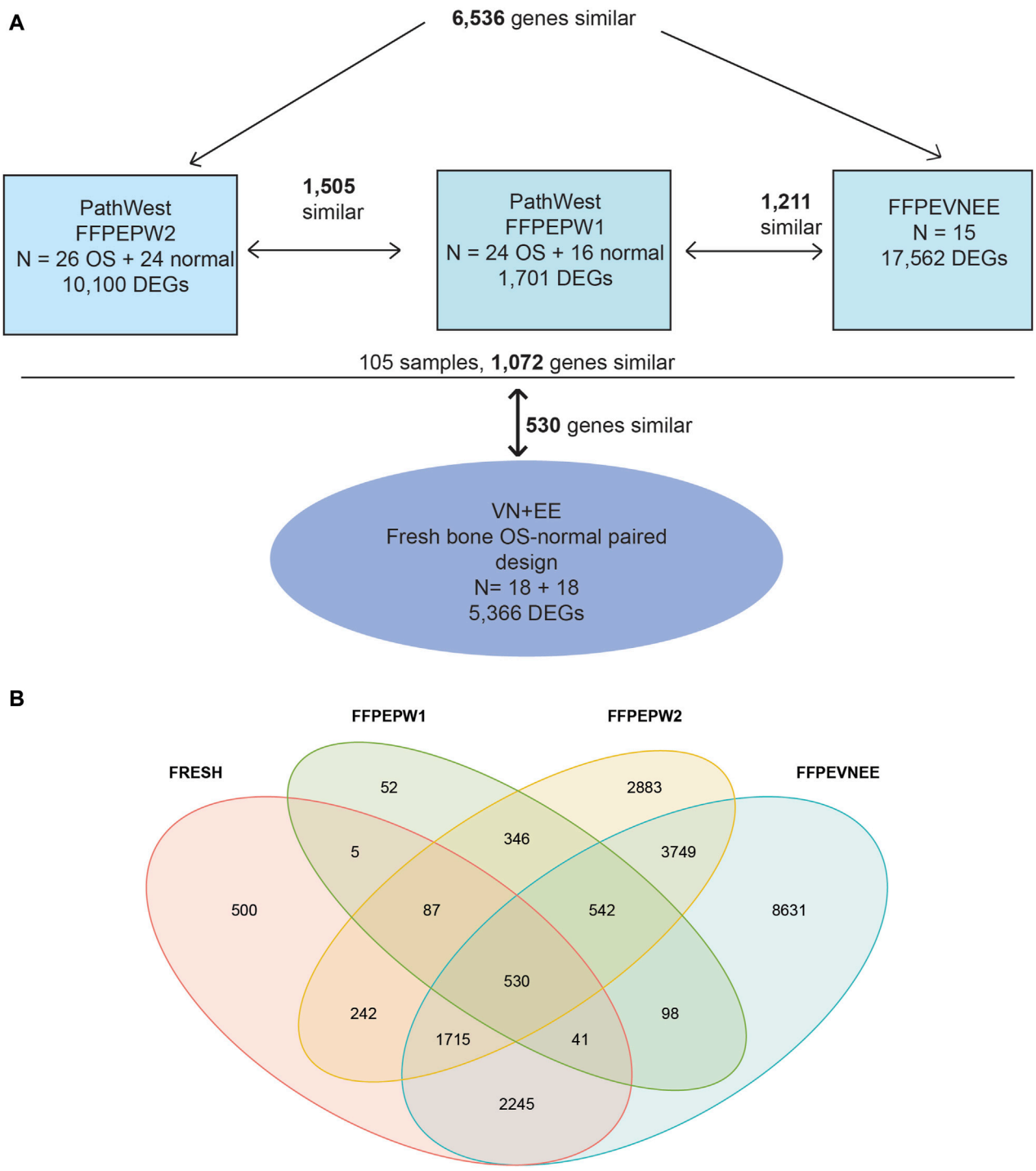

FIGURE 4
The meta-analysis. **(A)** Meta analysis design. Three formalin fixed paraffin embedded tissue-based study (FFPEVNEE, FFPEPW1, FFPEPW2) and one study with fresh bone samples were combined to identify the differentially expressed genes in osteosarcoma. VNEE–samples from Estonia and Vietnam B **(B)** Venn diagram showing the similarity and uniqueness of differentially expressed genes across four different studies.

Functional analysis was done to identify the cellular and molecular pathways that had changed in the OS samples. This lets us identify the common themes that connect these genes in this list.

KEGG pathway analysis is shown in Figure 10, and it describes the activation of the ribosome and protein processing in the endoplasmic reticulum. The KEGG pathway

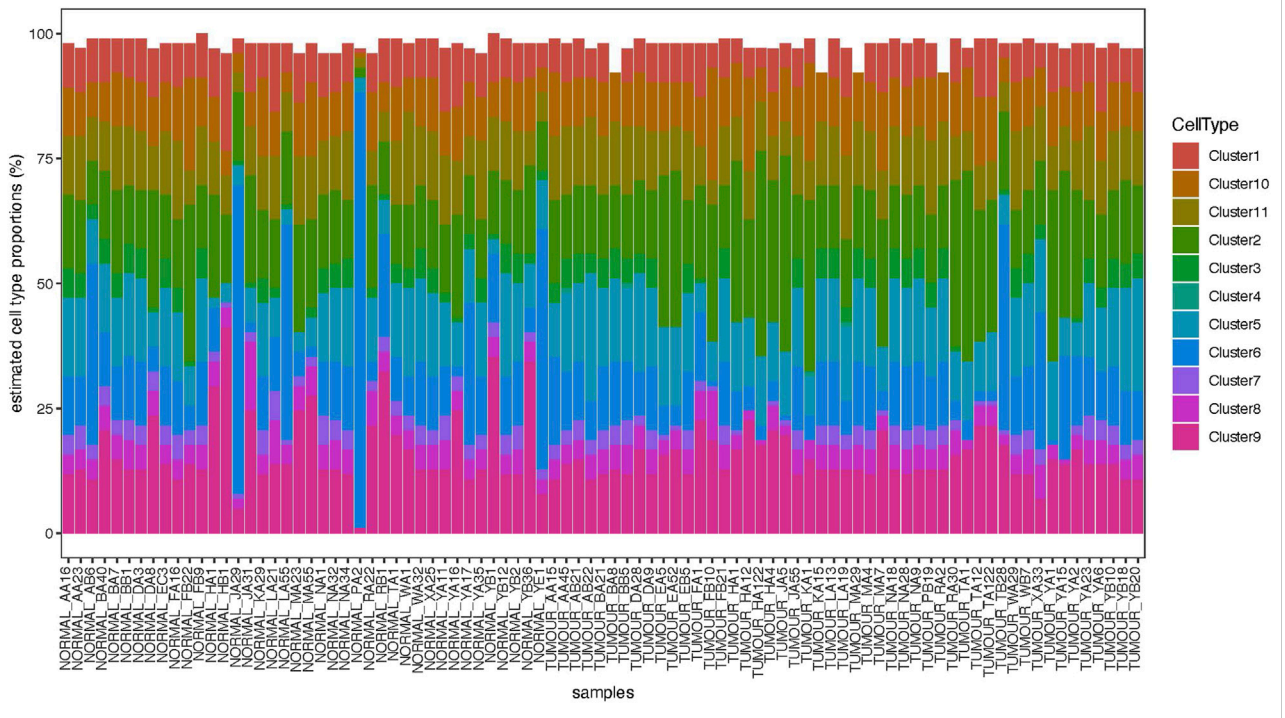

FIGURE 5
Proportions of cell clusters in different normal and tumour samples.

system is a unified canonical system to develop pathway maps for different cellular and biological functions. These maps comprehensively describe variable biological functions and provide maps for visualisation. The maps help us to define these molecular functions that are affected by osteosarcoma. KEGG pathway analysis also identified viral carcinogenesis pathways with some immune-regulated pathways.

Interestingly, a Parkinson's disease-related pathway was also identified (Figure 10). This finding possibly reflects the overlap between protein processing and Parkinson's pathogenesis pathways. It is important to mention here that the *PARK7* gene was identified as differentially expressed in all OS studies and samples we have analysed and the upregulation of P*ARK7* is a constant finding in OS cases. Therefore, activation of this pathway seems to be feasible and functionally plausible. *PARK7* is a gene that supports cell survival, and its upregulation has been shown to be related to aggressive brain cancer progression [21]. The functional deficiency of *PARK7* and mutations in this gene cause autosomal recessive early-onset Parkinson's disease.

Gene set enrichment analysis (GSEA) pathway enrichment

GSEA pathway enrichment was carried out to describe the common themes in the activated gene lists. This is based on the gene set enrichment comparison by using the ranked gene list of the differential expression output. This way only statistically significant differences will be analysed against the existing genes sets [22]. In the OS samples, with the GSEA analysis, it was observed that many gene sets related to the cell cycle and mitosis regulation indicating presence of the malignant disease in OS in comparison to normal. To visualise the GSEA analysis results, we developed dot plots to illustrate the gene number and the statistical significance level for different gene sets and pathway that were activated in OS samples. Figure 11 shows the reactome pathways that are enriched in OS samples. Top 15 highly significant reactome pathways are shown with corresponding adjusted *p*-value and normalized count (Figure 11). Some of the major identified pathways in the plot are protein translation, cell cycle check points, gene silencing and keratinization.

Figures 11, 12 show statistical significance and gene numbers in different GSEA pathways. These illustrations combine the magnitude of the gene activation with the statistical significance. In both the figures we see the activation of cell cycle related pathways and mitosis signals that all reflect the activated malignant processes (Figure 12). Therefore, the genes we identified as differentially expressed in osteosarcoma samples with some indicated in Table 2 is reflective of the malignant process. Functional analysis of the gene activation networks can be even more specific and can go

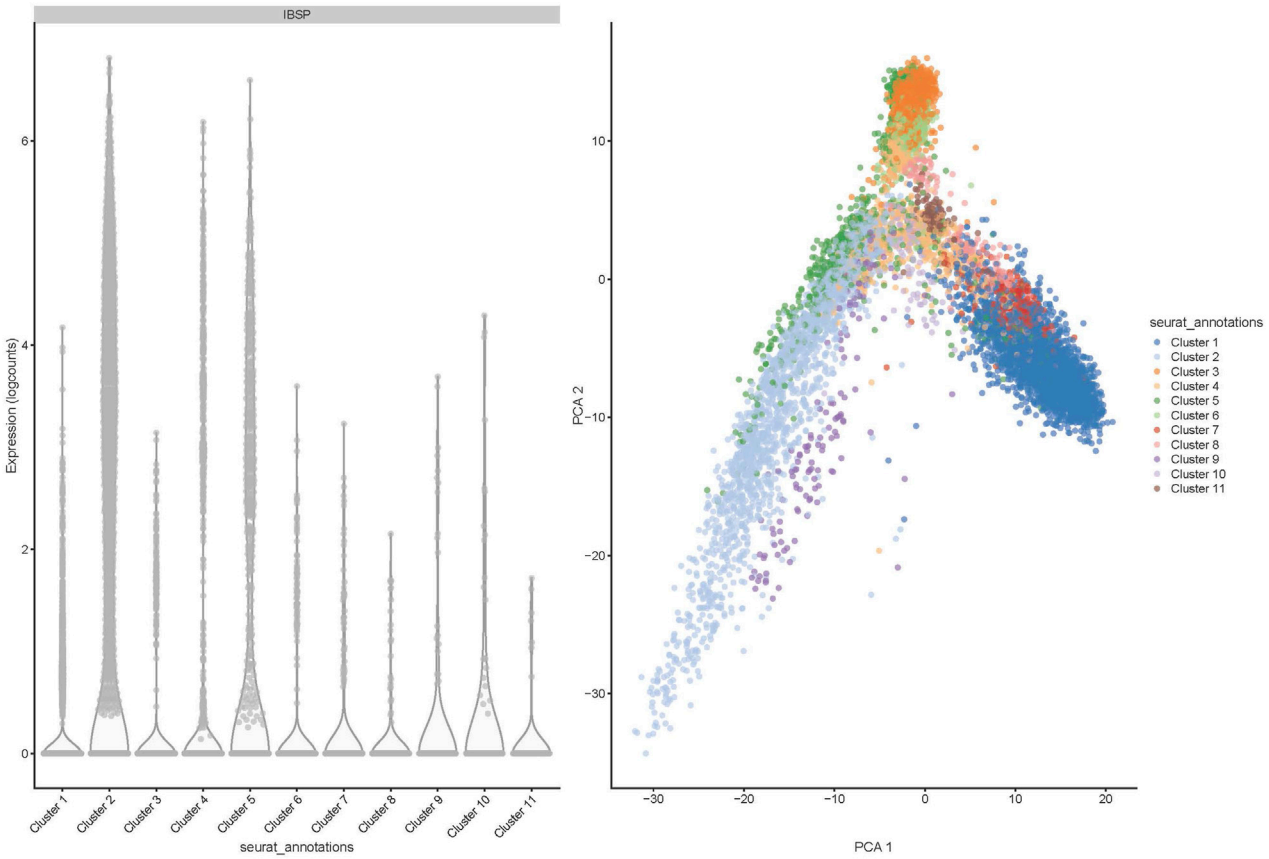

FIGURE 6
Distribution of 11 clusters of cells (shown in PCA1) and bone sialoprotein or integrin-binding sialoprotein (IBSP) expression in 11 different cell clusters shown as logcounts.

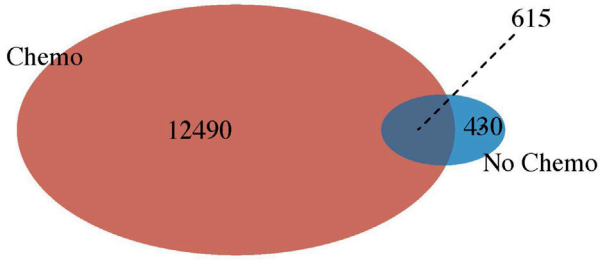

FIGURE 7
Venn diagram showing relationship between chemo-therapy verses non chemo-therapy.

from canonical pathways to the practical analysis of the disease pathologies. Gene set enrichment data were further analysed in the context of known pathologies and diseases by using disease ontology annotation. Interestingly, our dataset only indicated malignant diseases including different cancers, bone development and movement disease (Figure 9). Most remarkably the top disease ontology matches were osteosarcoma and bone cancer.

Discussion

Highly upregulated genes in OS

IFITM5 (Interferon-induced transmembrane protein 5) gene was overexpressed in osteosarcoma samples compared to normal samples. It has been shown that *IFITM5* is expressed predominantly in bone tissue and plays a key role in the formation and mineralisation of bone [23, 24]. In particular, several studies have shown that *IFITM5* is overexpressed in osteosarcoma and also it was reported that the overexpression of IFITM5 has been shown to promote the growth and invasion of osteosarcoma cells *in vitro* and *in vivo* [24, 25]. The exact mechanism by which *IFITM5* promotes the development and progression of osteosarcoma is still not fully understood. However, it is thought that *IFITM5* may regulate the activity

TABLE 2 Top downregulated genes in osteosarcoma based on FFPE PathWest 2 study.

Gene name	Symbol	Base mean	Log2FoldChange	Padj
Hemoglobin subunit alpha 1	HBA1	133.6	−6.3	7.21E-25
Regulator of G protein signaling 6	RGS6	13.9	−4.2	2.36E-17
ATPase Na+/K+ transporting subunit alpha 2	ATP1A2	44.0	−4.1	2.62E-11
Keratin 2	KRT2	10.7	−4.0	1.51E-13
Hemoglobin subunit beta	HBB	61.0	−4.0	3.33E-11
LIM domain binding 3	LDB3	40.4	−3.9	8.24E-11
Desmocollin 1	DSC1	9.8	−3.9	5.88E-14
Polymeric immunoglobulin receptor	PIGR	9.6	−3.8	2.33E-13
Myosin binding protein C1	MYBPC1	29.4	−3.7	8.11E-09
Keratin 1	KRT1	7.7	−3.6	6.32E-13
WNK lysine deficient protein kinase 2	WNK2	23.3	−3.3	5.73E-09
Perilipin 4	PLIN4	19.8	−3.3	1.46E-09
Adenylate cyclase 5	ADCY5	14.2	−3.3	1.06E-09
GPR176 divergent transcript	GPR176-DT	10.1	−3.3	5.11E-11
Hemoglobin subunit alpha 2	HBA2	40.6	−3.2	1.08E-07
XK related 4	XKR4	20.8	−3.2	1.36E-08
Complement C7	C7	20.2	−3.1	1.22E-07
Cardiomyopathy associated 5	CMYA5	65.3	−3.1	1.12E-06
Fatty acid binding protein 4	FABP4	10.0	−3.1	4.29E-10
FosB proto-oncogene, AP-1 transcription factor subunit	FOSB	227.3	−3.1	1.55E-05
Tubulointerstitial nephritis antigen like 1	TINAGL1	27.2	−3.1	1.27E-07
G0/G1 switch 2	G0S2	19.4	−3.0	1.86E-08
Adiponectin, C1Q and collagen domain containing	ADIPOQ	36.3	−3.0	1.31E-06
Synaptophysin like 2	SYPL2	12.0	−3.0	2.06E-08
Potassium voltage-gated channel subfamily A regulatory beta subunit 1	KCNAB1	14.8	−3.0	3.75E-08
Hemicentin 2	HMCN2	17.9	−2.9	1.87E-07
G protein-coupled receptor class C group 5 member A	GPRC5A	19.4	−2.8	3.85E-07
Ceruloplasmin	CP	12.2	−2.8	1.30E-07
Enamelin	ENAM	8.7	−2.8	3.91E-09
Sorbin and SH3 domain containing 1	SORBS1	60.6	−2.8	6.77E-06

of osteoblasts and osteoclasts, which are cells that form and break down bone tissue, respectively. In addition, *IFITM5* may modulate the expression of genes that are important for cell proliferation, invasion, and survival. Overall, while more research is needed to fully understand the role of *IFITM5* in bone cancer, these findings suggest that *IFITM5* may be a potential target for the development of new treatments for osteosarcoma and other bone cancers.

Collagen triple helix repeat containing 1 (*CTHRC1*) is a gene that has been repeatedly shown to be overexpressed in osteosarcoma and is not only involved in carcinogenesis but is also a prognostic marker for malignancy, progression, and OS survival [26]. The high expression of *CTHRC1* has been shown to be correlated with differentiation, recurrency, chemotherapy response, and metastasis in patients with OS [27]. In addition, the survival analysis suggested that high expression of *CTHRC1*

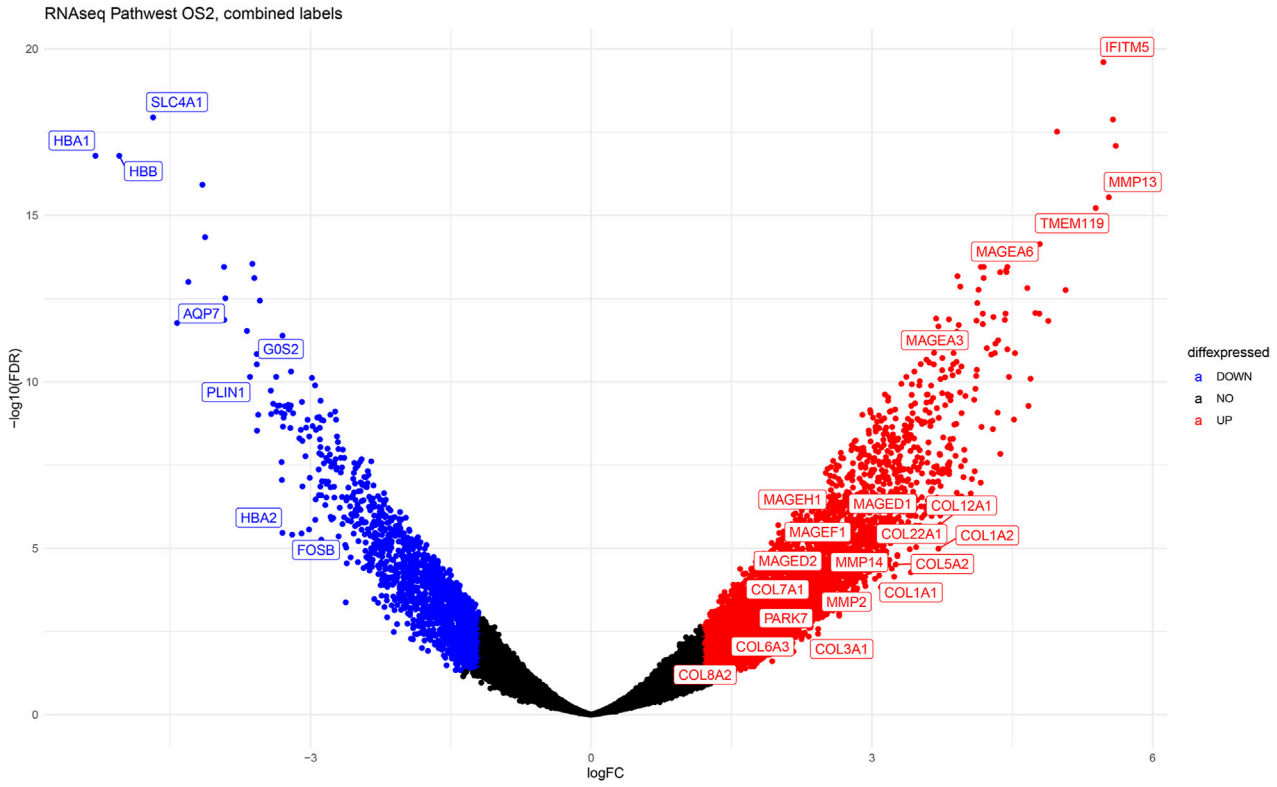

FIGURE 8
The volcano plot illustrating the differentially expressed genes in osteosarcoma. The y-axis represents -Log10 (FDR) values and x-axis represents Log2-fold -change (Log2Fc). Each spot represents a gene on the graph. The blue dots represent downregulated genes and the red dots on the right are upregulated genes.

in OS patients correlates with a significantly shorter survival time. *CTHRC1* is related to metastasis development and osteosarcoma invasion. Recent research has shown that *CTHRC1* plays an important role in osteosarcoma progression. Lentivirus-mediated short hairpin RNA (shRNA) against *CTHRC1* significantly inhibited cell proliferation and colony formation in U2OS and SW1353 cells [26]. Flow cytometry assay showed that knockdown of *CTHRC1* increased the cell percentage of G0/G1 phase, resulting in cell cycle arrest in U2OS cells. Moreover, *CTHRC1* silencing induced the cell cycle arrest by a decrease in the cell percentage in G0/G1 phase and increased in G2/M phase in SW1353 cells. In addition, crystal violet staining suggested *CTHRC1* silencing inhibited migration of U2OS and SW1353 cells. Downregulation of *CTHRC1* would be an excellent target to stop the metastases of osteosarcoma.

Pannexin 3 is a member of the pannexin family of proteins and observed to be highly expressed in osteosarcoma compared to normal sample. *PANX3* regulates bone growth and differentiation [28] and is expressed in cartilage and regulates chondrocyte proliferation and differentiation [28]. A phenotypic analysis of Panx3-KO mice has indicated that *PANX3* regulates the terminal differentiation of chondrocytes by promoting vascular endothelial growth factor (VEGF) and matrix metalloproteinase (MMP13) [29]. Therefore, *PANX3* is directly involved in the proliferation of the bone progenitor cells. In our studies, we observed *PANX3* was overexpressed in OS samples every time.

The next genes in our list with significant upregulation was the matrix metallopeptidase 13 (*MMP13*). This gene is very well known to be involved in the development of osteosarcoma [30, 31]. *MMP13* is involved in aggressive invasion and migration of the OS. It has been repeatedly shown that inhibition of the MMP13 expression will stop the invasion and growth of the OS [32]. Moreover, MMP13 interacts with other MMPs to form a network for osteosarcoma genes. *MMP13, MMP2, and MMP14* have been identified to interact with each other and to promote the progression and invasion of osteosarcoma [33, 34]. This network also interacts with the COL gene family. Furthermore, the upregulation of matrix metallopeptidase genes, including *MMP1, MMP2, MMP9, MMP11*, and *MMP16*, has been observed in osteosarcoma (OS) [35]. Previous studies have demonstrated the overexpression of

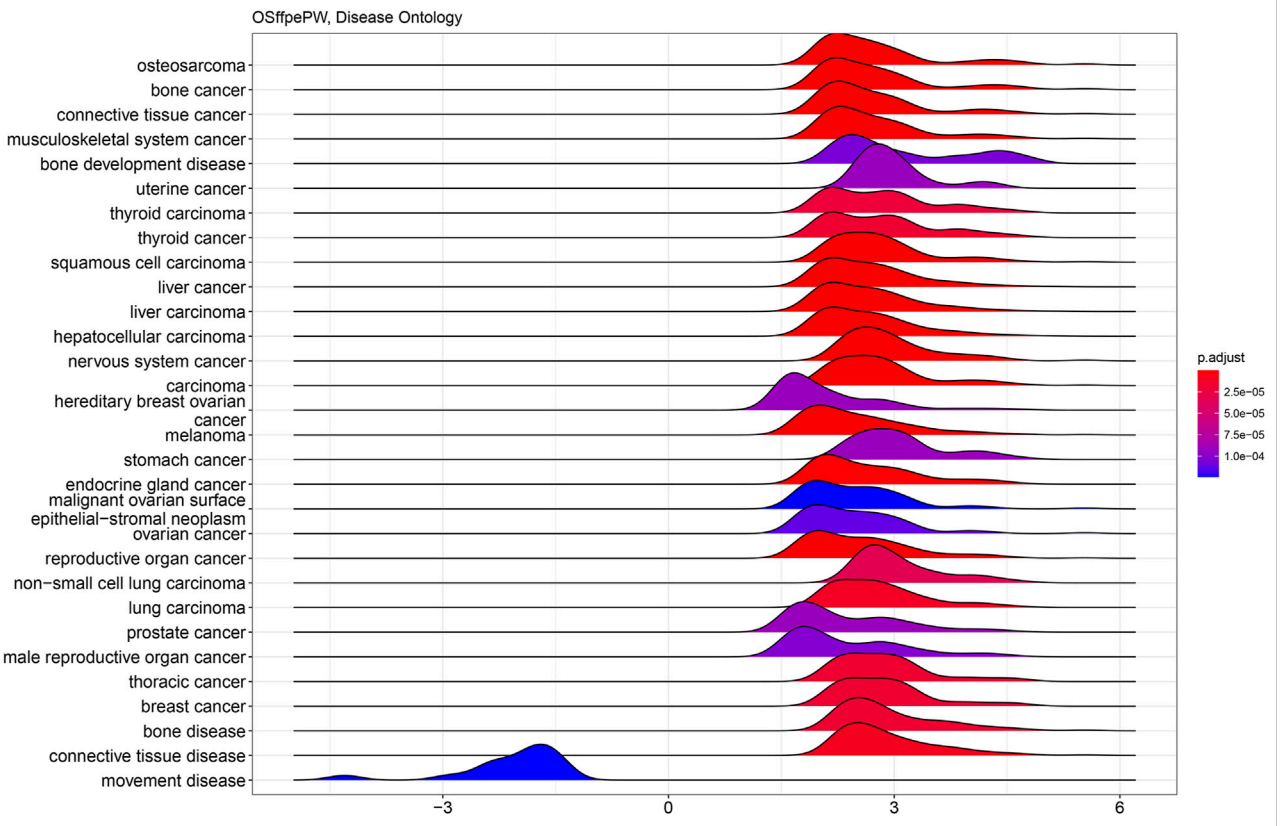

FIGURE 9
Ridge plot showing disease ontology analysis of PathWest samples. The y-axis represents -Log10 (FDR) values and x-axis represents *p*-value (p adjust). The blue ridge shown in left is correlated with downregulated genes and the ridges on right observed for upregulated genes. Related diseases are shown through X-axis.

these genes not only in OS but also in various types of cancers, where they play a crucial role in cancer survival [36, 37]. Consequently, MMPs could serve as promising diagnostic markers and potential drug targets for osteosarcoma.

TMEM119 (transmembrane protein 119) was observed to be highly upregulated in osteosarcoma derived samples as compared to healthy samples. The level of *TMEM119* protein expression was shown to be strongly associated with tumour size, clinical stage, distant metastases, and overall survival time [38]. Moreover, the gene set enrichment analysis revealed that *TMEM119* expression in osteosarcoma tissues is positively correlated with cell cycle, apoptosis, metastasis and TGF-β signaling. The reduction of the *TMEM119* expression in U2OS and MG63 cells using small interfering RNA revealed that downregulation of *TMEM119* could inhibit the proliferation of osteosarcoma cells by inducing cell cycle arrest in G0/G1 phase and apoptosis [38]. It was also found that *TMEM119* knockdown significantly inhibited cell migration and invasion and decreased the expression of TGF-β pathway-related factors. Several genes of the TMEM family have been shown to predict the survival of osteosarcoma patients.

Another important gene centromere protein F (*CENPF*) was found to be overexpressed in OS samples in compared to normal samples. *CENPF* has shown to play a key role in regulating the cell cycle and it was also shown that the increased level contributed to accelerate the cell proliferation by mediating apoptosis and cell cycle in OS [39].

Haemoglobin related genes are downregulated in OS

Similarly, *HBA1, HBA2,* and *HBB* were downregulated in osteosarcoma samples. These are genes that encode haemoglobin subunits and are additionally involved in the malignancies. It was shown that overexpression of *HBA1* and *HBB* inhibits the cell proliferation, induces cellular apoptosis and block the cell cycle at the G2/M phase [40]. *HBB* and *HBA1* are now anti-metastatic factors in other cancers [40, 41] and the downregulation of these genes may be indicative for enhanced formation of metastases. *HBA1* and *HBB* mediate apoptosis and growth arrest on malignant cells, therefore the upregulation of these genes might be beneficial for the OS patients.

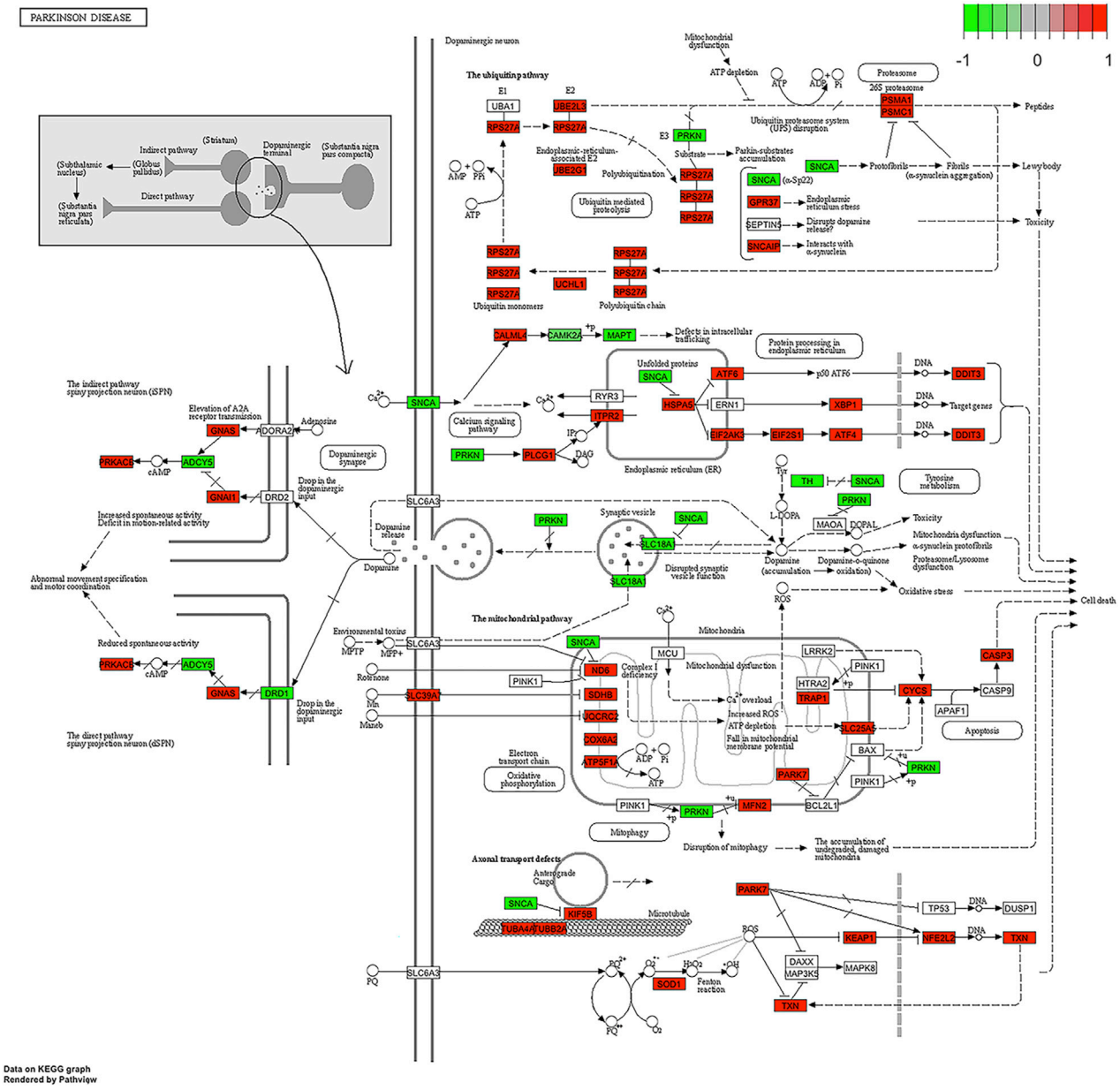

FIGURE 10
Parkinson disease pathway. The roles of PARK7 protein in Parkinson disease are highlighted.

FosB and cell cycle check point protein G0S2 are reduced in OS

FosB is a gene named as FBJ murine osteosarcoma viral oncogene homolog B and this gene was downregulated in OS samples. *FosB* is thought to play a role in the development and progression of osteosarcoma by promoting the proliferation and survival of cancer cells. In addition, *FosB* has been found to be involved in the regulation of genes that are important for bone formation, such as osteocalcin and collagen. This suggests that *FosB* may also contribute to the development of osteosarcoma by altering the normal processes of bone formation and remodeling [42, 43]. Overall, while the exact role of *FosB* in osteosarcoma is still being studied, there is evidence to suggest that it may be a potential target for the development of new treatments for this aggressive form of bone cancer. The overexpression of *FosB* gene attenuated lung cancer growth and induced the death of the cancer cells. The downregulation of *FosB* has been shown to be negatively correlated with the cancer grade. Interestingly, the studies from other groups have found that *FosB* is a tumour

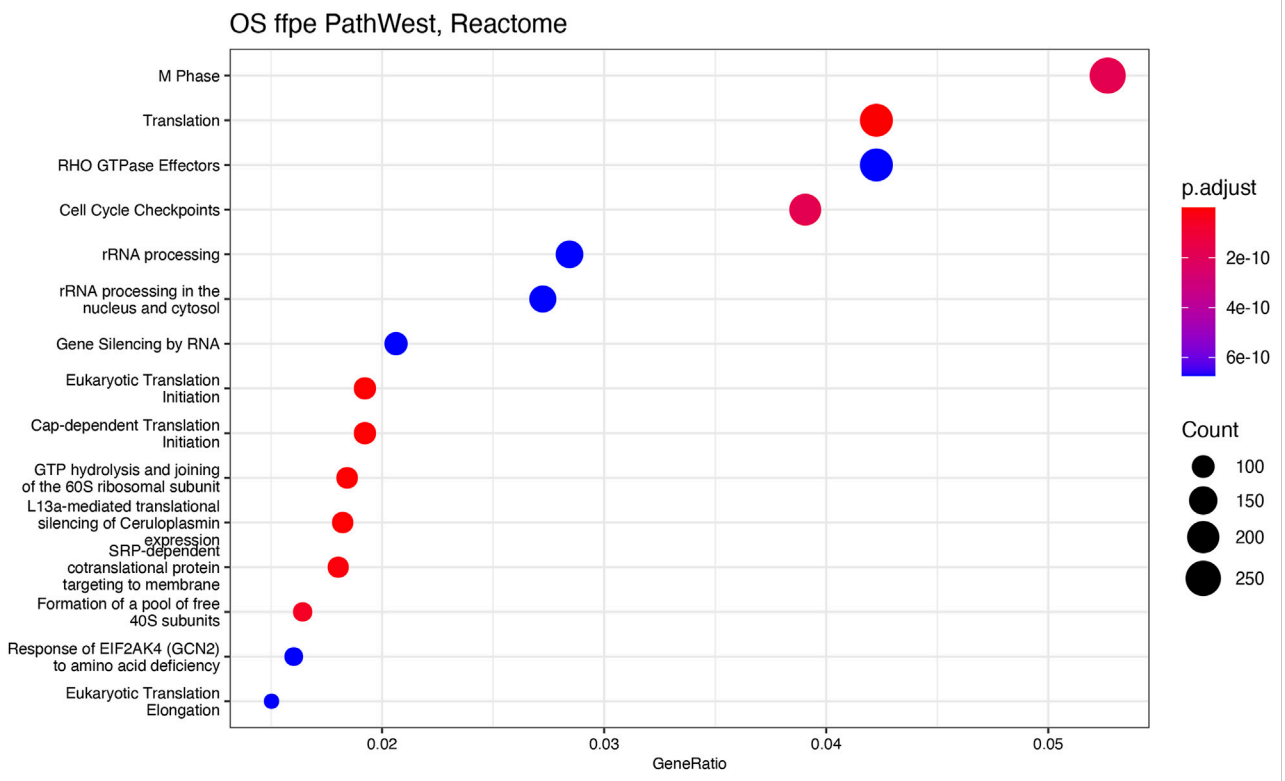

FIGURE 11
Reactome analysis. The y-axis represents gene ratio values and x-axis represents *p*-value (p adjust). Related pathways with OS are shown on X-axis.

suppressor gene [44]. Research has shown that the expression of *FosB* is reduced in osteosarcoma cells compared to normal bone cells.

G0S2 is a G0/G1 switch gene 2 which was observed to be downregulated in osteosarcoma. It is a basic protein that inhibits the proliferation of stem cells. *G0S2* gene is a switch that has been reported to be involved in migration and invasiveness of the malignant cells [45, 46]. *G0S2* gene controls the cell cycle and the down regulation of this gene in the OS samples possibly indicates the mechanisms how OS evades the cell cycle control [47].

This study indicates that even using the partially degraded FFPE samples and with variable quality, the signature of the molecular genetic changes that are indicative for osteosarcoma can be identified. This finding validates our approach and makes the genes listed in Table 2 highly accurate for the OS analysis. The number of similar DEGs that exactly matched across our different independent studies were 530, this number seems to be low in comparison to the observed DEGs in some populations. This could be due to the heterogenic nature of our samples. However, the listed genes do not match with the top DEGs published by Yang et al., in 2014 [48]. It might be due to the heterogeneity of samples and the type of control samples used for the comparison. The enrichment of the GSEA sets and its comparison to the disease ontology showed very clearly that the transcriptional profile we have discovered is related to the osteosarcoma and the genes we have identified are relevant for the OS pathology. GSEA enrichment indicated highly significant enrichment of the genetic networks related to osteosarcoma, bone cancer and connective tissue cancer. The first part of our analysis can be concluded that the FFPE sample analysis resulted in functionally meaningful and feasible results as we were able to identify the gene expression profile that is recognised by the complex computational enrichment analysis as osteosarcoma molecular network. Moreover, genes in Table 2 that is our formal list of statistically significant genes, contains many genes that are identified malignancy genes in literature. These malignancy genes are involved in osteosarcoma, other sarcomas, and in brain cancer.

Conclusion

Although the prevalence of osteosarcoma is relatively modest compared to other human cancers, the degree of malignancy is extremely high and poses a serious hazard to young patients [2, 3, 6]. The fact that neither the newly developed gene targeting therapy nor immunotherapy, which have been showing inspiring clinical effects in many other tumours, have received a positive

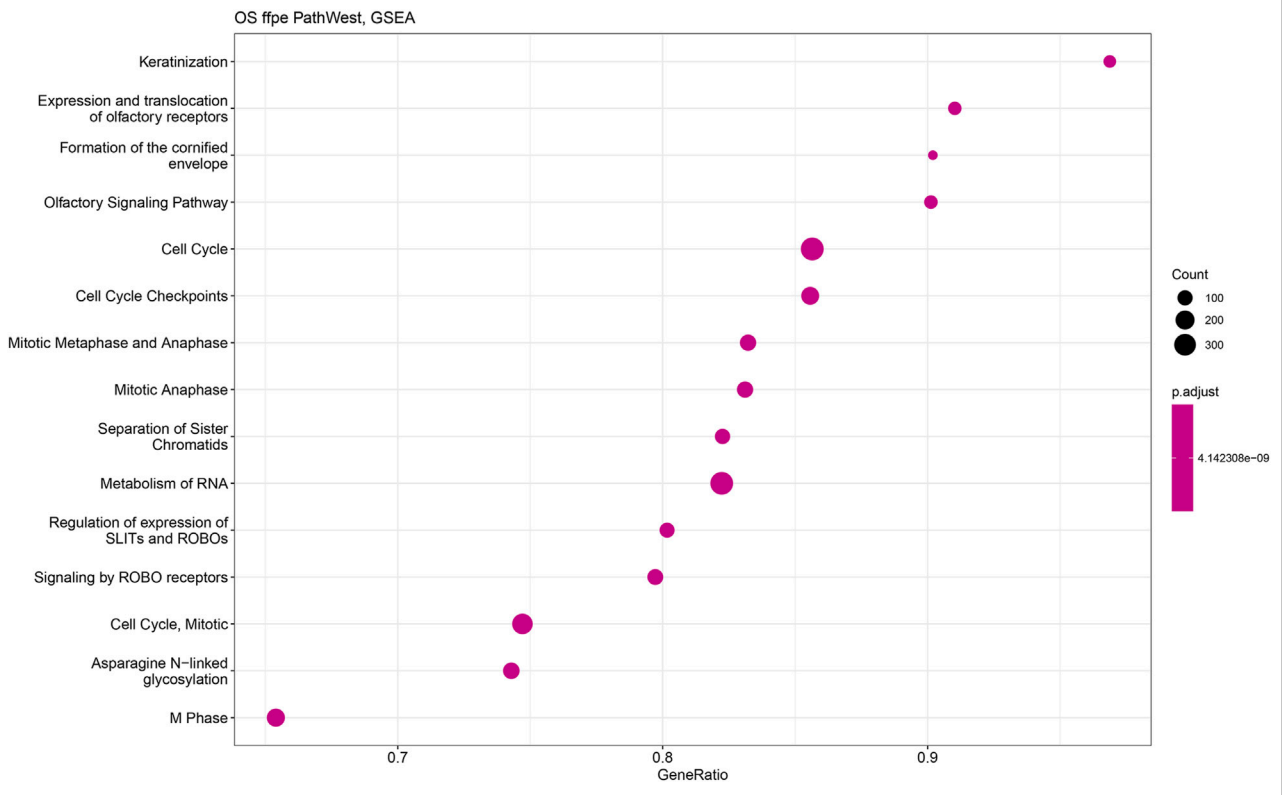

FIGURE 12
Gene set enrichment analysis of PathWest FFPE samples. The y-axis represents gene ratio values and x-axis represents *p*-value (p adjust). Related pathways with OS are shown on X-axis.

response in osteosarcoma, has contributed no notable improvement in patient survival over the past 30 years [6, 49]. It is important to explore the genetics of osteosarcoma in order to screen for prospective genes involved in cancer development and find promising targets. Analysis of differentially expressed gene expression could be a first step to identifying and establishing the marker and may potentially lead to the development of a potential drug target specific to osteosarcoma. From this study we were able to report the top upregulated and downregulated genes specific to OS in comparison to normal tissue which could assist to develop an efficient prognostic marker and therapeutic intervention specific to osteosarcoma.

We observed 530 differentially expressed genes in OS comparison to normal across our four different studies. The top highly expressed genes in OS comparison to normal controls are mostly found to be associated with extra cellular matrix related genes and have shown promise as clinical biomarker and therapeutics target in OS which needs further evaluations in preclinical models. Nevertheless, additional data analysis is required using fresh bone samples and validation of differential gene expression with qPCR and immunocytochemistry. The challenge lies in obtaining fresh bone samples, as not all patients undergo surgery. Another limitation in our study was the heterogeneous nature of the samples in terms of treatment; some underwent drug therapy, and such treatments may impact the gene expression pattern.

Author contributions

BP analyzed the data and wrote the manuscript. SK analyzed the data and reviewed and edited the manuscript.

Data availability

The datasets presented in this study can be found in online repositories. The names of the repository/repositories and accession number(s) can be found below: https://www.ncbi.nlm.nih.gov/, GSE253548.

Ethics statement

The studies involving humans were approved by the Ethics Review Committee of the University of Western Australia and Sir Charles Gairdner Hospital (2019/RA/4/20/5211). The studies were conducted in accordance with the local legislation and institutional requirements. Written informed consent for participation in this study was provided by the participants' legal guardians/next of kin.

Funding

The author(s) declare that financial support was received for the research, authorship, and/or publication of this article. This research was funded by Abbie Basson Sarcoma Foundation (Sock it to Sarcoma!) and The Johana Sewell Memorial Fund.

Acknowledgments

We thank Emel Rothzerg for extracting RNA from FFPE samples and helping with the initial statistical analysis.

Conflict of interest

The authors declare that the research was conducted in the absence of any commercial or financial relationships that could be construed as a potential conflict of interest.

Supplementary material

The Supplementary Material for this article can be found online at: https://www.ebm-journal.org/articles/10.3389/ebm.2024.10161/full#supplementary-material

References

1. Jafari F, Javdansirat S, Sanaie S, Naseri A, Shamekh A, Rostamzadeh D, et al. Osteosarcoma: a comprehensive review of management and treatment strategies. *Ann Diagn Pathol* (2020) **49**:151654. doi:10.1016/j.anndiagpath.2020.151654

2. Taran R, Taran S, Malipatil NB. Pediatric osteosarcoma: an updated review. *Indian J Med Paediatr Oncol* (2017) **38**(1):33–43. doi:10.4103/0971-5851.203513

3. Ritter J, Bielack SS. Osteosarcoma. *Ann Oncol* (2010) **21**(Suppl. 7):vii320–5. doi:10.1093/annonc/mdq276

4. Fuchs B, Pritchard DJ. Etiology of osteosarcoma. *Clin Orthopaedics Relat Res* (2002) **397**:40–52. doi:10.1097/00003086-200204000-00007

5. Isakoff MS, Bielack SS, Meltzer P, Gorlick R. Osteosarcoma: current treatment and a collaborative pathway to success. *J Clin Oncol* (2015) **33**(27):3029–35. doi:10.1200/jco.2014.59.4895

6. Rathore R, Van Tine BA. Pathogenesis and current treatment of osteosarcoma: perspectives for future therapies. *J Clin Med* (2021) **10**(6):1182. doi:10.3390/jcm10061182

7. Dracham CB, Shankar A, Madan R. Radiation induced secondary malignancies: a review article. *Radiat Oncol J* (2018) **36**(2):85–94. doi:10.3857/roj.2018.00290

8. Morton LM, Onel K, Curtis RE, Hungate EA, Armstrong GT. The rising incidence of second cancers: patterns of occurrence and identification of risk factors for children and adults. *Am Soc Clin Oncol Educ Book* (2014) **34**:e57–67. doi:10.14694/edbook_am.2014.34.e57

9. Xin S, Wei G. Prognostic factors in osteosarcoma: a study level meta-analysis and systematic review of current practice. *J Bone Oncol* (2020) **21**:100281. doi:10.1016/j.jbo.2020.100281

10. Jiang Z, Zhou X, Li R, Michal JJ, Zhang S, Dodson MV, et al. Whole transcriptome analysis with sequencing: methods, challenges and potential solutions. *Cell Mol Life Sci* (2015) **72**(18):3425–39. doi:10.1007/s00018-015-1934-y

11. Yang IS, Kim S. Analysis of whole transcriptome sequencing data: workflow and software. *Genomics Inform* (2015) **13**(4):119–25. doi:10.5808/gi.2015.13.4.119

12. von Ahlfen S, Missel A, Bendrat K, Schlumpberger M. Determinants of RNA quality from FFPE samples. *PLoS One* (2007) **2**(12):e1261. doi:10.1371/journal.pone.0001261

13. Patro R, Duggal G, Love MI, Irizarry RA, Kingsford C. Salmon provides fast and bias-aware quantification of transcript expression. *Nat Methods* (2017) **14**(4):417–9. doi:10.1038/nmeth.4197

14. Varet H, Brillet-Guéguen L, Coppée JY, Dillies MA. SARTools: a DESeq2-and EdgeR-based R pipeline for comprehensive differential analysis of RNA-seq data. *PLoS One* (2016) **11**(6):e0157022. doi:10.1371/journal.pone.0157022

15. Love MI, Huber W, Anders S. Moderated estimation of fold change and dispersion for RNA-seq data with DESeq2. *Genome Biol* (2014) **15**(12):550. doi:10.1186/s13059-014-0550-8

16. Ho XD, Phung P, Q Le V, H Nguyen V, Reimann E, Prans E, et al. Whole transcriptome analysis identifies differentially regulated networks between osteosarcoma and normal bone samples. *Exp Biol Med (Maywood)* (2017) **242**(18):1802–11. doi:10.1177/1535370217736512

17. Liu Y, Feng W, Dai Y, Bao M, Yuan Z, He M, et al. Single-cell transcriptomics reveals the complexity of the tumor microenvironment of treatment-naive osteosarcoma. *Front Oncol* (2021) **11**:709210. doi:10.3389/fonc.2021.709210

18. Polanin JR, Hennessy EA, Tanner-Smith EE. A review of meta-analysis packages in R. *J Educ Behav Stat* (2016) **42**:206–42. doi:10.3102/1076998616674315

19. Du J, Yuan Z, Ma Z, Song J, Xie X, Chen Y. KEGG-PATH: Kyoto encyclopedia of genes and genomes-based pathway analysis using a path analysis model. *Mol Biosyst* (2014) **10**(9):2441–7. doi:10.1039/c4mb00287c

20. Chen L, Zhang YH, Wang S, Zhang Y, Huang T, Cai YD. Prediction and analysis of essential genes using the enrichments of gene ontology and KEGG pathways. *PLoS One* (2017) **12**(9):e0184129. doi:10.1371/journal.pone.0184129

21. Jin W. Novel insights into PARK7 (DJ-1), a potential anti-cancer therapeutic target, and implications for cancer progression. *J Clin Med* (2020) **9**(5):1256. doi:10.3390/jcm9051256

22. Subramanian A, Tamayo P, Mootha VK, Mukherjee S, Ebert BL, Gillette MA, et al. Gene set enrichment analysis: a knowledge-based approach for interpreting genome-wide expression profiles. *Proc Natl Acad Sci U S A* (2005) **102**(43):15545–50. doi:10.1073/pnas.0506580102

23. Sun Y, Zhang C, Fang Q, Zhang W, Liu W. Abnormal signal pathways and tumor heterogeneity in osteosarcoma. *J Transl Med* (2023) **21**(1):99. doi:10.1186/s12967-023-03961-7

24. Patoine A, Husseini A, Kasaai B, Gaumond MH, Moffatt P. The osteogenic cell surface marker BRIL/IFITM5 is dispensable for bone development and homeostasis in mice. *PLoS One* (2017) **12**(9):e0184568. doi:10.1371/journal.pone.0184568

25. Jiang H, Du H, Liu Y, Tian X, Xia J, Yang S. Identification of novel prognostic biomarkers for osteosarcoma: a bioinformatics analysis of differentially expressed genes in the mesenchymal stem cells from single-cell sequencing data set. *Translational Cancer Res* (2022) **11**(10):3841–52. doi:10.21037/tcr-22-2370

26. Sang W, Zhu L, Ma J, Lu H, Wang C. Lentivirus-mediated knockdown of CTHRC1 inhibits osteosarcoma cell proliferation and migration. *Cancer Biother Radiopharm* (2016) **31**(3):91–8. doi:10.1089/cbr.2014.1758

27. Mei D, Zhu Y, Zhang L, Wei W. The role of CTHRC1 in regulation of multiple signaling and tumor progression and metastasis. *Mediators Inflamm* (2020) **2020**:9578701–13. doi:10.1155/2020/9578701

28. Iwamoto T, Nakamura T, Doyle A, Ishikawa M, de Vega S, Fukumoto S, et al. Pannexin 3 regulates intracellular ATP/cAMP levels and promotes chondrocyte differentiation. *J Biol Chem* (2010) **285**(24):18948–58. doi:10.1074/jbc.m110.127027

29. Ishikawa M, Yamada Y. The role of pannexin 3 in bone biology. *J Dent Res* (2017) **96**(4):372–9. doi:10.1177/0022034516678203

30. Cui J, Dean D, Hornicek FJ, Chen Z, Duan Z. The role of extracelluar matrix in osteosarcoma progression and metastasis. *J Exp Clin Cancer Res* (2020) **39**(1):178. doi:10.1186/s13046-020-01685-w

31. Li S, Pritchard DM, Yu LG. Regulation and function of matrix metalloproteinase-13 in cancer progression and metastasis. *Cancers (Basel)* (2022) **14**(13):3263. doi:10.3390/cancers14133263

32. Ma O, Cai WW, Zender L, Dayaram T, Shen J, Herron AJ, et al. MMP13, Birc2 (cIAP1), and Birc3 (cIAP2), amplified on chromosome 9, collaborate with p53 deficiency in mouse osteosarcoma progression. *Cancer Res* (2009) **69**(6):2559–67. doi:10.1158/0008-5472.can-08-2929

33. Tang H, Tang Z, Jiang Y, Wei W, Lu J. Pathological and therapeutic aspects of matrix metalloproteinases: implications in osteosarcoma. *Asia-Pacific J Clin Oncol* (2019) **15**(4):218–24. doi:10.1111/ajco.13165

34. Wang Z, Jian M, Li X. Profiling of multiple matrix metalloproteinases activities in the progression of osteosarcoma by peptide microarray-based fluorescence assay on polymer brush-coated zinc oxide nanorod substrate. *Methods Mol Biol* (2023) **2578**:161–75. doi:10.1007/978-1-0716-2732-7_11

35. Zhou J, Liu T, Wang W. Prognostic significance of matrix metalloproteinase 9 expression in osteosarcoma: a meta-analysis of 16 studies. *Medicine (Baltimore)* (2018) **97**(44):e13051. doi:10.1097/md.0000000000013051

36. Amakye D, Gyan PO, Santa S, Aryee NA, Adu-Bonsaffoh K, Quaye O, et al. Extracellular matrix metalloproteinases inducer gene polymorphism and reduced serum matrix metalloprotease-2 activity in preeclampsia patients. *Exp Biol Med (Maywood)* (2023) **248**(18):1550–5. doi:10.1177/15353702231199464

37. Quintero-Fabian S, Arreola R, Becerril-Villanueva E, Torres-Romero JC, Arana-Argáez V, Lara-Riegos J, et al. Role of matrix metalloproteinases in angiogenesis and cancer. *Front Oncol* (2019) **9**:1370. doi:10.3389/fonc.2019.01370

38. Jiang ZH, Peng J, Yang HL, Fu XL, Wang JZ, Liu L, et al. Upregulation and biological function of transmembrane protein 119 in osteosarcoma. *Exp Mol Med* (2017) **49**(5):e329. doi:10.1038/emm.2017.41

39. Zou PA, Yang ZX, Wang X, Tao ZW. Upregulation of CENPF is linked to aggressive features of osteosarcoma. *Oncol Lett* (2021) **22**(3):648. doi:10.3892/ol.2021.12909

40. Luo P, Liu X, Tang Z, Xiong B. Decreased expression of HBA1 and HBB genes in acute myeloid leukemia patients and their inhibitory effects on growth of K562 cells. *Hematology* (2022) **27**(1):1003–9. doi:10.1080/16078454.2022.2117186

41. Liu X, Gao Y, Zhao B, Li X, Lu Y, Zhang J, et al. Discovery of microarray-identified genes associated with ovarian cancer progression. *Int J Oncol* (2015) **46**(6):2467–78. doi:10.3892/ijo.2015.2971

42. Inoue D, Kido S, Matsumoto T. Transcriptional induction of FosB/ΔFosB gene by mechanical stress in osteoblasts. *J Biol Chem* (2004) **279**(48):49795–803. doi:10.1074/jbc.m404096200

43. Lam SW, Cleven AHG, Kroon HM, Briaire-de Bruijn IH, Szuhai K, Bovée JVMG. Utility of FOS as diagnostic marker for osteoid osteoma and osteoblastoma. *Virchows Arch* (2020) **476**(3):455–63. doi:10.1007/s00428-019-02684-9

44. Tang C, Jiang Y, Shao W, Shi W, Gao X, Qin W, et al. Abnormal expression of FOSB correlates with tumor progression and poor survival in patients with gastric cancer. *Int J Oncol* (2016) **49**(4):1489–96. doi:10.3892/ijo.2016.3661

45. Fukunaga T, Fujita Y, Kishima H, Yamashita T. Methylation dependent down-regulation of G0S2 leads to suppression of invasion and improved prognosis of IDH1-mutant glioma. *PLoS One* (2018) **13**(11):e0206552. doi:10.1371/journal.pone.0206552

46. Yim CY, Sekula DJ, Hever-Jardine MP, Liu X, Warzecha JM, Tam J, et al. G0S2 suppresses oncogenic transformation by repressing a MYC-regulated transcriptional program. *Cancer Res* (2016) **76**(5):1204–13. doi:10.1158/0008-5472.can-15-2265

47. Heckmann BL, Zhang X, Xie X, Liu J. The G0/G1 switch gene 2 (G0S2): regulating metabolism and beyond. *Biochim Biophys Acta (Bba) - Mol Cell Biol Lipids* (2013) **1831**(2):276–81. doi:10.1016/j.bbalip.2012.09.016

48. Yang Z, Chen Y, Fu Y, Yang Y, Zhang Y, Chen Y, et al. Meta-analysis of differentially expressed genes in osteosarcoma based on gene expression data. *BMC Med Genet* (2014) **15**:80. doi:10.1186/1471-2350-15-80

49. Prudowsky ZD, Yustein JT. Recent insights into therapy resistance in osteosarcoma. *Cancers (Basel)* (2020) **13**(1):83. doi:10.3390/cancers13010083

EBM Experimental Biology and Medicine

TYPE Original Research
PUBLISHED 21 June 2024
DOI 10.3389/ebm.2024.10081

OPEN ACCESS

*CORRESPONDENCE
Genesy Pérez Jorge,
g211546@dac.unicamp.br,
genesyperezj@gmail.com
Marcelo Brocchi,
mbrocchi@unicamp.br

RECEIVED 23 December 2023
ACCEPTED 07 May 2024
PUBLISHED 21 June 2024

CITATION
Pérez Jorge G, Gontijo M, Silva MFe, Goes ICRDS, Jaimes-Florez YP, Coser LdO, Rocha FJS, Giorgio S and Brocchi M (2024), Attenuated mutants of *Salmonella enterica* Typhimurium mediate melanoma regression via an immune response.
Exp. Biol. Med. 249:10081.
doi: 10.3389/ebm.2024.10081

Attenuated mutants of *Salmonella enterica* Typhimurium mediate melanoma regression via an immune response

Genesy Pérez Jorge [1,2]*, Marco Gontijo [1,3], Marina Flóro e Silva [1,4], Isabella Carolina Rodrigues Dos Santos Goes [1], Yessica Paola Jaimes-Florez [1,5], Lilian de Oliveira Coser [6], Francisca Janaína Soares Rocha [7], Selma Giorgio [4] and Marcelo Brocchi [1]*

[1]Departamento de Genética, Evolução, Microbiologia e Immunologia, Instituto de Biologia, Universidade Estadual de Campinas—UNICAMP, Campinas, SP, Brazil, [2]Research Group: Statistics and Mathematical Modeling Applied to Educational Quality, University of Sucre, Sincelejo, Sucre, Colombia, [3]Department of Molecular Genetics and Microbiology, Duke University Medical Center, Duke Medicine Cir, Durham, NC, United States, [4]Departamento de Biologia Animal, Instituto de Biologia, Universidade Estadual de Campinas, Campinas—UNICAMP, Campinas, SP, Brazil, [5]GIMBIO Group, Department of Microbiology, Faculty of Basic Sciences, Universidad de Pamplona, Pamplona, Colombia, [6]Departamento de Biologia Estrutural e Funcional, Laboratório de Regeneração Nervosa, Instituto de Biologia, Universidade Estadual de Campinas—UNICAMP, Campinas, SP, Brazil, [7]Área Acadêmica de Medicina Tropical, Centro de Ciências Médicas, Universidade Federal de Pernambuco, Recife, Pernambuco, Brazil

Abstract

The lack of effective treatment options for an increasing number of cancer cases highlights the need for new anticancer therapeutic strategies. Immunotherapy mediated by *Salmonella enterica* Typhimurium is a promising anticancer treatment. Candidate strains for anticancer therapy must be attenuated while retaining their antitumor activity. Here, we investigated the attenuation and antitumor efficacy of two *S. enterica* Typhimurium mutants, Δ*tolRA* and Δ*ihfABpmi*, in a murine melanoma model. Results showed high attenuation of Δ*tolRA* in the *Galleria mellonella* model, and invasion and survival in tumor cells. However, it showed weak antitumor effects *in vitro* and *in vivo*. Contrastingly, lower attenuation of the attenuated Δ*ihfABpmi* strain resulted in regression of tumor mass in all mice, approximately 6 days after the first treatment. The therapeutic response induced by Δ*ihfABpmi* was accompanied with macrophage accumulation of antitumor phenotype (M1) and significant increase in the mRNAs of proinflammatory mediators (TNF-α, IL-6, and iNOS) and an apoptosis inducer (Bax). Our findings indicate that the attenuated Δ*ihfABpmi* exerts its antitumor activity by inducing macrophage infiltration or reprogramming the

10.3389/ebm.2024.10081

immunosuppressed tumor microenvironment to an activated state, suggesting that attenuated *S. enterica* Typhimurium strains based on nucleoid-associated protein genes deletion could be immunotherapeutic against cancer.

KEYWORDS

***S. enterica* Typhimurium, melanoma, mutants, anticancer, macrophage**

Impact statement

Melanoma is the most common form of malignancy in Caucasians globally. Recent advances in cancer treatment are still insufficient to mitigate mortality and recurrence rates, primarily due to tumor heterogeneity. Live tumor-targeting bacteria represent a unique therapeutic option to overcome cancer therapeutics' high toxicity, drug penetration, and resistance. Here, we show that live attenuated *Salmonella enterica* Typhimurium mutants have antitumor potential *in vivo* against the aggressive melanoma model with no observable side effects. Intratumoral injection of attenuated *S. enterica* Typhimurium mediated the reduction of the tumor mass. Furthermore, we demonstrate that the tumor regression caused by our triple mutant is related to a shift to a pro-inflammatory response. These findings delineate new mutants

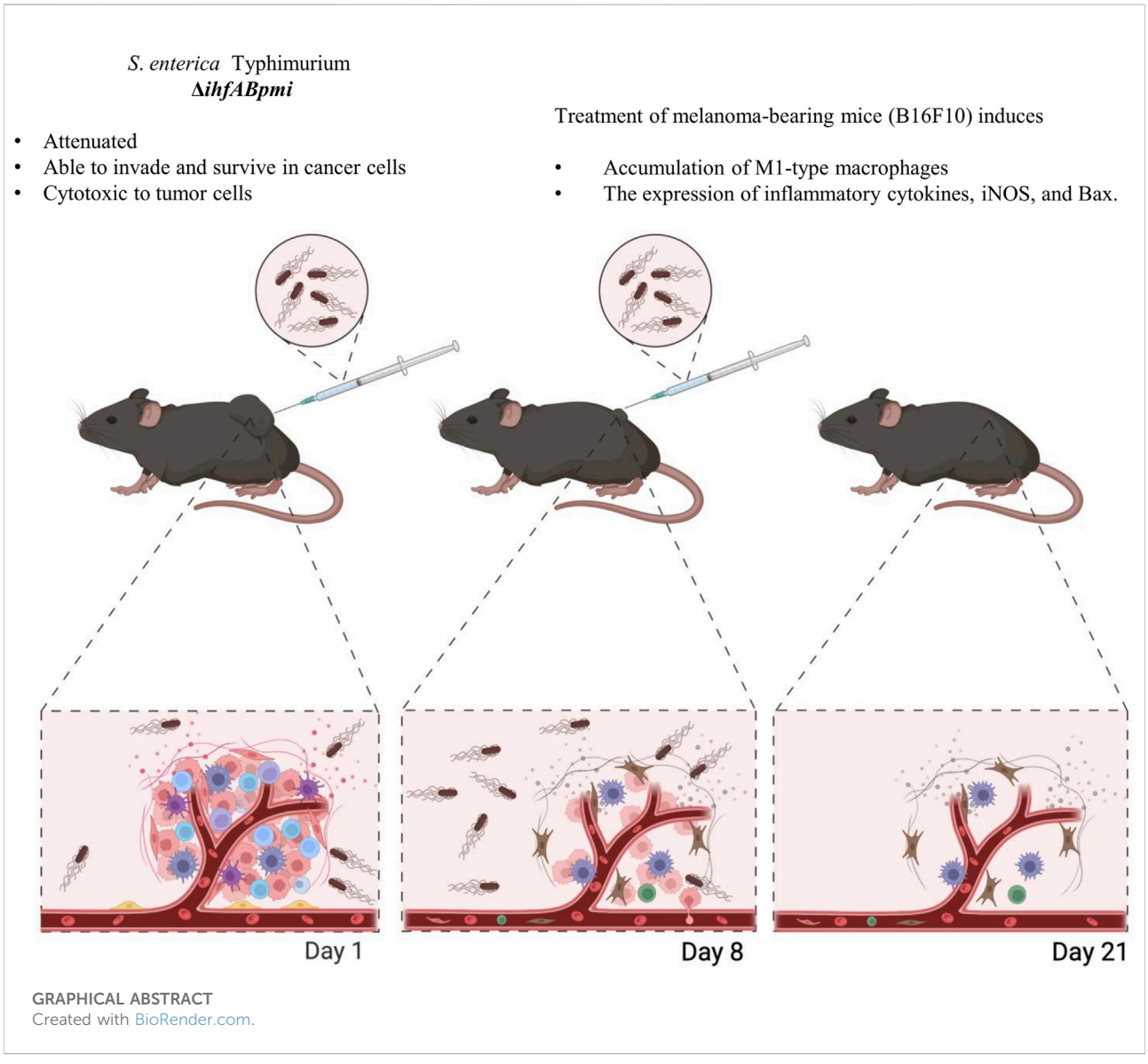

GRAPHICAL ABSTRACT
Created with BioRender.com.

in the fight against cancer and possible mechanisms of localized bacteria-mediate inflammation leading to mouse tumor regression. Advances in our understanding of bacteria-mediated cancer treatment will help guide the development of new and improved cancer treatment therapies.

Introduction

Cancer is a malignant disease difficult to treat efficiently, resulting in significant global, social, and economic burden [1]. Despite major advances in cancer treatment, including the development of surgery, chemotherapy, radiotherapy, and antibody immunotherapy, mortality and recurrence rates remain high due to the complexity of the disease and limitations of currently available treatment options [1–3]. Surgical resection of tumors with surrounding healthy tissue represents the primary and most favorable treatment option for patients with early-stage cancer (when the tumor is small and localized). However, due to the silent nature of oncogenesis, most patients are often diagnosed at advanced stages of the disease when surgical resection is not a viable treatment option. The standard anticancer treatments of chemo- and radiotherapy have low specificity and high toxicity, resulting in severe side effects [4]. Therapies based on monoclonal antibodies also show limited immune response and penetration, with only a minority of patients that respond to treatment [5]. Therefore, new therapeutic approaches for efficient treatment of cancer patients are urgently needed. In this context, *Salmonella enterica* Typhimurium–mediated immunotherapy represents a viable solution for cancer treatment.

Salmonella enterica Typhimurium strains have been extensively explored in cancer immunotherapy due to several innate characteristics, including the targeting of intrinsic tumors, penetration of hypoxic areas [6, 7] and intrinsic antitumor activity [8]. The antitumor activity of *S. enterica* Typhimurium is mainly attributed to activation of the immune system [8–12]. Infection by *S. enterica* Typhimurium in the tumor microenvironment alerts the immune system, activating oncolytic mechanisms such as increased expression of interferon γ, inducible nitric oxide synthase (iNOS), interleukin-1β (IL-1β), and tumor necrosis factor α (TNF-α) [10], as well as decreased levels of transforming growth factor-β (TGF-β), vascular endothelial growth factor (VEGF), and anti-inflammatory cytokines. Moreover, *S. enterica* Typhimurium can promote the recruitment of immune cells, such as dendritic cells, neutrophils, lymphocytes, and macrophages [10–13]. Taken together, these mechanisms alter the immunosuppressed antitumor microenvironment into an immunoactive environment that promotes tumor cell destruction.

Macrophage infiltration and phenotype after *S. enterica* administration in the tumor microenvironment has been little studied [13]. Alternately activated macrophages or M2-type macrophages promote immunosuppression and are characterized by decreased iNOS and TNF-α expression, and positively influence tumor growth, metastases, angiogenesis, and extracellular matrix remodeling, while classically activated or M1-type macrophages exhibit phagocytic activity, can promote a Th1 response, and are associated with tumor growth suppression [10, 14, 15]. Lipopolysaccharide (LPS) can induce phenotypic changes in macrophages [15, 16]. Previously, it was shown that *S. enterica* Typhimurium mutants could induce macrophage infiltration and reprogram the M2 to M1 macrophage polarization [10, 11, 16], suggesting their potential use to combat tumor progression.

Different strains of *S. enterica* Typhimurium have shown promising results *in vitro* and *in vivo* [17–22]. However, strains evaluated in clinical trials have not shown antitumor efficacy [23–25], making it essential to explore new strains of *S. enterica* Typhimurium with antitumor potential. A good anticancer therapy candidate must have a balance between attenuation and antitumor activity. Wild-type *S. enterica* Typhimurium strains are unsuitable for cancer therapy because they can cause severe sepsis in the host. Highly attenuated strains are inefficient because they cannot stimulate the immune system for tumor elimination [26].

Considering the need to develop safe strains with antitumor efficacy, in this study, we constructed two mutants of *S. enterica* Typhimurium and evaluated their therapeutic efficacy, as well the induction of macrophage infiltration and production of inflammatory mediators in tumors. The Δ*tolRA* mutant strain lacks two cell envelope proteins, and the Δ*ihfABpmi* mutant is deficient in 6-phosphomannose isomerase and integration host factor (IHF), a nucleoid-associated protein. Both mutants showed attenuation of virulence and antitumor potential in a murine melanoma model. Furthermore, the antitumor efficacy of the Δ*ihfABpmi* mutant was associated with the accumulation of phenotype M1 macrophages in melanoma tumors.

Materials and methods

Bacterial strains, plasmids, primers, and culture media

The bacterial strains, plasmids, and primers used in this study are described in Supplementary Table S1. Bacteria were grown aerobically at 37°C on LB agar, LB broth (prepared according to Sambrook and Russell, 2001 [27]), MacConkey (Kasvi, Brazil), and Salmonella-Shigella (SS) media (Oxoid, United Kingdom). Ampicillin (100 μg/mL; Sigma, Spain), Kanamycin (50 μg/mL; Sigma, Spain), chloramphenicol (25 μg/mL; USB, United Kingdom), or mannose (0.5%, Sigma, Spain) were used, as required. The bacterial strains used in this study were stored at −80°C in 20% glycerol in an LB medium.

In vitro growing conditions

Bacteria were seeded on LB agar and incubated at 37°C for 16–18 h. Colonies grown on LB agar were inoculated into LB broth and cultured for 16–18 h at 37°C under agitation (150 rpm). The next day, the culture was diluted 1:100 in fresh LB broth and grown to the exponential phase (~10^8 CFU/mL) under the above conditions. The culture was centrifuged at 4,000 × g for 5 min, and the pellet was suspended in PBS. Subsequently, the bacteria were diluted to the appropriate concentration for *in vitro* and *in vivo* experiments. In all experiments, mannose was added to the culture medium (LB agar or LB broth) for the growth of the Δ*ihfABpmi* mutant.

Construction of mutants

The new triple mutant Δ*ihfABpmi* was constructed using the λ Red recombination system followed by transduction with phage p22. We initially constructed the Δ*pmi*:*Kan* mutant by recombination-mediated allelic exchange of the *pmi* gene with the kanamycin cassette. The deletion of the *pmi* gene was verified by PCR using the detection primers described in Supplementary Table S1. Subsequently, Δ*pmi*:*Kan* was used as the donor strain for transduction with the p22 phage, and the Δ*ihfAB* mutant was used as the recipient strain, resulting in the Δ*ihfABpmi* mutant.

The double mutant Δ*tolRA* was constructed using the λ Red system as previously described [28]. We deleted the *tolR* and *tolA* genes from the ATCC 14028 chromosome in a single step, by red-mediated recombination and allelic exchange of the *tolR* and *tolA* genes with the kanamycin resistance gene. The gene deletion was confirmed by PCR using the tolRADT-F and tolRADT-R primers described in Supplementary Table S1.

Cancer cell lineage

Cell lines B16F10 (mouse melanoma) and 5,637 (human bladder cancer) were used in this study. Cells were grown at 37°C in humidified air with 5% CO_2. Dulbecco's Modified Eagle medium (Thermo Fisher Scientific, Carlsbad, CA, United States) (DMEM) was used to grow B16F10 cells and RPMI 1640 (Thermo Fisher Scientific) medium was used to grow 5,637 cells. Both media were supplemented with 10% fetal bovine serum, penicillin (100 U/mL) and streptomycin (100 μg/mL) for cell growth.

Growth curve

The *in vitro* growth of the mutants was assessed in LB broth as previously described [29]. Briefly, a 16–18 h culture was diluted (1:1,000) in LB broth and incubated at 37°C and 150 rpm. Growth was monitored for 12 h employing hourly optical density readings and CFU determination by plating on LB-agar. Three independent experiments were performed.

Virulence in the *Galleria mellonella* model

Virulence attenuation of engineered mutants of *S. enterica* Typhimurium was evaluated *in vivo* in the *Galleria mellonella* infection model by inoculating 10 μL of a 1 × 10^6 CFU/mL bacterial (mutant or wild-type strain) suspension in the last proleg of larvae between 200 and 250 mg. Ten larvae were used per group. Larvae survival was observed for 96 h after inoculation. The experiment was performed three times.

LPS extraction and analysis by sodium dodecyl sulfate polyacrylamide gel electrophoresis (SDS-PAGE)

The integrity of LPS, which is associated with bacterial immunogenicity, was also analyzed by profiling LPS on a polyacrylamide gel. LPS from the mutants and wild-type strain was extracted as previously described [30]. Briefly, colonies grown on LB-agar plates were homogenized in deionized water until an OD_{600} between 0.4 and 0.5 was reached. The bacterial suspension was centrifuged at 10,000 rpm for 2 min, and the supernatant was discarded. The pellet was homogenized in a Laemmli buffer (Tris-HCl, pH 6.8 0.625 M, 2% SDS, 25% glycerol, and 0.01% bromophenol blue) incubated at 100°C for 10 min. Then, 10 μL of Proteinase K solution (2.5 mg/mL) was added, and the suspension was homogenized and incubated at 60°C for 1 h. The LPS samples were analyzed by SDS-PAGE. Polyacrylamide electrophoresis was performed in a 5% stacking gel and in a 12% separating gel, with exposure to a constant voltage of 100 V for 2 h. The separated LPS was stained with silver stain [31], by initially incubating the gel in a fixative solution (40% ethanol and 5% acetic acid) for 16 h, followed by incubation in an oxidizing solution for 10 min. After three washes in deionized water, the gel was stained for 10 min with a silver solution (0.02M NaOH, 1.5% ammonium hydroxide, and 0.7% silver nitrate), followed by three wash-steps in deionized water. Bands were developed in 0.02% formaldehyde and 0.005% acetic acid solution. After the appearance of the bands, the gel was washed in deionized water and photographed. *Pseudomonas aeruginosa* (kindly donated by Dr. Regina Lúcia Baldini—Department of Biochemistry, Instituto de Química, Universidade de São Paulo) containing the *wzz* gene deletion was used as a control for the absence of LPS. The *wzz* gene is essential for LPS biosynthesis. In *Pseudomonas aeruginosa*, strains with a deletion of this gene cannot produce LPS.

Invasion and survival assay

The invasiveness and survival capabilities of the mutants were measured using gentamicin resistance, as previously described, with some modifications [22, 32]. Briefly, 1×10^5 melanoma or bladder cancer cells per well were seeded in 24-well plates with antibiotic-free medium (RPMI for bladder cancer cells or DMEM for melanoma cells) supplemented with 10% fetal bovine serum and incubated at 37°C, 5% CO_2 for 20 h; two 24-well plates were prepared, one for the invasion assay and one for the survival assay. The next day, 2×10^6 CFU of bacteria were added over the cells to reach a multiplicity of infection (MOI) of 10:1 and incubated at 37°C, 5% CO_2 for 1 h. After three washes with PBS, a medium (RPMI for bladder cancer cells or DMEM for melanoma cells) containing 100 μg/mL gentamicin was added to each well and incubated for 1 h to kill extracellular bacteria. Then, each well was rewashed with PBS. For the invasion assay, tumor cells from one of the plates were immediately lysed with 0.5% Triton X-100 solution in PBS, followed by CFU determination by plating on LB-agar medium. For the survival assay, the other plate was incubated with medium (RPMI or DMEM) containing 20 μg/mL gentamicin and incubated for 4 h. Then, the tumor cells were washed with PBS and lysed for CFU determination. We performed three independent experiments, with three replicates from each strain.

In vitro toxicity tests

The MTT assay evaluated the cytotoxic effect of the mutants as previously described [33]. A total of 1×10^4 cells were seeded in 96-well plates with antibiotic-free medium (RPMI for bladder cancer cells or DMEM for melanoma cells) supplemented with 10% fetal bovine serum. Cells were incubated for 20 h at 37°C and 5% CO_2. Then, the cells were washed with PBS and treated with 2×10^6 CFU of bacteria to reach an MOI of 100:1. The plate was incubated at 37°C under 5% CO_2 for 1 h. Cells were rewashed with PBS and incubated with medium (RPMI or DMEM) containing 100 μg/mL gentamicin for 2 h at 37°C under 5% CO_2. Then, the cells were rewashed and incubated with a medium (RPMI or DMEM) containing 20 μg/mL of gentamicin for 24 h under appropriate culture conditions. After the incubation, the medium was removed, the cells were rewashed and the cells were re-incubated for 4 h with MTT (5 mg/mL) diluted in RPMI or DMEM medium. MTT diluted in the medium was discarded, and crystals were dissolved with dimethyl sulfoxide (DMSO-Sigma, Saint Louis, MO, United States). Absorbance was read at 570 nm. The viability of cells treated with the mutants was compared to that of untreated (control) cells. We performed three independent experiments, with three replications of each strain.

Animals

6–8-week-old C57BL/6JUnib females were used in this study. All animals were obtained from the Multidisciplinary Center for Biological Research (CEMIB—UNICAMP). The animal care committee of Universidade Estadual de Campinas approved all experiments with mice under protocol numbers 5769-1/2021 and 5895-1/2021. The animals were kept under specific pathogen-free conditions. The mice were acclimatized for 2 weeks before the start of the experiments. Mice were 8 weeks old at the time of the first inoculations. The mice were shaved on the right flank 2 days before starting the experiments to facilitate subcutaneous inoculations.

Treatment safety tests

The animals were randomly divided into four groups of five and injected subcutaneously with 60 μL in the right flank. Group I: mice received 10^5 CFU of Δ*ihfABpmi* weekly for 2 weeks, two inoculations total. Group II: the animals received 10^6 CFU of Δ*tolRA* weekly for 2 weeks. Group III: the animals received 10^7 CFU of Δ*tolRA* weekly for 2 weeks. Group IV: mice received phosphate-buffered saline (PBS) weekly for 2 weeks. During the experiment, the animals were weighed thrice a week, and the appearance of any signs of disease (ocular discharge, piloerection, lethargy) was analyzed. They were euthanized 2 weeks after the last inoculation. In addition, parts of the liver, spleen, lung, and kidneys were collected and immediately fixed in 4% paraformaldehyde solution for organ damage analysis. Tissues were stained in H&E and analyzed under a Leica DM5500 B optical microscope (Wetzlar, Hesse, Germany). Two independent experiments were performed.

To quantify bacterial distribution and persistence at the end of the experiment, part of the liver, blood, and spleen were aseptically collected and homogenized in PBS with a tissue homogenizer (Omni Mixer Homogenizer, Vernon Hills, IL, United Stated), as previously described [29]. The homogenized tissues were plated on LB-agar, MacConkey, and SS with appropriate antibiotics to determine CFU. Two independent experiments were performed using 5 mice per group in each experiment.

In vivo antitumor efficacy

The antitumor efficacy of the mutants was evaluated in a murine melanoma model. B16F10 cells were diluted in antibiotic-free and fetal bovine serum-free DMEM medium. B16F10 cells (3×10^6) were inoculated subcutaneously into the dorsal flank region of C57BL/6JUnib mice. When the tumor reached 100 mm^3 (10–12 days after tumor cell inoculation), the tumor-bearing animals were randomly assigned to groups (PBS, Δ*ihfABpmi,* and Δ*tolRA*), seven mice per group. Mice were inoculated intratumorally with 60 μL of mutant strains suspensions (10^5 CFU of Δ*ihfABpmi* or 10^6 CFU of Δ*tolRA*) or

PBS once a week for 2 weeks. Tumor size was measured every 2–3 days, and tumor volume was calculated as previously described [19]. Two independent experiments were performed using 7 mice per group in each experiment.

Tumor-bearing mice that reached 2000 mm^3 or showed signs of pain were euthanized to avoid suffering. The body weight of the mice was also measured every 2–3 days, and the mice were observed for any signs of disease throughout the treatment period. At the end of the experiments, the mice were euthanized by intraperitoneal injection of 5 mg/kg of xylazine and 40 mg/kg of ketamine, followed by cervical dislocation. Liver, spleen, kidney, and lung samples were collected, fixed in 4% formaldehyde, and stained with H&E for histopathological examination. The experiment was repeated twice.

To quantify bacterial distribution and persistence at the end of the experiment, tissues were weighed and homogenized with a tissue homogenizer (Omni Mixer Homogenizer, Vernon Hills, IL, United Stated), as previously described [29]. The mixed tissue suspension was plated in LB-agar, MacConkey, and SS with appropriate antibiotics to determine CFU. This experiment was performed twice.

The potential therapeutic antitumor of mutants was also evaluated intraperitoneally. Mice bearing B16F10 tumors (100 mm^3) were treated intraperitoneally with 10^5 CFU of Δ*ihfABpmi*, 10^6 CFU of Δ*tolRA* or PBS once a week for 2 weeks. Tumor size was measured every 2–3 days. The mice were euthanized 19 days after starting the treatments. One independent experiment was performed using 5 mice per group.

Immune response involved in the antitumor effect

To understand the immune response involved in the antitumor effect mediated by the Δ*ihfABpmi* mutant, mice bearing tumors of approximately 100 mm^3 were inoculated intratumorally with 10^5 CFU of Δ*ihfABpmi* or PBS. Four days later, the mice were euthanized. The tumor mass was divided into two parts, one for macrophage analysis by flow cytometry and another for analysis of the expression of genes involved in the antitumor response.

Macrophage analysis by flow cytometry

A suspension of isolated cells was prepared from the tumor tissue. Tumor tissue was cut into small fragments and digested in 200 U/mL collagenase IV buffer at 37°C for 1 h, then passed through a 70 μm cell filter. The samples were incubated with fluorochrome-labeled antibodies [CD80-Pe, CD206-APC, CD11b-Percp, F4/80-Fitc (Elabscience. Houston, United States)] for 20 min at 4°C and 50,000 events were analyzed using the cytometer of NovoCyte flow using the following panel macrophage (F4/80+ CD11b+), M1 macrophage (F4/80+ $CD80^+$) and M2 macrophage (F4/80+ CD260+). The data were analyzed with the software NovoExpress 1.5.0 software.

Quantitative RT-PCR (qRT-PCR) for the detection of gene expression

mRNA expression was analyzed by qRT-PCR. Total RNA extraction from tumor tissue was performed using a Direct-zol RNA MiniPrep Plus kit (Zymo Research, Irvine, CA, United States) and Trizol reagent (Invitrogen, United States) according to the manufacturer's instructions. RNA integrity was confirmed by agarose gel followed by ethidium bromide staining. RNA purity and concentration were verified using NanoDrop 2000c (Thermo Scientific, United States). The RNA was treated with DNase I Amplification grade (Sigma-Aldrich. Louis, MO, United States) to eliminate genomic DNA contamination. As a contamination control, a PCR was performed on all samples to verify the absence of genomic DNA. Reverse transcription was performed to synthesize cDNA using the High-Capacity cDNA Reverse Transcription kit (Applied Biosystems. United States). Then, the real-time PCR reaction was performed using the 2x qPCRBioSyGreen Mix Separate-Rox kit (PCRBIOSYSTEMS. Wayne, Pennsylvania, United States), according to the manufacturer's instructions, in a MicroAmp Optical 96-Well Reaction Plate microplate (Thermo Scientific, United States), using the StepOnePlus Real-Time PCR System (Applied Biosystems, United States). The dissociation Curve was made to verify the specificity and quality of the primers used. The mRNA expression was normalized to the expression of β-actin and GAPDH, which were used as endogenous controls. Relative mRNA expression levels were calculated using the $2^{-\Delta\Delta CT}$ method. The sequences of the primers used are shown in Supplementary Table S2.

Statistical analysis

Statistical analysis was performed using GraphPad Prism version 8 (GraphPad, San Diego, CA, United States). One-way ANOVA followed by Dunnett's test was used in experiments with three or more experimental groups. Student's t-test was used to analyze data from experiments from two experimental groups. Data were represented as the mean ± Standard Deviation of the mean (SEM), and $p < 0.05$ was considered statistically significant.

Results

In vitro growth of mutants and attenuation of virulence in the *Galleria mellonella* model

First, we verified the potential effects of gene deletions on bacterial growth by comparing the mutants (Δ*ihfABpmi* and Δ*tolRA*) with the parental strain 14028 WT. For *in vitro* growth in LB broth (37°C, 150 rpm), we observed similar OD_{600} values

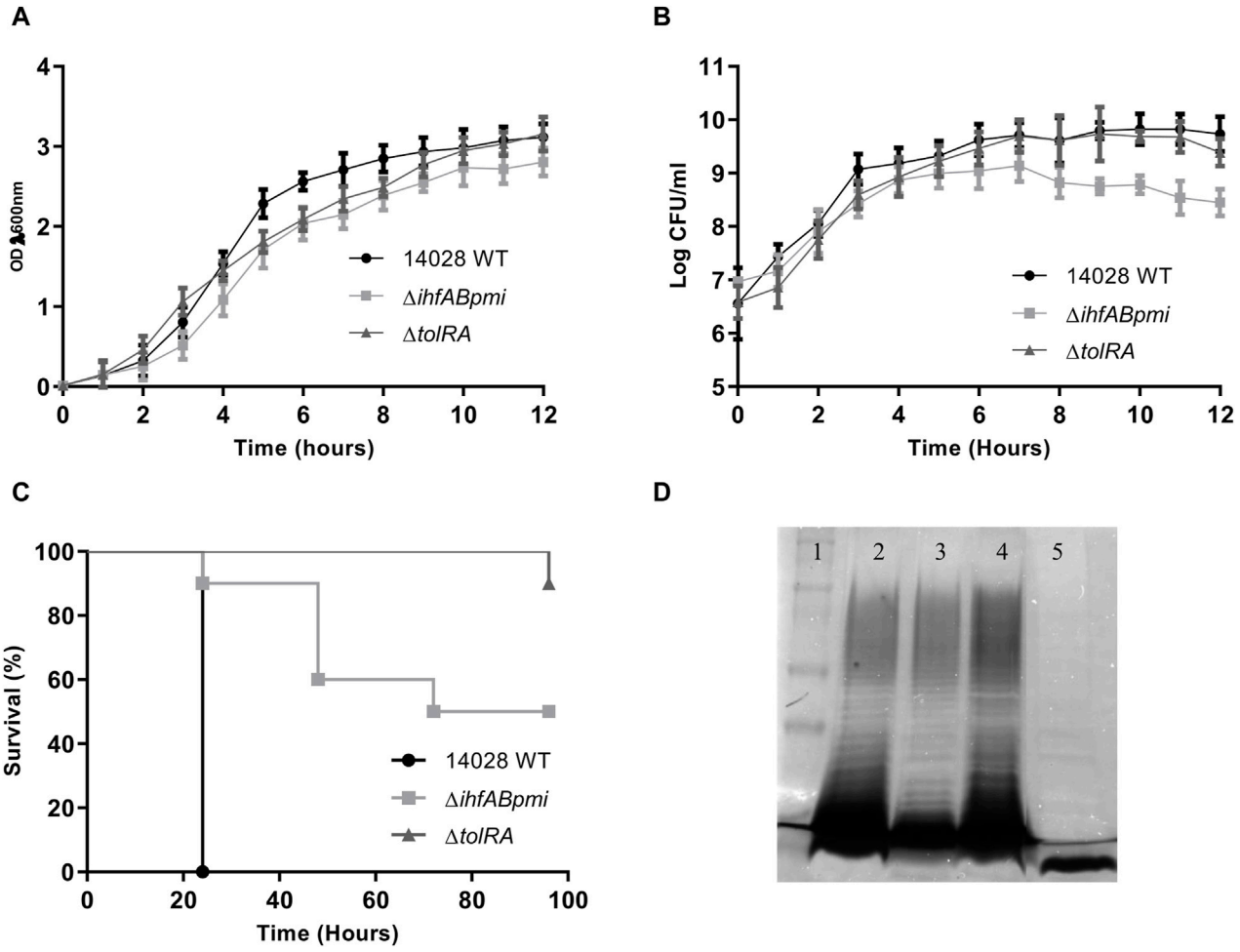

FIGURE 1
Bacterial growth and virulence of mutants. **(A)** Growth of the mutants and wild-type strain, monitored for 12 h by measuring the OD (λ 600 nm); **(B)** number of colony forming units (CFU) per ml of the mutants and wild-type strain monitored every hour. Growth curves were performed three times. The graph shows the mean ± SD of three independent experiments. **(C)** Virulence of mutants and wild-type strains in the *Galleria mellonella* model. Larvae were inoculated with 10^4 CFU in the last proleg, and survival was observed for 96 h. **(D)** Electrophoretic profile of lipopolysaccharides (LPS). Polyacrylamide gel stained with silver to confirm bacterial LPS integrity. 1. Dual color molecular weight standard (Bio-rad); 2. *Salmonella enterica* Typhimurium 14028; 3. *S. enterica* Typhimurium 14028 Δ*ihfABpmi*; 4. *S. enterica* Typhimurium 14028 Δ*tolRA*. 5. *Pseudomonas aeruginosa* (Δ*wzz*). The graphs show representative values from three independent experiments.

between the mutants and the parental strain (Figure 1A). However, analysis of colony forming units (CFU) number counts showed that the growth rate of Δ*ihfABpmi* was lower than that of 14028 WT (Figure 1B), and Δ*ihfABpmi* had a lower number of CFUs in the stationary phase of growth as compared to 14028 WT. Δ*tolRA* showed a growth pattern similar to 14028 WT (Figure 1B).

Next, we investigated whether the deleted genes affected the virulence of 14028 WT by inoculating *G. mellonella* larvae with 1×10^6 CFU of Δ*ihfABpmi*, Δ*tolRA*, and 14028 WT (Figure 1C and Supplementary Figure S1). We observed lower mortality of larvae inoculated with the mutants than with the parental strain. Here, 90% and 50% of larvae inoculated with Δ*tolRA* and Δ*ihfABpmi*, respectively, survived 96 h post-inoculation, while all larvae inoculated with 14028 WT died within 24 h of inoculation. These results suggest that the Δ*ihfABpmi* and Δ*tolRA* mutants are virulence-attenuated.

Electroporation, used for constructing mutants, can result in the selection of mutant colonies with incomplete LPS. However, LPS is critical for bacterial immunogenicity. Therefore, we investigated the LPS integrity of the mutants by performing LPS preparations on polyacrylamide gels, followed by periodic acid oxidation and silver staining. We observed similar LPS profiles of the mutants and the wild-type strain, suggesting that the constructed mutants had a complete LPS layer (Figure 1D).

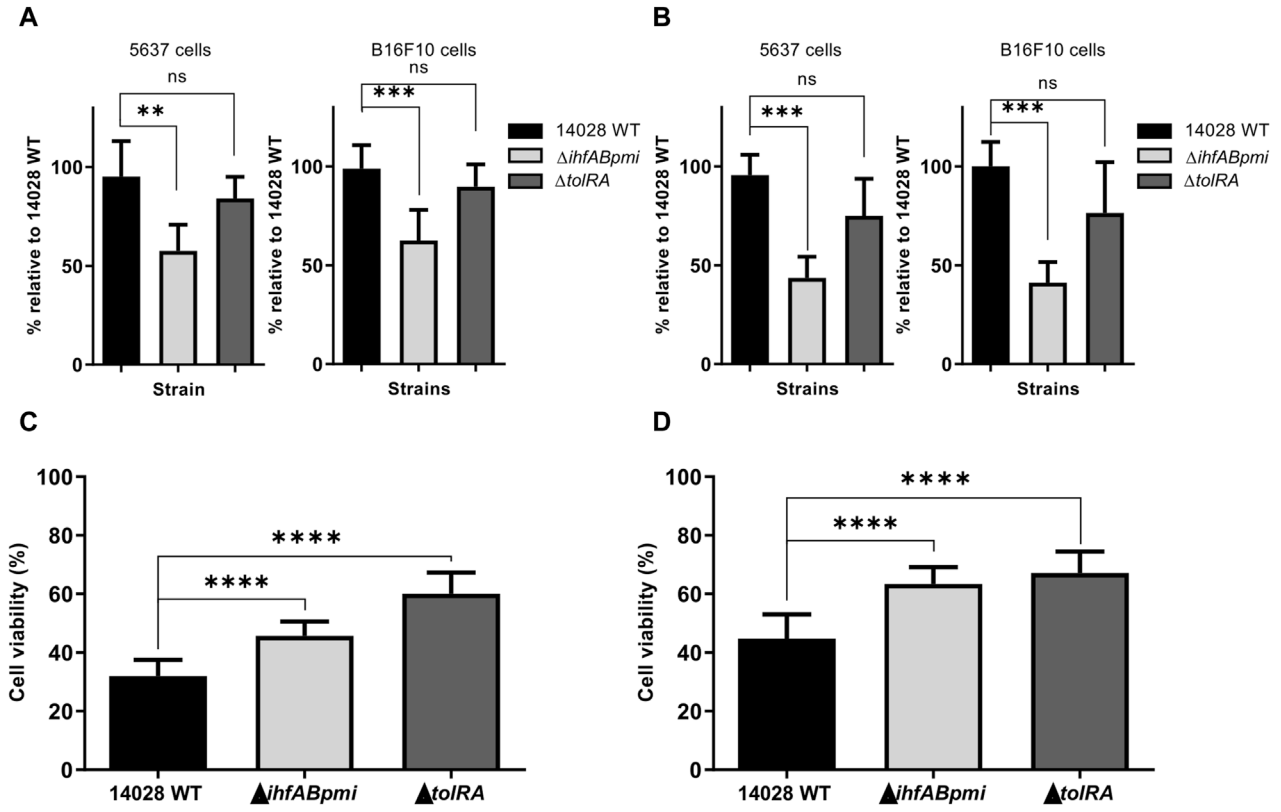

FIGURE 2
Invasion, survival, and cytotoxicity of mutant strains in bladder carcinoma (5,637) and melanoma (B16F10) cells. Cancer cells were infected *in vitro* with mutant strains for 2 and 6 h at an MOI of 10:1, after which the ability of invasion **(A)** and survival **(B)** of the mutant strains in cancer cells was determined by measuring intracellular CFU. 14028 WT was used as a positive control. Percentage of viable 5,637 **(C)** and B16F10 **(D)** cancer cells after 24 h of bacterial strain infections. The results were normalized to those of the uninfected cells. Results are represented as mean ± SD of three independent experiments performed in triplicate wells. Statistical significance was determined by one-way ANOVA followed by Multiplex Comparison Test *$p < 0.05$; **$p < 0.01$; ***$p < 0.005$; ****$p < 0.0001$.

Invasion and survival capability of mutants in cancer cells

We determined whether gene deletion affected the invasiveness and survival of 14028 WT in tumor cells by infecting two cancer cell lines with the mutant and 14028 WT strains for 2 and 6 h, followed by determining the number of intracellular CFU after tumor cell lysis. In B16F10 murine melanoma cells, Δ*tolRA* showed a similar invasion and survival profile to the parental strain. However, the Δ*ihfABpmi* mutant showed a statistically significant reduction in invasiveness and survival, and similar results were observed with bladder carcinoma 5,637 cells (Figures 2A, B).

Cytotoxicity of *S. enterica* Typhimurium mutants in tumor cells

In addition to invasion and survival, potential *S. enterica* Typhimurium mutants must also exert a cytotoxic effect. We assessed the *in vitro* antitumor potential of the mutants by performing the colorimetric assay with 3-(4,5-dimethylthiazol-2-yl)-2,5-diphenyltetrazolium bromide (MTT) in B16F10 melanoma and 5,637 bladder carcinoma cells (Figures 2C, D). The MTT assay was performed with previously proposed modifications for the elimination of bacterial contribution to MTT reduction [33]. Cancer cells without the addition of bacteria were used as a negative control (100% viability), while cells treated with 14028 WT were used as a positive control. We observed that 14028 WT, Δ*tolRA* mutant and Δ*ihfABpmi* mutant significantly decreased the viability of both cell lines (melanoma and bladder carcinoma cells). Treatment with 14028 WT decreased viability by 55%–68%, Δ*ihfABpmi* mutant treatment decreased viability by 36%–54%, while the Δ*tolRA* mutant decreased viability by 32%–40%. B16F10 melanoma cells were more resistant to the cytotoxic effect of both mutants and the parental strain, likely due to their aggressive and metastatic phenotype.

10.3389/ebm.2024.10081

Safety analysis of treatment with attenuated *S. enterica* Typhimurium mutants

We assessed treatment tolerance with attenuated mutants of *S. enterica* Typhimurium by inoculating healthy mice subcutaneously with the mutants once a week for 2 weeks, for a total of two doses (the experimental design is shown in Figure 3A). The mutant Δ*ihfABpmi* dose (10^5 CFU) was chosen based on our previous studies that showed that the double mutant Δ*ihfAB* is an attenuated strain and 10^5 CFU of the Δ*ihfAB* mutant is a safe and efficient dose to treat bladder cancer in mice (unpublished data). Based on these results, we chose 10^5 CFU of the triple mutant Δ*ihfABpmi* as the experimental dose here. A previous study reported that the Δ*tolRA* mutant is highly attenuated [28], and our results in *G. mellonella* further confirmed this attenuation (Figure 1C and Supplementary Figure S1). Thus, we tested two doses of 10^6 and 10^7 CFU of the Δ*tolRA* mutant in safety analysis experiments.

The body weight of the mice was determined as a sign of general health. After the first inoculation, we observed that mice inoculated with 10^7 CFU of the Δ*tolRA* mutant lost ±2 g (12% of body weight) with signs of disease, such as eye discharge, piloerection, and lethargy. However, 1 week after the first inoculation with 10^7 CFU of the Δ*tolRA* mutant, the mice regained weight, and the disease symptoms disappeared (Figure 3B). In mice inoculated with PBS, 10^6 CFU of the Δ*tolRA* mutant, or 10^5 CFU of the Δ*ihfABpmi* mutant, we did not observe weight loss or signs of systemic disease such as ocular discharge, piloerection, lethargy throughout the experiment (Figure 3B). Despite the symptoms, no mortality was observed in the mice throughout the experiment (Table 1).

The mice were euthanized 21 days after the initial inoculation, and the organs were collected for bacterial persistence and histopathological analysis. To analyze bacterial distribution and persistence at the end of the experiment, homogenized or macerated blood samples from the liver and spleen were diluted and plated on LB agar, SS, and MacConkey with appropriate antibiotics for subsequent CFU counting of our mutants. However, no bacterial colonies were detected in any of the three media tested or any tissue group, even when samples were plated without dilution. The fact that no mutants were isolated suggests that the bacteria cannot persist in these organs 21 days after the first inoculation and 15 days after the second inoculation.

Macroscopic examination of the organs showed hepatomegaly and splenomegaly in the group inoculated with 10^7 CFU of the Δ*tolRA* mutant. Significant differences in spleen and liver weights were observed in mice inoculated with 10^7 CFU of the Δ*tolRA* mutant, as compared to the group inoculated with PBS (Figures 3C, D). However, we did not observe significant differences between organ weights of mice inoculated with 10^6 CFU of the Δ*tolRA* mutant or 10^5 CFU of the Δ*ihfABpmi* mutant compared with mice inoculated with PBS (Figures 3C, D).

Microscopic analysis of spleen, liver, lung, and kidney samples from mice inoculated with PBS revealed typical histological structures (Supplementary Figure S2). The spleen, liver, kidney, and lung of mice inoculated with the Δ*ihfABpmi* mutant showed no signs of tissue damage. However, histological changes related to mild inflammation were observed in the liver, lung, and spleen. Interestingly, we also observed an increase in the megakaryocyte number in the spleen of mice inoculated with the Δ*ihfABpmi* mutant as compared to that in mice inoculated with PBS. Megakaryocytes have previously been related to inflammation [34]. Despite these effects, no histological architectural changes were observed in the evaluated organs, suggesting that subcutaneous inoculation of 10^5 CFU of the Δ*ihfABpmi* mutant is safe for use as a treatment.

Antitumor efficacy of attenuated *S. enterica* Typhimurium mutants in the murine melanoma model

Based on the safety analysis described above, we performed the antitumor efficacy tests with 10^6 CFU of the Δ*tolRA* mutant and 10^5 CFU of the Δ*ihfABpmi* mutant since, at these concentrations, no weight loss, splenomegaly, or hepatomegaly were observed, suggesting that these mutants are well-tolerated in mice at these concentrations. The antitumor efficacy of the mutants was evaluated in terms of the survival rate of the mice and the ability to reduce tumor mass. B16F10 cells (3×10^6) were implanted subcutaneously in the dorsal flank region of female C57BL/6JUnib mice. When the tumor reached 100 mm^3 (10–12 days after tumor cell inoculation), mice bearing B16F10 tumors were treated intratumorally or intraperitoneal with 10^6 CFU of the Δ*tolRA* mutant or 10^5 CFU of the Δ*ihfABpmi* mutant. Mice bearing B16F10 tumors inoculated with PBS were used as a negative control. As shown in Figure 4, both the Δ*tolRA* mutant and the Δ*ihfABpmi* mutant treatments reduced tumor growth compared with the PBS-treated group (control), and treatment with the Δ*ihfABpmi* mutant was more efficient in reducing melanoma tumors than treatment with the Δ*tolRA* mutant.

Figures 4C, I show the tumor size at the end point of the experiment (19 days after the first dose of treatment with the mutants). Intratumoral treatment with the Δ*ihfABpmi* mutant eliminated the tumor from all mice, leaving only a scar at the tumor site (Figure 4C). Moreover, we also observed that the Δ*ihfABpmi* mutant completely reduced the tumor mass of all mice 6 days after the first dose of treatment, which did not grow back in the following 15 days (Figure 4E). Intraperitoneal treatment with the Δ*ihfABpmi* mutant eliminated the tumor in two of the five treated mice (Figure 4I). On the other hand, although intratumor or intraperitoneal treatment with the

10.3389/ebm.2024.10081

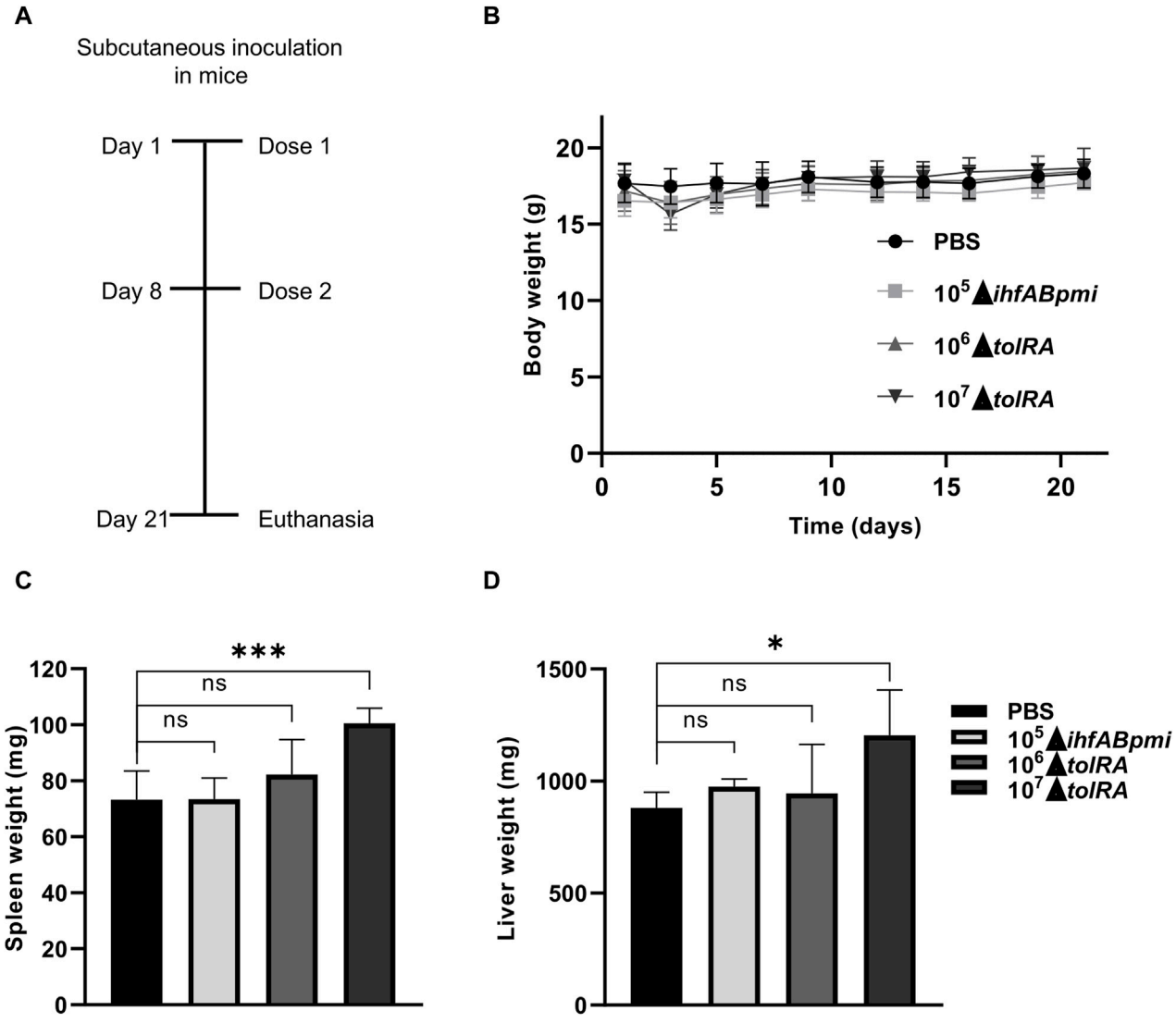

FIGURE 3
Safety assessment of treatment with attenuated mutants of *Salmonella enterica* Typhimurium. **(A)** Experimental design to test the toxicity and safety of mutants in mice inoculated by the subcutaneous route. **(B)** Body weight of mice inoculated with attenuated mutants throughout the experiment. Weight of spleens **(C)** and livers **(D)** of mice inoculated with attenuated mutants. In the graphics, the error bars represent the average ± SD of 5 mice per group. Data are from one experiment representative of two independent experiments. Each experiment performed with 5 mice per group. Statistical significance was determined by one-way ANOVA followed by Multiplex Comparison Test *$p < 0.05$; **$p < 0.01$; ***$p < 0.005$; ****$p < 0.0001$.

TABLE 1 Safety trial of treatment with subcutaneous attenuated mutants in C57BL/6JUnib mice (5 per group).

Groups	CFU	Survivors/inoculates
PBS		5/5
ΔihfABpmi	10^5	5/5
ΔtolRA	10^7	5/5
ΔtolRA	10^6	5/5

Data are from one experiment representative of two independent experiments. Each experiment performed with 5 mice per group. In both experiments, survival was 100% in all groups analyzed.

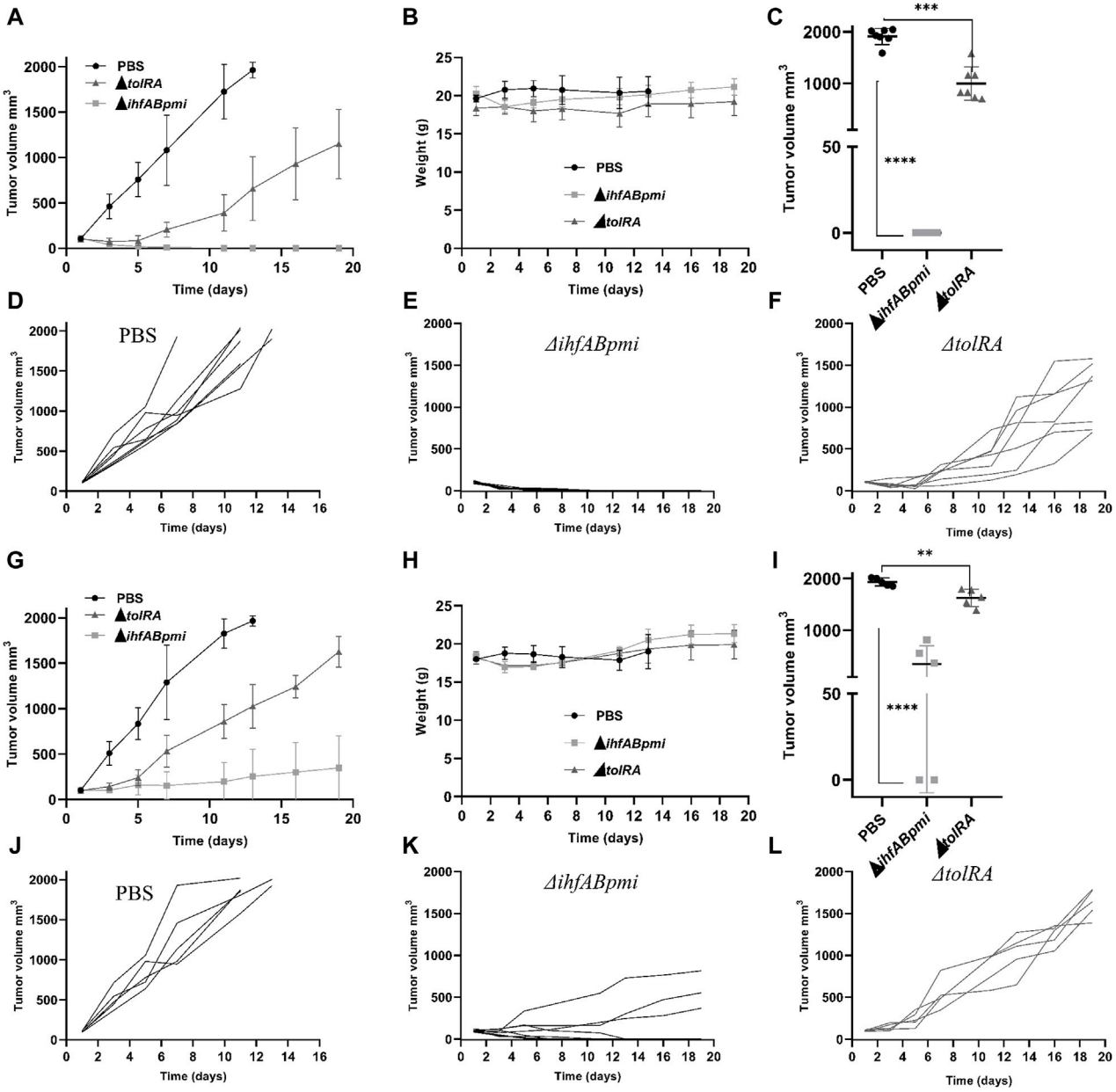

FIGURE 4
Antitumor efficacy of attenuated mutants of *Salmonella enterica* Typhimurium in a B16F10 subcutaneous tumor model. C57BL/6JUnib mice were inoculated with B16F10 cells (3×10^6), subcutaneously in the dorsal flank region. When the tumor reached 100 mm^3 (10–12 days after tumor cell inoculation), 10^6 CFU of the Δ*tolRA* mutant, 10^5 CFU of the Δ*ihfABpmi* mutant or PBS was injected intratumorally ($n = 7$) or intraperitoneal ($n = 5$) once a week for 2 weeks ($n = 7$). **(A)** Tumor growth after starting treatments intratumorally. **(B)** Weight of mice during treatments intratumorally. Data reported in graphs A and B are average values ± SD. **(C)** Tumor size at the endpoint of the treatments intratumorally. **(D–F)** Kinetics of individual tumor growth in groups treated intratumorally with PBS, Δ*ihfABpmi* mutant, and Δ*tolRA* mutant, respectively. Day one is considered when the tumor reaches 100 mm^3. Two independent experiments were performed, using seven mice per group. **(G)** Tumor growth after starting treatments intraperitoneal. **(H)** Weight of mice during treatments intraperitoneal. Data reported in graphs **(G, H)** are average values ± SD. **(I)** Tumor size at the endpoint of the treatments intraperitoneal. **(J–L)** Kinetics of individual tumor growth in groups treated intraperitoneal with PBS, Δ*ihfABpmi* mutant, and Δ*tolRA* mutant, respectively. Day one is considered when the tumor reaches 100 mm^3. One experiment was performed, using five mice per group. Statistical significance was determined by one-way ANOVA followed by Multiplex Comparison Test $^*p < 0.05$; $^{**}p < 0.01$; $^{***}p < 0.005$; $^{****}p < 0.0001$.

Δ*tolRA* mutant inhibited tumor growth compared to the PBS control, it did not eliminate tumors in mice.

All mice inoculated with the mutants survived until the endpoint of the experiment. However, the mice in the PBS group were euthanized 1 week before the end point of the experiment to avoid further suffering due to substantial tumor growth. We did not observe any significant differences between the weight of the mice inoculated with the mutants and the PBS group (Figures 4B, H). We also did not observe any signs of disease in mice intraperitoneally or intratumorally treated with the Δ*ihfABpmi* mutant.

In the endpoint of the experiment intratumorally, blood, liver, spleen, and tumor samples were homogenized or macerated and plated on LB agar, SS, and MacConkey for subsequent CFU counting. However, no bacterial colonies were detected in the analyzed groups (mice treated with PBS, Δ*ihfABpmi*, or Δ*tolRA*), even when samples were plated without dilution. The non-isolation of the mutants suggests that the bacteria either cannot persist in these organs or get eliminated by the immune system of the mice. It would be interesting to determine the colonization efficiency of the two mutants tested in the tumor microenvironment to see if differences in antitumor activity can be attributed to bacterial fitness. Future analyses will include the analysis of bacterial colonization after 24, 48 and 72 h of treatment with the mutants.

Hematoxylin and Eosin (H&E) staining of tissues revealed inflammatory foci (infiltration of mononuclear and polymorphonuclear cells) in the liver and spleen of mice treated with the Δ*ihfABpmi* mutant (Figure 5). However, we did not observe pathological changes in the architecture of the analyzed organs.

Analysis of the immune response involved in the antitumor effect

The immunological responses underlying the antitumor effects of *S. enterica* Typhimurium remain poorly understood. Recent evidence suggests the involvement of cells of the innate immune system, such as macrophages, and the production of pro-inflammatory cytokines in tumor elimination [15]. We used the Δ*ihfABpmi* mutant to analyze the immune responses involved in its antitumor response because treatment with the Δ*ihfABpmi* mutant showed a more significant tumor inhibition than treatment with the Δ*tolRA* mutant. Mice were euthanized, and tumor tissue was collected 4 days after treatment with 10^5 CFU of the Δ*ihfABpmi* mutant, as the Δ*ihfABpmi* mutant rapidly inhibited tumor growth.

Tumor cell suspensions prepared from tumor tissue were labeled and analyzed using the following panel macrophage (F4/80+ CD11b+), M1 macrophage (F4/80+ $CD80^+$) and M2 macrophage (F4/80+ CD260+). Flow cytometric analysis showed significant difference between the proportion of macrophages from mice treated with the Δ*ihfABpmi* mutant and mice treated with PBS (Figure 6B). Next, we examined the phenotype of intratumoral macrophages, and observed that treatment with the Δ*ihfABpmi* mutant significantly reduced the proportion of M2-type macrophages and increased the proportion of M1-type macrophages compared to PBS-treated mice (Figure 6C). This suggests that the tumor elimination ability of Δ*ihfABpmi* is associated with the induction of the accumulation of macrophages with antitumor phenotype and the reduction of pro-tumor immunosuppressive macrophages.

We evaluated the expression of cell proliferation genes (Ki-67), angiogenesis (VEGF), apoptosis (Bax), and pro-inflammatory (IL-6, TNF-α, and iNOS) markers to further investigate the immune responses underlying the antitumor effects of Δ*ihfABpmi*. Tumor tissue from mice treated with the Δ*ihfABpmi* mutant or PBS was collected after 4 days to measure the levels of mRNA expression using qRT-PCR. We observed that treatment with the Δ*ihfABpmi* mutant induced a statistically significant upregulation of the mRNA levels of Bax, IL-6, TNF-α, and iNOS (Figures 7A, B, D, F, respectively). Thus, pro-inflammatory cytokines secreted by immune cells such as macrophages can contribute to tumor cell death and trigger a strong tumor-specific immune response [35].

Discussion

Bacteria-based anticancer therapy is a promising option for treating cancer [22, 36]. Facultative anaerobic bacteria such as *S. enterica* are the focus of anticancer research due to their natural ability to attack tumors with variable oxygen concentrations and their immunogenicity, which leads to the activation of the immune system to destroy tumors in animal models [37, 38]. However, *S. enterica* is also a pathogen that causes Salmonellosis in humans [39]. Therefore, their virulence must be attenuated for *S. enterica* strains to be considered in cancer therapy to ensure safe use [22].

The virulence of *S. enterica* can be attenuated by mutating or eliminating pathogenicity genes or genes essential for survival [19, 40, 41]. However, the mutation of these genes can also compromise their anticancer activity and their ability to invade and destroy tumor cells [42]. For example, deletion of the genes for LPS biosynthesis (Δ*rfG* and Δ*rfD*) decreases the intrinsic antitumor effect of *S. enterica* Typhimurium 14028 (Frahm et al., 2015). Strains KST0651 (Δ*relA* Δ*spoT*) and KST0649 (Δ*ptsI* Δ*crr*) lost the ability to replicate in macrophages and epithelial cells [43, 44]. The low yield of the VNP20009 strain, modified in lipid A (Δ*msbB*Δ*purI*), as evidenced by the lack of tumor colonization and antitumor activity in clinical trials, has been attributed to the deletion of the *msbB* gene [23, 24, 45]. Therefore, careful selection of *S. enterica* strains is required to maintain their tumor-attacking ability while achieving their attenuation.

We demonstrated the antitumor efficacy of two strains of *S. enterica* Typhimurium, whose antitumor potential has not been

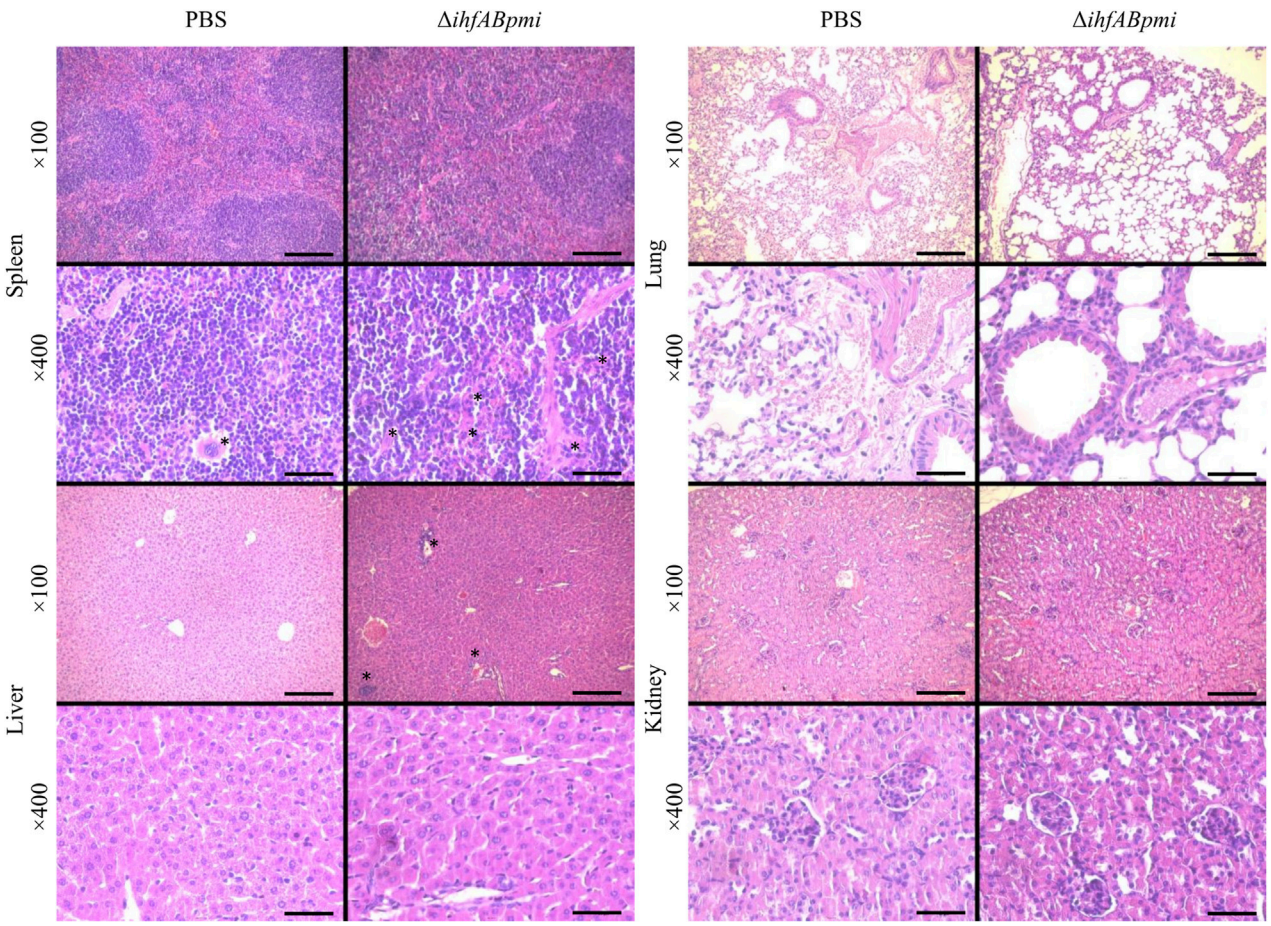

FIGURE 5
Histological analysis of normal tissues. Tumor-bearing mice were treated with 10^5 CFU of Δ*ihfABpmi* mutant or PBS, twice a week for 2 weeks. After 1 week of the last inoculation, the spleen, liver, lung, and kidney were collected for histological analysis using H&E staining of organ sections. Slight inflammation was observed in the liver and spleen of mice treated with Δ*ihfABpmi* mutant. The asterisks indicate the megakaryocytes in the spleens and inflammatory foci in the liver. Scale bar: 200 μm for ×100 and 50 μm for ×400.

explored yet. The strains were designed by deleting chromosomal genes. The double mutant Δ*tolRA* lacks two proteins critical for maintaining the integrity of the bacterial membrane (TolR and TolA), and the triple mutant Δ*ihfABpmi* lacks two proteins, IHF, a nucleoid-associated protein that also functions as a transcriptional regulator and is involved in the expression of pathogenicity genes, and 6-phosphomannose isomerase, a key enzyme for lipopolysaccharide O production. Of these mutants, the Δ*tolRA* mutant was highly attenuated, but its ability to eliminate melanoma tumors was compromised, at least in the mouse model. The Δ*ihfABpmi* mutant, in turn, showed less attenuation than the Δ*tolRA* mutant, but maintained its tumor-eliminating ability.

The TolR and TolA proteins are part of the Tol-Pal system, a critical multiprotein complex for maintaining the integrity of Gram-negative bacteria's cell envelope associated with bacterial virulence [46, 47]. The Tol-Pal system crosses the inner, periplasm, and outer membrane [48]. TolR and TolA are anchored to the inner membrane through a single region near the N-terminus [49]. Inactivation of any of the Tol-Pal system genes negatively affects outer membrane integrity, results in leakage from the periplasm, increases susceptibility to toxic compounds, and increases outer membrane vesicle production [46].

In addition to maintaining the cell envelope structure, TolR and TolA proteins also have other biological functions. In *E. coli*, the TolR protein is involved in the retrograde transport of phospholipids. In *Shigella flexneri*, strains lacking the *tolR* gene are more sensitive to antibiotics and bile salts and are less virulent [50, 51]. In *S. enterica* Typhimurium, the TolR protein has motility-related functions, and deletion of the *tolR* gene significantly increases outer membrane vesicle production [52, 53].

Deletion of the gene encoding the TolA protein in *S. enterica* Typhimurium increases its sensitivity to bile salts and reduces

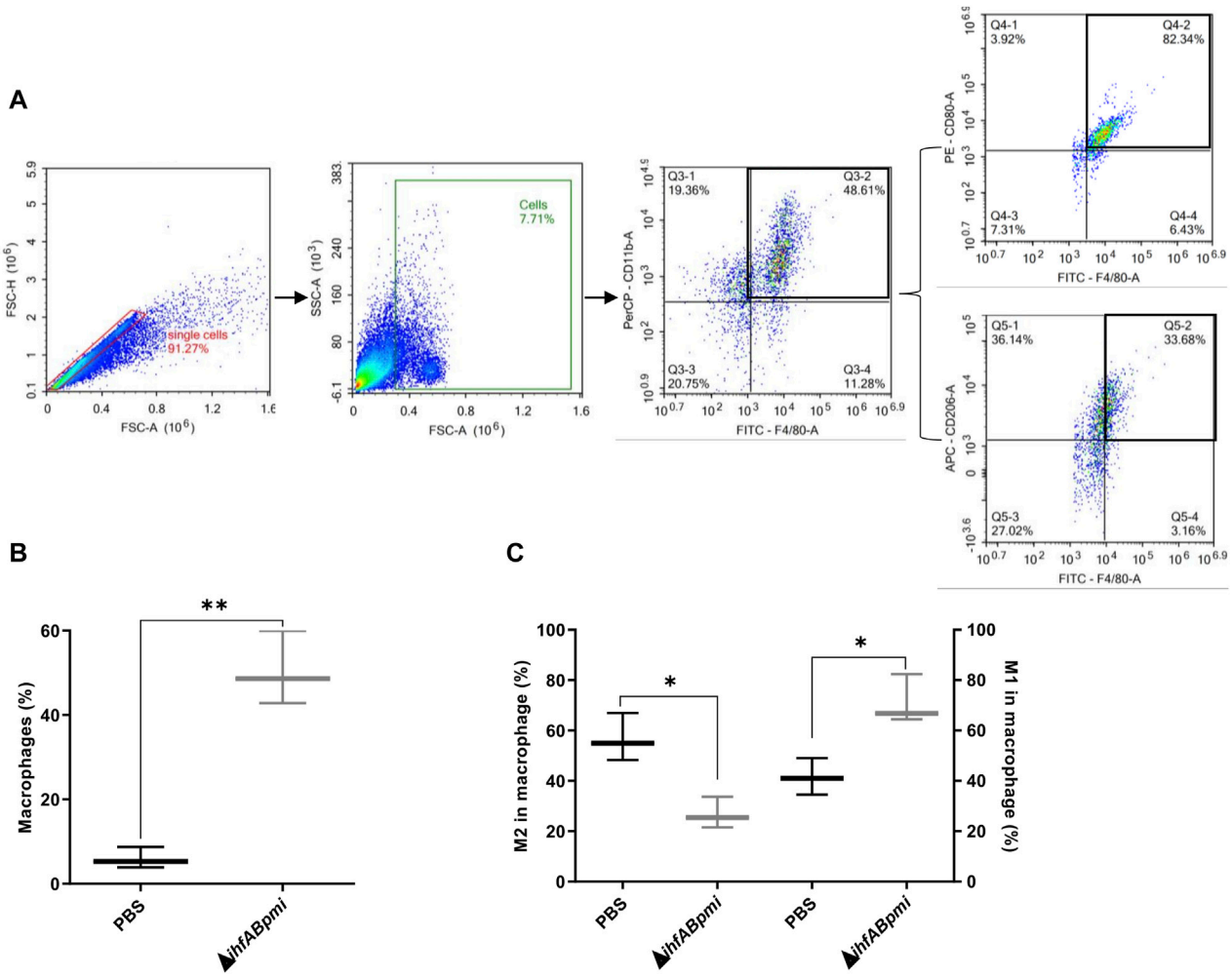

FIGURE 6
Immunophenotyping of macrophages infiltrated in B16F10 tumors. **(A)** Representative gating strategy to identify macrophage (F4/80+ CD11b+), M1 macrophage (F4/80+ $CD80^+$) and M2 macrophage (F4/80+ CD206+). **(B)** Macrophage population and **(C)** Macrophage phenotype (M1 or M2 type) after intratumoral treatment with 10^5 CFU of the Δ*ihfABpmi* mutant or PBS in a murine model of melanoma (three mice per group). Results are presented as the mean ± SD (n = 6). Statistical significance was calculated by Student's t-test. *$p < 0.05$; **$p < 0.01$.

motility and bacterial load in the spleen, liver, Peyer's patches, and lymph nodes compared with *S. enterica* wild-type. *Salmonella enterica* Typhimurium Δ*tolA* is considered highly attenuated in mice and *G. mellonella* and is more sensitive to the complement system than wild-type strains, a feature that has also been reported for mutants lacking *tolR* [50, 52, 54, 55]. Our virulence results for the Δ*tolRA* mutant are consistent with previous reports. In the *G. mellonella* model, the Δ*tolRA* mutant was highly attenuated as 90% of larvae inoculated with the Δ*tolRA* mutant survived. In contrast, all larvae inoculated with the wild-type strain died 24 h after inoculation (Figure 1C).

The attenuation and hypervesiculation profiles of mutants lacking the *tolR* and *tolA* genes made these strains and the outer membrane vesicles isolated from these mutants a research focus in the development of vaccines against *S. enterica*, *Mycobacterium tuberculosis*, *E. coli,* and SARS-CoV-2 [28, 54, 56, 57]. However, its anticancer potential has not been investigated yet. In this study, we investigated whether *S. enterica* Typhimurium Δ*tolRA* double mutant possesses antitumor activity *in vitro* and *in vivo*. The Δ*tolRA* mutant exhibits essential features for a potential antitumor strain, such as strong attenuation of virulence (Figure 1C), ability to invade and survive similar to the wild-type strain (Figures 2A, B), and toxicity in bladder cancer and melanoma cells (Figures 2C, D). The main feature of the Δ*tolRA* mutant observed in this study was its ability to inhibit melanoma growth in a murine model. The Δ*tolRA* mutant was not sufficient to eradicate the tumor mass (Figure 4). The high attenuation of this strain likely compromised its antitumor efficacy.

To date, none of the analyzed strains is capable of eradicating human tumors, so research into new antitumor strains is

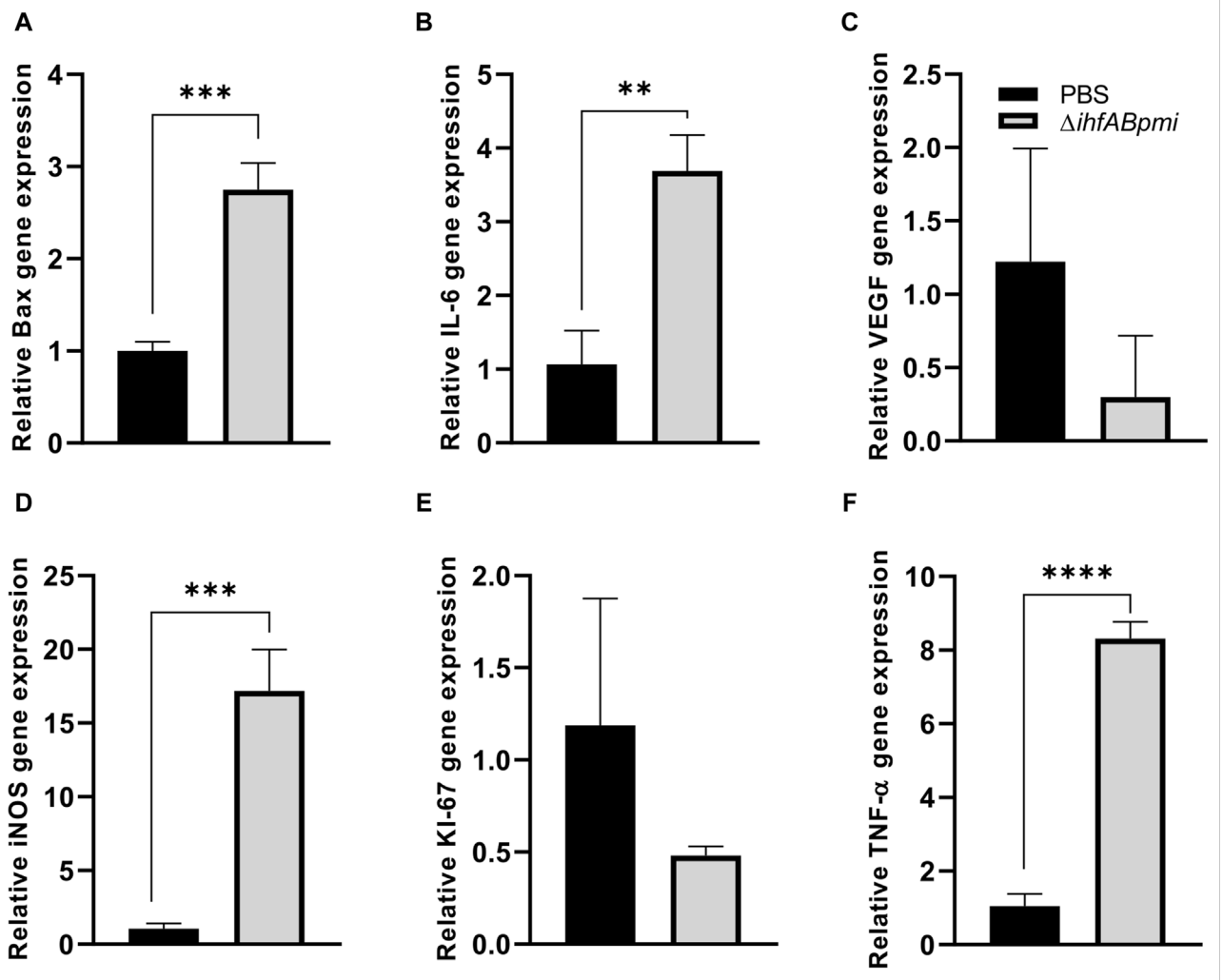

FIGURE 7
Effect of the Δ*ihfABpmi* mutant on gene expression. The relative level of RNA expression of Bax **(A)**, IL-6 **(B)**, VEGF **(C)**, iNOS **(D)**, Ki-67 **(E)**, and TNF-α **(F)** genes. Tumor tissue from B16F10 tumor-bearing mice was collected after 4 days of an intratumoral injection with 10^5 CFU of the Δ*ihfABpmi* mutant or PBS ($n = 6$). Results are presented as the mean ± SD. Statistical significance was calculated by Student's t-test. *$p < 0.05$; **$p < 0.01$; ***$p < 0.005$; ****$p < 0.0001$.

necessary to obtain more effective and safer strains that can be used in anticancer treatment [23, 24, 45]. We previously showed that the mutant for the *ihfA* gene of *S. enterica* Typhimurium attenuates virulence and reduces tumor mass in a murine model. However, this strain exhibited high toxicity *in vivo*, with 70% of mice treated intratumorally with *S. enterica* Typhimurium Δ*ihfA* dying 15 days after inoculation with a 10^5 CFU dose [19].

The *ihfA* and *ihfB* genes encode the α and β subunits of the heterodimeric IHF protein [58, 59]. IHF binds to specific transcriptional promoters and induces their bending >120°. Influencing transcription by facilitating the interaction between RNA polymerase and regulatory proteins [60, 61]. A recent study in *Pseudomonas putida* revealed that IHF influences homologous recombination and mutagenic processes and that recombination and mutation rates are lower in mutants for the IHF protein [62]. In *S. enterica* Typhimurium, IHF positively controls the expression of several virulence genes and cell invasion [63]. Strains lacking *ihfA* and *ihfB* are attenuated, leading to global transcriptional dysregulation [64, 65]. Previous studies have shown that the homodimeric forms of IHF (αα or ββ) are biologically active but less stable [66]. However, mutations lacking *ihfA* or *ihfB* are still capable of producing homodimeric proteins which might explain the increased toxicity of the single Δ*ihfA* mutant in our previous study [19].

To solve the toxicity problems of the Δ*ihfA* mutant, we constructed an IHF-deficient strain (homodimer or heterodimer) by deleting *ihfA* and *ihfB*. The double mutant

ihfA and *ihfB* of *S. enterica* Typhimurium 14028 did not presented toxicity as exhibited by the Δ*ihfA* single mutant [19]. We also showed that the double mutant *ihfA* and *ihfB* of *S. enterica* Typhimurium 14028 and violacein exerted an antitumor effect on bladder cancer in a murine model (unpublished data). Considering these results and to improve the safety and attenuation of the double mutant of *S. enterica* Typhimurium 14028 Δ*ihfA*Δ*ihfB*, we constructed a new triple mutant in this study by additionally deleting the *pmi* gene.

The *pmi* gene encodes 6-phosphomannose isomerase, an enzyme that performs the reversible interconversion of fructose-6-phosphate to mannose-6-phosphate, a precursor of mannose GDP. Since GDP-mannose is required for the synthesis of the O antigen side chain of LPS, strains with a *pmi* gene mutation grow in the absence of mannose but cannot synthesize the O antigen. These mutants can only produce complete LPS in the presence of exogenous mannose [67, 68]. Mutants with a deletion in the *pmi* gene have already been studied previously, as they allow obtaining strains with regulated delayed attenuation, a strategy implemented for constructing safe and immunogenic vaccine strains [68–70]. Δ*pmi* mutants are grown in a mannose-supplemented culture medium, allowing optimal host colonization in the initial stages of invasion. After several generations of *in vivo* growth, the O antigen is gradually lost, and the Δ*pmi* mutant is attenuated by the absence of mannose in animal tissues [68].

In this study, we deleted the *pmi* gene based on previous studies demonstrating that these mutants are attenuated and immunogenic, with the advantage of ceasing the expression of complete LPS *in vivo* [67]. This characteristic gives the strain greater security for the host since strains with incomplete LPS are more susceptible to the immune system [67, 70].

Our results suggest that the Δ*ihfABpmi* mutant is an attenuated strain with antitumor potential that balances attenuation and antitumor efficacy. Although the triple mutant Δ*ihfABpmi* is an attenuated strain, its attenuation profile was lower than the attenuation profile of the Δ*tolRA* mutant (Figure 1C). The Δ*ihfABpmi* could invade and survive inside tumor cells, but not as efficiently as the wild type (Figures 2A, B). Despite its decreased survivability, the Δ*ihfABpmi* mutant efficiently decreased the viability of tumor cells *in vivo* and *in vitro* (Figures 2C, D). Mutations in the *ihfA*, *ihfB*, and *pmi* genes did not compromise the antitumor capacity of *S. enterica* Typhimurium, as treatment with the triple mutant led to complete regression of B16F10 tumors (Figure 4) without harmful effects on normal organs (Figure 5). Several studies have shown that *S. enterica* Typhimurium exerts its antitumor activity by activating the immune system [11, 17, 35], thus the immunogenicity of the bacterium is the key to eliminating tumors.

After a few replication cycles, the inability to produce full LPS in the Δ*pmi* mutant allows the mutant to activate the immune system and acquire an additional attenuation phenotype through mannose deficiency [67]. A closer examination of the antitumor effect showed that treatment of tumors with the Δ*ihfABpmi* mutant leads to accumulation of macrophages of phenotype M1 and decrease of macrophages of phenotype M2. We found that M2-type macrophages were more abundant in mice from the control group (PBS) tumor tissue than in the Δ*ihfABpmi*-treated group. In contrast, the percentage of macrophages and M1-type macrophages was higher in the mutant-treated group (Figure 6). Our data do not allow us to know whether the accumulation M1-type macrophages and decrease of M2-type macrophages observed in tumors of mice treated with Δ*ihfABpmi* are due to Δ*ihfABpmi* induces the reprogramming of intratumoral macrophages from pro-tumor phenotype to anti-tumor phenotype or whether Δ*ihfABpmi* induces the infiltration of anti-tumor macrophages in antigenically poor tumors. Further studies are needed to elucidate this finding. Accumulation of M1-type macrophages was also accompanied with a significant increase in the mRNA of inflammatory cytokines (TNF-α and IL-6), iNOS, and Bax (Figure 7). In addition, the cytokines TNF-α, IFN-γ, IL-6, and IL-12P70 have been associated with antitumor activity in previous studies [33, 71]. Together, our results suggest that the Δ*ihfABpmi* mutant induces accumulation of M1-type macrophages, which leads to apoptosis and suppresses tumor growth by secreting cytokines with antitumor activity.

Macrophages have been demonstrated to be activated by LPS and flagellin to specifically kill tumor cells [11, 16]. LPS and flagellin present in *S. enterica* Typhimurium can stimulate the infiltration of immune cells, such as macrophages, by TLR5 and TLR4 signaling, respectively. Immune cells produce pro-inflammatory mediators such as TNF-α, IL-6, IL-1, IL-12, and iNOS, leading to reprogramming the immunosuppressive tumor microenvironment into an immunogenic one to aid in the elimination of tumors [35]. At the time of inoculation, the Δ*ihfABpmi* mutant has complete LPS, allowing the bacterium to colonize efficiently and leading to reprogramming of the tumor microenvironment, evidenced by the percentage of M1 macrophages and the significant increase in iNOS, an indicator of type M1 macrophages. Our results are consistent with previous reports in models of melanoma, lymphoma, colon adenocarcinoma, and breast cancer that also show that *S. enterica* Typhimurium can induce the accumulation of macrophage phenotype to the M1 phenotype and induce the secretion of inflammatory cytokines in tumors [7, 11, 16, 35, 72].

TNF-α production is associated with apoptosis-induced tumor cell death [72, 73]. Previous studies have shown that *S. enterica* Typhimurium has an apoptotic effect by increasing Bax production [7, 74]. The data presented here show that treatment with the Δ*ihfABpmi* mutant significantly increases the expression of genes involved in the apoptosis pathway, suggesting that *S. enterica* Typhimurium exerts its antitumor activity by activating apoptosis.

Bacterial toxicity is a barrier to their use in cancer immunotherapy. The triple mutant explored in this study loses complete LPS after a few generations, which makes the bacterium more susceptible to the immune system and can be eliminated from the host without causing serious toxicity. At the endpoint of the experiment, we did not detect the Δ*ihfABpmi*

mutant in the blood, tumor, liver, or spleen of mice, suggesting that our mutant reduced the tumor mass and was subsequently eliminated by the immune system. Furthermore, mutations in the genes coding for the IHF protein reduce the risk that the Δ*ihfABpmi* mutant makes homologous recombination with microbiota bacteria or that random mutations will appear. In addition, IHF mutants are further attenuated as discussed previously. It is important to mention that *S. enterica* mutants for HU, another NAP, were also attenuated and induced a protective immunological response in the murine model [29]. Altogether, these data indicate that NAP proteins represent a new target for the development of *S. enterica* attenuated strains with vaccine and antitumor potential.

In the present study, we report two attenuated mutants of *S. enterica* Typhimurium and explored their antitumor activity *in vitro* and *in vivo*. The first mutant was shown to be highly attenuated, but with compromised antitumor activity. The second mutant, *ΔihfABpmi* showed a lower attenuation profile but maintained its ability to invade and survive in tumor cells. Additionally, it was efficient in eliminating melanoma. Our results also suggest that the antitumor effect of treatment with the *ΔihfABpmi* mutant induces the accumulation of macrophages from M1-type macrophages, that secrete pro-inflammatory mediators, leading to the apoptosis of tumor cells. Taken together, our data provide a basis for understanding the activity of *S. enterica* Typhimurium in cancer immunotherapy.

Data availability

The experimental data that support the findings of this study are available in: https://doi.org/10.6084/m9.figshare.25962253.

Author contributions

GP performed the design and methodology of the experiments, analyzed the data, drafted the Figures, and wrote the manuscript. MG assisted with experiments *in vitro*, assisted with animal experiments, and analyzed the data. MS assisted with the animal experiments and analyzed the data. IG assisted with the animal experiments. YJ-F assisted with *in vitro* experiments. LC performed flow cytometry analysis. FR performed histological analysis. SG analyzed and discussed the data. MB conceived and designed the study, supervised the experiments, reviewed the data, and co-wrote the manuscript. All authors contributed to the article and approved the submitted version.

Ethics statement

The animal care committee approved all experiments with mice of Universidade Estadual de Campinas under protocol numbers 5769-1/2021 and 5895-1/2021. The study was conducted in accordance with the local legislation and institutional requirements.

Funding

The authors declare financial support was received for the research, authorship, and/or publication of this article. This work was supported by the CNPq grant numbers 309380/2019-7, 309678/2022-6, and FAPESP grant numbers 2021/00465-0 and 2021/10577-0. GP was supported by the administrative department of science, technology, and innovation (COLCIENCIAS) (2016/772) and FAPESP (2022/11399-0). MG was supported by the National Council for Scientific and Technological Development (no. 130553/2020-4) and FAPESP (no. 2020/01535-9). MS was supported by FAPESP (no. 2019/17091-5). IG was supported by coordination for the improvement of higher-level personnel (CAPES) (no. 88887.516158/2020-00). YJ-F was supported by CAPES (no. 888882.329494/2019-01 and 88887.595532/2020-00). LC was supported by CNPq (140027/2020-3). SG is a research fellow of CNPq (304309/2021-4). MB is a research fellow of CNPq (309380/2019-7 and 309678/2022-6).

Conflict of interest

The authors declare that the research was conducted in the absence of any commercial or financial relationships that could be construed as a potential conflict of interest.

Supplementary material

The Supplementary Material for this article can be found online at: https://www.ebm-journal.org/articles/10.3389/ebm.2024.10081/full#supplementary-material

References

1. Sung H, Ferlay J, Siegel RL, Laversanne M, Soerjomataram I, Jemal A, et al. Global cancer statistics 2020: GLOBOCAN estimates of incidence and mortality worldwide for 36 cancers in 185 countries. *CA: A Cancer J Clinicians* (2021) **71**: 209–49. doi:10.3322/caac.21660

2. Eggermont AMM, Bellomo D, Arias-Mejias SM, Quattrocchi E, Sominidi-Damodaran S, Bridges AG, et al. Identification of stage I/IIA melanoma patients at high risk for disease relapse using a clinicopathologic and gene expression model. *Eur J Cancer* (2020) **140**:11–8. doi:10.1016/j.ejca.2020.08.029

3. Bacon JVW, Müller DC, Ritch E, Annala M, Dugas SG, Herberts C, et al. Somatic features of response and relapse in non–muscle-invasive bladder cancer treated with Bacillus calmette-guérin immunotherapy. *Eur Urol Oncol* (2022) **5**: 677–86. doi:10.1016/j.euo.2021.11.002

4. Boardman CH, Brady WE, Dizon DS, Kunos CA, Moore KN, Zanotti KM, et al. A phase I evaluation of extended field radiation therapy with concomitant cisplatin chemotherapy followed by paclitaxel and carboplatin chemotherapy in women with cervical carcinoma metastatic to the para-aortic lymph nodes: an NRG oncology/gynecologic oncology group study. *Gynecol Oncol* (2018) **151**:202–7. doi:10.1016/j.ygyno.2018.08.006

5. Zahavi D, Weiner L. Monoclonal antibodies in cancer therapy. *Antibodies (Basel)* (2020) **9**:34. doi:10.3390/antib9030034

6. Jiang T, Zhou C, Gu J, Liu Y, Zhao L, Li W, et al. Enhanced therapeutic effect of cisplatin on the prostate cancer in tumor-bearing mice by transfecting the attenuated Salmonella carrying a plasmid co-expressing p53 gene and mdm2 siRNA. *Cancer Lett* (2013) **337**:133–42. doi:10.1016/j.canlet.2013.05.028

7. Mateos-Chávez AA, Muñoz-López P, Becerra-Báez EI, Flores-Martínez LF, Prada-Gracia D, Moreno-Vargas LM, et al. Live attenuated *Salmonella enterica* expressing and releasing cell-permeable Bax BH3 peptide through the MisL autotransporter system elicits antitumor activity in a murine xenograft model of human B non-hodgkin's lymphoma. *Front Immunol* (2019) **10**:2562. doi:10.3389/fimmu.2019.02562

8. Avogadri F, Martinoli C, Petrovska L, Chiodoni C, Transidico P, Bronte V, et al. Cancer immunotherapy based on killing of Salmonella-infected tumor cells. *Cancer Res* (2005) **65**:3920–7. doi:10.1158/0008-5472.can-04-3002

9. Chang W-W, Lee C-H. Salmonella as an innovative therapeutic antitumor agent. *Int J Mol Sci* (2014) **15**:14546–54. doi:10.3390/ijms150814546

10. Kaimala S, Mohamed YA, Nader N, Issac J, Elkord E, Chouaib S, et al. Salmonella-mediated tumor regression involves targeting of tumor myeloid suppressor cells causing a shift to M1-like phenotype and reduction in suppressive capacity. *Cancer Immunol Immunother* (2014) **63**:587–99. doi:10.1007/s00262-014-1543-x

11. Chen J, Qiao Y, Chen G, Chang C, Dong H, Tang B, et al. Salmonella flagella confer anti-tumor immunological effect via activating Flagellin/TLR5 signalling within tumor microenvironment. *Acta Pharmaceutica Sinica B* (2021) **11**:3165–77. doi:10.1016/j.apsb.2021.04.019

12. Tan W, Duong MT-Q, Zuo C, Qin Y, Zhang Y, Guo Y, et al. Targeting of pancreatic cancer cells and stromal cells using engineered oncolytic *Salmonella typhimurium*. *Mol Ther* (2022) **30**:662–71. doi:10.1016/j.ymthe.2021.08.023

13. Johnson SA, Ormsby MJ, McIntosh A, Tait SWG, Blyth K, Wall DM. Increasing the bactofection capacity of a mammalian expression vector by removal of the f1 ori. *Cancer Gene Ther* (2019) **26**:183–94. doi:10.1038/s41417-018-0039-9

14. Perrotta C, Cervia D, Di Renzo I, Moscheni C, Bassi MT, Campana L, et al. Nitric oxide generated by tumor-associated macrophages is responsible for cancer resistance to cisplatin and correlated with syntaxin 4 and acid sphingomyelinase inhibition. *Front Immunol* (2018) **9**:1186. doi:10.3389/fimmu.2018.01186

15. Di Mitri D, Mirenda M, Vasilevska J, Calcinotto A, Delaleu N, Revandkar A, et al. Re-Education of tumor-associated macrophages by CXCR2 blockade drives senescence and tumor inhibition in advanced prostate cancer. *Cell Rep* (2019) **28**: 2156–68.e5. doi:10.1016/j.celrep.2019.07.068

16. Yang M, Xu J, Wang Q, Zhang A-Q, Wang K. An obligatory anaerobic *Salmonella typhimurium* strain redirects M2 macrophages to the M1 phenotype. *Oncol Lett* (2018) **15**:3918–22. doi:10.3892/ol.2018.7742

17. Lee C-H, Wu C-L, Shiau A-L. Systemic administration of attenuated *Salmonella choleraesuis* carrying thrombospondin-1 gene leads to tumor-specific transgene expression, delayed tumor growth and prolonged survival in the murine melanoma model. *Cancer Gene Ther* (2005) **12**:175–84. doi:10.1038/sj.cgt.7700777

18. Felgner S, Frahm M, Kocijancic D, Rohde M, Eckweiler D, Bielecka A, et al. aroA-deficient *Salmonella enterica* serovar typhimurium is more than a metabolically attenuated mutant. *mBio* (2016) **7**:e01220–16. doi:10.1128/mbio.01220-16

19. Hirsch Werle C, Damiani I, Paier Milanez G, Farias AS, Cintra Gomes Marcondes MC, Fabricio Culler H, et al. Antimelanoma effect of Salmonella Typhimurium integration host factor mutant in murine model. *Future Oncol* (2016) **12**:2367–78. doi:10.2217/fon-2015-0062

20. Li C-X, Yu B, Shi L, Geng W, Lin Q-B, Ling C-C, et al. Obligate' anaerobic Salmonella strain YB1 suppresses liver tumor growth and metastasis in nude mice. *Oncol Lett* (2017) **13**:177–83. doi:10.3892/ol.2016.5453

21. Miyake K, Murata T, Murakami T, Zhao M, Kiyuna T, Kawaguchi K, et al. Tumor-targeting *Salmonella typhimurium* A1-R overcomes nab-paclitaxel resistance in a cervical cancer PDOX mouse model. *Arch Gynecol Obstet* (2019) **299**:1683–90. doi:10.1007/s00404-019-05147-3

22. Pérez Jorge G, Módolo DG, Jaimes-Florez YP, Fávaro WJ, de Jesus MB, Brocchi M. p53 gene delivery via a recombinant *Salmonella enterica* Typhimurium leads to human bladder carcinoma cell death *in vitro*. *Lett Appl Microbiol* (2022) **75**: 1010–20. doi:10.1111/lam.13777

23. Toso JF, Gill VJ, Hwu P, Marincola FM, Restifo NP, Schwartzentruber DJ, et al. Phase I study of the intravenous administration of attenuated *Salmonella typhimurium* to patients with metastatic melanoma. *J Clin Oncol* (2002) **20**:142–52. doi:10.1200/jco.20.1.142

24. Heimann DM, Rosenberg SA. Continuous intravenous administration of live genetically modified salmonella typhimurium in patients with metastatic melanoma. *J Immunother* (2003) **26**:179–80. doi:10.1097/00002371-200303000-00011

25. Gniadek TJ, Augustin L, Schottel J, Leonard A, Saltzman D, Greeno E, et al. A phase I, dose escalation, single dose trial of oral attenuated *Salmonella typhimurium* containing human IL-2 in patients with metastatic gastrointestinal cancers. *J Immunother* (2020) **43**:217–21. doi:10.1097/cji.0000000000000325

26. Frahm M, Felgner S, Kocijancic D, Rohde M, Hensel M, Curtiss R, et al. Efficiency of conditionally attenuated *Salmonella enterica* serovar typhimurium in bacterium-mediated tumor therapy. *mBio* (2015) **6**:e00254-15. doi:10.1128/mBio.00254-15

27. Sambrook J, Russell DW. *Molecular cloning: a laboratory manual. Third*. New York: Cold Spring Harbor Laboratory Press (2001). Available from: https://www.sigmaaldrich.com/catalog/product/sigma/m8265 (Accessed May 21, 2021).

28. Daleke-Schermerhorn MH, Felix T, Soprova Z, ten Hagen-Jongman CM, Vikström D, Majlessi L, et al. Decoration of outer membrane vesicles with multiple antigens by using an autotransporter approach. *Appl Environ Microbiol* (2014) **80**: 5854–65. doi:10.1128/aem.01941-14

29. Milanez GP, Werle CH, Amorim MR, Ribeiro RA, Tibo LHS, Roque-Barreira MC, et al. HU-lacking mutants of *Salmonella enterica* enteritidis are highly attenuated and can induce protection in murine model of infection. *Front Microbiol* (2018) **9**:1780. doi:10.3389/fmicb.2018.01780

30. Hitchcock PJ, Brown TM. Morphological heterogeneity among Salmonella lipopolysaccharide chemotypes in silver-stained polyacrylamide gels. *J Bacteriol* (1983) **154**:269–77. doi:10.1128/jb.154.1.269-277.1983

31. Tsai CM, Frasch CE. A sensitive silver stain for detecting lipopolysaccharides in polyacrylamide gels. *Anal Biochem* (1982) **119**:115–9. doi:10.1016/0003-2697(82)90673-x

32. Elsinghorst EA. Measurement of invasion by gentamicin resistance. *Methods Enzymol* (1994) **236**:405–20. doi:10.1016/0076-6879(94)36030-8

33. Grille S, Moreno M, Bascuas T, Marqués JM, Muñoz N, Lens D, et al. *<scp>S</scp>almonella enterica* serovar Typhimurium immunotherapy for B-cell lymphoma induces broad anti-tumour immunity with therapeutic effect. *Immunology* (2014) **143**:428–37. doi:10.1111/imm.12320

34. Cunin P, Nigrovic PA. Megakaryocytes as immune cells. *J Leukoc Biol* (2019) **105**:1111–21. doi:10.1002/jlb.mr0718-261rr

35. Zheng JH, Nguyen VH, Jiang S-N, Park S-H, Tan W, Hong SH, et al. Two-step enhanced cancer immunotherapy with engineered *Salmonella typhimurium* secreting heterologous flagellin. *Sci Transl Med* (2017) **9**:eaak9537. doi:10.1126/scitranslmed.aak9537

36. Chen W, Zhu Y, Zhang Z, Sun X. Advances in Salmonella Typhimurium-based drug delivery system for cancer therapy. *Adv Drug Deliv Rev* (2022) **185**: 114295. doi:10.1016/j.addr.2022.114295

37. Zhou S, Gravekamp C, Bermudes D, Liu K. Tumour-targeting bacteria engineered to fight cancer. *Nat Rev Cancer* (2018) **18**:727–43. doi:10.1038/s41568-018-0070-z

38. Gao S, Jung J-H, Lin S-M, Jang A-Y, Zhi Y, Bum Ahn K, et al. Development of oxytolerant *Salmonella typhimurium* using radiation mutation technology (RMT) for cancer therapy. *Sci Rep* (2020) **10**:3764. doi:10.1038/s41598-020-60396-6

39. Rogers AWL, Tsolis RM, Bäumler AJ. Salmonella versus the microbiome. *Microbiol Mol Biol Rev* (2021) **85**:e00027–19. doi:10.1128/mmbr.00027-19

40. Leite B, Werle CH, Carmo CP, Nóbrega DB, Milanez GP, Culler HF, et al. Integration host factor is important for biofilm formation by *Salmonella enterica* Enteritidis. *Pathog Dis* (2017) **75**:ftx074. doi:10.1093/femspd/ftx074

41. Jiang Y, Gao X, Xu K, Wang J, Huang H, Shi C, et al. A novel cre recombinase-mediated *in vivo* minicircle DNA (CRIM) vaccine provides partial protection against newcastle disease virus. *Appl Environ Microbiol* (2019) **85**:e00407-19. doi:10.1128/AEM.00407-19

42. Arrach N, Cheng P, Zhao M, Santiviago CA, Hoffman RM, McClelland M. High-throughput screening for salmonella avirulent mutants that retain targeting of solid tumors. *Cancer Res* (2010) **70**:2165–70. doi:10.1158/0008-5472.can-09-4005

43. Zhi Y, Lin SM, Jang A-Y, Ahn KB, Ji HJ, Guo H-C, et al. Effective mucosal live attenuated Salmonella vaccine by deleting phosphotransferase system component genes ptsI and crr. *J Microbiol* (2019) **57**:64–73. doi:10.1007/s12275-019-8416-0

44. Na HS, Kim HJ, Lee H-C, Hong Y, Rhee JH, Choy HE. Immune response induced by *Salmonella typhimurium* defective in ppGpp synthesis. *Vaccine* (2006) **24**:2027–34. doi:10.1016/j.vaccine.2005.11.031

45. Nemunaitis J, Cunningham C, Senzer N, Kuhn J, Cramm J, Litz C, et al. Pilot trial of genetically modified, attenuated Salmonella expressing the *E. coli* cytosine deaminase gene in refractory cancer patients. *Cancer Gene Ther* (2003) **10**:737–44. doi:10.1038/sj.cgt.7700634

46. Nevermann J, Silva A, Otero C, Oyarzún DP, Barrera B, Gil F, et al. Identification of genes involved in biogenesis of outer membrane vesicles (OMVs) in *Salmonella enterica* serovar typhi. *Front Microbiol* (2019) **10**:104. doi:10.3389/fmicb.2019.00104

47. Li Q, Li Z, Fei X, Tian Y, Zhou G, Hu Y, et al. The role of TolA, TolB, and TolR in cell morphology, OMVs production, and virulence of Salmonella Choleraesuis. *AMB Express* (2022) **12**:5. doi:10.1186/s13568-022-01347-4

48. Hirakawa H, Suzue K, Takita A, Awazu C, Kurushima J, Tomita H. Roles of the Tol-Pal system in the Type III secretion system and flagella-mediated virulence in enterohemorrhagic *Escherichia coli*. *Sci Rep* (2020) **10**:15173. doi:10.1038/s41598-020-72412-w

49. Santos TMA, Lin T-Y, Rajendran M, Anderson SM, Weibel DB Polar localization of E*scherichia coli* chemoreceptors requires an intact Tol–Pal complex. *Mol Microbiol* (2014) **92**:985–1004. doi:10.1111/mmi.12609

50. Pastor Y, Camacho AI, Zúñiga-Ripa A, Merchán A, Rosas P, Irache JM, et al. Towards a subunit vaccine from a Shigella flexneri ΔtolR mutant. *Vaccine* (2018) **36**:7509–19. doi:10.1016/j.vaccine.2018.10.066

51. Boags AT, Samsudin F, Khalid S. Binding from both sides: TolR and full-length OmpA bind and maintain the local structure of the *E. coli* cell wall. *Structure* (2019) **27**:713–24.e2. doi:10.1016/j.str.2019.01.001

52. Lahiri A, Ananthalakshmi TK, Nagarajan AG, Ray S, Chakravortty D. TolA mediates the differential detergent resistance pattern between the *Salmonella enterica* subsp. enterica serovars Typhi and Typhimurium. *Microbiology (Reading)* (2011) **157**:1402–15. doi:10.1099/mic.0.046565-0

53. Marchant P, Carreño A, Vivanco E, Silva A, Nevermann J, Otero C, et al. 'One for all': functional transfer of OMV-mediated polymyxin B resistance from *Salmonella enterica* sv. Typhi ΔtolR and ΔdegS to susceptible bacteria. *Front Microbiol* (2021) **12**:672467. doi:10.3389/fmicb.2021.672467

54. Paterson GK, Northen H, Cone DB, Willers C, Peters SE, Maskell DJ. Deletion of tolA in Salmonella Typhimurium generates an attenuated strain with vaccine potential. *Microbiology (Reading)* (2009) **155**:220–8. doi:10.1099/mic.0.021576-0

55. Morgan JK, Ortiz JA, Riordan JT. The role for TolA in enterohemorrhagic *Escherichia coli* pathogenesis and virulence gene transcription. *Microb Pathogenesis* (2014) **77**:42–52. doi:10.1016/j.micpath.2014.10.010

56. Hays MP, Houben D, Yang Y, Luirink J, Hardwidge PR. Immunization with skp delivered on outer membrane vesicles protects mice against enterotoxigenic *Escherichia coli* challenge. *Front Cell Infect Microbiol* (2018) **8**:132. doi:10.3389/fcimb.2018.00132

57. Jiang L, Driedonks TAP, Jong WSP, Dhakal S, Bart van den Berg van Saparoea H, Sitaras I, et al. A bacterial extracellular vesicle-based intranasal vaccine against SARS-CoV-2 protects against disease and elicits neutralizing antibodies to wild-type and Delta variants. *J Extracellular Vesicles* (2022) **11**:e12192. doi:10.1002/jev2.12192

58. Bushman W, Yin S, Thio LL, Landy A. Determinants of directionality in lambda site-specific recombination. *Cell* (1984) **39**:699–706. doi:10.1016/0092-8674(84)90477-x

59. Pozdeev G, Beckett MC, Mogre A, Thomson NR, Dorman CJ. Reciprocally rewiring and repositioning the Integration Host Factor (IHF) subunit genes in *Salmonella enterica* serovar Typhimurium: impacts on physiology and virulence. *Microb Genomics* (2022) **8**:000768. doi:10.1099/mgen.0.000768

60. Velmurugu Y, Vivas P, Connolly M, Kuznetsov SV, Rice PA, Ansari A. Two-step interrogation then recognition of DNA binding site by Integration Host Factor: an architectural DNA-bending protein. *Nucleic Acids Res* (2018) **46**:1741–55. doi:10.1093/nar/gkx1215

61. Swinger KK, Rice PA. IHF and HU: flexible architects of bent DNA. *Curr Opin Struct Biol* (2004) **14**:28–35. doi:10.1016/j.sbi.2003.12.003

62. Mikkel K, Tagel M, Ukkivi K, Ilves H, Kivisaar M. Integration Host Factor IHF facilitates homologous recombination and mutagenic processes in Pseudomonas putida. *DNA Repair (Amst)* (2020) **85**:102745. doi:10.1016/j.dnarep.2019.102745

63. Mangan MW, Lucchini S, Danino V, Cróinín TÓ, Hinton JCD, Dorman CJ. The integration host factor (IHF) integrates stationary-phase and virulence gene expression in *Salmonella enterica* serovar Typhimurium. *Mol Microbiol* (2006) **59**:1831–47. doi:10.1111/j.1365-2958.2006.05062.x

64. Prieto AI, Kahramanoglou C, Ali RM, Fraser GM, Seshasayee ASN, Luscombe NM. Genomic analysis of DNA binding and gene regulation by homologous nucleoid-associated proteins IHF and HU in *Escherichia coli* K12. *Nucleic Acids Res* (2012) **40**:3524–37. doi:10.1093/nar/gkr1236

65. Reverchon S, Meyer S, Forquet R, Hommais F, Muskhelishvili G, Nasser W. The nucleoid-associated protein IHF acts as a 'transcriptional domainin' protein coordinating the bacterial virulence traits with global transcription. *Nucleic Acids Res* (2021) **49**:776–90. doi:10.1093/nar/gkaa1227

66. Zulianello L, de la Gorgue de Rosny E, van Ulsen P, van de Putte P, Goosen N. The HimA and HimD subunits of integration host factor can specifically bind to DNA as homodimers. *EMBO J* (1994) **13**:1534–40. doi:10.1002/j.1460-2075.1994.tb06415.x

67. Collins LV, Attridge S, Hackett J. Mutations at rfc or pmi attenuate *Salmonella typhimurium* virulence for mice. *Infect Immun* (1991) **59**:1079–85. doi:10.1128/iai.59.3.1079-1085.1991

68. Mitra A, Łaniewski P, Curtiss R, Roland KL. A live oral fowl typhoid vaccine with reversible O-antigen production. *Avian Dis* (2015) **59**:52–6. doi:10.1637/10885-061014-reg

69. Kong W, Clark-Curtiss J, Curtiss III R. Utilizing Salmonella for antigen delivery: the aims and benefits of bacterial delivered vaccination. *Expert Rev Vaccin* (2013) **12**:345–7. doi:10.1586/erv.13.7

70. Laniewski P, Mitra A, Karaca K, Khan A, Prasad R, Curtiss R, et al. Evaluation of protective efficacy of live attenuated *Salmonella enterica* serovar Gallinarum vaccine strains against fowl typhoid in chickens. *Clin Vaccin Immunol* (2014) **21**:1267–76. doi:10.1128/cvi.00310-14

71. Vendrell A, Gravisaco MJ, Goin JC, Pasetti MF, Herschllik L, Toro JD, et al. Therapeutic effects of *Salmonella typhi* in a mouse model of T-cell lymphoma. *J Immunother* (2013) **36**:171–80. doi:10.1097/cji.0b013e3182886d95

72. Hu C-W, Chang Y-C, Liu C-H, Yu Y-A, Mou KY. Development of a TNF-α-mediated Trojan Horse for bacteria-based cancer therapy. *Mol Ther* (2022) **30**:2522–36. doi:10.1016/j.ymthe.2022.04.008

73. Sanlioglu AD, Aydin C, Bozcuk H, Terzioglu E, Sanlioglu S. Fundamental principals of tumor necrosis factor-alpha gene therapy approach and implications for patients with lung carcinoma. *Lung Cancer* (2004) **44**:199–211. doi:10.1016/j.lungcan.2003.11.017

74. Zhao C, He J, Cheng H, Zhu Z, Xu H. Enhanced therapeutic effect of an antiangiogenesis peptide on lung cancer *in vivo* combined with salmonella VNP20009 carrying a Sox2 shRNA construct. *J Exp Clin Cancer Res* (2016) **35**:107. doi:10.1186/s13046-016-0381-4

EBM Experimental Biology and Medicine

TYPE Original Research
PUBLISHED 24 May 2024
DOI 10.3389/ebm.2024.10037

OPEN ACCESS

*CORRESPONDENCE
M. Freesmeyer,
martin.freesmeyer@med.uni-jena.de

RECEIVED 16 October 2023
ACCEPTED 07 May 2024
PUBLISHED 24 May 2024

CITATION
Perkas O, Schmidt A, Kuehnel C, Greiser J, Hermeyer H, Klingner C, Freesmeyer M and Winkens T (2024), Different narcotic gases and concentrations for immobilization of ostrich embryos for *in-ovo* imaging. *Exp. Biol. Med.* 249:10037. doi: 10.3389/ebm.2024.10037

Different narcotic gases and concentrations for immobilization of ostrich embryos for *in-ovo* imaging

O. Perkas[1,2], A. Schmidt[3,4], C. Kuehnel[1,2], J. Greiser[1,2], H. Hermeyer[1], C. Klingner[3,4], M. Freesmeyer[1,2]* and T. Winkens[1,2]

[1]Clinic of Nuclear Medicine, Jena University Hospital, Jena, Thuringia, Germany, [2]Translational Nuclear Medicine and Radiopharmacy, Clinic of Nuclear Medicine, Jena University Hospital, Jena, Thuringia, Germany, [3]Department of Neurology, Jena University Hospital, Jena, Germany, [4]Biomagnetic Center, Jena University Hospital, Jena, Germany

Abstract

In-ovo imaging using avian eggs has been described as a potential alternative to animal testing using rodents. However, imaging studies are hampered by embryonal motion producing artifacts. This study aims at systematically comparing isoflurane, desflurane and sevoflurane in three different concentrations in ostrich embryos. Biomagnetic signals of ostrich embryos were recorded analyzing cardiac action and motion. Ten groups comprising eight ostrich embryos each were investigated: Control, isoflurane (2%, 4%, and 6%), desflurane (6%, 12%, and 18%) and sevoflurane (3%, 5%, and 8%). Each ostrich egg was exposed to the same narcotic gas and concentration on development day (DD) 31 and 34. Narcotic gas exposure was upheld for 90 min and embryos were monitored for additional 75 min. Toxicity was evaluated by verifying embryo viability 24 h after the experiments. Initial heart rate of mean 148 beats/min (DD 31) and 136 beats/min (DD 34) decreased over time by 44–48 beats/minute. No significant differences were observed between groups. All narcotic gases led to distinct movement reduction after mean 8 min. Embryos exposed to desflurane 6% showed residual movements. Isoflurane 6% and sevoflurane 8% produced motion-free time intervals of mean 70 min after discontinuation of narcotic gas exposure. Only one embryo death occurred after narcotic gas exposure with desflurane 6%. This study shows that isoflurane, desflurane and sevoflurane are suitable for ostrich embryo immobilization, which is a prerequisite for motion-artifact free imaging. Application of isoflurane 6% and sevoflurane 8% is a) safe as no embryonal deaths occurred after exposure and b) effective as immobilization was observed for approx. 70 min after the end of narcotic

gas exposure. These results should be interpreted with caution regarding transferability to other avian species as differences in embryo size and incubation duration exist.

KEYWORDS

in-ovo imaging, ostrich eggs, animal model, biomagnetism, alternative animal testing, narcotic gases, magnet-ovography

Impact statement

In-ovo imaging represents an adequate alternative for preclinical imaging sparing animal research using rodents. In order to avoid image artifacts caused by embryonal motion, use of isoflurane has been described previously. This work systematically investigated different narcotic gases and concentrations, showing successful immobilization for more than one hour after exposure using highest concentrations of isoflurane, desflurane and sevoflurane. This information is needed for planning and execution of in-ovo imaging experiments.

Introduction

In-ovo imaging has been described as a potential alternative concept to animal testing using rats or mice [1–4]. According to national and international legislation, research using eggs does not qualify as animal testing as long as all experiments are carried out before hatching [5–8].

In-ovo methods comprise experiments using chorio-allantois membrane (CAM), vaccine research and production, toxicity studies as well as cardiovascular research, just to name a few. The largest research area is covered by CAM assays, because this highly vascularized membrane enables basic research regarding cancer (tumor cell growth [9], xenografts [10], epithelial-mesenchymal transition [11], circulating tumor cells [12]), angiogenesis (pro- and antiangiogenetic drugs) [13, 14], wound healing, stem cells [15] and even serves as training platform for surgical procedures [16]. As these models have been shown to provide essential information about cell interactions, cancer and drug effects [17], they are suitable to answer important questions of basic research [18, 19]. Regarding the role of *in-ovo* methods within the landscape of research in general, drug development is chosen as an example: It is commonly accepted that new drugs are tested on animals (i.e., rodents) before first application in humans in order to sort out drug candidates which are associated with toxicities. If there was a tool that allowed for an even earlier selection of promising drug candidates, this would reduce the number of animals needed.

With regard to preclinical imaging, *in-ovo* methods contribute to reduction of classic animal research using rodents as it can serve as a "pre-selection tool" in order to test and dismiss unfavorable experimental approaches (e.g., radiopharmaceutical substances for nuclear medicine imaging), so only promising experimental approaches are tested on rodents. Thus, *in-ovo* research complies with the principles of modern animal testing (3R) as established by Russel and Burch in 1959 [20].

Usually, chicken embryos are used for *in-ovo* imaging, however, this requires dedicated small animal imaging devices which represents a disadvantage regarding limited access [1, 2, 4]. A concept using substantially larger ostrich eggs and imaging devices commonly used in routine clinical examinations in humans (e.g., computed tomography, CT; magnet resonance imaging, MRI; and positron emission tomography, PET) has been published before [1, 2, 4].

Preclinical *in-vivo* imaging requires immobilization in order to produce artifact-free imaging [21, 22]. In rodents, isoflurane anesthesia is an established method [23]. Previous publications report on the effect of isoflurane on chicken and ostrich embryos and have investigated feasibility and success of reduction of embryonal movements [1, 22]. However, there are no studies that explore the effect of different narcotic gases and different concentrations.

Thus, this study aims at comparing isoflurane, desflurane and sevoflurane in three different concentrations. The frequency of movements and heart rate is assessed using biomagnetic signals. Furthermore, embryo survival after narcotic gas exposure is evaluated. Two different development stages of ostrich embryos are investigated, i.e., development day (DD) 31 and 34.

Materials and methods

Ostrich eggs

Ostrich eggs were obtained from a local ostrich farm 15 km from the research facility between April and September. Artificial incubation was started 1–4 days after laying and was carried out using a multistage egg incubator (Sofie 3, Hemel, Verl, and Germany) with constant incubation properties at 36.5°C and 25% air humidity as described elsewhere [2, 4]. The ostrich eggs used in this study were part of a larger research project comprising different experiments. During the time period, a total of 373 ostrich eggs were obtained. Non-fertilized eggs and eggs containing dead embryos were discarded. After 31 days of incubation, 188 ostrich embryos were available for

different experiments and of these, 85 ostrich embryos were randomly chosen to be investigated with different narcotic gases as described in this study. Initial egg weight was 1,398 ± 112 g.

If artificially incubated, ostrich eggs usually hatch after 42 days [24]. As it was a requirement to end all experiments before hatching, studies were performed on DD 31 and DD 34. This embryo study did not qualify as an animal research study according to the Federal German Animal Protection Act. Registration took place with the Office for Consumer Protection of the Thuringia State, registration number 22-2684-04-02-114/16. Thus, ethic committee's approval was waived.

Magnet-ovography (MOG)

Methodological aspects of detecting embryonal movement and cardiac action using standard magnetencephalograph (MEG, Neuromag, Elekta, Sweden) systems have been published before [1]. In short, MEG consists of multiple magnetometers, measuring magnetic flux and background noise [25]. Each magnetometer produces a graph (channel) showing the magnetic field change over time. Due to the negative influence of ferromagnetic objects close to the investigation site, all components have to be designed metal-free and thus, remote controls consisting of tubes and a chamber to hold the ostrich egg were used to apply different narcotic gases as described before [1].

Data acquisition and post-processing

Data acquisition followed chronological steps as outlined by Freesmeyer et al. comprising optimal egg positioning via visual verification of heart signals, followed by automated signal recording of each magnetometer channel [1]. Regarding data post-processing, cardiac signals were detected using a method which has been validated for human fetus observations described by Schmidt et al. in 2019, analyzing information about the signal amplitude (minimum-maximum), the overall signal strength, signal space angle and moving correlation coefficient [26]. Movement signals were evaluated by methods of Schmidt et al. (i.e., advanced automatic movement detection, using position changes of the heart signal vector over time) and Freesmeyer et al. (i.e., manual movement detection, using a threshold-based analysis of different signal frequency-bands of each magnetograph channel) [1, 26]. In order to ensure comparability for both methods, a data set comprising two groups (control, isoflurane 6%) from Freesmeyer et al. was analyzed using both methods and agreement was determined using Bland-Altmann plots. The individual embryos studied by Freesmeyer et al. were the same as investigated in this analysis [1]. The other groups (isoflurane 4%, isoflurane 2%, desflurane, sevoflurane) were evaluated only using advanced automatic movement detection method due to time aspects. This schedule was deemed adequate in view of time efficiency as estimated duration for manual movement detection (Freesmeyer et al.) [1] is longer than advanced automatic movement detection (Schmidt et al.) [26].

Experimental design

Isoflurane (Piramal Healthcare, Mumbai, India), Desflurane (Suprane, Baxxter Inc., Illinois, United States) and Sevoflurane (Abbvie Inc., Illinois, United States) were used in three different concentrations according to the available range which was predefined by the respective vaporizers (Vapor 2000 Isofluran, Vapor 2000 Desfluran, Vapor 2000 Sevofluran each by Draeger, Luebeck, Germany). The lowest and highest possible concentration was investigated as well as a concentration in between. Ten groups were investigated: Control, isoflurane (2%, 4%, and 6%), desflurane (6%, 12%, and 18%) and sevoflurane (3%, 5%, and 8%). For each concentration, eight ostrich embryos were investigated on DD 31 and the same ostrich embryos were investigated on DD 34 again. Additionally, a control group comprising 8 ostrich eggs was evaluated without exposure to narcotic gases.

The experiments were conducted as described elsewhere [1]. In short, eggs were removed from the incubator and transferred to MEG facility. Surface temperature was measured using an infrared contactless thermometer (VOLTCRAFT IR 900-30S, Conrad Electronic, Hirschau, Germany) before and after MOG.

Eggs were placed into chamber connected to tubes which enabled in- and outflow of narcotic gases and ambient air. The chamber was set into the MEG device and signal quality was visually assessed. If a positive cardiac signal was visible, experiment started according to Figure 1. After a resting phase of 15 min, narcotic gas exposure was started and continuously monitored using a gas measurement module for anesthetic care (Scio Four Oxi, Draeger, Luebeck, Germany). In order to extract the respective narcotic gas from the vapor, ambient air (21% oxygen, 79% nitrogen) was used. The flow was set at 2 L/min and adjusted as needed, always verifying the desired narcotic gas concentration via the gas measurement module. Narcotic gas exposure was upheld for 90 min and then vaporizer was closed. Data acquisition was continued for additional 75 min (follow-up phase) assessing possible re-appearance of embryonal movement. In total, data were continuously acquired for 180 min. During resting phase and follow-up phase, ambient air was inflated into the chamber holding the ostrich egg, preventing accumulation of carbon dioxide and subsequent embryo suffocation. In the control group, ambient air was inflated into the chamber for 180 min at a flow of 2 L/min. After the experiment, eggs were transferred into incubator and viability of ostrich embryos was investigated

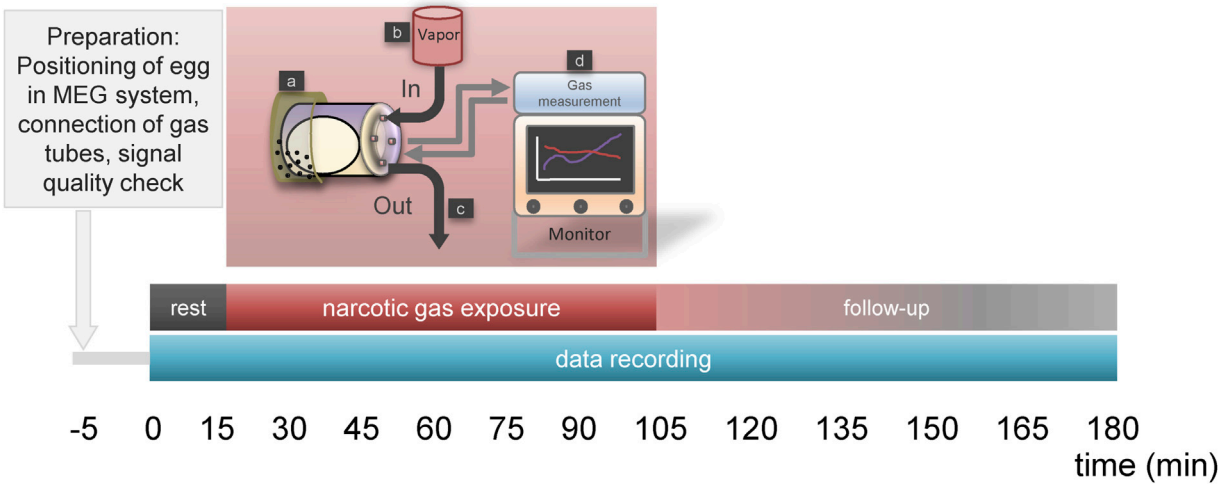

FIGURE 1
Time schedule for narcotic gas exposure. Phase "rest" (15 min) allows for reduction of embryonal arousal after egg transport to MEG-facility. This phase is followed by "narcotic gas exposure" (90 min) and a "follow-up phase" (75 min). During rest and follow-up phase, ambient air is inflated into the chamber holding the ostrich eggs. During "narcotic gas exposure," respective narcotic gas is applied. In control group, during this phase ambient air is inflated. During 180 min MOG, the ostrich egg is held by a container which is located at the head rest (a) of the MEG system. Narcotic gas inflow is provided by specific vapor (b) and narcotic gas outflow (c) is provided by exhaustion system. During the whole experiment, narcotic gas concentration was continuously measured using a gas measurement module (d) for anesthetic care (Scio Four Oxi, Draeger, Luebeck, Germany), ensuring adequate concentration of narcotic gas within the chamber holding the ostrich egg.

approx. 24 h later by 5 min MOG measurement assessing for cardiac signals; thus, experiment toxicity was evaluated. After the last experiment (on DD 35; viability assessment), ostrich embryos were subjected to imaging studies on DD 37 after which they were sacrificed on DD 37 at the latest using sodium-pentobarbital. Necropsy comprising organ removal was performed aiming at verification of imaging studies.

Statistics

Individual embryo heart rate was determined for each minute and median values within each group were calculated and compared. Graphs were designed to visually compare heart rate change over time. ANOVA method was used to determine differences between narcotic gases and concentrations regarding heart rate reduction over time.

Method agreement between manual movement detection and advanced automatic movement detection was evaluated by determination of levels of agreement described by Bland and Altmann [27].

Embryo movement was normalized for individual motion signal level during resting phase. Relative signal change was recorded for each minute and median values within each group were calculated. Groups were compared using graphs. Furthermore, a sigmoid fitting curve was calculated for each experiment and inflection points were determined as the time point of successful immobilization ("sleep") and re-appearance of movement during follow-up phase ("awake"). Time points were compared for each group using Kruskal-Wallis-Test and $p = 0.05$ as a level of significance.

Results

In total, 168 MOG comprising 85 ostrich eggs were carried out. Eight data sets from 5 ostrich eggs were excluded from analysis due to erroneous data recording, corrupt data files and inconsistent duration of narcotic gas exposure. One of 80 ostrich embryos died after exposure to desflurane (6%) on DD 34. In 79 ostrich embryos, positive heart signal was obtained approx. 24 h after the last experiment, indicating survival. Necropsy revealed no abnormal findings attributable to narcotic gas exposure.

Between MOG start and end, mean temperature reduction was 6.1°C and different narcotic gases did not differ significantly regarding temperature decrease.

Data reconstruction was successful using advanced automatic movement detection method. Comparison with manual movement detection method showed good agreement between control group and isoflurane 6% regarding motion analysis (Figure 2). Duration of data reconstruction and evaluation ranged from 20 min to 160 min per data file comprising 180 min.

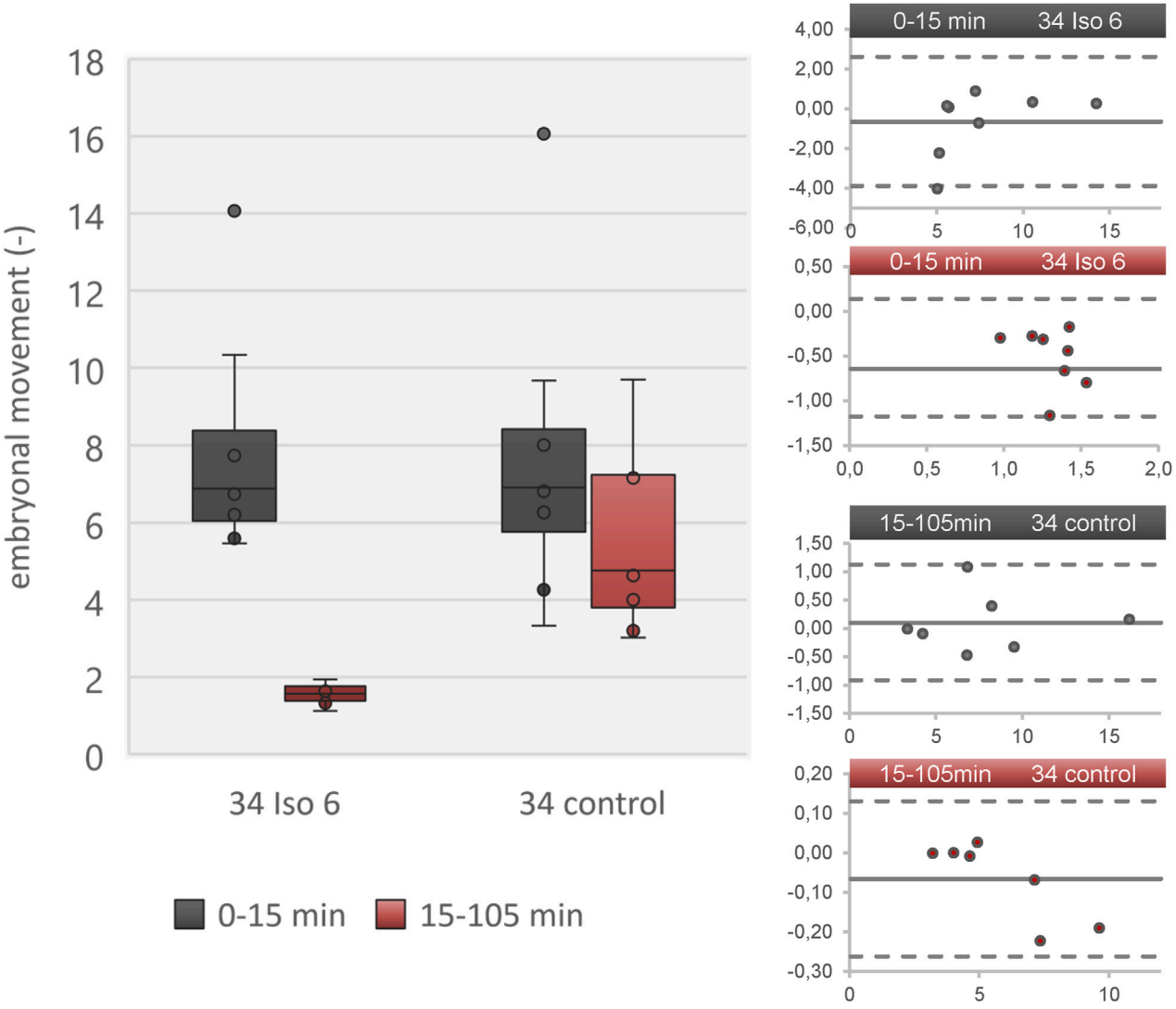

FIGURE 2
Embryonal movement using advanced automated movement detection according to [26] in a data set derived from [1]. Left: Boxplot diagram showing level of activity during resting phase (0–15 min; grey) and isoflurane/ambient air (15–105 min; red) in two groups (isoflurane 6% and control) on DD 34. Right: Four Bland-Altmann plots showing adequate agreement of advanced automated movement detection and manual movement detection. The four plots refer to the four boxes in the boxplot diagram. The Bland-Altmann plots compare each value between advanced automated movement detection and manual movement detection. The dots indicate the difference between both methods (y-axis) over absolute value (embryonal movement; x-axis) and the solid line represents the mean value of all dots. Dashed lines indicate 2x standard deviation of all differences. All values are in the range of 2x standard deviation, indicating no significant underestimation or overestimation.

Heart rate

Heart rate change over time is shown in Figure 3 for all embryos on DD 31 and DD 34, respectively. On DD 34, ostrich embryos showed significant lower heart rate (106.9 ± 14.6/min) than ostrich embryos on DD 31 (140.9 ± 15.8/min) during the first 5 min after exposure to narcotic gases ($p < 0.001$).

Figure 4 visualizes effects of isoflurane, desflurane and sevoflurane over time. Mean heart rate reduction between time intervals 0–15 min and 151–180 min was 43.8/min on DD 31 and 47.7/min on DD 34, respectively; there was no significant difference between control group and narcotic gases and different concentrations (Figure 5).

Embryonal movement

Embryonal movement over time is shown in Figure 6, aiming at visualization of immobilization effect. Control groups on DD 31 and DD 34 (grey lines) differ slightly

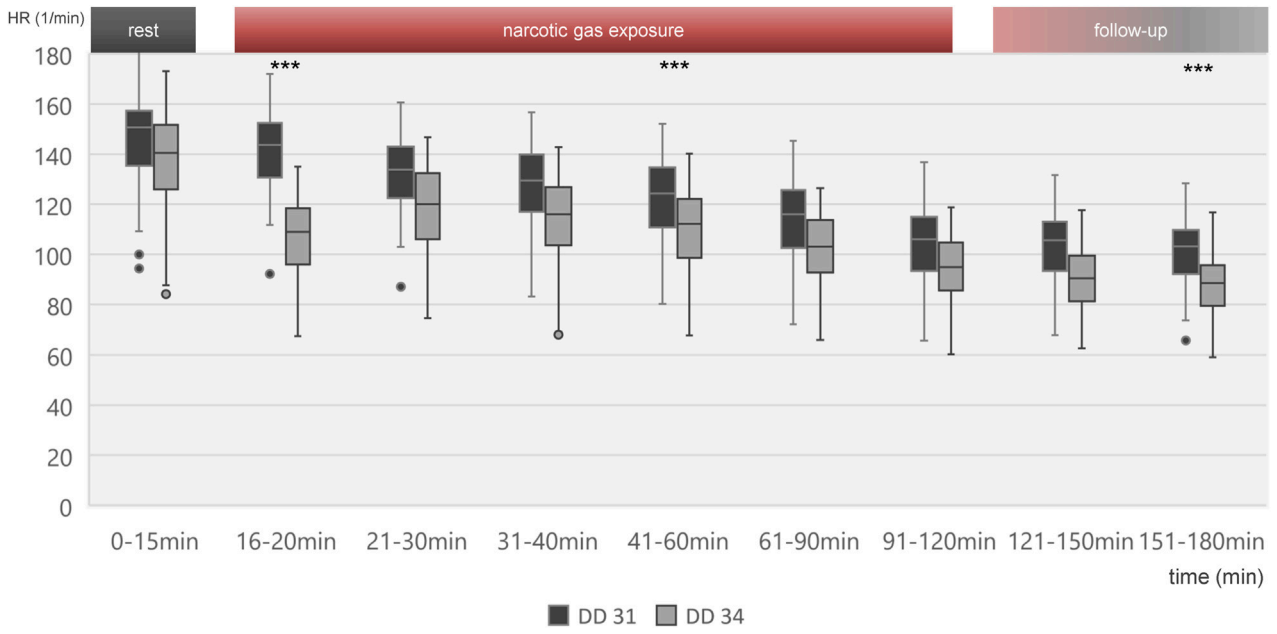

FIGURE 3
Boxplot diagram of heart rate during different time intervals of all 80 ostrich embryos investigated on DD 31 and 34. Significant differences between DD 31 and DD 34 occur within the first 5 min after initiation of narcotic gas exposure, in the middle of narcotic gas exposure and at the end of follow-up. Aggregated data of all groups including control group was deemed appropriate in view of Figures 4, 5, excluding significant differences between control group and narcotic gases. ***$p < 0.001$.

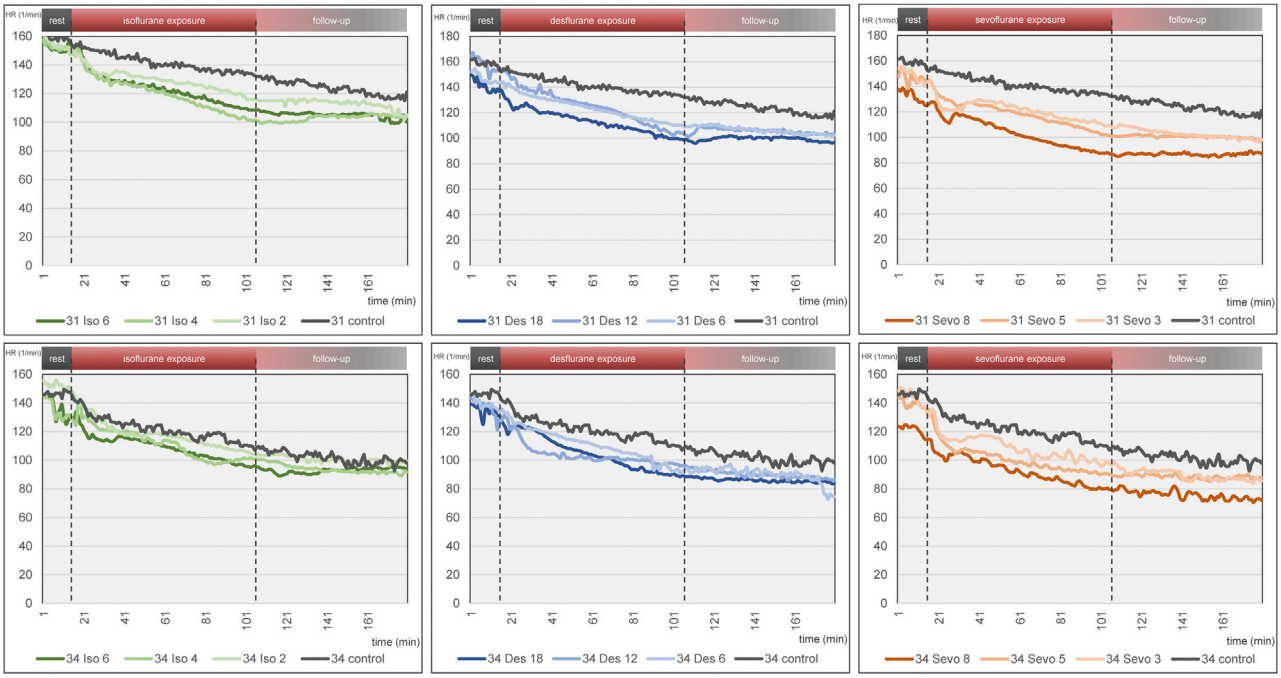

FIGURE 4
Mean heart rate over time for each narcotic gas and concentration (green: isoflurane, blue: desflurane; orange: sevoflurane). Top row: DD 31; bottom row: DD 34. In each graph, control group is depicted in grey. Dashed lines represent start and end of narcotic gas exposure. In each group, eight ostrich embryos on DD 31 and 34 were investigated, respectively.

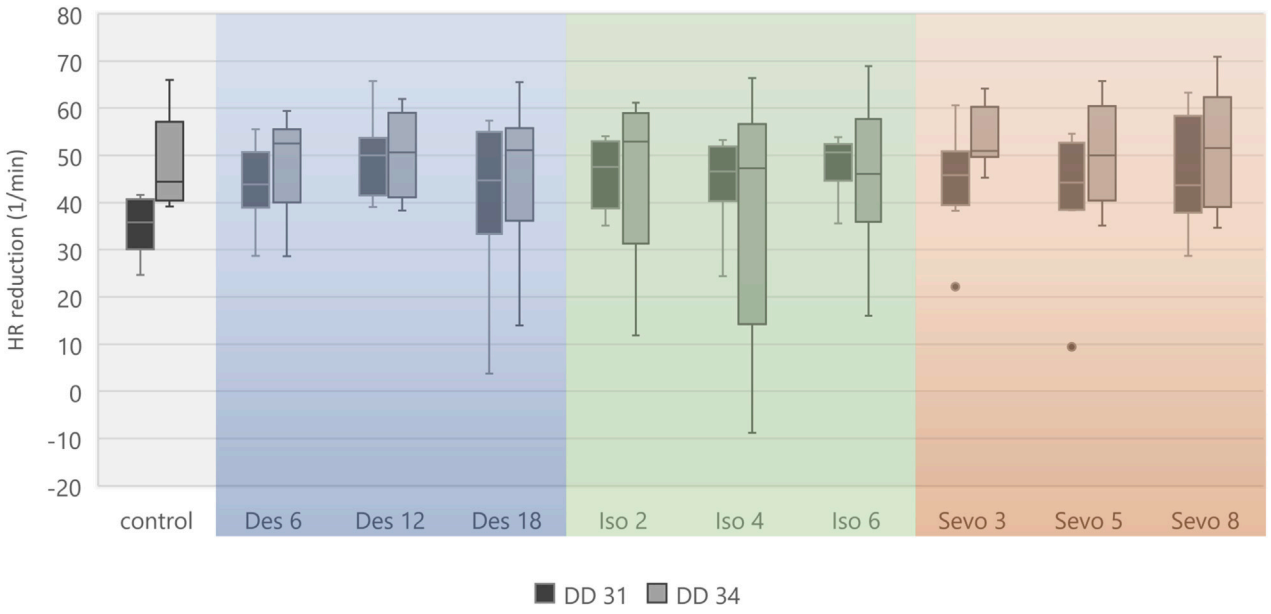

FIGURE 5
Boxplot diagram of mean heart rate reduction (difference) between 0–15 min and 151–180 min for each narcotic gas and concentration. Considering DD 31 and DD 34 separately, comparison between control group and each narcotic gas and concentration revealed no significant differences.

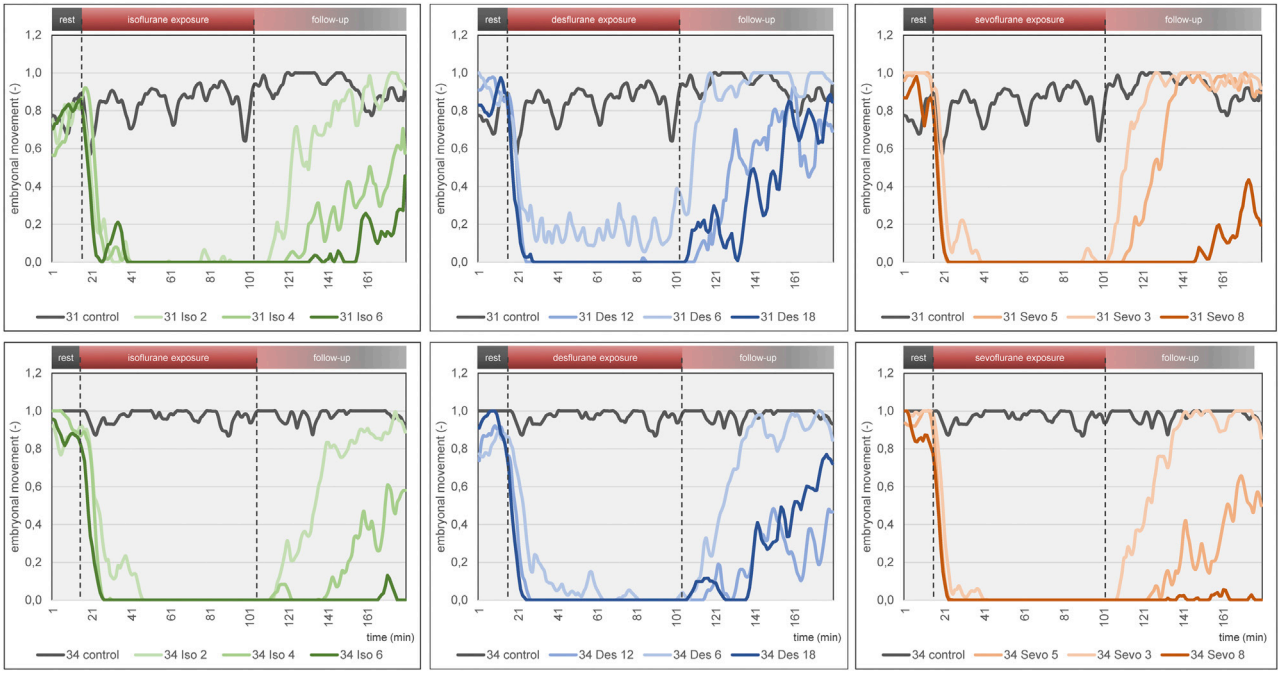

FIGURE 6
Mean embryonal movement over time for each narcotic gas and concentration (green: isoflurane, blue: desflurane; orange: sevoflurane). Top row: DD 31; bottom row: DD 34. In both rows, results of control groups are depicted in grey. Dashed lines represent start and end of narcotic gas exposure. Note the light blue graph on DD 31 and DD 34 (desflurane 6%) during narcotic gas exposure (15–105 min) which indicates residual movement whereas the other graphs (desflurane 12%, 18%; sevoflurane, isoflurane) show almost constant 0 values. This figure mainly focuses on visualization of group differences. For quantification of effectiveness of immobilization, see Figure 7.

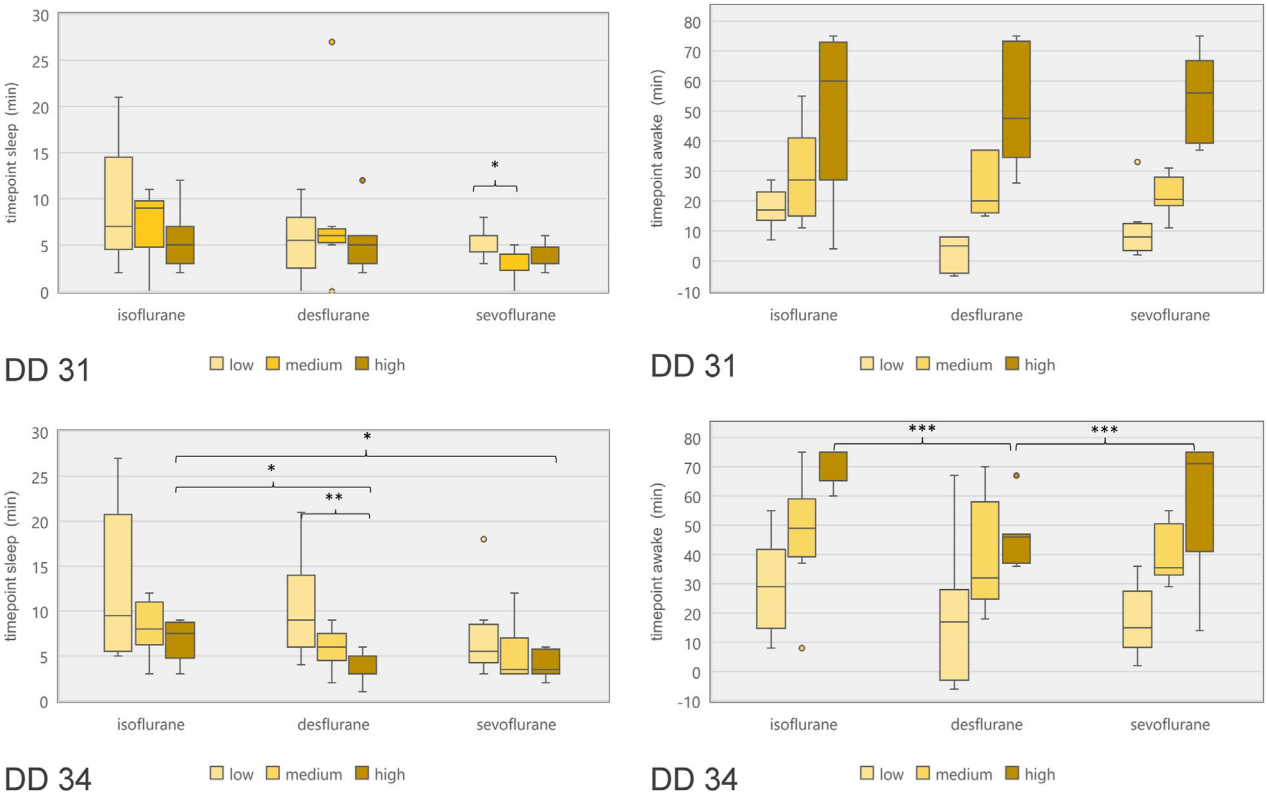

FIGURE 7
Boxplot diagram of duration between start of narcotic gas exposure and reduction of movements ("time point sleep"; left diagrams) as well as duration between end of narcotic gas exposure and re-appearance of movements ("time point awake"; right diagrams) for ostrich embryos on DD 31 (top row) and DD 34 (bottom row). In order to compare concentration levels of narcotic gases, categories "low," "medium" and "high" were used as provided by dedicated vaporizers. Note the shorter time until re-appearance of movements for desflurane [as compared to sevoflurane and isoflurane (highest concentrations)] on DD 34. *$p < 0.05$; **$p < 0.01$; ***$p < 0.001$.

without significant differences while less embryonal movement is detectable when using highest concentrations for isoflurane, desflurane and sevoflurane, respectively. Figure 7 visualizes effectiveness of immobilization using time points "sleep" and "awake" in minutes after starting and ending narcotic gas inflow, respectively. On DD 34, highest concentration of isoflurane, desflurane and sevoflurane lead to a significantly different median time point "sleep" of 7.5 ± 2.1 min, 3.0 ± 1.5 min and 3.5 ± 1.4 min, respectively ($p = 0.0169$) and a significantly different time point "awake" of 75.0 ± 5.7 min, 46.0 ± 9.6 min, and 71.0 ± 21.4 min, respectively ($p = 0.0252$). There is no significant difference between low, medium and high concentration within each narcotic gas group. On DD 31 and DD 34, sevoflurane produces a significantly shorter median time for the ostrich embryo to "sleep" (DD 31: 4.0 ± 1.7 min; DD 34: 4.0 ± 3.5 min) than isoflurane (DD 31: 7.0 ± 4.7 min; DD 34: 8.0 ± 5.5 min) and desflurane (DD 31: 6.0 ± 5.3 min; DD 34: 6.0 ± 4.5 min) (DD 31: $p = 0.0143$; DD 34: $p = 0.0015$). Over all narcotic gas groups and concentrations, ostrich embryos awake earlier on DD 31 (24.0 ± 22.1 min) than on DD 34 (37.0 ± 22.6 min) ($p = 0.0016$).

Discussion

Isoflurane, desflurane and sevoflurane were compared in three different concentrations regarding effect on ostrich embryo motion and heart rate.

Method agreement

Both methods of movement detection, i.e., manual movement detection and advanced automatic movement detection showed a good agreement in a dataset (comprising control group and isoflurane 6% on DD 34) retrieved from [1], thus confirming appropriateness of automatic movement detection. As data reconstruction and evaluation was shorter for the automatic approach, this method was chosen for

comparison of different narcotic gases and concentrations. Initially, the algorithm for automatic movement detection was designed for human fetuses of 34–38 weeks of gestational age [26, 28]. Human fetuses of that age weigh approx. 2400–3400 g [29], which is about ten times heavier than an ostrich embryo of approx. 350 g on DD 34 and 220 g on DD 31, respectively. However, less weight did not hamper MOG signal detection as the algorithm produced adequate results. This study revealed that data reconstruction and evaluation using the automatic approach (as short as 20 min) was faster than manual movement detection which required at least 45 min for a 90 min-data file, as reported by Freesmeyer et al. [1].

Embryonal movement

The three narcotic gases show comparable results regarding efficacy of movement reduction during exposure. After less than 8 min, ostrich embryos show a distinct cessation of movements and sevoflurane was most effective with this regard. Only one group (desflurane 6%) which represents the lowest concentration for this gas, showed residual movements during narcotic gas exposure (15–105 min) (Figure 6). After discontinuation of narcotic gas exposure, ostrich embryos having been exposed to desflurane showed a significantly shorter time until reappearance of first movements than isoflurane and sevoflurane, indicating inferior immobilization effects of desflurane (Figure 7). As expected, highest concentrations of each narcotic gas produced a longer immobilization than lowest concentration (Figure 6), however, this result was not significant (Figure 7). This finding is in line with results showing more depression of motor evoked potentials in rats being exposed to higher concentrations of isoflurane [30].

Regarding ostrich eggs, only one study has addressed the effect of immobilization using narcotic gases, i.e., isoflurane [1]; however not investigating different concentrations. Heidrich et al. have successfully used isoflurane in chicken embryos in order to enable artifact free imaging, but also did not investigate different concentrations of isoflurane [22]. Dose-dependent effects of desflurane and other narcotic gases are well-known [31] and adjustment of concentrations represent common clinical practice in anesthetic management of patients. Chambers holding ostrich eggs and preventing leakage of narcotic gases might produce image artifacts [4, 32], thus, the setup described in this study aimed at narcotic gas exposure before imaging procedure. In this context, it is very important to consider the time from the end of narcotic gas exposure and reappearance of movements. This time span is required to establish a vessel access in order to intravenously administer substances, e.g., radiopharmaceuticals for *in-vivo* imaging. On DD 34, desflurane in its highest concentration (18%) led to an earlier reappearance of movements in ostrich embryos than isoflurane and sevoflurane, respectively (Figure 7). Thus, desflurane is less suitable to suppress embryonal movement, whereas isoflurane and sevoflurane allow for artifact-free imaging after mean 70 min after the end of narcotic gas exposure.

Heart rate

Heart rate reduction over time was present in all individuals including control group which indicates factors independent from narcotic gases as the underlying reason. Continuous cooling of ostrich eggs during experiments is considered the main factor as a mean reduction of 6.1°C was observed in this study. Similar effects were reported previously using the same methodological approach [1]. MOG requires a complex MEG-system shielding of the entire room to suppress external magnetic field changes interfering with detection of magnetic flux. Also, MEG-system relies on constant room temperature of 25°C which makes cooling of the ostrich eggs inevitable. Due to close proximity of ostrich eggs and magnetometers, thermal support with heating pads was not possible as it would have also increased the temperature of magnetometers, thus hampering MOG. Interpreting the heart rate reduction over time for each narcotic gas and concentration separately indicates a slightly pronounced decrease after initiation of narcotic gas exposure (16–20 min) and continuous (linear) reduction during narcotic gas exposure and follow-up; however, this difference is not significant (Figures 4, 5). Concluding, heart rate reduction is present in all ostrich embryos and occurs independently from narcotic gas exposure.

This study revealed low toxicity of repeated narcotic gas exposure as all individual survived experiments on DD 31 and 79/80 embryos survived experiments on DD 34. The assessment of viability 24 h after the last experiment was deemed appropriate to verify lethality. Regarding toxicity, da Rosa et al. investigated effects of isoflurane and sevoflurane in low concentrations on fertility of mice [33] and Liu et al. reported on long-term neurotoxicity of isoflurane and sevoflurane in neonatal mice [34]; however, both studies consider long-term effects and not short-term survival as in this study. Ostrich embryos were sacrificed on DD 37 at the latest, i.e., three days after last exposure to narcotic gases. Therefore, long-term effects of narcotic gases on ostrich embryos cannot be assessed using the current experimental setup.

All ostrich embryos underwent narcotic gas exposure on DD 31 and DD 34. This approach was chosen in order to show feasibility and safety of narcotic gases even in repeated experiments. As it is the goal to enable artifact-free imaging of ostrich embryos, repeated experiments in the same animal is desirable in order to reduce the number of embryos used in an experiment. Few differences were present between these two development stages which are predominantly characterized by embryo growth; organogenesis is complete at this late time point [2, 24, 35]. Namely, significant lower heart rate was observed in

embryos on DD 34 in the first 5 minutes after initiation of narcotic gas exposure as well as at the end of follow-up-phase (Figure 3) and ostrich embryos on DD 31 show a faster re-appearance of movements after discontinuation of narcotic gas exposure than embryos on DD 34. These are unexpected results as the applied narcotic gas divided by embryo weight is much higher in embryos on DD 31 (data not shown) and should lead to a stronger effect than in further developed embryos. It is well known that in general, heart rate is higher in smaller and younger individuals; however, this does not explain the differences in reaction to narcotic gas exposure. One possible explanation is the repetition of narcotic gas exposure.

All embryos investigated on DD 34 had been investigated with the same narcotic gas in the same concentration 3 days before. This might indicate a cumulative effect of narcotic gases; however, this assumption cannot be proven with the current setup and would require experiments comprising a control group of embryos on DD 34 without prior narcotic gas exposure.

Limitations

This study addresses important questions regarding the effect of narcotic gases; however, the following limitations have to be considered: The experiments investigated only two time points during development, i.e., DD 31 and 34. Especially considering unexpected results between both time points regarding heart rate, experiments on further time points, i.e., DD 37 and 28 are important to transfer feasibility of immobilization via narcotic gases.

The system setup of MOG is rather elaborate due to extensive shielding and necessary metal-free environment. More compact and mobile systems would be desirable in order to enable simultaneous detection of cardiac action/movements and acquisition of images (CT, MRI, and PET).

The concept of using ostrich embryos as an alternative for animal testing is rather new and not (yet) widely distributed and results cannot be transferred without limitations to more commonly used chicken eggs or even mammals. Furthermore, it is unknown whether narcotic gases might influence experiments (e.g., normal biodistribution of radiopharmaceuticals) in ostrich embryos.

Conclusion

This study investigated desflurane, isoflurane and sevoflurane in three different concentrations for immobilization of ostrich embryos in order to enable motion artifact-free imaging. Minor methodological changes regarding automation of data reconstruction were successfully applied. Isoflurane and sevoflurane in their respective highest concentration (as permitted by the dedicated vaporizers), i.e. 6 % and 8%, respectively, were most suitable for immobilization which lasted for approx. 70 min after discontinuation of narcotic gas exposure. All three narcotic gases are considered safe as only one of 80 embryos (160 experiments) died after narcotic gas (i.e., desflurane) exposure and heart rate did not change significantly when compared to a control group.

Author contributions

Conceptualization: MF and TW, methodology: AS, JG, CrK, and TW; formal analysis and investigation: AS, HH, and OP, resources and supervision: MF, TW, and CaK, writing–original draft preparation: OP and TW, Writing–review and editing: all authors, Project administration and Funding Acquisition: MF and TW. All authors contributed to the article and approved the submitted version.

Data availability statement

The raw data supporting the conclusion of this article will be made available by the authors, without undue reservation.

Ethics statement

The requirement of ethical approval was waived by Office for Consumer Protection of the Thuringia State, registration number 22-2684-04-02-114/16 for the studies involving animals because this embryo study did not qualify as an animal research study according to the Federal German Animal Protection Act. The studies were conducted in accordance with the local legislation and institutional requirements.

Funding

The author(s) declare that financial support was received for the research, authorship, and/or publication of this article. MF and TW disclose receipt of the following financial support for the research, authorship, and publication of this article: This work was supported by the Deutsche Forschungsgemeinschaft (grant number FR 2724/2-1) and (grant number WI 5346/2-1).

Acknowledgments

Anna Christl, Wiebke Neuschulz, Michelle Wallrodt, Oliver Hinze, Ferdinand Ndum and Veronika Porwoll are

acknowledged for assistance in data analysis. We thank Prof. Dr. Otto W. Witte for granting access to Neuromag system and Dr. Ralph Huonker for technical support with Neuromag system. PD Dr. Thomas Bartels and Dr. Sabine Bischoff are acknowledged for veterinary support.

Conflict of interest

The authors declare that the research was conducted in the absence of any commercial or financial relationships that could be construed as a potential conflict of interest.

References

1. Freesmeyer M, Hermeyer H, Kuehnel C, Perkas O, Greiser J, Witte OW, et al. In-ovo imaging using ostrich eggs: biomagnetism for detection of cardiac signals and embryonal motion. *Exp Biol Med (Maywood)* (2022) **247**:996–1004. doi:10.1177/15353702221082046

2. Winkens T, Christl A, Kuehnel C, Ndum F, Seifert P, Greiser J, et al. In-ovo imaging using ostrich eggs-Evaluation of physiological embryonal development on computed tomography. *Acta Zoologica* (2021) **103**:492–502. doi:10.1111/azo.12400

3. Winkens T, Kuehnel C, Freesmeyer M. In-ovo imaging using ostrich eggs - replacement of animal studies? *J Nucl Med* (2020) **61**:1122.

4. Freesmeyer M, Kuehnel C, Opfermann T, Niksch T, Wiegand S, Stolz R, et al. The use of ostrich eggs for in ovo research: making preclinical imaging research affordable and available. *J Nucl Med* (2018) **59**:1901–6. doi:10.2967/jnumed.118.210310

5. Leary S, Anthony R, Cartner S, Grandin T, Greenacre C, Gwaltney-Brant S, et al. *AVMA guidelines for the euthanasia of animals: 2020 edition*. Schaumburg, IL, USA: American Veterinary Medical Association (2020).

6. Europäisches Parlament und Rat. *Richtlinie 2010/63/EU zum Schutz der für wissenschaftliche Zwecke verwendeten Tiere* (2010).

7. Bundesministerium der Justiz und für Verbraucherschutz. *Tierschutzgesetz* (2016).

8. United States Department of Agriculture. *Animal welfare act and animal welfare regulations* (2013).

9. Schneider-Stock R, Flügen G. Editorial for special issue: the chorioallantoic membrane (CAM) model-traditional and state-of-the art applications: the 1st international CAM conference. *Cancers (Basel)* (2023) **15**:772. doi:10.3390/cancers15030772

10. Tai YK, Chan KKW, Fong CHH, Ramanan S, Yap JLY, Yin JN, et al. Modulated TRPC1 expression predicts sensitivity of breast cancer to doxorubicin and magnetic field therapy: segue towards a precision medicine approach. *Front Oncol* (2021) **11**:783803. doi:10.3389/fonc.2021.783803

11. Sheng G. Defining epithelial-mesenchymal transitions in animal development. *Development* (2021) **148**:dev198036. doi:10.1242/dev.198036

12. Fluegen G, Avivar-Valderas A, Wang Y, Padgen MR, Williams JK, Nobre AR, et al. Phenotypic heterogeneity of disseminated tumour cells is preset by primary tumour hypoxic microenvironments. *Nat Cell Biol* (2017) **19**:120–32. doi:10.1038/ncb3465

13. Swaminathan A, Balaguru UM, Manjunathan R, Bhuvaneswari S, Kasiviswanathan D, Sirishakalyani B, et al. Live imaging and analysis of vasoactive properties of drugs using an in-ovo chicken embryo model: replacing and reducing animal testing. *Microsc Microanal* (2019) **25**:961–70. doi:10.1017/s1431927619000588

14. Farzaneh M, Attari F, Khoshnam SE, Mozdziak PE. The method of chicken whole embryo culture using the eggshell windowing, surrogate eggshell and ex ovo culture system. *Br Poult Sci* (2018) **59**:240–4. doi:10.1080/00071668.2017.1413234

15. Pinto MT, Ribeiro AS, Paredes J. The chick CAM as an *in vivo* system to study stem cell activity. *Methods Mol Biol* (2023) **2572**:155–66. doi:10.1007/978-1-0716-2703-7_12

16. Leng T, Miller JM, Bilbao KV, Palanker DV, Huie P, Blumenkranz MS. The chick chorioallantoic membrane as a model tissue for surgical retinal research and simulation. *Retina* (2004) **24**:427–34. doi:10.1097/00006982-200406000-00014

17. Barnett SE, Herrmann A, Shaw L, Gash EN, Poptani H, Sacco JJ, et al. The chick embryo xenograft model for malignant pleural mesothelioma: a cost and time efficient 3Rs model for drug target evaluation. *Cancers (Basel)* (2022) **14**:5836. doi:10.3390/cancers14235836

18. Rashidi H, Sottile V. The chick embryo: hatching a model for contemporary biomedical research. *Bioessays* (2009) **31**:459–65. doi:10.1002/bies.200800168

19. Ribatti D. The chick embryo chorioallantoic membrane (CAM). A multifaceted experimental model. *Mech Dev* (2016) **141**:70–7. doi:10.1016/j.mod.2016.05.003

20. Russell W, Burch R. Principles of humane experimental-technique - russell,Wms, Burch. *Rl Roy Soc Health J* (1959) **79**:700.

21. Gebhardt P, Würbach L, Heidrich A, Heinrich L, Walther M, Opfermann T, et al. Dynamic behaviour of selected PET tracers in embryonated chicken eggs. *Revista Española de Medicina Nucl e Imagen Mol* (2013) **32**:371–7. doi:10.1016/j.remnie.2013.09.013

22. Heidrich A, Wurbach L, Opfermann T, Saluz HP. Motion-artifact-free *in vivo* imaging utilizing narcotized avian embryos in ovo. *Mol Imaging Biol* (2011) **13**:208–14. doi:10.1007/s11307-010-0355-4

23. Neag M-A, Mitre A-O, Catinean A, Mitre C-I. An overview on the mechanisms of neuroprotection and neurotoxicity of isoflurane and sevoflurane in experimental studies. *Brain Res Bull* (2020) **165**:281–9. doi:10.1016/j.brainresbull.2020.10.011

24. Gefen E, Ar A. Morphological description of the developing ostrich embryo: a tool for embryonic age estimation. *Isr J Zoolog* (2001) **47**:87–97. doi:10.1092/h2t8-1h2u-81h1-p5xy

25. Hämäläinen M, Hari R, Ilmoniemi RJ, Knuutila J, Lounasmaa OV. Magnetoencephalography theory, instrumentation, and applications to noninvasive studies of the working human brain. *Rev Mod Phys* (1993) **65**:413–97. doi:10.1103/revmodphys.65.413

26. Schmidt A, Witte R, Swiderski L, Zöllkau J, Schneider U, Hoyer D. Advanced automatic detection of fetal body movements from multichannel magnetocardiographic signals. *Physiol Meas* (2019) **40**:085005. doi:10.1088/1361-6579/ab3c96

27. Bland JM, Altman DG. Statistical methods for assessing agreement between two methods of clinical measurement. *Lancet* (1986) **1**:307–10.

28. Schmidt A, Schneider U, Witte OW, Schleußner E, Hoyer D. Developing fetal motor-cardiovascular coordination analyzed from multi-channel magnetocardiography. *Physiol Meas* (2014) **35**:1943–59. doi:10.1088/0967-3334/35/10/1943

29. Fenton TR. A new growth chart for preterm babies: babson and Benda's chart updated with recent data and a new format. *BMC Pediatr* (2003) **3**:13. doi:10.1186/1471-2431-3-13

30. Haghighi SS, Green DK, Oro JJ, Drake RK, Kracke GR. Depressive effect of isoflurane anesthesia on motor evoked potentials. *Neurosurgery* (1990) **26**:993–7. doi:10.1227/00006123-199006000-00012

31. Weiskopf RB. Cardiovascular effects of desflurane in experimental-animals and volunteers. *Anaesthesia* (1995) **50**:14–7. doi:10.1111/j.1365-2044.1995.tb06184.x

32. Winkens T. *In-ovo Bildgebung an Straußeneiern – Evaluierung einer Alternative zum klassischen Tierversuch*. Habilitation. Jena: Friedrich-Schiller Universität Jena (2022).

33. Rosa AC, Beier SL, Oleskovicz N, Mezzalira JC, Miquelutti DJ, Mezzalira A, et al. Effects of exposure to halothane, isoflurane, and sevoflurane on embryo viability and gestation in female mice. *Semina: Ciências Agrárias* (2015) **36**:871–81. doi:10.5433/1679-0359.2015v36n2p871

34. Liu J, Zhao Y, Yang J, Zhang X, Zhang W, Wang P. Neonatal repeated exposure to isoflurane not sevoflurane in mice reversibly impaired spatial cognition at juvenile-age. *Neurochem Res* (2017) **42**:595–605. doi:10.1007/s11064-016-2114-7

35. Brand Z, Cloete SWP, Malecki IA, Brown CR. Ostrich (*Struthio camelus*) embryonic development from 7 to 42 days of incubation. *Br Poult Sci* (2017) **58**:139–43. doi:10.1080/00071668.2016.1259529

EBM Experimental Biology and Medicine

TYPE Original Research
PUBLISHED 31 May 2024
DOI 10.3389/ebm.2024.10051

OPEN ACCESS

*CORRESPONDENCE
Feng Wan,
wfthebest@163.com

RECEIVED 13 November 2023
ACCEPTED 07 May 2024
PUBLISHED 31 May 2024

CITATION
Tang Y-W, Jiang M-Y, Cao J-W and Wan F (2024), Triptolide decreases podocytes permeability by regulating TET2-mediated hydroxymethylation of ZO-1.
Exp. Biol. Med. 249:10051.
doi: 10.3389/ebm.2024.10051

Triptolide decreases podocytes permeability by regulating TET2-mediated hydroxymethylation of ZO-1

Yue-Wen Tang[1,2], Meng-Ya Jiang[1], Jia-Wei Cao[1] and Feng Wan[1,2]*

[1]Department of Nephrology, Hangzhou TCM Hospital Affiliated to Zhejiang Chinese Medical University, Hangzhou, China, [2]Key Laboratory of Kidney Disease Prevention and Control Technology, Hangzhou, China

Abstract

Podocyte injury or dysfunction can lead to proteinuria and glomerulosclerosis. Zonula occludens 1 (ZO-1) is a tight junction protein which connects slit diaphragm (SD) proteins to the actin cytoskeleton. Previous studies have shown that the expression of ZO-1 is decreased in chronic kidney disease (CKD). Thus, elucidation of the regulation mechanism of ZO-1 has considerable clinical importance. Triptolide (TP) has been reported to exert a strong antiproteinuric effect by inhibiting podocyte epithelial mesenchymal transition (EMT) and inflammatory response. However, the underlying mechanisms are still unclear. We found that TP upregulates ZO-1 expression and increases the fluorescence intensity of ZO-1 in a puromycin aminonucleoside (PAN)-induced podocyte injury model. Permeablity assay showed TP decreases podocyte permeability in PAN-treated podocyte. TP also upregulates the DNA demethylase TET2. Our results showed that treatment with the DNA methyltransferase inhibitors 5-azacytidine (5-AzaC) and RG108 significantly increased ZO-1 expression in PAN-treated podocytes. Methylated DNA immunoprecipitation (MeDIP) and hydroxymethylated DNA immunoprecipitation (hMeDIP) results showed that TP regulates the methylation status of the ZO-1 promoter. Knockdown of TET2 decreased ZO-1 expression and increased methylation of its promoter, resulting in the increase of podocyte permeability. Altogether, these results indicate that TP upregulates the expression of ZO-1 and decreases podocyte permeability through TET2-mediated 5 mC demethylation. These findings suggest that TP may alleviate podocyte permeability through TET2-mediated hydroxymethylation of ZO-1.

KEYWORDS

Triptolide, TET2, hydroxymethylation, ZO-1, podocytes permeability

Highlights

- Triptolide upregulates ZO-1 to decrease podocyte permeability in PAN-induced podocyte injury model.
- Triptolide regulates the methylation status of ZO-1 promoter in podocyte.
- Knockdown of TET2 decreases ZO-1 expression, accompanied by an increase in ZO-1 promoter methylation levels.

Impact statement

Proteinuria is one of the most common manifestations of chronic kidney disease (CKD) and also one of the most important independent risk factors for CKD progression. Podocyte injury is the major cause of proteinuria. Zonula occludens 1 (ZO-1) maintains podocyte structure by connecting the slit diaphragm (SD) proteins to the actin cytoskeleton. Numerous studies have confirmed that the expression of ZO-1 is decreased in CKD. Therefore, clarifying the regulatory mechanism of ZO-1 is of great significance. Triptolide (TP) can alleviate proteinuria through various mechanisms. In this study, we aimed to clarify the mechanism by which TP regulates ZO-1 from the novel perspective of epigenetics. Accordingly, a puromycin aminonucleoside (PAN)-induced podocyte injury model was developed and treated with TP. The results showed that TP upregulates the expression of ZO-1 and decreases podocyte permeability through TET2-mediated hydroxymethylation of the ZO-1 promoter. Our study reveals the novel mechanism by which TP can reverse podocyte damage.

Introduction

Chronic kidney disease (CKD) is a highly progressive disease, which has becoming one of the leading causes of death in the 21st century [1]. Proteinuria is not only an early clinical manifestation of CKD, but also an independent prognostic risk factor for CKD progression [2]. Podocytes, also known as glomerular epithelial cells, are highly differentiated cells that are attached to the glomerular basement membrane (GBM) and located in the outermost layer of the GBM [3]. Podocytes are connected to each other by the slit diaphragm (SD), and the integrity of this connection plays an important role in preventing renal protein loss. Podocyte injury or dysfunction can lead to proteinuria and glomerulosclerosis [4]. Therefore, effective prevention and treatment of podocyte injury is an important issue.

Zonula Occludens 1 (ZO-1) belongs to the uridine kinase family. It was the first tight junction proteins to be identified, and contains the PDZ, SH3 and uridine acid regions [5]. ZO-1 is mainly expressed on the cytoplasmic side of the foot process of glomerular podocytes near the SD and links the SD proteins through its PDZ domain to the actin cytoskeleton [6]. Accumulating studies have shown that the expression of ZO-1 is significantly reduced in CKD [7–9]. Therefore, the correct localization and expression of ZO-1 in the tight junction between the podocytes are particularly important for the maintenance of podocyte permeability.

Triptolide (TP) is a major active component of the medicinal plant *Tripterygium wilfordii* Hook. f., and is widely used for the treatment of inflammation and autoimmune disorders. Animal experiments have suggested that TP can relieve proteinuria by various mechanisms, including anti-inflammatory, and antioxidant effects, inhibition of epithelial mesenchymal transition, and promotion of autophagy [10–14]. However, whether TP can affect the expression of ZO-1 in podocytes remains unclear.

In the present study, we used a puromycin aminonucleoside (PAN)-induced podocyte injury model to explore the effect of TP on ZO-1 expression, podocyte permeability as well as to detect the methylation status of the promoter of ZO-1.

Materials and methods

Cell culture and treatment

Human conditionally immortalized glomerular podocytes (HPCs) were cultured in complete RPMI 1640 medium containing 10% fetal bovine serum (Gibco, Gaithersburg, MD, United States) and insulin-transferrin-selenium (1×, Thermo Fisher Scientific, Waltham, MA, United States) at 33°C in 5% CO_2. After differentiation at 37°C for 10–14 days, the mature podocytes were randomly divided into three groups: Control, PAN-stimulated group (PAN, 50 μg/mL, GLPBIO), and TP intervention group (5 nM, Yuanye Bio-Technology Co., Ltd, Shanghai). Additionally, 5′-azacytidine (5-AzaC, 10 μM in phosphate-buffered saline [PBS], MCE, United States) or RG108 (Beyotime, Shanghai, China) were used as the DNA methyltransferase inhibitors. Lentivirus (Lv) carrying the TET2 short-hairpin RNA (shRNA) and control lentivirus (scramble Lv) were purchased from GeneChem (Shanghai, China). After incubation for 24–72 h, cells were collected for subsequent experiments.

Detection of reactive oxygen species (ROS) level

HPCs were treated with PAN and TP for 24 h, then incubated with 10 μM DCFH-DA (Beyotime, Shanghai, China) for 30 min, followed by washing three times with PBS. Thereafter, the fluorescence intensity of DCFH-DA was detected using fluorescent microscopy.

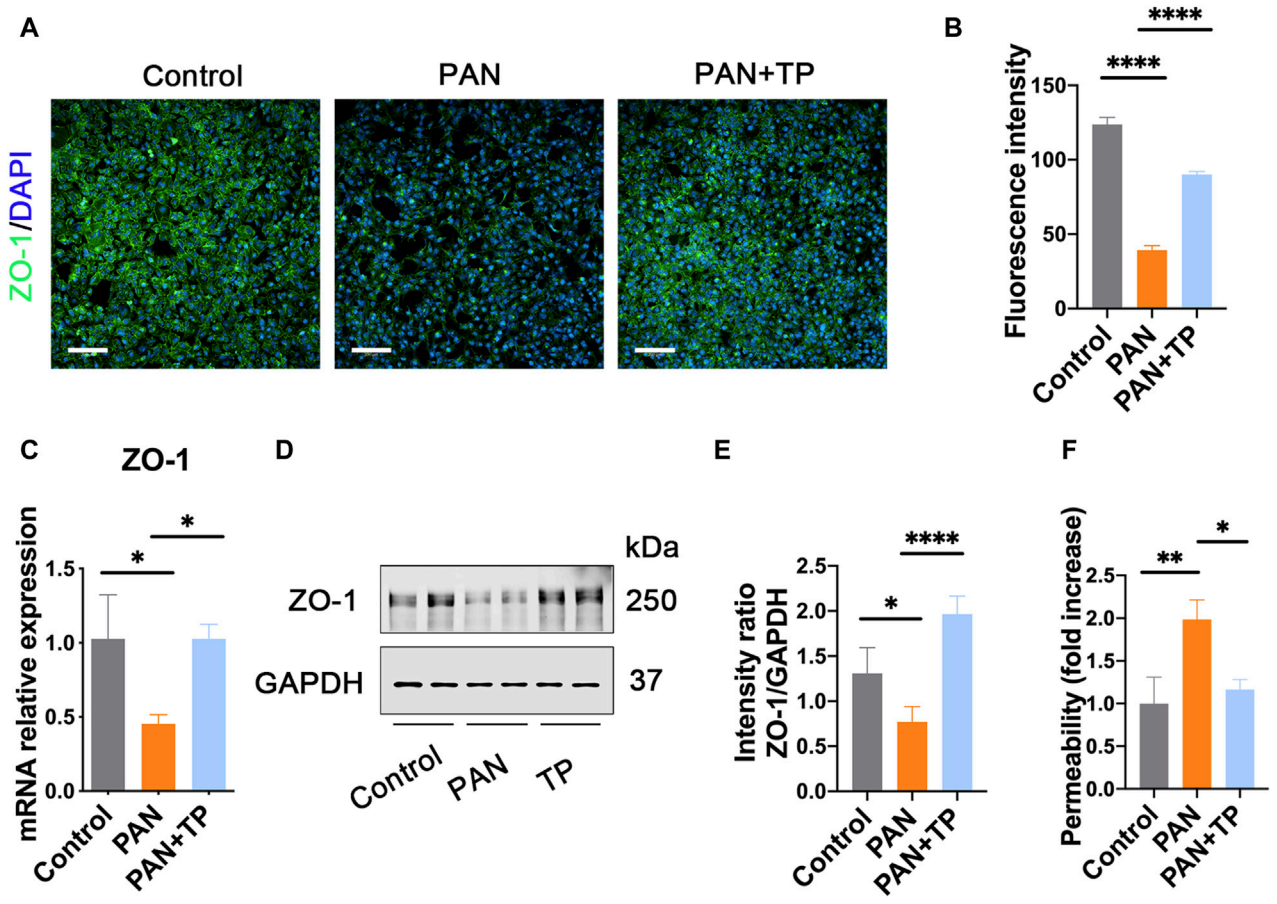

FIGURE 1
TP upregulates ZO-1 expression and decreases podocyte permeability in PAN-induced podocytes. **(A)** Immunofluorescence staining for ZO-1 in each group. Scale bar, 200 μm. **(B)** Semi-quantitative analysis of the fluorescence intensity of ZO-1. ****$p < 0.0001$. **(C)** The mRNA expression of ZO-1 in each group. Data are shown as mean ± SD. *$p < 0.05$. **(D)** The protein expression of ZO-1 in each group. **(E)** Relative protein level was calculated by the band intensity against GAPDH, respectively. *$p < 0.05$, ****$p < 0.0001$. **(F)** The podocyte permeability was detected using FITC-labeled bovine serum albumin in a transwell chamber. *$p < 0.05$, **$p < 0.01$.

Permeability assay

The permeability assay was conducted as previously described [15]. Briefly, HPCs (1×10^5/well/200 μL) were seeded in the upper layer of the transwell chamber (24 well plate, NEST Biotechnology Co. Ltd, Wuxi, China). Cells were treated with PAN (50 μg/mL) or TP (5 nM) after undergoing starvation. After 36 h, fluorescein isothiocyanate (FITC)-labeled bovine serum albumin (0.25 mg/mL, Solarbio, Beijing, China) was added to the upper chamber of the transwell chamber for 10 min at room temperature. The fluorescence intensity of the medium in the lower chamber, reflecting the podocyte monolayer permeability, was detected using a multifunctional enzyme-linked immunosorbent assay reader (excitation: 493 nm, emission: 550 nm; Thermo Fisher Scientific, Waltham, MA, United States).

Quantitative real-time polymerase chain reaction (qRT-PCR)

Total RNA was extracted from HPCs using the TRIzol reagent and reverse-transcribed to cDNA using a Primescript™ reagent kit (TaKaRa, Kusatsu, Shiga, Japan). The primers used were as follows: ZO-1-Forward: 5′-CAA CATACAGTGACGCTTCACA′, ZO-1-Reverse: 5′-CACTAT TGACGTTTCCCCACTC-3′; TET2-Forward: 5′-TCCTGG TGGCAGCTCTGAACG-3′, TET2-Reverse: 5′-TGGTGGTGG TGGTGTGGTAGTG-3’; GAPDH-Forward: 5′-ACCACAGTC CATGCCATCAC-3′, GAPDH-Reverse: 5′-TCCACCACCCTG TTGCTGTA-3′. PCR was performed using a QuantStudio 5 real-time PCR system (Applied Biosystems, Waltham, MA, United States). GAPDH was used as an internal reference. Each experiment was performed in triplicate.

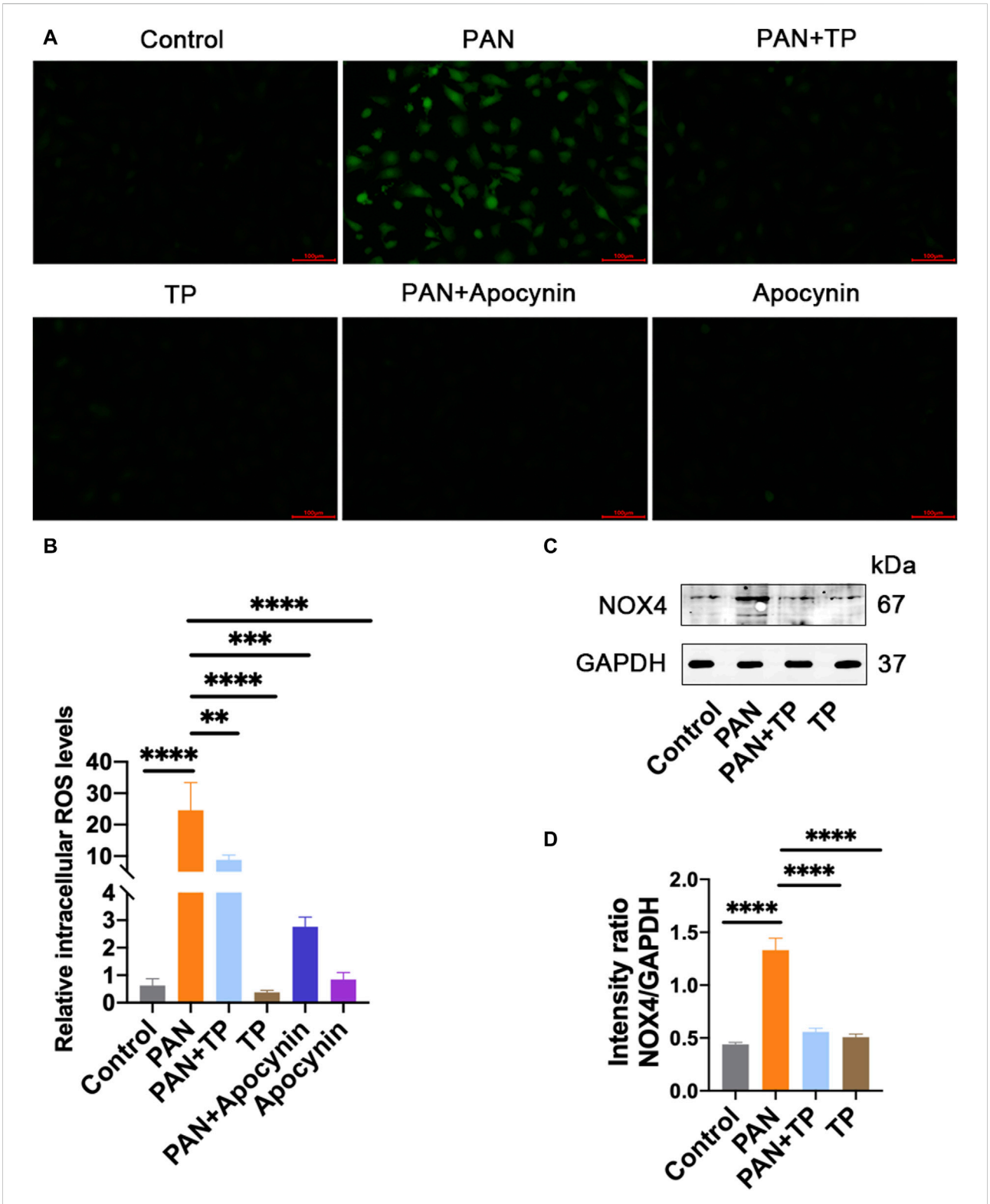

FIGURE 2
TP reduces PAN-induced increase in cellular ROS and NOX4. **(A)** The cellular ROS level was detected using DCFH-DA staining. Scale bar, 100 μm. **(B)** Quantification of ROS level. $^{**}p < 0.01$, $^{***}p < 0.001$, $^{****}p < 0.0001$. **(C)** The protein expression of NOX4 in each group. **(D)** Relative protein level was calculated by the band intensity against GAPDH, respectively. $^{****}p < 0.0001$.

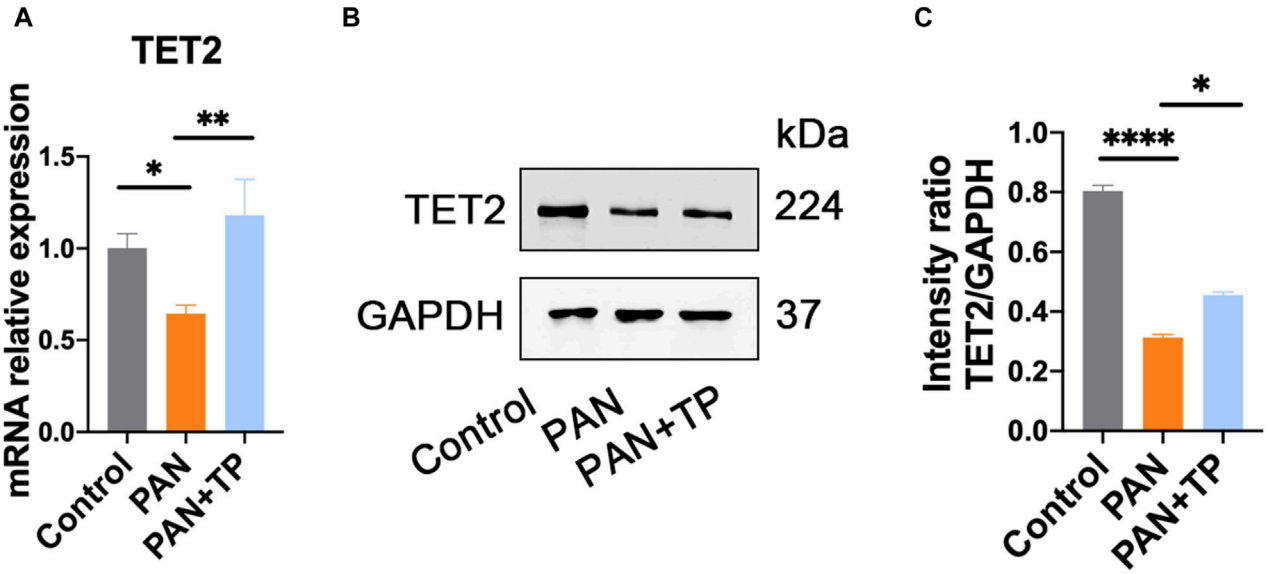

FIGURE 3
TP upregulates TET2 expression in PAN-treated podocytes. **(A)** The mRNA expression of TET2 in each group. Data are shown as mean ± SD. *$p < 0.05$, **$p < 0.01$. **(B)** The protein expression of TET2 in each group. **(C)** Relative protein level was estimated by the band intensity against GAPDH, respectively. *$p < 0.05$, ****$p < 0.0001$.

Western blotting

HPCs were lysed using RIPA buffer containing a proteinase inhibitor cocktail at 4°C for 30 min and centrifuged at 10,000 × *g* for 10 min. The BCA reagent kit (Beyotime, Shanghai, China) was used to calculate the protein concentration in the supernatant, followed by mixing with SDS-PAGE sample loading buffer (2×) and boiling at 95°C for 10 min. Equal amounts of protein were separated using SDS-PAGE and transferred to nitrocellulose membranes. Membranes were blocked with 5% skim milk, and then incubated with primary antibodies, including TET2 (Abcam, Cambridge, UK, ab94580), ZO-1 (ABclonal, Wuhan, China, A0659), NOX4 (ProteinTech, Rosemont, IL, United States, 67,681-1-1g), and GAPDH (ProteinTech, Rosemont, IL, United States, 60,004-1-Ig) at 4°C overnight, followed by incubation with infrared-labeled anti-rabbit/mouse IgG antibody. Reactive bands were observed using an Odyssey infrared imaging system (LI-COR Biosciences, Lincoln, NE, United States).

Immunofluorescence

Podocytes were fixed with 10% formalin for 10 min at room temperature, blocked with 5% goat serum, and incubated with rabbit anti-ZO-1 (ABclonal, Wuhan, China) at 4°C for 1 h. Podocytes were then incubated with FITC-conjugated goat anti-rabbit IgG (Thermo Fisher Scientific, Waltham, MA, United States) at 4°C for 1 h after washing with PBS three times. Cells were photographed under a fluorescence microscope (Olympus) after staining with DAPI.

DNA isolation and shearing

DNA was isolated using the genome extraction kit (Genefist, Shanghai, China), according to the manufacturer's protocol. The genome was broken into 200–1000 bp segments by ultrasonic fragmentation. The ultrasonic conditions were set as: sonicate 3-4 pulses of 10 s each at 50 W, followed by 30 s rest on ice between each pulse. The sonicated cell lysate was analyzed by agarose gel analysis before subsequent use.

Methylated/hydroxymethylated DNA immunoprecipitation (MeDIP/hMeDIP)

Methylated DNA was isolated from sonicated DNA (1.0 μg) using the EpiQuik™ Methylated DNA Immunoprecipitation Kit (Epigentek, Farmingdale, NY, United States), according to the manufacturer's protocol. The EpiQuik™ Hydroxymethylated DNA Immunoprecipitation Kit (Epigentek, Farmingdale, NY, United States) was used to extract hydroxymethylated DNA

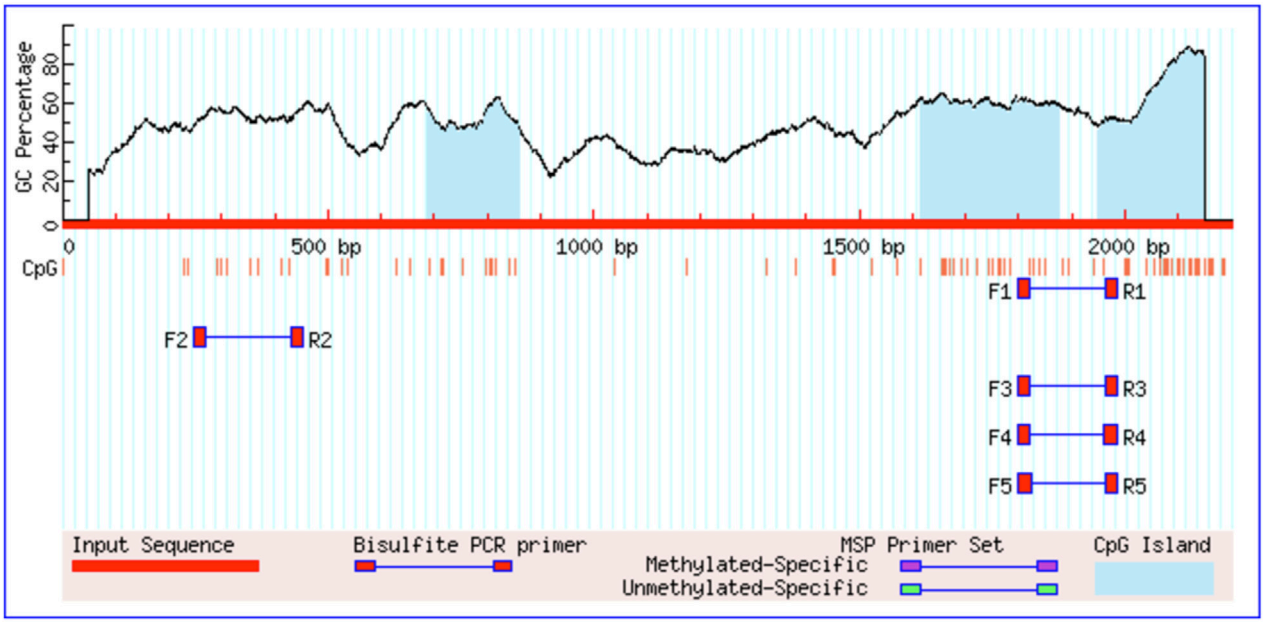

	Size (bp)	Start-End
Island 1	171	688-858
Island 2	261	1614-1874
Island 3	196	1950-2145

FIGURE 4
CpG island prediction results. Three CpG islands were found in the promoter region of ZO-1. The criteria used were as follows: Island size >100, GC Percent >50.0, and Obs/Exp >0.6.

from the sonicated DNA (0.5 μg) in each group. Meanwhile, total sonicated DNA was used as the input DNA for equal loading.

Amplification of methylated and hydroxymethylated ZO-1

For DNA amplification, the PCR reactions were performed with a volume of 20 μL containing: TaKaRa Ex Taq® (2×) 10 μL, forward primer (10 μM) 1 μL, reverse primer (10 μM) 1 μL, eluted DNA 2 μL, and ddH_2O 6 μL. The primer sequences were as follows: Pro-ZO-1-Forward: 5′-AACGAG AGCAACGCTTCTGA-3′ and Pro-ZO-1-Reverse: 5′-GTC CACTTGCTCCTCGACAA-3′. All reactions were performed on a Veriti® 96-Well Thermal Cycle (Thermo Fisher Scientific), and the PCR products were observed using a Gel Imaging System.

Statistical analysis

Statistical analyses were performed using SPSS (version 20.0, IBM Corp., Armonk, NY, United States). Values are presented as mean ± standard deviation. Quantitative data were compared between the two groups using the student's t-test. One-way analysis of variance was used for multiple group comparisons. p-value <0.05 was considered statistically significant.

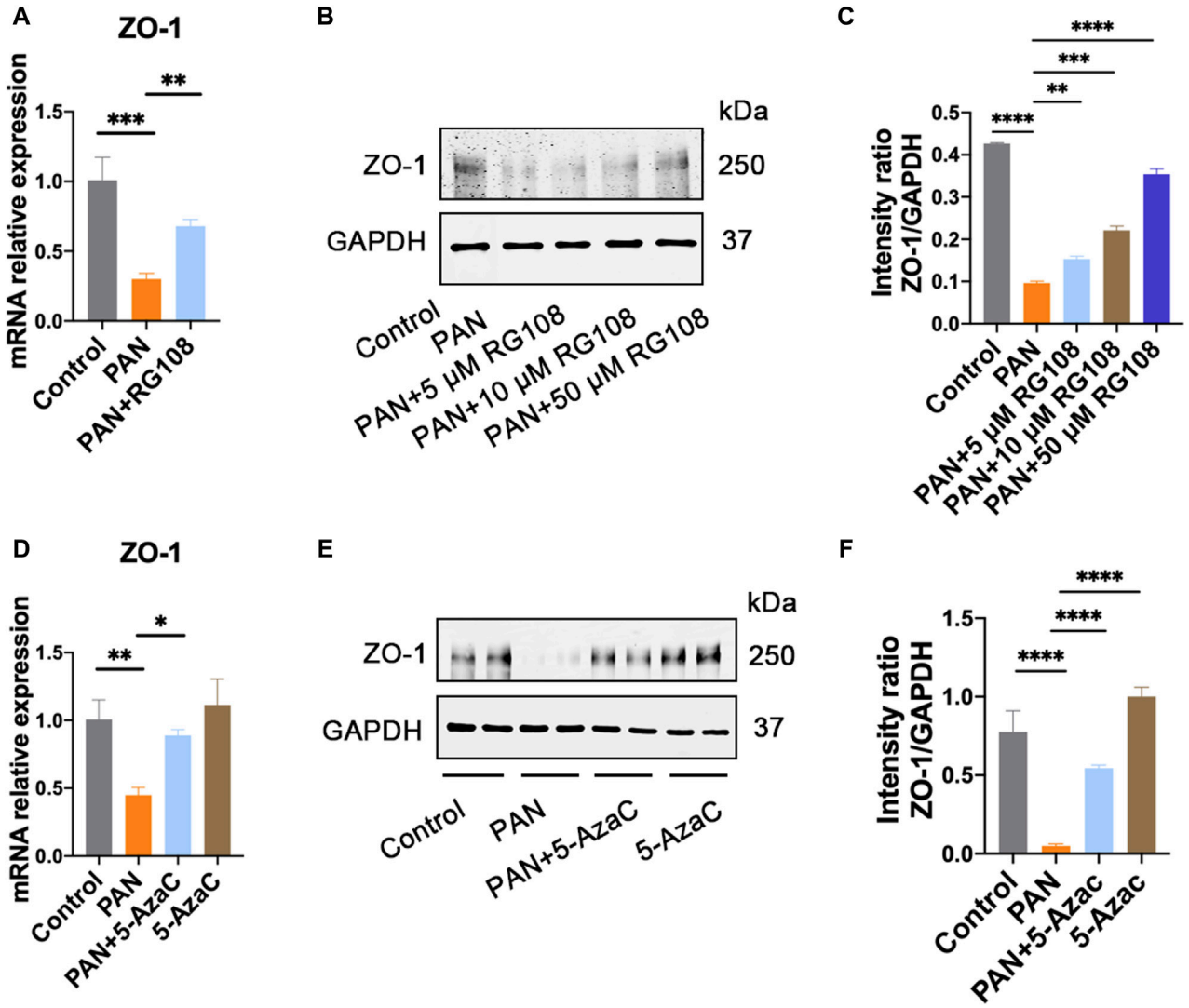

FIGURE 5
ZO-1 expression is regulated by epigenetics. **(A)** The expression of ZO-1 in each group was determined by qRT-PCR. Data are shown as mean ± SD. $^{**}p < 0.01$, $^{***}p < 0.001$. Control: control podocyte; PAN: podocyte treated with 50 μg/mL PAN; PAN + RG108: podocyte treated with 50 μg/mL PAN and RG108 (5 μM, 10 μM, and 50 μM). **(B)** The expression of ZO-1 in each group was determined by western blot. **(C)** Relative protein level was calculated by the band intensity against GAPDH, respectively. $^{**}p < 0.01$, $^{***}p < 0.001$, $^{****}p < 0.0001$. **(D)** The expression of ZO-1 in each group was determined by qRT-PCR. Data are shown as mean ± SD. Control: control podocyte; PAN: podocyte treated with 50 μg/mL PAN; PAN+5-AzaC: podocyte treated with 50 μg/mL PAN and 10 μM 5-AzaC; 5-AzaC: podocyte treated with 10 μM 5-AzaC. $^{*}p < 0.05$, $^{**}p < 0.01$. **(E)** The expression of ZO-1 in each group was determined by western blot. **(F)** Relative protein level was calculated by the band intensity against GAPDH, respectively. $^{****}p < 0.0001$.

Results

TP upregulates ZO-1 to decrease podocyte permeability

PAN induces podocyte injury by causing decreased expression and abnormal distribution of SD proteins, including ZO-1 [16]. Similarly, in our study, we observed a decrease in the fluorescence intensity of ZO-1, along with its discontinuous distribution in PAN-stimulated podocytes (Figures 1A, B). ZO-1 mRNA and protein expression levels were also decreased (Figures 1C–E). However, TP treatment markedly increased the fluorescence intensity and upregulated ZO-1 expression levels. Next, we assessed podocyte permeability using a transwell chamber, and found that the permeability of PAN-treated podocytes was nearly twice of that of untreated podocytes (Figure 1F). However, TP intervention significantly decreased the podocyte permeability of the PAN-treated

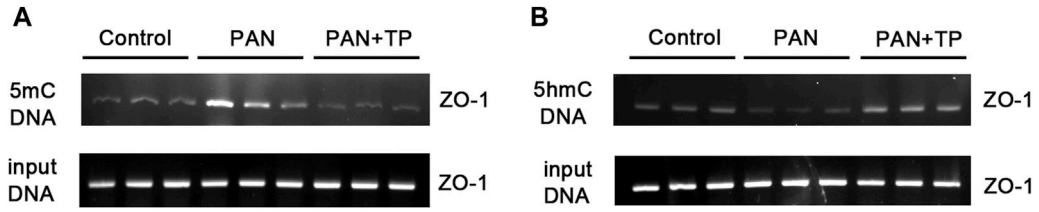

FIGURE 6
TP regulates the methylation status of the ZO-1 gene promoter. **(A)** Agarose gel electrophoresis images of the ZO-1 promoter amplified by polymerase chain reaction of methylated DNA obtained by methylated DNA immunoprecipitation (MeDIP). **(B)** Agarose gel electrophoresis images of the ZO-1 promoter amplified by polymerase chain reaction of hydroxymethylated DNA obtained by hydroxymethylated DNA immunoprecipitation (hMeDIP). The input DNA was used as the control for equal loading.

group. These findings suggest that TP can decrease podocyte permeability by upregulating ZO-1 expression.

Many studies have shown that PAN-induced podocyte injury is associated with the overproduction of ROS [8]. Considering that podocytes express various NADPH oxidase subunits, including NOX4, we determined the cellular NOX4 and ROS levels. The results showed that PAN significantly increased the cellular ROS level and NOX4 expression (Figures 2A, C). However, TP significantly reduced the ROS level and NOX4 expression, which was confirmed by quantitative analysis (Figures 2B, D). Apocynin, an inhibitor of NADPH oxidase activity, led to a significant reduction in the ROS level induced by PAN. These results correlate with the changes in podocyte permeability, and indicate that PAN-induced oxidative stress might be involved in the increased podocyte permeability.

TP upregulates expression of demethylase TET2

Growing evidence has shown that epigenetics played an important role in the evolvement of podocyte injury. Therefore, we detected the expression of DNA demethylase TET family proteins. qRT-PCR and western blotting results indicated that the expression of TET2 was significantly reduced in the PAN group compared with the control group (Figure 3). After TP treatment, the expression of TET2 increased significantly (Figure 3). However, TET2 and TET3 demonstrated no significant differences among the groups (data not shown). These results indicate that TP may selectively regulate the expression of TET2 in PAN-induced podocyte injury model.

ZO-1 expression is regulated by epigenetics

It is well known that the TET family proteins play a crucial role in passive and active demethylation [17]. The synchronous upregulation of TET2 and ZO-1 suggests that ZO-1 expression may be regulated by TET2. To test our hypothesis, we firstly obtained the promoter region of ZO-1 by retrieving the upstream 2,200 bp sequence of the transcription start site from the human genome. Using the online methylation analysis software MethPrimer[1], we found that the ZO-1 promoter region contains three CpG islands (688–858 bp, 1,614–1,874 bp, and 1,950–2,145 bp; Criteria used: Island size >100, GC Percent >50.0, Obs/Exp >0.6), indicating that the expression of ZO-1 may be epigenetically regulated (Figure 4). Subsequently, we used the DNA methyltransferase inhibitors 5-azacytidine (5-AzaC) and RG108 to treat the podocytes. The results showed that ZO-1 expression was significantly increased in podocytes treated with 5-AzaC and RG108 compared with the PAN alone stimulated group (Figure 5). Taken together, these results suggest ZO-1 expression is closely related to epigenetic regulation.

TP can regulate the methylation status of the ZO-1 gene promoter

To further test whether TP regulates the methylation status of the ZO-1 promoter, we used MeDIP and hMeDIP methods to analyze the methylation status of ZO-1 in genomic DNA samples isolated from podocytes. As expected, the decreased expression of ZO-1 in the PAN group was associated with increased promoter methylation, while the promoter methylation levels of ZO-1 in the TP treatment group were significantly reduced (Figure 6A). Furthermore, we observed that ZO-1 demethylation upon TP intervention corresponded with increased ZO-1 hydroxymethylation (Figure 6B), suggesting that TP can mediate ZO-1 demethylation, which is accompanied by ZO-1 hydroxymethylation.

1 http://www.urogene.org/methprimer/

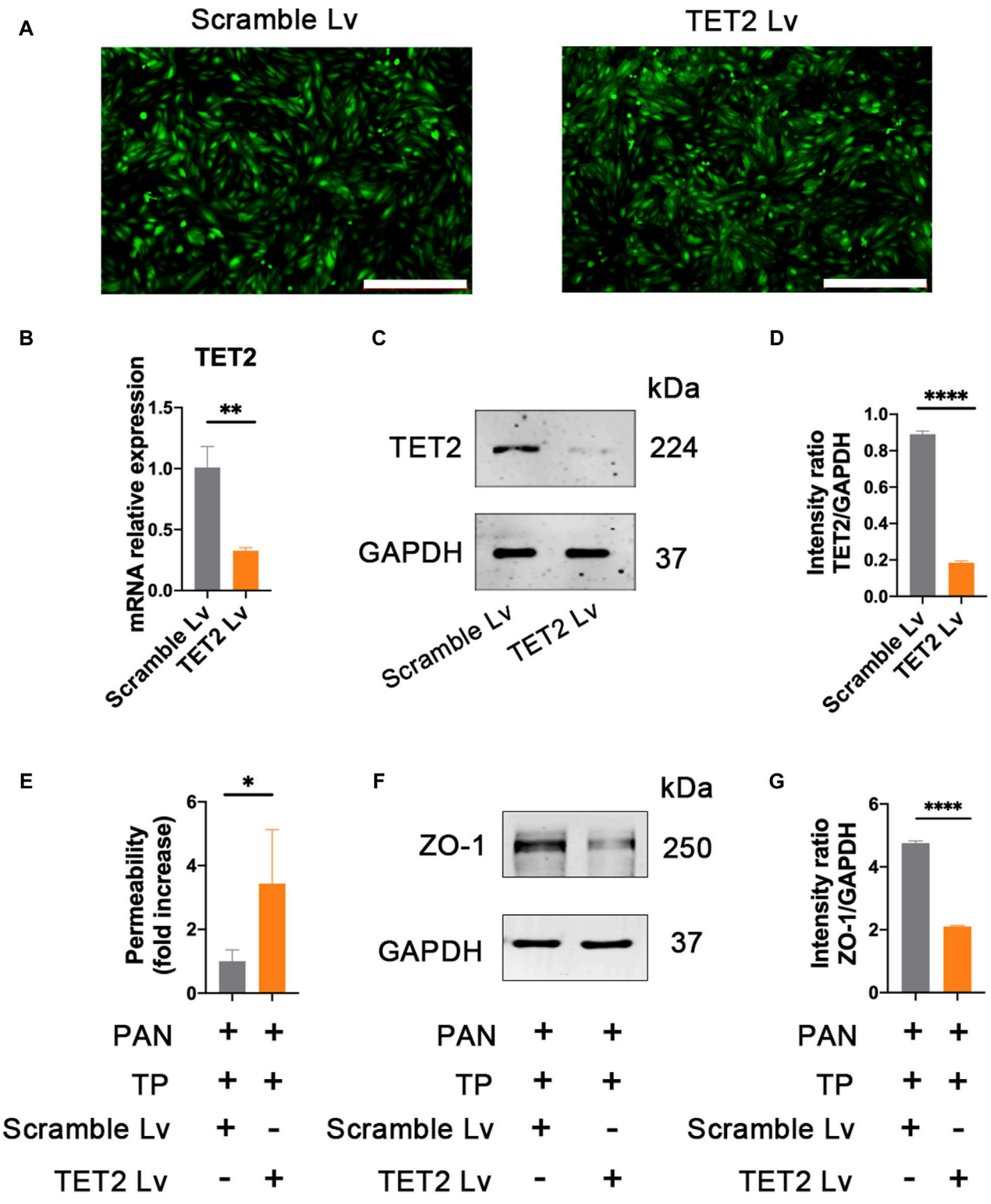

FIGURE 7
Knockdown *TET2* affects the expression of ZO-1. **(A)** The infection rates of lentivirus (Lv) carrying TET2 shRNA and scarmble Lv were evaluated by observing GFP fluorescence under a fluorescence microscope. Scale bar, 200 μm. **(B)** Efficacy of the Lv targeting TET2 was evaluated by qRT-PCR. Podocytes treated with TET2 Lv and scramble Lv were collected at 72 h $^{**}p < 0.01$. **(C)** Efficacy of the Lv targeting TET2 was assessed by western

(*Continued*)

FIGURE 7 (Continued)
blot. **(D)** Relative protein level was calculated by the band intensity against GAPDH, respectively. ****$p < 0.0001$. **(E)** Podocyte permeability was measured using FITC-labeled bovine serum albumin in a transwell chamber. *$p < 0.05$. **(F)** Expression of ZO-1 was detected after knocking down of *TET2*. Lv targeting TET2 and scramble Lv were transfected into the podocytes, respectively. After 72 h of transfection, podocytes were treated with PAN (50 μg/mL) and TP (5 nM). Cells were collected for western blotting analyses after 48 h of incubation. **(G)** Relative protein level was calculated by the band intensity against GAPDH, respectively. ****$p < 0.0001$.

FIGURE 8
Knockdown *TET2* affected the methylation level of ZO-1. **(A)** Agarose gel electrophoresis images of ZO-1 promoter amplified by polymerase chain reaction of methylated DNA obtained by MeDIP. **(B)** Agarose gel electrophoresis images of ZO-1 promoter amplified by polymerase chain reaction of hydroxymethylated DNA obtained by hMeDIP. The input DNA was used as the control for equal loading.

TP upregulates the expression of ZO-1 through TET2

In order to determine the role of TET2 in ZO-1 expression and methylation, we knocked down *TET2* using a lentivirus-mediated shRNA prior to TP intervention. After 72 h of infection, most podocytes strongly expressed GFP, indicating strong infectivity of the Lv (Figure 7A). qRT-PCR results showed the mRNA expression of TET2 in the TET2 Lv treatment group decreased by approximately 67.57% compared to that in the control group (Figure 7B). Western blot results also revealed that TET2 was significantly inhibited after Lv treatment (Figures 7C, D). The podocyte permeability increased significantly in the *TET2* knockdown group compared with the scrambled Lv group (Figure 7E). Moreover, the expression of ZO-1 was decreased significantly in the *TET2* knockdown group compared with the scrambled Lv group, even after treatment with TP (Figures 7F, G). Meanwhile, compared with the control group, increased promoter methylation of ZO-1 was observed in the *TET2* knockdown group (Figure 8A), accompanied by decreased ZO-1 hydroxymethylation (Figure 8B). Altogether, these results indicate TP may upregulate the expression of ZO-1 through TET2-mediated 5 mC demethylation.

Discussion

Growing evidence shows that TP has a strong antiproteinuric effect through multiple mechanisms. Notably, the current studies on TP intervention in podocyte injury at home and abroad mainly focus on the changes in the podocyte phenotypic molecules and the related signaling pathways. Few studies have considered the perspective of epigenetics. This study explored the relationship between TP, TET2, and ZO-1 from the novel perspective of epigenetics.

ZO-1 is a tight junction protein which plays an essential role in maintaining the integrity of the podocyte filtration barrier [18–20]. Previous studies have demonstrated that podocyte-specific depletion of ZO-1 leads to damage to SD integrity, thus causing proteinuria [18]. Besides, ZO-1 can not only regulate the stability of the SD protein nephrin but can also regulate cytoskeleton organization by binding to F-actin [20–22]. Therefore, clarification of the regulation mechanism of ZO-1 holds considerable clinical importance.

TET proteins mediate DNA demethylation by converting 5-methylcytosine (5 mC) to 5-hydroxymethylcytosine (5 hmC). We have previously shown that TET1–3 have a differential expression pattern in the podocytes, with relatively high expression of TET2 and low expression of TET1 and TET3 [23]. Other studies have also confirmed the expression of TET2 and TET3 is higher than that of TET1 in the kidney [24]. Furthermore, we found TET2 was downregulated in the TGF-β1-induced podocyte injury model, and TP could reverse podocyte EMT by TET2-mediated podocyte SD gene demethylation. TET2 was consistently demonstrated to play an important role in both cisplatin-induced and ischemia reperfusion-induced acute kidney injury [24–26]. These findings studies suggest that TET2 plays an important role in the pathophysiological processes in the kidney.

In this study, multi-level experiments showed a correlation between TET2 and ZO-1 expression. Firstly, TET2 expression synchronized with ZO-1 expression in the PAN-induced podocyte injury model and TP intervention group. Secondly, three predicted CpG islands were found in the promoter of ZO-1 using MethPrimer online analysis software. Treatment with 5-AzaC and RG108 upregulated ZO-1 expression compared with the

PAN-induced group. Thirdly, increased ZO-1 promoter methylation level, decreased ZO-1 expression level, and increased podocyte permeability were found in the *TET2* knockdown group compared with the scrambled Lv group, even after treatment with TP. All these findings indicate that TET2-mediated ZO-1 promoter demethylation reverses podocyte injury.

Currently, there are conflicting reports on the toxicity and therapeutic effects of TP on the kidney [10, 27, 28]. TP showed renoprotection effects against metronidazole-induced injury in zebrafish, puromycin-induced nephropathy, PM 2.5-induced podocyte injury, and deoxycorticosterone acetate-salt hypertension-induced renal injury in mice subjected to uninephrectomy [13, 29, 30]. In contrast, TP was also shown to exert nephrotoxicity in normal BALB/c mice and renal tubular epithelial cell lines NRK-52E and HK-2 [31–33]. Besides, Lixin Sun *et al.* found that TP-induced nephrotoxicity in rats leads to changes in the barrier and permeability of the proximal tubular epithelium by altered localization of ZO-1 [32]. Similarly, Huang Shan *et al.* demonstrated that TP caused decreased expression and abnormal subcellular localization of ZO-1 in a TP-induced cholestasis model [34]. In contrast, our study provides evidence that TP has a protective effect on PAN-induced podocyte injury through the upregulation of ZO-1 expression and decreased podocyte permeability. These contradictory effects may be attributed to various factors, including the dosage of TP and differences among the experimental subjects. Research on TP nephrotoxicity mostly focuses on normal cells, while its protective effect is mostly investigated in damaged cells. Taken together, these results indicate that TP is a double-edged sword, and only its correct and standardized use can avoid the side effects.

The limitation of our study is that we mainly focused on the cellular level to explore the epigenetic regulation of podocyte tight junction protein ZO-1 by of TP. We plan to use a CKD-related animal model to reveal the exact molecular mechanism and provide more *in vivo* evidence in the future.

In summary, the present study shows that TP can reverse ZO-1 expression by regulating TET2-mediated DNA demethylation. TET2 could be a promising target for developing a treatment strategy for podocyte injury. Our observations may also provide new ideas for further studies on the mechanism underlying the therapeutic effect of TP on CKD.

Author contributions

FW contributed to the conception and design of the study. Y-WT conducted cell culture, performed MeDIP and hMeDIP, and drafted the manuscript. M-YJ conducted qRT-PCR, western blotting and immunofluorescence. J-WC participated in DNA isolation and data analyses. All authors contributed to the article and approved the submitted version.

Data availability

The original contributions presented in the study are included in the article/supplementary material, further inquiries can be directed to the corresponding author.

Funding

The author(s) declare that financial support was received for the research, authorship, and/or publication of this article. This work was supported by grants from the Zhejiang Province Medical and Health Technology Plan Project (2024KY1375) and the National Natural Science Foundation of China (81803911).

Conflict of interest

The authors declare that the research was conducted in the absence of any commercial or financial relationships that could be construed as a potential conflict of interest.

References

1. Kovesdy CP. Epidemiology of chronic kidney disease: an update 2022. *Kidney Int Supplements* (2022) **12**:7–11. doi:10.1016/j.kisu.2021.11.003

2. Sharma S, Smyth B. From proteinuria to fibrosis: an update on pathophysiology and treatment options. *Kidney Blood Press Res* (2021) **46**:411–20. doi:10.1159/000516911

3. Lu CC, Wang GH, Lu J, Chen PP, Zhang Y, Hu ZB, et al. Role of podocyte injury in glomerulosclerosis. *Adv Exp Med Biol* (2019) **1165**:195–232. doi:10.1007/978-981-13-8871-2_10

4. Mo H, Ren Q, Song D, Xu B, Zhou D, Hong X, et al. CXCR4 induces podocyte injury and proteinuria by activating β-catenin signaling. *Theranostics* (2022) **12**:767–81. doi:10.7150/thno.65948

5. Stevenson BR, Siliciano JD, Mooseker MS, Goodenough DA. Identification of ZO-1: a high molecular weight polypeptide associated with the tight junction (zonula occludens) in a variety of epithelia. *J Cel Biol* (1986) **103**:755–66. doi:10.1083/jcb.103.3.755

6. Fanning AS, Van Itallie CM, Anderson JM. Zonula occludens-1 and -2 regulate apical cell structure and the zonula adherens cytoskeleton in polarized epithelia. *Mol Biol Cel* (2012) **23**:577–90. doi:10.1091/mbc.e11-09-0791

7. Kuo WT, Odenwald MA, Turner JR, Zuo L. Tight junction proteins occludin and ZO-1 as regulators of epithelial proliferation and survival. *Ann N.Y Acad Sci* (2022) **1514**:21–33. doi:10.1111/nyas.14798

8. Ha TS, Park HY, Seong SB, Ahn HY. Puromycin aminonucleoside increases podocyte permeability by modulating ZO-1 in an oxidative stress-dependent manner. *Exp Cel Res* (2016) **340**:139–49. doi:10.1016/j.yexcr.2015.12.001

9. Rincon-Choles H, Vasylyeva TL, Pergola PE, Bhandari B, Bhandari K, Zhang JH, et al. ZO-1 expression and phosphorylation in diabetic nephropathy. *Diabetes* (2006) **55**:894–900. doi:10.2337/diabetes.55.04.06.db05-0355

10. Jiang S, Wan F, Lian H, Lu Z, Li X, Cao D, et al. Friend or foe? The dual role of triptolide in the liver, kidney, and heart. *Biomed Pharmacother* (2023) **161**:114470. doi:10.1016/j.biopha.2023.114470

11. Ma R, Liu L, Liu X, Wang Y, Jiang W, Xu L. Triptolide markedly attenuates albuminuria and podocyte injury in an animal model of diabetic nephropathy. *Exp Ther Med* (2013) **6**:649–56. doi:10.3892/etm.2013.1226

12. Ren L, Wan R, Chen Z, Huo L, Zhu M, Yang Y, et al. Triptolide alleviates podocyte epithelial-mesenchymal transition via kindlin-2 and EMT-related TGF-β/smad signaling pathway in diabetic kidney disease. *Appl Biochem Biotechnol* (2022) **194**:1000–12. doi:10.1007/s12010-021-03661-2

13. Wang L, Zhang L, Hou Q, Zhu X, Chen Z, Liu Z. Triptolide attenuates proteinuria and podocyte apoptosis via inhibition of NF-κB/GADD45B. *Sci Rep* (2018) **8**:10843. doi:10.1038/s41598-018-29203-1

14. Zheng CX, Chen ZH, Zeng CH, Qin WS, Li LS, Liu ZH. Triptolide protects podocytes from puromycin aminonucleoside induced injury *in vivo* and *in vitro*. *Kidney Int* (2008) **74**:596–612. doi:10.1038/ki.2008.203

15. Dey M, Baldys A, Sumter DB, Göoz P, Luttrell LM, Raymond JR, et al. Bradykinin decreases podocyte permeability through ADAM17-dependent epidermal growth factor receptor activation and zonula occludens-1 rearrangement. *J Pharmacol Exp Ther* (2010) **334**:775–83. doi:10.1124/jpet.110.168054

16. Guan N, Ding J, Deng J, Zhang J, Yang J. Key molecular events in puromycin aminonucleoside nephrosis rats. *Pathol Int* (2004) **54**:703–11. doi:10.1111/j.1440-1827.2004.01683.x

17. Joshi K, Liu S, Breslin Sj P, Zhang J. Mechanisms that regulate the activities of TET proteins. *Cell Mol Life Sci* (2022) **79**:363. doi:10.1007/s00018-022-04396-x

18. Itoh M, Nakadate K, Horibata Y, Matsusaka T, Xu J, Hunziker W, et al. The structural and functional organization of the podocyte filtration slits is regulated by Tjp1/ZO-1. *PLoS One* (2014) **9**:e106621. doi:10.1371/journal.pone.0106621

19. Itoh M, Nakadate K, Matsusaka T, Hunziker W, Sugimoto H. Effects of the differential expression of ZO-1 and ZO-2 on podocyte structure and function. *Genes to Cells* (2018) **23**:546–56. doi:10.1111/gtc.12598

20. Itoh M, Nagafuchi A, Moroi S, Tsukita S. Involvement of ZO-1 in cadherin-based cell adhesion through its direct binding to α catenin and actin filaments. *J Cel Biol* (1997) **138**:181–92. doi:10.1083/jcb.138.1.181

21. Odenwald MA, Choi W, Buckley A, Shashikanth N, Joseph NE, Wang Y, et al. ZO-1 interactions with F-actin and occludin direct epithelial polarization and single lumen specification in 3D culture. *J Cel Sci* (2017) **130**:243–59. doi:10.1242/jcs.188185

22. Fanning AS, Jameson BJ, Jesaitis LA, Anderson JM. The tight junction protein ZO-1 establishes a link between the transmembrane protein occludin and the actin cytoskeleton. *J Biol Chem* (1998) **273**:29745–53. doi:10.1074/jbc.273.45.29745

23. Wan F, Tang YW, Tang XL, Li YY, Yang RC. TET2 mediated demethylation is involved in the protective effect of triptolide on podocytes. *Am J Transl Res* (2021) **13**:1233–44.

24. Yan H, Tan L, Liu Y, Huang N, Cang J, Wang H. Ten-eleven translocation methyl-cytosine dioxygenase 2 deficiency exacerbates renal ischemia-reperfusion injury. *Clin Epigenetics* (2020) **12**:98. doi:10.1186/s13148-020-00892-8

25. Bao Y, Bai M, Zhu H, Yuan Y, Wang Y, Zhang Y, et al. DNA demethylase Tet2 suppresses cisplatin-induced acute kidney injury. *Cell Death Discov* (2021) **7**:167. doi:10.1038/s41420-021-00528-7

26. Huang N, Tan L, Xue Z, Cang J, Wang H. Reduction of DNA hydroxymethylation in the mouse kidney insulted by ischemia reperfusion. *Biochem Biophysical Res Commun* (2012) **422**:697–702. doi:10.1016/j.bbrc.2012.05.061

27. Song J, He GN, Dai L. A comprehensive review on celastrol, triptolide and triptonide: insights on their pharmacological activity, toxicity, combination therapy, new dosage form and novel drug delivery routes. *Biomed Pharmacother* (2023) **162**:114705. doi:10.1016/j.biopha.2023.114705

28. Cui D, Xu D, Yue S, Yan C, Liu W, Fu R, et al. Recent advances in the pharmacological applications and liver toxicity of triptolide. *Chemico-Biological Interactions* (2023) **382**:110651. doi:10.1016/j.cbi.2023.110651

29. Lv C, Cheng T, Zhang B, Sun K, Lu K. Triptolide protects against podocyte injury in diabetic nephropathy by activating the Nrf2/HO-1 pathway and inhibiting the NLRP3 inflammasome pathway. *Ren Fail* (2023) **45**:2165103. doi:10.1080/0886022x.2023.2165103

30. Zhang J, Zhu M, Zhang S, Xie S, Gao Y, Wang Y. Triptolide attenuates renal damage by limiting inflammatory responses in DOCA-salt hypertension. *Int Immunopharmacology* (2020) **89**:107035. doi:10.1016/j.intimp.2020.107035

31. Pan J, Shen F, Tian K, Wang M, Xi Y, Li J, et al. Triptolide induces oxidative damage in NRK-52E cells through facilitating Nrf2 degradation by ubiquitination via the GSK-3β/Fyn pathway. *Toxicol Vitro* (2019) **58**:187–94. doi:10.1016/j.tiv.2019.03.032

32. Sun L, Li H, Huang X, Wang T, Zhang S, Yang J, et al. Triptolide alters barrier function in renal proximal tubular cells in rats. *Toxicol Lett* (2013) **223**:96–102. doi:10.1016/j.toxlet.2013.08.014

33. Lu J, Zhang Y, Dong H, Sun J, Zhu L, Liu P, et al. New mechanism of nephrotoxicity of triptolide: oxidative stress promotes cGAS-STING signaling pathway. *Free Radic Biol Med* (2022) **188**:26–34. doi:10.1016/j.freeradbiomed.2022.06.009

34. Huang S, Liu L, Mei HF, Zhang QW, Zhang X, Xu XT, et al. Altered integrity of hepatocyte tight junctions in rats with triptolide-induced cholestasis. *Chin J Nat Medicines* (2021) **19**:188–94. doi:10.1016/s1875-5364(21)60020-1

EBM Experimental Biology and Medicine

TYPE Review
PUBLISHED 27 June 2024
DOI 10.3389/ebm.2024.10142

OPEN ACCESS

*CORRESPONDENCE
Yu-Chi Liu,
liuchiy@gmail.com

RECEIVED 10 February 2024
ACCEPTED 12 June 2024
PUBLISHED 27 June 2024

CITATION
Chow BJ, Lee IXY, Liu C and Liu Y-C (2024), Potential therapeutic effects of peroxisome proliferator-activated receptors on corneal diseases. *Exp. Biol. Med.* 249:10142. doi: 10.3389/ebm.2024.10142

Potential therapeutic effects of peroxisome proliferator-activated receptors on corneal diseases

Bing Jie Chow[1], Isabelle Xin Yu Lee[2], Chang Liu[2] and Yu-Chi Liu[2,3,4]*

[1]Barts and the London School of Medicine and Dentistry, Queen Mary University of London, London, United Kingdom, [2]Tissue Engineering and Cell Therapy Group, Singapore Eye Research Institute, Singapore, Singapore, [3]Department of Cornea and External Eye Disease, Singapore National Eye Centre, Singapore, Singapore, [4]Ophthalmology and Visual Sciences Academic Clinical Program, Duke-National University of Singapore (NUS) Medical School, Singapore, Singapore

Abstract

The cornea is an avascular tissue in the eye that has multiple functions in the eye to maintain clear vision which can significantly impair one's vision when subjected to damage. Peroxisome proliferator-activated receptors (PPARs), a family of nuclear receptor proteins comprising three different peroxisome proliferator-activated receptor (PPAR) isoforms, namely, PPAR alpha (α), PPAR gamma (γ), and PPAR delta (δ), have emerged as potential therapeutic targets for treating corneal diseases. In this review, we summarised the current literature on the therapeutic effects of PPAR agents on corneal diseases. We discussed the role of PPARs in the modulation of corneal wound healing, suppression of corneal inflammation, neovascularisation, fibrosis, stimulation of corneal nerve regeneration, and amelioration of dry eye by inhibiting oxidative stress within the cornea. We also discussed the underlying mechanisms of these therapeutic effects. Future clinical trials are warranted to further attest to the clinical therapeutic efficacy.

KEYWORDS

cornea, proliferator-activated receptors, neovascularisation, wound healing, inflammation, fibrosis, nerve regeneration

Impact statement

The cornea constitutes a vital element of the ocular structure which exerts a profound impact on vision when compromised. The application of peroxisome proliferator-activated receptor (PPAR) agents has been widely documented particularly in the treatment of metabolic conditions such as hyperlipidemia and diabetes. Yet, their therapeutic potential in the context of corneal diseases remains not well-understood. This review article summarises the reported therapeutic effects of PPAR agents in the management of corneal inflammation, neovascularisation, wound healing, fibrosis, nerve

regeneration, and dry eye. With further clinical validation, PPAR agents may serve as a new avenue in the treatment of a variety of corneal diseases.

The cornea

The cornea is an avascular tissue that sits at the anterior-most surface of the eye. It comprises both cellular and acellular components; the former includes epithelial cells, keratocytes, and endothelial cells, and the latter includes mainly collagen and glycosaminoglycans.

Functionally, the cornea fulfills several crucial roles, including protecting ocular integrity, preserving optical clarity, and providing refractive power to the eye. The cornea provides a protective barrier against the environment, facilitated by the intercellular junctions within its epithelium and the continuous regeneration of the corneal epithelial cells [1, 2]. Consequently, damage to the cornea through trauma renders it compromised, which in turn triggers a corneal wound healing response consisting of inflammatory and fibrotic reactions. Excessive corneal wound healing responses lead to corneal scarring and opacification, profoundly impacting vision. The World Health Organization stated that cornea opacity is a priority eye disease and is one of the main causes of low vision and visual impairment, affecting 146 million people worldwide with an increase of 1.5–2.0 million new cases every year [3, 4]. This underscores the importance of corneal wound healing process, emphasizing a need to develop more efficacious interventions to accelerate this restorative process.

The cornea is also the most densely innervated tissue in our body, richly supplied by sensory and autonomic nerve fibres [5]. Corneal nerves sustain corneal health and homeostasis by facilitating tear secretion and providing trophic support to epithelial and stromal cells [6, 7]. In conditions such as diabetic keratopathy or corneal surgery, corneal nerve degeneration manifests, causing decreased corneal sensitivity and increased vulnerability to corneal ulceration [8, 9]. Therefore, interventions targeting corneal nerve regeneration constitute a pivotal approach to enhancing cornea health.

Researchers have previously explored potential therapeutic agents aimed at these fundamental aspects of corneal health. In this review, we explore a promising therapeutic avenue, namely, the peroxisome proliferator-activated receptor family, on corneal diseases.

The expression of PPARs in eyes

The PPARs are a group of transcription factors belonging to the nuclear hormone receptor family [10]. The PPAR family comprises three isotypes: PPAR alpha (α), PPAR gamma (γ), and PPAR delta (δ), each exhibiting distinct tissue expression patterns and involved in the regulation of diverse biological functions [11]. At the molecular level, while the PPAR isoforms exhibit a sequence identity of 60%–70% within their ligand-binding domains (LBDs), significant variations in the overall pocket size of the three-dimensional structures of these LBDs exist, leading to distinctive binding affinities of each PPAR isoform with specific compounds [12]. The discovery of PPAR's mechanism as a distinct transcription factor capable of targeted activation by peroxisome proliferators for potential therapeutic application, by Issemann and Green in 1990, paved the groundwork for further research into PPAR [13]. Since then, prior research has firmly established the role of PPARs as modulators of adipocyte differentiation, glucose and lipid metabolism, and inflammation [11, 13, 14]. Within the eye, all 3 PPAR isoforms exhibit distinct localisation patterns within ocular structures [15]. Specifically, PPARα and PPARγ are found in the cornea, conjunctiva, retina, meibomian, and lacrimal glands, whereas PPARδ is expressed in the cornea, retina, and lacrimal glands, all demonstrating varied levels of expression across various tissue types [15, 16]. Beyond the eye, PPARα is localised in the kidneys, liver, muscle, and heart; PPARδ displays ubiquitously across numerous organs and tissues, while PPARγ is found in adipocytes and small intestines [17, 18]. Clinically, they are routinely used as therapeutic agents such as fenofibrate, a PPARα agonist, for hyperlipidaemia, as well as pioglitazone, a PPARγ agonist for diabetes [19, 20].

All 3 PPAR isoforms have been reported to exhibit expression within the retina, each with differing functions. PPARα has been reported to possess protective and anti-inflammatory effects in the retina across several studies [21–24]. A study reported the PPARα's anti-apoptotic properties in retinal ischaemia [21], whilst another demonstrated anti-oxidative and anti-angiogenic effects of PPARα in age-related macular degeneration [22]. In a similar vein, PPARα has illustrated their anti-inflammatory role in treating diabetic retinopathy and experimental autoimmune uveoretinitis [23, 24]. PPARγ has been reported to exhibit neuroprotective effects on retinal ganglion cells, preventing retinal dysfunction following optic nerve crush [25]. The existing therapeutic options to address corneal pathological processes remains limited. Within corneal inflammation, topical corticosteroid or non-steroidal anti-inflammatory drugs (NSAIDs) serve as the main agents for treatment. However, both anti-inflammatory treatment options are accompanied by significant adverse side-effects, including increased intraocular pressure, cataract formation due to corticosteroid use [26], and NSAID-induced corneal melting [27]. The current treatment options of steroids or mitomycin C for corneal fibrosis also present with limitations with particular concerns pertaining to long-term drug safety profile [28]. Lastly, recombinant nerve growth factor (NGF) emerges as the singular drug approved by the Food and Drug Administration (FDA) to treat neurotrophic keratopathy. However, this treatment option

remains costly and dictates the need for frequent topical administration [29]. Given that inflammation and angiogenesis are closely associated with corneal scar tissue formation, the various therapeutic effects of PPAR agents, positions them as promising therapeutic candidates for corneal diseases. Additionally, several PPAR agents such as fenofibrate and rosiglitazone are existing drugs widely used in the treatment of metabolic diseases, offering the advantages of drug repurposing in contrast to *de novo* drug discovery. This includes reduced developmental time and costs, alongside well-established pharmacokinetic considerations [30]. In this review, we focus on the therapeutic potential and underlying work of action of the different PPAR isoforms on corneal diseases, including corneal wound healing, corneal inflammation, fibrosis, neovascularisation, corneal nerve regeneration, and dry eye disease.

PPARs on corneal wound healing

Corneal wound healing is a complex process driven by local molecular factors and endogenous soluble factors. It is a widely accepted notion that transforming growth factor-beta (TGF-β) and tumour necrosis factor alpha (TNF-α) play pivotal roles in regulating cellular responses during wound healing [31, 32]. Previous studies examined the 3 PPAR isoforms in relation to corneal wound healing, uncovering mechanisms that accelerate the process.

PPARα's involvement in corneal wound healing has been recently elucidated through its role in regulating corneal cell metabolism [33]. *In vitro* studies have revealed that mitochondrial oxidative phosphorylation is a primary source of adenosine triphosphate (ATP) production for human corneal epithelial cells. Significantly reduced mitochondria metabolism and subsequently, impaired corneal healing process in PPARα knockout mice, compared to wild-type mice, were found, suggesting the role of PPARα as a key regulator of mitochondrial metabolism and corneal wound healing. In addition, PPARα expression was downregulated in diabetic human corneas compared to non-diabetic groups, reinforcing the role of PPARα in mitochondria metabolism and corneal healing in light of well-documented delayed wound healing observed in diabetic corneas. Administration of fenofibrate, a PPARα agonist, ameliorated mitochondrial dysfunction and enhanced corneal wound healing in diabetic mice and humans, further underscoring the role of PPARα in corneal wound healing [33].

Regarding the role of PPARγ in corneal wound healing, *in-vitro* epithelial cell proliferation was significantly accelerated following adenoviral gene transfer of PPARγ [34]. Additionally, PPARγ effectively preserved the corneal epithelial basement membrane in the alkali-burned corneas subjected to adenoviral gene transfer. Expression of matrix metalloproteinase-2 (MMP-2) and TGF-β within the corneal epithelium was significantly suppressed by PPARγ gene transfer using real-time RT-PCR [34]. Given the TGF-β's inhibitory role in epithelial cell growth and MMP's role in extracellular matrix degradation, this indicates PPARγ's participation in corneal wound healing.

PPARδ has also been shown to promote corneal healing via facilitating proliferative capacity in rat alkali burn models [35]. This was evidenced by significantly increased Ki67-positive cells and Ki67 mRNA expression following four topical administration of 0.05% GW50516 solution, a PPARδ agonist [35]. Compensatory elevation of PPARδ expression during corneal wound healing in both animal and human corneal models was reported, and topical administration of PPARδ agonist further inhibited corneal epithelial cell death, thereby facilitating corneal wound healing [36].

PPARs on corneal inflammation

PPARα's involvement in corneal inflammation has been explored by assessing the anti-inflammatory effects in rat corneal chemical injury models [37, 38]. Significant suppression of inflammatory cell infiltration was observed in the cornea following alkali burn after the instillation of 0.05% fenofibrate twice daily for 14 days, in comparison to the vehicle group [38]. Western blotting also demonstrated a significantly reduced expression of nuclear factor-kappa B (NF-κB), a key transcription factor in inflammation, in the PPARα group versus the vehicle group [38].

Similarly, another study investigating the anti-inflammatory effects of fenofibrate following rat corneal alkali injury demonstrated a reduction in corneal inflammatory processes [37]. This was evidenced by significantly reduced mRNA expression of proinflammatory cytokines and chemokines such as interleukin-1 (IL-1), IL-6, IL-8 and monocyte chemoattractant protein-1 (MCP-1) [37]. Following corneal chemical injury, staining with a PPARα antibody highlighted the primary localisation of PPARα-positive cells within the regenerating epithelial basement cell, indicating the vital role of PPARα in inflammatory responses [37].

PPARγ was also explored for its potential corneal anti-inflammatory effects [39]. Similar to the effects observed with PPARα, topical application of PPARγ agonist, specifically pioglitazone hydrochloride, significantly decreased neutrophilic and macrophage infiltration after alkali-burn injury in rats, whilst significantly increasing anti-inflammatory M2 macrophages. Further real-time reverse transcription polymerase chain reaction (RT-PCR) analysis revealed the suppression of IL-1, IL-6, IL-8, TGF-β1, and MCP-1 in corneas [39]. Similarly, in another study using an alkali injury model, a significant reduction in TNF-α mRNA expression and upregulation of M2 macrophage

polarisation upon PPARγ agonist treatment were observed, enhancing the role of PPARγ in the context of corneal inflammation [40].

Topical application of a synthetic PPARδ-specific agonist, GW5015116, twice daily for 7 days, also significantly inhibited neutrophil and macrophage infiltration in rat corneal alkali burn models. Significantly lower expression levels of NF-Kb and inflammatory cytokines were also observed in the PPARδ group compared to the vehicle group on the real-time RT-PCR analysis [41].

The anti-inflammatory effects of the PPAR agonists within the cornea have been postulated to be orchestrated through several pathways. Western blotting analyses indicate that the interference of the PPAR isoforms with activity of key proinflammatory transcription factors such as NF-kB pathway, which may underlie the significantly decreased immune cell infiltration observed in the cornea across these studies. This is in line with previous studies which has shown that the attenuation of NF-kB activity by PPARα agents may be achieved through the maintenance of a negative regulator, nuclear expression of the kappa light polypeptide gene enhancer in the B cell inhibitor, alpha (I_kB-α), which plays a role in inhibiting NF-kB activation [42]. Additionally, PPAR agonists may exert immunomodulatory effects in corneal inflammation by enhancing monocyte differentiation to M2 macrophages. In the context of macrophage-driven inflammation, M1 macrophages are distinguished as tissue injury-type macrophages which serve as potent effector cells that kill microorganisms and produce pro-inflammatory cytokines such as IL-6 and TNF-α, inducing inflammation [43]. Conversely, M2 macrophages function to dampen inflammation through the production of anti-inflammatory factors, promoting tissue remodelling and repair [44]. The decrease in pro-inflammatory cytokines like MCP-1 may additionally contribute to the reduced immune cell infiltration, given its crucial role in promoting immune cell infiltration [45]. Thus, the observed reduction in pro-inflammatory cytokine expression in these studies may be ascribed to the immunomodulatory effects of PPAR agonists during corneal inflammation.

Suppression of corneal fibrosis of PPARs

Corneal fibrosis arises from abnormalities in corneal wound healing, characterised by excessive production of aberrant extracellular matrix (ECM) proteins and corneal crystalline enzymes by myofibroblasts. Whilst corneal fibrogenesis acts to restore corneal integrity following injury, excessive wound remodeling causes corneal scars, resulting in visual impairment or blindness [46]. In corneal fibrogenesis, TGF-β1 is a key cytokine responsible for promoting keratocyte differentiation into active myofibroblasts [47, 48]. The profibrotic properties of TGF-β1 are achieved through multiple intracellular signaling pathways such as Smad, p38 mitogen-activated protein kinase (MAPK), and extracellular signal-regulated kinase (Erk) [49, 50]. Given the established anti-fibrotic properties of PPARγ in the lungs and kidneys [51, 52], corneal studies have explored the possible role of PPARγ in alleviating corneal scarring [53–56].

Instillations of pioglitazone, a PPARγ agonist, demonstrated a significant inhibitory effect on corneal fibroblast migration, conducted on cultured corneal fibroblasts using scrape-wound assays [53]. It also led to a significant reduction in corneal lattice contraction, as illustrated by significantly greater lattice diameters in corneal fibroblasts seeded in free-floating collagen gels. Significant decreases in matrix metalloproteinase-2 (MMP-2) and MMP-9 secretion, alongside significantly reduced collagen I and fibronectin protein synthesis, demonstrated in western blotting, were also observed.

Moreover, PPARγ downregulated the expression of TGF-β1-induced connective tissue growth factor (CTGF), which is a major autocrine growth factor enhancing TGF-β1's pro-fibrogenic role in myofibroblast differentiation [54]. This highlights PPARγ's anti-fibrotic effect on corneal fibroblasts by inhibiting crucial components in developing corneal scarring. PPARγ is involved in two distinct profibrotic signaling pathways, specifically in the p38 MAPK and Smad signalling pathways. Within the p38 MAPK signalling pathway, PPARγ ligands, including troglitazone, rosiglitazone, and 15d-PGJ2, significantly reduced the levels of phosphorylated p38 MAPK in a dose-dependent manner [55]. Addition of PPARγ ligands down-regulated β-catenin expression—a component of p38 MAPK signalling by blocking the TGF-β1-induced p38 MAPK phosphorylation. The involvement of β-catenin acts as a downstream mediator of p38 MAPK signalling, significantly enhancing α-SMA production in western blot analysis [56].

PPARγ's anti-fibrotic action in the TGF-β1-induced Smad signalling has been demonstrated through the application of lobeglitazone, a PPARγ agonist, in a combination of type I collagen and corneal fibroblast isolated from the human stroma. Notably, western blot analysis of Smad2/3 and P-Smad2, key proteins in the Smad signalling pathway, indicated a significant inhibition in Smad signalling and myofibroblast differentiation [57].

The application of PPARs for corneal nerve regeneration

Degeneration of corneal nerves can occur in conditions such as diabetic keratopathy, which is a common microvascular complication of diabetes. This arises from the accumulation of advanced glycation end products and the generation of reactive

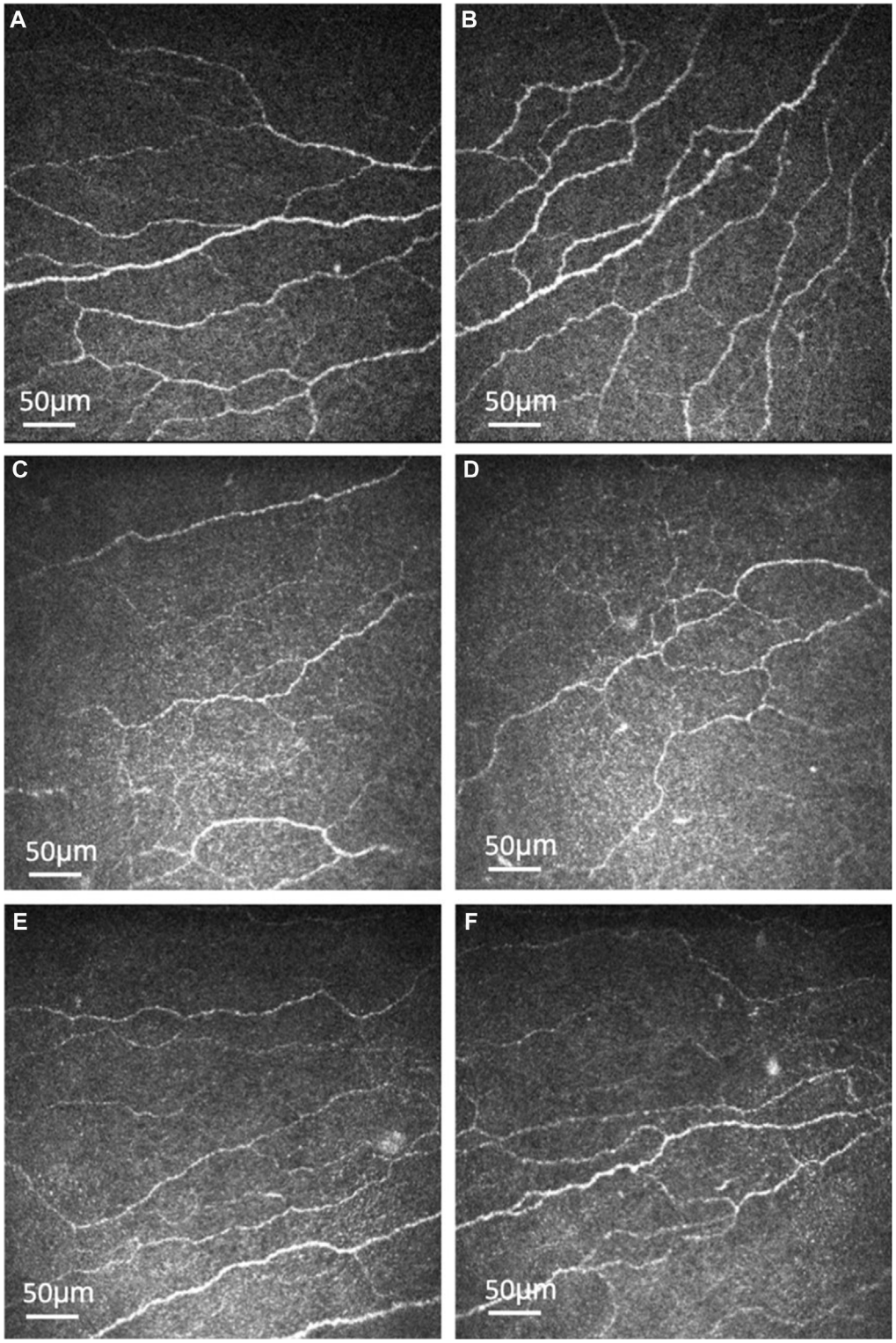

FIGURE 1
Representative corneal subbasal nerve images of healthy controls and type 2 diabetic patients before and after oral fenofibrate treatment. Corneal subbasal nerve of healthy controls **(A, B)**. Corneal subbasal nerve before **(C**, **D)** and after **(E**, **F)** oral fenofibrate treatment, demonstrating an increase in nerve fiber density (9.25 $\pm$ *4.24* vs. 18.99 $\pm$ 8.49 n/mm^2) and corneal nerve fiber width (0.0215 $\pm$ 0.0002 vs. 0.0224 $\pm$ 0.0005 μm^2/mm^2) after treatment.

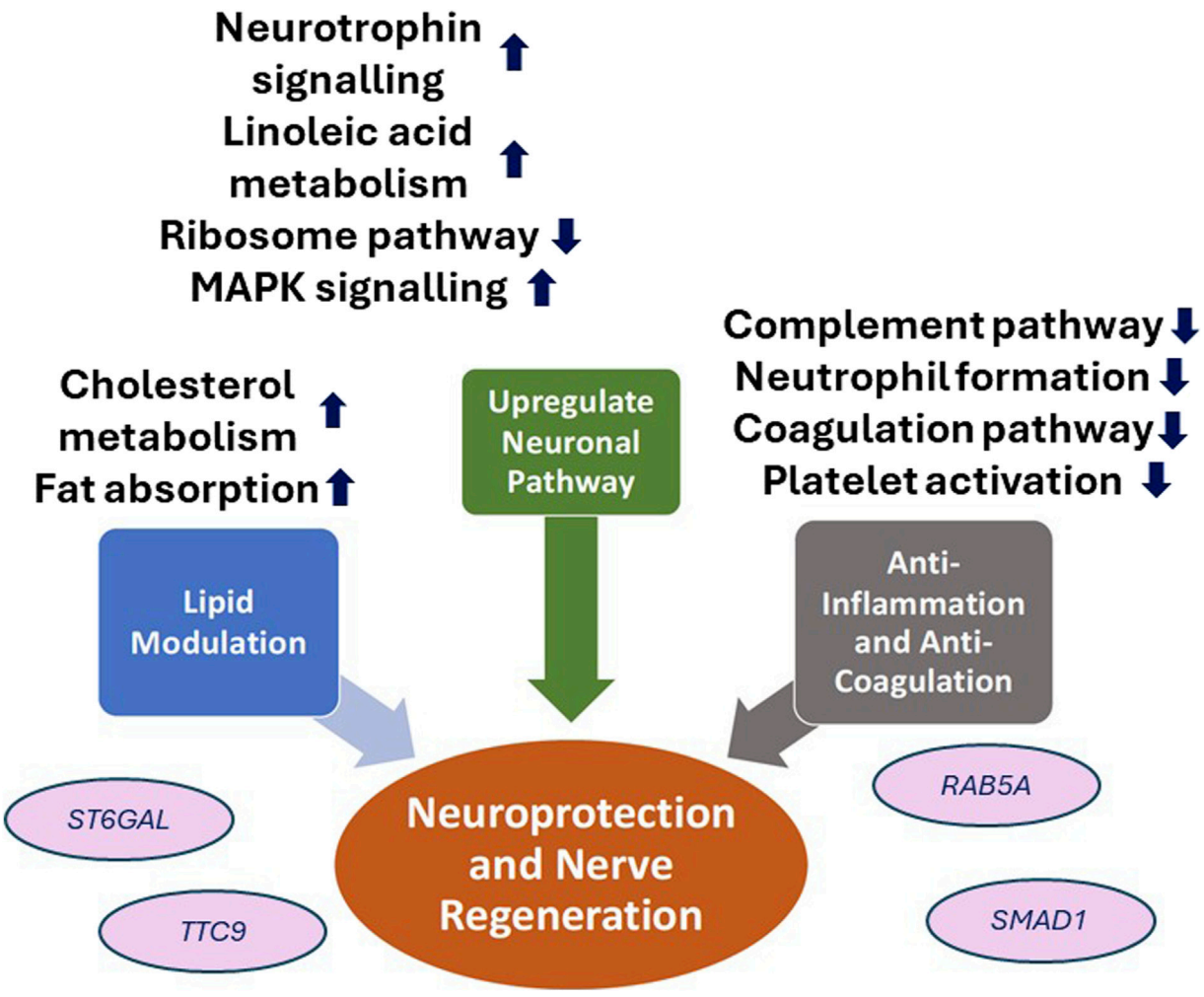

FIGURE 2
Schematic diagram of the neuroprotective effects of PPARα agent, fenofibrate, in diabetic corneal neuropathy. ST6GAL1, Beta-galactoside alpha-2,6-sialytransferase 1; TTC9, Tetratricopeptide repeat protein 9A; RAB5A, ras-related protein; SMAD1, Suppressor of mothers against decapentaplegic homolog 1.

oxygen species (ROS) [58], triggered by prolonged hyperglycaemia, which reduces microvascular supply to Schwann cells and neurons through increased oxidative stress and inflammation impacting the capillaries [59]. As hyperlipidemia is a known risk factor for diabetic neuropathy [8], PPARα has been explored for its potential therapeutic effects in diabetic corneal neuropathy.

PPARα-knockout mice presented with significant decrease in corneal nerve fiber density (CNFD), as well as significantly decreased corneal sensitivity, compared to the wild-type mice [60], suggesting PPARα's supportive role in maintaining corneal nerve health. The protective role of PPARα agonist in diabetic corneal neuropathy further revealed that fenofibrate had a significantly positive effect in ameliorating corneal nerve degeneration in diabetic rat models. A restoration of PPARα expression in corneal epithelium and significantly increased CNFD were observed following treatment with chow containing 0.014% fenofibrate, a PPARα agonist, for 4 months [60]. Our group further demonstrated that topical fenofibrate eye drops enhanced the CNFD, corneal nerve fiber length, and ocular surface integrity, as well as suppressed the corneal neuroinflammation, in diabetic keratopathy [61].

More recently, our group published a clinical trial in which 30 patients with type 2 DM were treated with oral fenofibrate for 1 month. On *in vivo* confocal microscopy evaluation, there was significant stimulation of corneal nerve regeneration and a reduction in nerve oedema after oral fenofibrate treatment, as evidenced by significant improvement in CNFD and corneal nerve fiber width, respectively (Figure 1). There was also a significant improvement in the corneal epithelial cell

morphology in terms of cell circularity. More importantly, fenofibrate significantly improved patients' neuropathic ocular surface status by increasing tear breakup time along with a reduction of corneal and conjunctival punctate keratopathy. Amelioration of ocular surface neuroinflammatory status was also found, evidenced by a significant increase in tear substance P level. On the quantitative proteomic analysis, fenofibrate significantly upregulated and modulated the neurotrophin, MAPK signaling pathways and linoleic acid (LA) metabolism, which may account for the neurotrophic effects of fenofibrate clinically [62; 63]. In addition, the expression of proteins involved in the regulation of nervous system function such as beta-galactoside alpha-2,6-sialytransferase 1 (ST6GAL1), tetratricopeptide repeat protein 9A (TTC9), ras-related protein (RAB5A) and suppressor of mothers against decapentaplegic homolog 1 (SMAD1) were significantly increased post-treatment [63]. On the pathway analysis, we identified the following potential underlying therapeutic mechanisms in corneal nerve regeneration: 1) Upregulation of neuronal pathways 2) lipid modulation, 3) anti-inflammation and 4) anti-coagulation.

Fenofibrate demonstrated an upregulation of the neurotrophin, MAPK signaling pathway and linoleic acid metabolism which are crucial key players in neuroprotection. Neurotrophins are a class of growth factors that regulate neuronal development, survival, death and plasticity [6]. Within the cornea, neutrophins facilitates corneal nerve branching, maintenance of corneal nerve density, and promoting nerve regeneration [7]. Activation of MAPK has been demonstrated to mediate neurite outgrowth-promoting effects *in vitro* [64]. In addition, the metabolism of LA is highly important given its role of gamma LA production, an vital component of neuronal membrane phospholipid, as well as playing a role to preserve nervous blood flow to coordinate nerve regeneration [65]. Suppression of the ribosome family expression by fenofibrate may also account for its neuroprotective effects [63], particularly as axonal ribosomes are associated as a marker for diseased axons in neurogenerative conditions (Figure 2) [66].

The therapeutic effect of fenofibrate in corneal regeneration and peripheral nerve improvements may also be attributed to its well-established effect as an anti-hyperlipidaemic agent. Fenofibrate's antihyperlipidaemic effect is expressed through the stimulation of lipoprotein lipase activation, which promotes the synthesis of high-density lipoprotein (HDL) cholesterol and fatty acid oxidation pathway whilst conversely facilitating a rapid degradation of low-density lipoprotein (LDL) and triglycerides within tissues [67]. Given that hypertriglyceridemia, hyperlipidemia and decreased HDLc serve as significant risk factors for diabetic peripheral neuropathy, the lipid-modulating effects of fenofibrate may partly account for its neuroprotective impact in both peripheral neuropathy and corneal nerve regeneration. Other studies have also postulated that the peripheral neuroprotective role of PPARα agents is achieved through PPARα activation in satellite glial cells of dorsal root ganglia to stimulate axon regeneration and the activation of the PPAR-α-AMPK-PGC-1α pathway to ameliorate neuronal and endothelial damage [68–70]. This is also reinforced in the Fenofibrate Intervention and Event Lowering in Diabetes (FIELD) study which reported that fenofibrate significantly reduced microvascular complications such as diabetic neuropathy alongside a 37% risk reduction of amputation in T2DM patients [71].

The anti-inflammatory effect of fenofibrate through the suppression of NF-κB expression, as explored earlier, also plays a neuroprotective role through the reduction of neuroinflammation whilst promoting neurodevelopmental processes such as neurogenesis, neuritogenesis and axoneogenesis [40, 72–74]. Fenofibrate has also been reported to play a role in anti-coagulation by inhibiting complement and coagulation cascades alongside platelet activation pathways [63]. We contend that this results in knock-on effects on fenofibrate's neuroprotective effects given the significant association between low platelet time and platelecrit levels with decreased nerve conduction function and prevalence of neuropathy in T2DM patients [75].

PPARs on dry eye disease

Dry eye diseases have multifaceted origins and are characterised by a loss of homeostasis of the tear film [76]. These conditions are accompanied by ocular symptoms, including tear film instability, hyperosmolarity, ocular surface inflammation and damage, and neurosensory abnormalities [77, 78]. Dry eye conditions have been associated with oxidative stress [79], and diabetes given that the generation of oxidative stress is a core pathological mechanism of diabetes [80]. The pathogenic processes associated with oxidative stress encompass a disruption in the equilibrium between the oxidative and antioxidant systems, culminating in hindered neutralisation of oxygen free radicals [81]. The crucial role of PPARγ expression in the lacrimal and meibomian glands and dry eye has been explored in mouse models [16]. Qualitative PCR revealed that rats with dry eyes had significantly decreased PPARγ expression compared to healthy rats [16]. PPARγ agents have been shown to directly influence the transcription of antioxidants through the activation of PPAR response elements located in their respective promoter regions, such as catalases, superoxide dismutases 1 and 2 [82]. As such, they have been employed in the inhibition of the occurrence of oxidative stress [83].

Rosiglitazone, a PPARγ agonist, has been evaluated in the context of diabetes-related and hyperlipidemia-related dry eye in mouse models [82, 84]. Daily rosiglitazone administration effectively reduced ROS accumulation in the lacrimal glands of diabetes-related dry eye rat models in 4 weeks [82]. This effect was observed through a significant decrease in ROS fluorescein intensity in the rosiglitazone-treated group, distinguishing itself from both the non-treatment and vehicle groups of diabetes-related dry eye rat models [82].

Further real-time RT-PCR analysis revealed significantly increased mRNA expression levels of antioxidant enzymes glutathione peroxidase 3 (GPx3) and heme oxygenase-1 (HO-1) in the lacrimal gland of the rosiglitazone-treated group [82]. Tear production was also significantly increased following rosiglitazone administration. Apart from its beneficial effects in stimulating tear production in the lacrimal glands, it alleviated ocular surface damage as evidenced by significant improvements in corneal fluorescein staining score compared to the non-treatment group [82]. Additionally, rosiglitazone led to significantly decreased ROS levels within the cornea, determined through comparisons of ROS fluorescein intensity [82]. In a separate study, rosiglitazone effectively reduced pro-inflammatory cytokines and inflammatory cell infiltration within the meibomian glands of hyperlipidaemic rat models, yielding favourable effects in alleviating meibomian gland dysfunction and evaporative dry eye disease [84]. These findings highlight the potential therapeutic role of PPARγ in the management of dry eye disease.

Fenofibrate, a PPARα agonist, has been reported to suppress the formation of ocular surface squamous metaplasia, a pathological process of dry eye disease. In a rat model study where tear film instability was induced by topical benzalkonium chloride (BAC), topical fenofibrate demonstrated a reduction in abnormal corneal epidermal differentiation [85]. This reduction was evidenced by decreased expression of K10 keratin, an epidermal keratinocyte-specific intermediate filament, within the corneal epithelium of the fenofibrate-treated group compared to the non-treatment/vehicle groups through immunostaining [85]. Additionally, objective markers evaluating tear film instability, including corneal fluorescein sodium staining scoring was significantly improved in the fenofibrate-treated [85]. As such, fenofibrate has displayed its potential effectiveness in reducing the inflammatory response and offering a treatment option for use as a preventive agent in patients with high risks of dry eye [85].

PPARs on corneal neovascularisation

Corneal angiogenesis typically occurs in wound healing and tissue repair. The pathogenesis of corneal neovascularisation stems from an interplay of the disequilibrium between proangiogenic and anti-angiogenic factors [86]. Keratocytes have been suggested to be integral in corneal neovascularisation formation given their expression of vascular endothelial growth factors (VEGFs) and MMP-13. These factors are identified to degrade type 1 collagen in the cornea, thereby creating an environment conducive to corneal neovascularisation [87]. While the mainstay initial treatment for neovascular ophthalmopathy involves suppressing endothelial cell growth through anti-VEGF agents, it is accompanied by limitations including suboptimal treatment response, short-effect duration, and side effects [88]. With established PPARα expression in vascular endothelium and prior findings indicating fenofibrate's protective effects against retinal vasculopathy by inhibiting vascular endothelium function, combined with PPARγ's potent molecular inhibition of angiogenesis [89, 90], assessing PPAR agents as a therapeutic target holds promise for the management of corneal neovascularisation.

The expression of PPARα has demonstrated a notably inverse correlation with corneal neovascularisation formation and upregulation of VEGFr3 and MMP13 in alkali-burned corneas of wild-type and PPAR-knockout mice [91]. Additionally, in PPARα knockout mice, significantly higher VEGFr3 and MMP13 levels were exhibited versus wild-type mice following corneal alkali burns. Wild-type mice that were subjected to corneal alkali burn were divided into two groups and administered with 200 μM topical fenofibrate or vehicle solution daily for 5 days to investigate fenofibrate's impact on corneal neovascularisation. Corneal revascularisation was significantly reduced in the fenofibrate-treated group upon clinical slit-lamp examination compared to the vehicle group [91]. In another study, fenofibrate effectively reduced the expression of VEGF mRNA, as well as angiopoietin-1 (Ang-1) and Ang-2, which are proangiogenic factors, in post-alkali burn corneas. These findings suggest that PPARα may play an inhibitory role in the context of neovascularisation [38].

Sarayba et al. investigated the influence of PPARγ on corneal neovascularisation formation in rats with three experimental groups: implanted pellets containing both pioglitazone and VEGF, pellets containing VEGF alone, and controls. Quantitative image analysis based on digital ocular photographs demonstrated a significant reduction in the mean density of corneal neovascularisation formation in the corneas of the VEGF/PPARγ group in comparison to the VEGF group at day 7 after implantation, although there was no statistically significant difference in the mean corneal neovascularisation area between these two groups. This still illustrates, however, the potential anti-angiogenic effect of PPARγ agonist, in mitigating corneal neovascularisation [92].

Figure 3 summarizes the potentials and mechanisms of the 3 PPAR isoforms (PPARα, PPARγ, PPARδ) in mitigating the pathogenesis of various corneal diseases. Each of the 3 PPAR classes exhibited therapeutic effects in promoting corneal wound healing via distinct mechanisms: 1) PPARα enhanced the main energy source of corneal epithelial cells, specifically mitochondrial metabolism 2) PPARδ augmented corneal proliferative capacity, as illustrated by increased expression of Ki67, a marker of cell proliferation. 3) PPARγ contributed to the inhibition of MMP-2 and TGF-β, enzymes that impede corneal wound healing. The anti-inflammatory capabilities of PPAR agents have been evidenced by the modulation of key inflammatory transcription factor, NF-κB via PPARα and PPARδ and the pro-inflammatory cytokine expression by

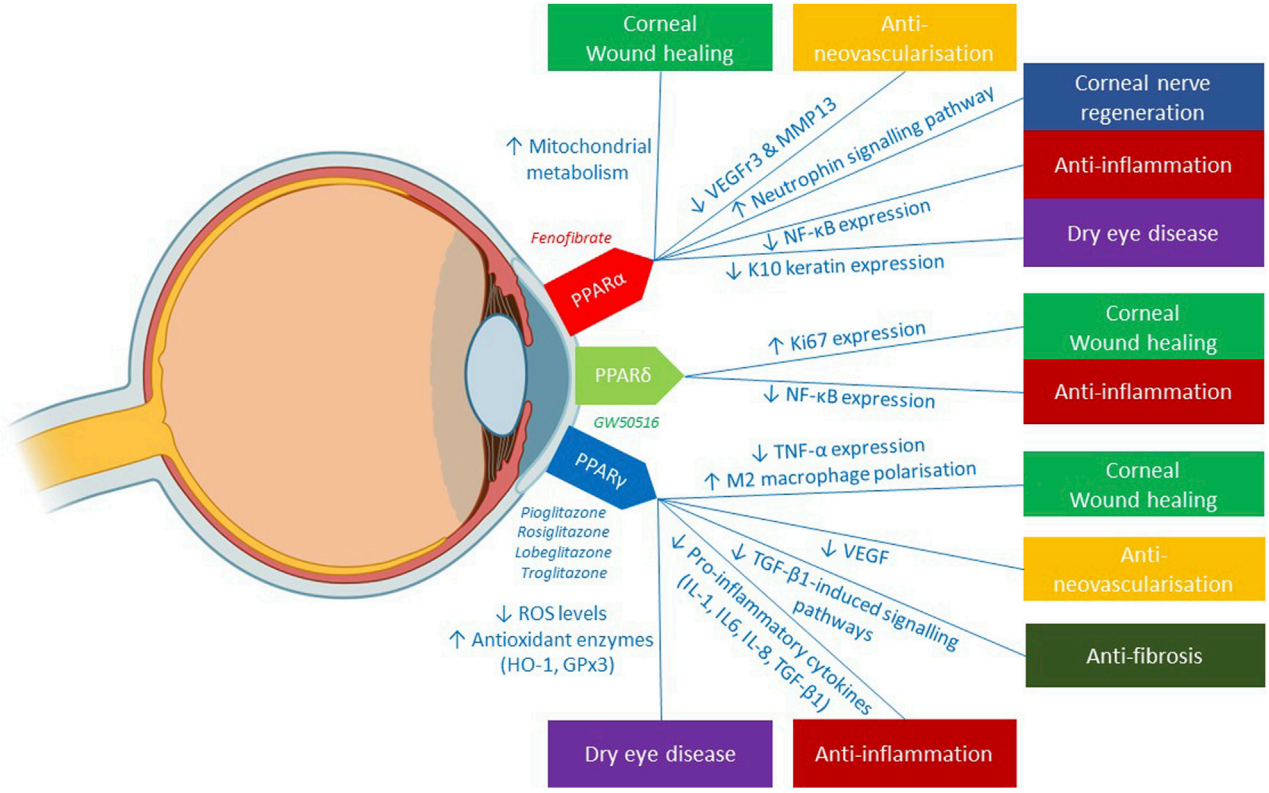

FIGURE 3
Illustration of the clinical applications of 3 PPAR isoforms in corneal diseases and its underlying mechanisms reported in the literature. Figure was created with BioRender.com.

PPARγ. In the realm of anti-neovascularisation, the suppression of pro-angiogenic factors like VEGFr3 and MMP13 by PPARα, as well as VEGF by PPARγ confers anti-angiogenic benefits in managing corneal neovascularisation. The therapeutic effects of PPAR agents in dry eye diseases has been delineated through two main mechanisms: firstly, the anti-oxidative function of PPARγ in diminishing corneal ROS levels, thereby mitigating ocular surface damage; and secondly, the role of PPARα in impeding aberrant corneal epidermal differentiation and consequent formation of ocular surface squamous metaplasia—a late sequelae of dry eye disease. The corneal neurotrophic effects of PPARα agent, fenofibrate, has also been highlighted through the enhanced activation of neuronal pathways involving MAPK, neurotrophin and LA metabolism. Additionally, fenofibrate's active role in anti-inflammation, anticoagulation, and lipid modulation contributes to secondary neurotrophic effects, creating an optimal environment for corneal nerve regeneration.

Clinical safety of PPAR agents

At present, the research of PPAR agents on ocular diseases remains limited, with most studies focusing on *in-vitro* and animal experiments, highlighting a paucity of data on the safety of topical PPAR agents in corneal diseases, However, the clinical application of systemic PPAR agents, notably the PPARα agonists belonging to the fibrates class such as fenofibrate and PPARγ agonists from the thiazolidinedione (TZD) class such as rosiglitazone, are well-validated in the treatment of dyslipidaemia and diabetes, respectively, with an established safety profile [19, 20].

Systemic administration of the fibrate drug class such as fenofibrate exhibits a relatively favourable side-effect profile, with minor associated adverse side-effects spanning from gastrointestinal discomfort, musculoskeletal symptoms, to headaches [15]. Rare instances of rhabdomyolysis has also been described in concurrent use of statin-fibrate therapy, and highlights an increased risk in patients with hypothyroidism, renal disease and diabetes mellitus [93]. Adverse effects of the TZD class includes adverse cardiovascular effects, particularly fluid retention, leading to congestive heart failure and peripheral tissue oedema [94]. Whilst a potential association between TZD use and the development of diabetic macular oedema in diabetic patients has been postulated [95], this remains a topic of debate with subsequent studies reporting no association between the TZD use and diabetic macular oedema [96, 97]. Conversely, there

is limited available data regarding the safety of PPARδ agonists. Of note, the early clinical trials involving the PPARδ agonists, GW501516, were halted due to concerns over accelerated carcinogenicity observed in animal models [98].

Future directions

While the concept of utilising PPAR agents in corneal diseases has gained momentum in recent years, additional efforts are needed to further elucidate the role of the specific PPAR isoforms. Firstly, there remains a need for a deeper understanding of the specific PPAR isoforms involved in specific corneal diseases. As illustrated in this review, different isoforms play distinct roles and further delineation of their functions within the cornea could open avenues for additional therapeutic interventions. Understanding the crosstalk between PPAR and other signalling pathways implicated in corneal diseases could uncover synergistic or antagonistic effects, providing a comprehensive picture of PPAR's role in maintaining corneal homeostasis.

Currently, the studies discussed in this article largely employ the utilisation of animal models, showcasing great promise and broadening our knowledge base on the underlying mechanisms of PPAR agents in treating corneal diseases while serving as a platform to test these novel PPAR therapeutic modalities. Further directions on this aspect may include using *in-vitro* three-dimensional human corneal models and human corneal cell culture models, reducing reliance on animal models, and offering the advantage of enhanced physiological resemblance to *in-vivo* studies. Additionally, conducting clinical trials assessing the efficacy and the long-term safety profile of PPAR agonists in treating specific corneal diseases in a real-world setting is imperative. Rigorous evaluation of the PPAR agents in diverse patient populations will validate their therapeutic potential and guide optimal dosing regimens.

Beyond the future endeavours aimed at establishing PPAR agents' efficacy in the landscape of corneal disease management, there remains a considerable scope to develop novel drug application techniques to bolster the efficacy of current PPAR agents for improved clinical outcomes. The conventional delivery method for the treatment of corneal diseases involves the application of therapeutic agents via topical eye drops. However, it presents with its own limitations, including rapid precorneal drug loss and inability to sustain therapeutic drug concentrations over extended periods [99]. Through nanomedicine which utilises the use of nano-particles as carriers to treat diseases, nano-based ocular delivery may offer a more optimal drug delivery profile, specifically targeting desired corneal cells to intercept pathological pathways [100]. The application of lipid nanoparticles for lipophilic agents like fenofibrate presents a promising avenue, particularly in light of its poor bioavailability due to limited penetration of corneal epithelium [101]. Within the realm of PPAR agents, the utilisation of nanomedicine as a carrier for PPARγ agent has been tested for the treatment of chronic liver disease and have shown to reduce liver fibrosis and inflammation [102]. As such, these studies provide insight into the feasibility of nanomedicine as an innovative delivery platform for PPAR formulations in future. By amalgamating these diverse research trajectories, the field can anticipate a more nuanced understanding and application of PPARs in the therapeutic landscape of corneal diseases.

Conclusion

This article has reviewed current studies detailing the therapeutic effects of PPAR agents in various corneal diseases. Many studies have validated the potential therapeutic effects of PPAR agents in addressing aspects of corneal pathology, including corneal wound healing, neovascularisation, inflammation, fibrosis, nerve regeneration, and dry eye disease. Future studies may involve more in-depth examination of the specific PPAR isoforms in corneal diseases and progress towards the integration of clinical trials, to further attest the beneficial roles of PPAR agents in corneal diseases.

Author contributions

BC: Writing–original draft, Writing–review and editing, Conceptualization, Data curation, Investigation. IL: Writing–review and editing, Data curation. CL: Writing–review and editing, Data curation. Y-CL: Data curation, Investigation, Methodology, Resources, Supervision, Writing–original draft, Writing–review and editing, Conceptualization.

Conflict of interest

The authors declare that the research was conducted in the absence of any commercial or financial relationships that could be construed as a potential conflict of interest.

References

1. Kurpakus-Wheater M, Kernacki KA, Hazlett LD. Maintaining corneal integrity how the "window" stays clear. *Prog Histochem Cytochem* (2001) **36**:179–259. doi:10.1016/s0079-6336(01)80003-6

2. Kaur S, Sohnen P, Swamynathan S, Du Y, Espana EM, Swamynathan SK. Molecular nature of ocular surface barrier function, diseases that affect it, and its relevance for ocular drug delivery. *Ocul Surf* (2023) **30**:3–13. doi:10.1016/j.jtos.2023.08.001

3. Whitcher JP, Srinivasan M, Upadhyay MP. Corneal blindness: a global perspective. *Bull World Health Organ* (2001) **79**:214–21.

4. World Health Organisation. World report on vision –Executive summary (2024). Available from: https://www.who.int/docs/default-source/documents/publications/world-report-on-vision-accessible-executive-summary.pdf (Accessed April 16, 2024).

5. Müller LJ, Marfurt CF, Kruse F, Tervo TMT. Corneal nerves: structure, contents and function. *Exp Eye Res* (2003) **76**:521–42. doi:10.1016/s0014-4835(03)00050-2

6. Al-Aqaba MA, Dhillon VK, Mohammed I, Said DG, Dua HS. Corneal nerves in health and disease. *Prog Retin Eye Res* (2019) **73**:100762. doi:10.1016/j.preteyeres.2019.05.003

7. Yang LWY, Mehta JS, Liu YC. Corneal neuromediator profiles following laser refractive surgery. *Neural Regen Res* (2021) **16**:2177–83. doi:10.4103/1673-5374.308666

8. So WZ, Qi Wong NS, Tan HC, Yu Lin MT, Yu Lee IX, Mehta JS, et al. Diabetic corneal neuropathy as a surrogate marker for diabetic peripheral neuropathy. *Neural Regen Res* (2022) **17**:2172–8. doi:10.4103/1673-5374.327364

9. Chin JY, Lin MTY, Lee IXY, Mehta JS, Liu YC. Tear neuromediator and corneal denervation following SMILE. *J Refract Surg* (2021) **37**:516–23. doi:10.3928/1081597x-20210423-01

10. Brown JD, Plutzky J. Peroxisome proliferator–activated receptors as transcriptional nodal points and therapeutic targets. *Circulation* (2007) **115**:518–33. doi:10.1161/circulationaha.104.475673

11. Desvergne B, Wahli W. Peroxisome proliferator-activated receptors: nuclear control of metabolism*. *Endocr Rev* (1999) **20**:649–88. doi:10.1210/er.20.5.649

12. Xu HE, Lambert MH, Montana VG, Plunket KD, Moore LB, Collins JL, et al. Structural determinants of ligand binding selectivity between the peroxisome proliferator-activated receptors. *Proc Natl Acad Sci* (2001) **98**:13919–24. doi:10.1073/pnas.241410198

13. Issemann I, Green S. Activation of a member of the steroid hormone receptor superfamily by peroxisome proliferators. *Nature* (1990) **347**:645–50. doi:10.1038/347645a0

14. Barbier O, Torra IP, Duguay Y, Blanquart C, Fruchart J-C, Glineur C, et al. Pleiotropic actions of peroxisome proliferator–activated receptors in lipid metabolism and atherosclerosis. *Arterioscler Thromb Vasc Biol* (2002) **22**:717–26. doi:10.1161/01.atv.0000015598.86369.04

15. Escandon P, Vasini B, Whelchel AE, Nicholas SE, Matlock HG, Ma J-X, et al. The role of peroxisome proliferator-activated receptors in healthy and diseased eyes. *Exp Eye Res* (2021) **208**:108617. doi:10.1016/j.exer.2021.108617

16. Mu P-Y, Chu C-C, Yu D, Shao Y, Zhao S-Z. PPARγ: the dominant regulator among PPARs in dry eye lacrimal gland and diabetic lacrimal gland. *Int J Ophthalmol* (2020) **13**:860–9. doi:10.18240/ijo.2020.06.02

17. Lee C-H, Olson P, Evans RM. Minireview: lipid metabolism, metabolic diseases, and peroxisome proliferator-activated receptors. *Endocrinology* (2003) **144**:2201–7. doi:10.1210/en.2003-0288

18. Li S, Nagothu K, Desai V, Lee T, Branham W, Moland C, et al. Transgenic expression of proximal tubule peroxisome proliferator–activated receptor-α in mice confers protection during acute kidney injury. *Kidney Int* (2009) **76**:1049–62. doi:10.1038/ki.2009.330

19. Derosa G, Sahebkar A, Maffioli P. The role of various peroxisome proliferator-activated receptors and their ligands in clinical practice. *J Cell Physiol* (2018) **233**:153–61. doi:10.1002/jcp.25804

20. Takada I, Makishima M. Peroxisome proliferator-activated receptor agonists and antagonists: a patent review (2014-present). *Expert Opin Ther Patents* (2020) **30**:1–13. doi:10.1080/13543776.2020.1703952

21. Moran E, Ding L, Wang Z, Cheng R, Chen Q, Moore R, et al. Protective and antioxidant effects of PPARα in the ischemic retina. *Invest Ophthalmol Vis Sci* (2014) **55**:4568–76. doi:10.1167/iovs.13-13127

22. del V Cano M, Gehlbach PL. PPAR-A ligands as potential therapeutic agents for wet age-related macular degeneration. *PPAR Res* (2008) **2008**:1–5. doi:10.1155/2008/821592

23. Hu Y, Chen Y, Ding L, He X, Takahashi Y, Gao Y, et al. Pathogenic role of diabetes-induced PPAR-α down-regulation in microvascular dysfunction. *Proc Natl Acad Sci U S A* (2013) **110**:15401–6. doi:10.1073/pnas.1307211110

24. Osada M, Sakai T, Kuroyanagi K, Kohno H, Tsuneoka H. Treatment of experimental autoimmune uveoretinitis with peroxisome proliferator-activated receptor α agonist fenofibrate. *Mol Vis* (2014) **20**:1518–26.

25. Zhu J, Zhang J, Ji M, Gu H, Xu Y, Chen C, et al. The role of peroxisome proliferator-activated receptor and effects of its agonist, pioglitazone, on a rat model of optic nerve crush: PPARγ in retinal neuroprotection. *PLoS One* (2013) **8**:e68935. doi:10.1371/journal.pone.0068935

26. Gaballa SA, Kompella UB, Elgarhy O, Alqahtani AM, Pierscionek B, Alany RG, et al. Corticosteroids in ophthalmology: drug delivery innovations, pharmacology, clinical applications, and future perspectives. *Drug Deliv Transl Res* (2021) **11**:866–93. doi:10.1007/s13346-020-00843-z

27. Rigas B, Huang W, Honkanen R. NSAID-induced corneal melt: clinical importance, pathogenesis, and risk mitigation. *Surv Ophthalmol* (2020) **65**:1–11. doi:10.1016/j.survophthal.2019.07.001

28. Jester JV, Nien CJ, Vasiliou V, Brown DJ. Quiescent keratocytes fail to repair MMC induced DNA damage leading to the long-term inhibition of myofibroblast differentiation and wound healing. *Mol Vis* (2012) **18**:1828–39.

29. Mastropasqua L, Lanzini M, Dua HS, D' Uffizi A, Di Nicola M, Calienno R, et al. *In vivo* evaluation of corneal nerves and epithelial healing after treatment with recombinant nerve growth factor for neurotrophic keratopathy. *Am J Ophthalmol* (2020) **217**:278–86. doi:10.1016/j.ajo.2020.04.036

30. Kulkarni VS, Alagarsamy V, Solomon VR, Jose PA, Murugesan S. Drug repurposing: an effective tool in modern drug discovery. *Russ J Bioorg Chem* (2023) **49**:157–66. doi:10.1134/s1068162023020139

31. Saika S. TGFβ pathobiology in the eye. *Lab Invest* (2006) **86**:106–15. doi:10.1038/labinvest.3700375

32. Wang X, Zhang S, Dong M, Li Y, Zhou Q, Yang L. The proinflammatory cytokines IL-1β and TNF-α modulate corneal epithelial wound healing through p16Ink4a suppressing STAT3 activity. *J Cell Physiol* (2020) **235**:10081–93. doi:10.1002/jcp.29823

33. Liang W, Huang L, Whelchel A, Yuan T, Ma X, Cheng R, et al. Peroxisome proliferator-activated receptor-α (PPARα) regulates wound healing and mitochondrial metabolism in the cornea. *Proc Natl Acad Sci USA* (2023) **120**:e2217576120. doi:10.1073/pnas.2217576120

34. Saika S, Yamanaka O, Okada Y, Miyamoto T, Kitano A, Flanders KC, et al. Effect of overexpression of pparγ on the healing process of corneal alkali burn in mice. *Am J Physiology-Cell Physiol* (2007) **293**:C75–C86. doi:10.1152/ajpcell.00332.2006

35. Tobita Y, Arima T, Nakano Y, Uchiyama M, Shimizu A, Takahashi H. Effects of selective peroxisome proliferator activated receptor agonists on corneal epithelial wound healing. *Pharmaceuticals (Basel)* (2021) **14**:88. doi:10.3390/ph14020088

36. Nakamura Y, Nakamura T, Tarui T, Inoue J, Kinoshita S. Functional role of PPARδ in corneal epithelial wound healing. *Am J Pathol* (2012) **180**:583–98. doi:10.1016/j.ajpath.2011.10.006

37. Nakano Y, Uchiyama M, Arima T, Nagasaka S, Igarashi T, Shimizu A, et al. PPARα agonist suppresses inflammation after corneal alkali burn by suppressing proinflammatory cytokines, MCP-1, and nuclear translocation of NF-κB. *Molecules* (2018) **24**:114. doi:10.3390/molecules24010114

38. Arima T, Uchiyama M, Nakano Y, Nagasaka S, Kang D, Shimizu A, et al. Peroxisome proliferator-activated receptor alpha agonist suppresses neovascularization by reducing both vascular endothelial growth factor and angiopoietin-2 in corneal alkali burn. *Sci Rep* (2017) **7**:17763. doi:10.1038/s41598-017-18113-3

39. Uchiyama M, Shimizu A, Masuda Y, Nagasaka S, Fukuda Y, Takahashi H. An ophthalmic solution of a peroxisome proliferator-activated receptor gamma agonist prevents corneal inflammation in a rat alkali burn model. *Mol Vis* (2013) **19**:2135–50.

40. Nakano Y, Arima T, Tobita Y, Uchiyama M, Shimizu A, Takahashi H. Combination of peroxisome proliferator-activated receptor (PPAR) alpha and gamma agonists prevents corneal inflammation and neovascularization in a rat alkali burn model. *Int J Mol Sci* (2020) **21**:5093. doi:10.3390/ijms21145093

41. Tobita Y, Arima T, Nakano Y, Uchiyama M, Shimizu A, Takahashi H. Peroxisome proliferator-activated receptor beta/delta agonist suppresses inflammation and promotes neovascularization. *Int J Mol Sci* (2020) **21**:5296. doi:10.3390/ijms21155296

42. Gervois P, Fruchart J-C, Delerive P, Staels B. Induction of IκBα expression as a mechanism contributing to the anti-inflammatory activities of peroxisome proliferator-activated receptor-α activators*. *J Biol Chem* (2000) **275**:36703–7. doi:10.1074/jbc.m004045200

43. Mosser DM. The many faces of macrophage activation. *J Leukoc Biol* (2003) **73**:209–12. doi:10.1189/jlb.0602325

44. Bouhlel MA, Derudas B, Rigamonti E, Dièvart R, Brozek J, Haulon S, et al. PPARγ activation primes human monocytes into alternative M2 macrophages with anti-inflammatory properties. *Cel Metab* (2007) **6**:137–43. doi:10.1016/j.cmet.2007.06.010

45. Yoshida S, Yoshida A, Matsui H, Takada Y, Ishibashi T. Involvement of macrophage chemotactic protein-1 and interleukin-1β during inflammatory but

not basic fibroblast growth factor–dependent neovascularization in the mouse cornea. *Lab Invest* (2003) **83**:927–38. doi:10.1097/01.lab.0000075642.11787.83

46. Wilson SE. Corneal myofibroblasts and fibrosis. *Exp Eye Res* (2020) **201**: 108272. doi:10.1016/j.exer.2020.108272

47. Tandon A, Tovey JCK, Sharma A, Gupta R, Mohan RR. Role of transforming growth factor beta in corneal function, biology and pathology. *Curr Mol Med* (2010) **10**:565–78. doi:10.2174/1566524011009060565

48. Lim RR, Tan A, Liu Y-C, Barathi VA, Mohan RR, Mehta JS, et al. ITF2357 transactivates Id3 and regulate TGFβ/BMP7 signaling pathways to attenuate corneal fibrosis. *Sci Rep* (2016) **6**:20841. doi:10.1038/srep20841

49. Kang JS, Liu C, Derynck R. New regulatory mechanisms of TGF-β receptor function. *Trends Cel Biol* (2009) **19**:385–94. doi:10.1016/j.tcb.2009.05.008

50. Mu Y, Gudey SK, Landström M. Non-Smad signaling pathways. *Cell Tissue Res* (2012) **347**:11–20. doi:10.1007/s00441-011-1201-y

51. Zhou B, Buckley ST, Patel V, Liu Y, Luo J, Krishnaveni MS, et al. Troglitazone attenuates TGF-β1-induced EMT in alveolar epithelial cells via a ppary-independent mechanism. *PLoS One* (2012) **7**:e38827. doi:10.1371/journal.pone.0038827

52. Liu Y, Dai B, Xu C, Fu L, Hua Z, Mei C. Rosiglitazone inhibits transforming growth factor-β1 mediated fibrogenesis in ADPKD cyst-lining epithelial cells. *PLoS One* (2011) **6**:e28915. doi:10.1371/journal.pone.0028915

53. Pan H, Chen J, Xu J, Chen M, Ma R. Antifibrotic effect by activation of peroxisome proliferator-activated receptor–γ in corneal fibroblasts. *Mol Vis* (2009) **15**:2279–86.

54. Jeon K-I, Phipps RP, Sime PJ, Huxlin KR. Inhibitory effects of PPARγ ligands on TGF-β1-induced CTGF expression in cat corneal fibroblasts. *Exp Eye Res* (2015) **138**:52–8. doi:10.1016/j.exer.2015.06.028

55. Jeon K-I, Kulkarni A, Woeller CF, Phipps RP, Sime PJ, Hindman HB, et al. Inhibitory effects of PPARγ ligands on TGF-β1–induced corneal myofibroblast transformation. *Am J Pathol* (2014) **184**:1429–45. doi:10.1016/j.ajpath.2014.01.026

56. Jeon K-I, Phipps RP, Sime PJ, Huxlin KR. Antifibrotic actions of peroxisome proliferator-activated receptor γ ligands in corneal fibroblasts are mediated by β-catenin–regulated pathways. *Am J Pathol* (2017) **187**:1660–9. doi:10.1016/j.ajpath.2017.04.002

57. Nuwormegbe S, Park N-Y, Kim SW. Lobeglitazone attenuates fibrosis in corneal fibroblasts by interrupting TGF-beta-mediated Smad signaling. *Graefes Arch Clin Exp Ophthalmol* (2022) **260**:149–62. doi:10.1007/s00417-021-05370-2

58. Teo AWJ, Zhang J, Zhou L, Liu Y-C. Metabolomics in corneal diseases: a narrative review from clinical aspects. *Metabolites* (2023) **13**:380. doi:10.3390/metabo13030380

59. Mansoor H, Tan HC, Lin MT-Y, Mehta JS, Liu Y-C. Diabetic corneal neuropathy. *J Clin Med* (2020) **9**:3956. doi:10.3390/jcm9123956

60. Matlock HG, Qiu F, Malechka V, Zhou K, Cheng R, Benyajati S, et al. Pathogenic role of PPARα downregulation in corneal nerve degeneration and impaired corneal sensitivity in diabetes. *Diabetes* (2020) **69**:1279–91. doi:10.2337/db19-0898

61. Mansoor H, Lee IXY, Lin MT-Y, Ang HP, Peh GSL, Tan HC, et al. Evaluation of the effect of topical and oral peroxisome proliferator-activated receptor α (PPARα) agonist on corneal nerve regeneration in diabetic mice. *Invest Ophthalmol Vis Sci* (2022) **63**:1220–A0220.

62. Liu YC, Lin MT, Mehta JS. Analysis of corneal nerve plexus in corneal confocal microscopy images. *Neural Regen Res* (2021) **16** (4):690–691. doi:10.4103/1673-5374.289435

63. Teo CHY, Lin MT-Y, Lee IXY, Koh S-K, Zhou L, Goh DS, et al. Oral peroxisome proliferator–activated receptor-α agonist enhances corneal nerve regeneration in patients with type 2 diabetes. *Diabetes* (2023) **72**:932–46. doi:10.2337/db22-0611

64. Agthong S, Kaewsema A, Tanomsridejchai N, Chentanez V. Activation of MAPK ERK in peripheral nerve after injury. *BMC Neurosci* (2006) **7**:45. doi:10.1186/1471-2202-7-45

65. Brownlee M, Aiello LP, Cooper ME, Vinik AI, Plutzky J, Boulton AJM. Chapter 33-complications of diabetes mellitus. In: Melmed S, Polonsky KS, Larsen PR, Kronenberg HM, editors. *Williams textbook of endocrinology (thirteenth edition)*. Philadelphia: Elsevier (2012). p. 1484–581.

66. Verheijen MHG, Peviani M, Hendricusdottir R, Bell EM, Lammens M, Smit AB, et al. Increased axonal ribosome numbers is an early event in the pathogenesis of amyotrophic lateral sclerosis. *PLOS ONE* (2014) **9**:e87255. doi:10.1371/journal.pone.0087255

67. Balfour JA, McTavish D, Heel RC. Fenofibrate. *Drugs* (1990) **40**:260–90. doi:10.2165/00003495-199040020-00007

68. Avraham O, Feng R, Ewan EE, Rustenhoven J, Zhao G, Cavalli V. Profiling sensory neuron microenvironment after peripheral and central axon injury reveals key pathways for neural repair. *Elife* (2021) **10**:e68457. doi:10.7554/elife.68457

69. Caillaud M, Patel NH, White A, Wood M, Contreras KM, Toma W, et al. Targeting Peroxisome Proliferator-Activated Receptor-α (PPAR- α) to reduce paclitaxel-induced peripheral neuropathy. *Brain Behav Immun* (2021) **93**: 172–85. doi:10.1016/j.bbi.2021.01.004

70. Cho YR, Lim JH, Kim MY, Kim TW, Hong BY, Kim Y-S, et al. Therapeutic effects of fenofibrate on diabetic peripheral neuropathy by improving endothelial and neural survival in db/db mice. *PLOS ONE* (2014) **9**:e83204. doi:10.1371/journal.pone.0083204

71. Keech A, Simes RJ, Barter P, Best J, Scott R, Taskinen MR, et al. Effects of long-term fenofibrate therapy on cardiovascular events in 9795 people with type 2 diabetes mellitus (the FIELD study): randomised controlled trial. *Lancet* (2005) **366**:1849–61. doi:10.1016/S0140-6736(05)67667-2

72. Koo JW, Russo SJ, Ferguson D, Nestler EJ, Duman RS. Nuclear factor-κB is a critical mediator of stress-impaired neurogenesis and depressive behavior. *Proc Natl Acad Sci U S A* (2010) **107**:2669–74. doi:10.1073/pnas.0910658107

73. Levenson JM, Choi S, Lee S-Y, Cao YA, Ahn HJ, Worley KC, et al. A bioinformatics analysis of memory consolidation reveals involvement of the transcription factor c-rel. *J Neurosci* (2004) **24**:3933–43. doi:10.1523/jneurosci.5646-03.2004

74. Gutierrez H, Davies AM. Regulation of neural process growth, elaboration and structural plasticity by NF-κB. *Trends Neurosciences* (2011) **34**:316–25. doi:10.1016/j.tins.2011.03.001

75. Qian Y, Zeng Y, Lin Q, Huang H, Zhang W, Yu H, et al. Association of platelet count and plateletcrit with nerve conduction function and peripheral neuropathy in patients with type 2 diabetes mellitus. *J Diabetes Invest* (2021) **12**:1835–44. doi:10.1111/jdi.13535

76. Han SB, Liu Y-C, Mohamed-Noriega K, Tong L, Mehta JS. Objective imaging diagnostics for dry eye disease. *J Ophthalmol* (2020) **2020**:1–11. doi:10.1155/2020/3509064

77. Craig JP, Nichols KK, Akpek EK, Caffery B, Dua HS, Joo C-K, et al. TFOS DEWS II definition and classification report. *Ocul Surf* (2017) **15**:276–83. doi:10.1016/j.jtos.2017.05.008

78. Teo CHY, Ong HS, Liu Y-C, Tong L. Meibomian gland dysfunction is the primary determinant of dry eye symptoms: analysis of 2346 patients. *Ocul Surf* (2020) **18**:604–12. doi:10.1016/j.jtos.2020.06.008

79. Seen S, Tong L. Dry eye disease and oxidative stress. *Acta Ophthalmologica* (2018) **96**:e412–e420. doi:10.1111/aos.13526

80. Maiese K. New insights for oxidative stress and diabetes mellitus. *Oxidative Med Cell Longevity* (2015) **2015**:875961–17. doi:10.1155/2015/875961

81. Pasupuleti VR, Arigela CS, Gan SH, Salam SKN, Krishnan KT, Rahman NA, et al. A review on oxidative stress, diabetic complications, and the roles of honey polyphenols. *Oxidative Med Cell Longevity* (2020) **2020**:1–16. doi:10.1155/2020/8878172

82. Wang J, Chen S, Zhao X, Guo Q, Yang R, Zhang C, et al. Effect of PPARγ on oxidative stress in diabetes-related dry eye. *Exp Eye Res* (2023) **231**:109498. doi:10.1016/j.exer.2023.109498

83. Li J, Shen X. Effect of rosiglitazone on inflammatory cytokines and oxidative stress after intensive insulin therapy in patients with newly diagnosed type 2 diabetes. *Diabetology Metab Syndr* (2019) **11**:35. doi:10.1186/s13098-019-0432-z

84. Li W, Bu J, Wu Y, Yu J, He X, He H, et al. Hyperlipidemia induces meibomian gland dysfunction. *Acta Ophthalmologica* (2019) **97**:777–86. doi:10.1111/j.1755-3768.2019.5281

85. He H, Liang M, Li L, Luo S, Fang X, He H, et al. PPAR-A agonist fenofibrate suppressed the formation of ocular surface squamous metaplasia induced by topical benzalkonium chloride. *Invest Opthalmology Vis Sci* (2020) **61**:54. doi:10.1167/iovs.61.3.54

86. Philipp W, Speicher L, Humpel C. Expression of vascular endothelial growth factor and its receptors in inflamed and vascularized human corneas. *Invest Ophthalmol Vis Sci* (2000) **41**:2514–22.

87. Ma J, Zhou D, Fan M, Wang H, Huang C, Zhang Z, et al. Keratocytes create stromal spaces to promote corneal neovascularization via MMP13 expression. *Invest Ophthalmol Vis Sci* (2014) **55**:6691–703. doi:10.1167/iovs.14-14746

88. Ghasemi Falavarjani K, Nguyen QD. Adverse events and complications associated with intravitreal injection of anti-VEGF agents: a review of literature. *Eye (Lond)* (2013) **27**:787–94. doi:10.1038/eye.2013.107

89. Plutzky J. Peroxisome proliferator-activated receptors in endothelial cell biology. *Curr Opin Lipidol* (2001) **12**:511–8. doi:10.1097/00041433-200110000-00006

90. Ding L, Cheng R, Hu Y, Takahashi Y, Jenkins AJ, Keech AC, et al. Peroxisome proliferator–activated receptor α protects capillary pericytes in the retina. *Am J Pathol* (2014) **184**:2709–20. doi:10.1016/j.ajpath.2014.06.021

91. Wang X, Tang L, Zhang Z, Li W, Chen Y. Keratocytes promote corneal neovascularization through VEGFr3 induced by PPARα-inhibition. *Exp Eye Res* (2020) **193**:107982. doi:10.1016/j.exer.2020.107982

92. Sarayba MA, Li L, Tungsiripat T, Liu NH, Sweet PM, Patel AJ, et al. Inhibition of corneal neovascularization by a peroxisome proliferator-activated receptor-γ ligand. *Exp Eye Res* (2005) **80**:435–42. doi:10.1016/j.exer.2004.10.009

93. Després J-P, Lemieux I, Robins SJ. Role of fibric acid derivatives in the management of risk factors for coronary heart disease. *Drugs* (2004) **64**:2177–98. doi:10.2165/00003495-200464190-00003

94. Nesto RW, Bell D, Bonow RO, Fonseca V, Grundy SM, Horton ES, et al. Thiazolidinedione use, fluid retention, and congestive heart failure. *Circulation* (2003) **108**:2941–8. doi:10.1161/01.cir.0000103683.99399.7e

95. Idris I, Warren G, Donnelly R. Association between thiazolidinedione treatment and risk of macular edema among patients with type 2 diabetes. *Arch Intern Med* (2012) **172**:1005–11. doi:10.1001/archinternmed.2012.1938

96. Gower EW, Lovato JF, Ambrosius WT, Chew EY, Danis RP, Davis MD, et al. Lack of longitudinal association between thiazolidinediones and incidence and progression of diabetic eye disease: the ACCORD eye study. *Am J Ophthalmol* (2018) **187**:138–47. doi:10.1016/j.ajo.2017.12.007

97. Ambrosius WT, Danis RP, Goff DC, Jr, Greven CM, Gerstein HC, Cohen RM, et al. Lack of association between thiazolidinediones and macular edema in type 2 diabetes: the ACCORD eye substudy. *Arch Ophthalmol* (2010) **128**:312–8. doi:10.1001/archophthalmol.2009.310

98. Sahebkar A, Chew GT, Watts GF. New peroxisome proliferator-activated receptor agonists: potential treatments for atherogenic dyslipidemia and non-alcoholic fatty liver disease. *Expert Opin Pharmacother* (2014) **15**:493–503. doi:10.1517/14656566.2014.876992

99. Patel A, Cholkar K, Agrahari V, Mitra AK. Ocular drug delivery systems: an overview. *World J Pharmacol* (2013) **2**:47–64. doi:10.5497/wjp.v2.i2.47

100. Chaurasia SS, Lim RR, Lakshminarayanan R, Mohan RR. Nanomedicine approaches for corneal diseases. *J Funct Biomater* (2015) **6**:277–98. doi:10.3390/jfb6020277

101. Liu Y-C, Lin MT-Y, Ng AHC, Wong TT, Mehta JS. Nanotechnology for the treatment of allergic conjunctival diseases. *Pharmaceuticals (Basel)* (2020) **13**:351. doi:10.3390/ph13110351

102. Moreno-Lanceta A, Medrano-Bosch M, Simón-Codina B, Barber-González M, Jiménez W, Melgar-Lesmes P. PPAR-Γ agonist GW1929 targeted to macrophages with dendrimer–graphene nanostars reduces liver fibrosis and inflammation. *Pharmaceutics* (2023) **15**:1452. doi:10.3390/pharmaceutics15051452

EBM Experimental Biology and Medicine

TYPE Retraction
PUBLISHED 10 June 2024
DOI 10.3389/ebm.2024.10243

OPEN ACCESS

*CORRESPONDENCE
EBM Editorial Office,
ebm@ebm-journal.org

RECEIVED 16 May 2024
ACCEPTED 16 May 2024
PUBLISHED 10 June 2024

CITATION
EBM Editorial Office (2024), Retraction: TRIM29 promotes the progression of colorectal cancer by suppressing EZH2 degradation. *Exp. Biol. Med.* 249:10243. doi: 10.3389/ebm.2024.10243

Retraction: TRIM29 promotes the progression of colorectal cancer by suppressing EZH2 degradation

EBM Editorial Office*

A Retraction of the Original Research Article
TRIM29 promotes the progression of colorectal cancer by suppressing EZH2 degradation

by By Chen Y, Ma J, Zhang M. (2023). Experimental Biology and Medicine. 248(18):1527-1536. doi: 10.1177/15353702231199070

Following publication, concerns were raised about the duplicate submission of the article cited above in Experimental Biology and Medicine and BMC Gastroenterology. The article was published on 14 October 2023.

On 20 March 2024 the Editor in Chief of BMC Gastroenterology made the Editor in Chief of EBM aware that the article had been submitted to BMC on 14 March 2023. The article was rejected from BMC.

In line with the evidence of misconduct and the EBM dual submission policy, this article is retracted.

The authors received communication regarding the retraction but did not respond. This communication has been recorded by the publisher.

Experimental Biology & Medicine Conference

Orlando, FL - October 13 -16, 2024

Please visit **exbiomedcon.org** or scan the QR code for more info.

Keynote Lecturers

Namandjè Bumpus, Ph.D.
Chief Scientist - US Food and Drug Administration

Advancing Emerging Technologies in Regulatory Science

Michael Friedlander, Ph.D.
Vice President - Health Sciences and Technology at Virginia Tech

All events will take place at the Embassy Suites by Hilton, Orlando Lake Buena Vista South

Cardiovascular

Delphine Gomez, Ph.D.
University of Pittsburgh

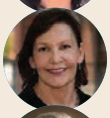

Karen Hirschi, Ph.D.
University of Virginia

Jay Humphrey, Ph.D.
Yale University

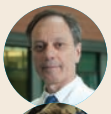

Ali J. Marian, M.D.
The University of Texas Health Science Center at Houston

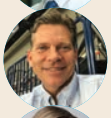

Joseph Miano, Ph.D.
Medical College of Georgia

Dianna Milewicz, M.D., Ph.D.
University of Texas Heath Science Center Houston

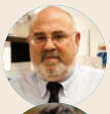

Robert Schwartz, Ph.D.
University of Houston

George Taffet, M.D.
Baylor College of Medicine

David Zawieja, Ph.D.
Texas A&M University Health Science Center

Neuroscience

Lique Coolen, Ph.D.
Kent State university

Michael Fehlings, M.D.
University of Toronto

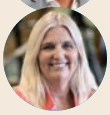

Susan Harkema, Ph.D.
University of Louisville

Maria Lehtinen, Ph.D.
Harvard University

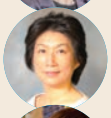

Fang Liu, Ph.D.
NCTR/US Food and Drug Administration

Agnes Luo, Ph.D.
University Cincinnati

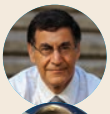

Mervyn Maze, MBChB
University of California San Francisco

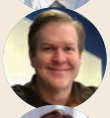

Dorian McGavern, Ph.D.
National Institute of Neurological Diorders and Stroke

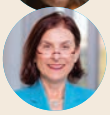

Vesna Jevtovic-Todorovic, M.D., Ph.D.
University of Colorado School of Medicine

Regenerative Medicine

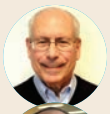

Arnold I. Caplan, Ph.D.
Case Western Reserve

Jian Feng, Ph.D.
State University of New York at Buffalo

Joshua Hare, M.D.
University of Miami

Karen Hasty, Ph.D.
University of Tennessee Health Science Center

Rajasingh Johnson, Ph.D.
University of Tennessee Health Science Center

Y. James Kang, DVM, Ph.D.
Sichuan University

Kwang-Soo Kim,Ph.D.
Harvard University

Joanne Kurtzberg, M.D.
Duke University

Jun Wu, Ph.D.
UT Southwestern

Trainees

Justin Boyd, Ph.D.
Vaxxinity

Udayan Apte, Ph.D.
U of Kansas Medical Center

Ram Kumar, Ph.D.
U of Kansas Medical Center

And More

Career Development
Short Talks
Poster Sessions
Member Blitz

SEBM SOCIETY FOR EXPERIMENTAL BIOLOGY AND MEDICINE

EBM Experimental Biology and Medicine

Scope

Experimental Biology and Medicine (EBM) is a global, peer-reviewed journal dedicated to the publication of multidisciplinary and interdisciplinary research in the biomedical sciences. The journal covers the spectrum of translational research from T0, basic research, to T4, population health. Articles in EBM represent cutting edge research at the overlapping junctions of the biological, physical and engineering sciences that impact upon the health and welfare of the world's population. EBM is particularly appropriate for publication of papers that are multidisciplinary in nature, are of potential interest to a wide audience, and represent experimental medicine in the broadest sense of the term. However, manuscripts reporting novel findings on any topic in the realm of experimental biology and medicine are most welcome.

EBM publishes Research, Reviews, Mini Reviews, and Brief Communications in the following categories.

- Anatomy/Pathology
- Artificial Intelligence/ Machine Learning Applications to Biomedical Research
- Biochemistry and Molecular Biology
- Bioimaging
- Biomedical Engineering
- Bionanoscience
- Cell and Developmental Biology
- Clinical Trials
- Endocrinology and Nutrition
- Environmental Health/Biomarkers/ Precision Medicine
- Genomics, Proteomics, and Bioinformatics
- Immunology/Microbiology/Virology
- Mechanisms of Aging
- Neuroscience
- Pharmacology and Toxicology
- Physiology and Pathophysiology
- Population Health
- Stem Cell Biology
- Structural Biology
- Synthetic Biology
- Systems Biology and Microphysiological Systems
- Translational Research

EBM Experimental Biology and Medicine

EBM is the official journal of the Society for Experimental Biology and Medicine

Led by Dr Steven Goodman, Experimental Biology and Medicine (EBM) is a global, peer-reviewed journal dedicated to the publication of multidisciplinary and interdisciplinary research in the biomedical sciences.

Discover more of our Special Issues

See more →

Contact

development@ebm-journal.org

See more

ebm-journal.org

publishingpartnerships.frontiersin.org/our-partners